

PHOTOPRODUCTION OF CHARGED PION PAIRS FROM HYDROGEN

AT ENERGIES UP TO 1500 MeV

Thesis by

Lyman Jefferson Fretwell, Jr.

In Partial Fulfillment of the Requirements

For the Degree of

Doctor of Philosophy

California Institute of Technology

Pasadena, California

1967

(Submitted June 9, 1966)

ACKNOWLEDGMENTS

I would like to thank my director of research, Dr. J.H. Mullins, for his willingness to counsel and help at any time throughout the many years it took this experiment to come to fruition. His help in designing and building the bubble chamber and getting the synchrotron to work properly were vital to the pursuit of this experiment.

Special thanks also go to my co-worker, Mr. D.G. Coyne, for his generous help in all phases of this experiment, from chamber construction to data analysis.

Gratitude is due the many people who have worked on this project in the past and have given me much help and advice, particularly Drs. J.M. Teem, E.D. Alyea, D.E. Groom, and C.W. Peck.

Help, support, and encouragement from Professors R.L. Walker, A.V. Tollestrup, and R.F. Bacher are gratefully acknowledged. Professor George Zweig provided valuable comments on result interpretation.

I want to thank the many members of our scanning and analysis crew. Although there are too many to mention each by name, I would like to thank Mrs. Phyllis Nilsson for her work analyzing and computing.

Thanks go to Mr. Herbert Juds, bubble chamber technician and later scanning technician, and to Mr. Larry Loucks and the rest of the synchrotron crew. I am grateful for much engineering help with the chamber and analysis equipment to Mr. Harry Coffey, Mr. Ed. Taylor,

and Mr. Dan Sell and the other members of the Central Engineering Services. Thanks for much help to Mrs. Beatrice Hall and Miss Cherry Carter. The staffs of the Central Shop and the Computing Center have also been very helpful. Thanks also to my patient typist, Miss Yvonne Dawson.

Financial Support of the National Science Foundation and the Atomic Energy Commission are gratefully acknowledged.

I especially want to thank my loving wife, Lenore, for help in setting up scanning and analysis procedures, as well as doing much of the work itself, and for inspiration carrying through to the last word of this thesis itself. To her I dedicate this thesis.

ABSTRACT

Charged pion pair photoproduction has been investigated up to a gamma energy of 1500 MeV, using the Caltech 12-inch heavy liquid bubble chamber with a small diameter, high intensity photon beam passing through a central beam tube gaseous hydrogen target surrounded by the sensitive freon. Scanning, analysis, and data reduction techniques have been developed to deal with the problems of two-view stereo, hidden event origins, absence of magnetic field, and the range-energy and multiple scattering relationships that occur in the heavy materials. Roughly 5700 pictures have been scanned and analyzed, yielding 754 acceptable events. Cross section and parameter distributions are generally consistent with the results of previous experiments. A statistically insignificant "bump" was observed in the dipion mass spectrum in the region of 400 MeV, the disputed σ meson mass. This region was investigated as carefully as the limited statistics would allow; dipion angular distributions are consistent with isotropy, and there is indication that some of the events in this region might come from decay of an intermediate $N_{11}^*(1425)$ into a proton and dipion.

Photographic materials on pp. 18, 20, 22, and 24 are essential and will not reproduce clearly on Xerox copies. Photographic copies should be ordered.

TABLE OF CONTENTS

	Page
ACKNOWLEDGMENTS	ii
ABSTRACT	iv
LIST OF ILLUSTRATIONS	viii
LIST OF TABLES	xi
CHAPTER	
I Introduction	1
II Experimental Method	8
III Experimental Procedures	15
IV Results	31
APPENDICES	
I Beam Line Configuration	95
II Beam Monitoring	107
III Scanning and Analysis Equipment	120
IV Scanning and Analysis Procedures	128
V Event Reconstruction	153
VI Background	198
VII Particle Momentum Measurement	217
VIII Multiple Scattering	232
IX Event Generation Computer Program	238
REFERENCES	247

APPENDICES

Appendix	Title	Page
I	Beam Line Configuration	95
	A. Radiator Placement and Beam Orbit	95
	B. Beam Hardening	96
	C. Collimation, Scraping, Sweeping and Shielding	100
	D. Target	103
	E. Beam Monitoring Equipment	104
	F. Component Alignment	105
II	Beam Monitoring	107
	A. Beam Monitoring Logic	107
	B. Early Beam Dump	109
	C. Beam Absorption	111
	D. Calibration of Ion Chamber	113
	E. Counter Telescope Electronics	115
	F. Beam Correction Summary	117
III	Scanning and Analysis Equipment	120
	A. The First Scanner	120
	B. The Analyzing Scanner	120
	C. The Data Recorder	123
	D. Scanning Aids	124
	1. Scanning Board	124
	2. Ray Tracer	125
	3. Epsilon Limiter	125
	4. Track Starter	125
	E. Operation and Stability for Analysis	126
IV	Scanning and Analysis Procedures	128
	A. Scanning Procedure	128
	B. Scanning Evaluation	132

	C. Analysis Calibrations	140
	D. Direction Measurement Technique	143
	E. Analyzing Table Procedure	146
	F. Computer Output Processing	147
	G. Analysis Evaluation	149
V	Event Reconstruction	153
	A. Program Logic	153
	B. Data Format	156
	C. Visible Track Reconstruction	157
	1. Bubble Chamber Optics Calculation	157
	a. Chamber Position Calculation	158
	b. Chamber Direction Calculation	166
	c. Film Image Calculation	169
	2. Corresponding Point Generation	171
	D. Event Synthesis	179
	1. Starting Parameter Estimation	181
	2. Likelihood Function Maximization	184
	3. Alternate Hypotheses	188
	4. Output	189
	E. Accuracy	189
VI	Background	198
	A. Visual Background	198
	B. Analysis Background	199
	C. Scanned Track Distributions	209
	D. Background Error Evaluation	213
VII	Particle Momentum Measurement	217
	A. Range-Energy Relationship	217
	B. Multiple Scattering Momentum Measurement	226
VIII	Multiple Scattering	232
	A. Single Medium Distribution	232
	B. Multiple Scattering in Two Media	234
IX	Event Generation Computer Program	238

LIST OF ILLUSTRATIONS

Figure	Text	Page
1	Feynman Diagrams for N_{33}^* Photoproduction	6
2	Feynman Diagrams for ρ_0 Photoproduction	7
3	Experimental Arrangement and Beam Area	11
4	Pion Pair Event	17
5	Pion Pair Event with Pion Star	19
6	Pion Pair Event with Background Track	21
7	Two Pion Pair Events within Scanning Resolution	23
8	Total Cross-Section Compared to Other Experiments	40
9	Model Contribution Compared to Other Experiments	44
10	Data Dipion Mass Distribution, $E_\gamma < 600$	47
11	Data Isobar Mass Distribution, $E_\gamma < 600$	48
12	Data Dipion Mass Distribution, $600 < E_\gamma < 1060$	49
13	Data Isobar Mass Distribution, $600 < E_\gamma < 1060$	50
14	Data Dipion Mass Distribution, $E_\gamma > 1060$	51
15	Data Isobar Mass Distribution, $E_\gamma > 1060$	52
16	Generated Phase Space Dipion Mass Distribution, $600 < E_\gamma < 1060$	53
17	Generated Phase Space Isobar Mass Distribution, $600 < E_\gamma < 1060$	54
18	Generated N_{33}^* Dipion Mass Distribution, $600 < E_\gamma < 1060$	55
19	Generated N_{33}^* Isobar Mass Distribution, $600 < E_\gamma < 1060$	56
20	Generated σ Dipion Mass Distribution, $600 < E_\gamma < 1060$	57

	Page
21 Generated σ Isobar Mass Distribution, $600 < E_{\gamma} < 1060$	58
22 Generated ρ Dipion Mass Distribution, $E_{\gamma} > 1060$	59
23 Generated ρ Isobar Mass Distribution, $E_{\gamma} > 1060$	60
24 Generated Phase Space Dipion Mass Distribution, $E_{\gamma} < 600$	61
25 Generated Phase Space Isobar Mass Distribution, $E_{\gamma} < 600$	62
26 Generated N_{33}^* Dipion Mass Distribution, $E_{\gamma} < 600$	63
27 Generated N_{33}^* Isobar Mass Distribution, $E_{\gamma} < 600$	64
28 General COM Polar Angle Distribution of Dipion, $E_{\gamma} < 600$	65
29 Dipion COM Polar Angle Distribution of Pion, $E_{\gamma} < 600$	66
30 Dipion COM Azimuthal Angle Distribution of Pion, $E_{\gamma} < 600$	67
31 General COM Polar Angle Distribution of Isobar, $E_{\gamma} < 600$	68
32 Isobar COM Polar Angle Distribution of Pion, $E_{\gamma} < 600$	69
33 Isobar COM Azimuthal Angle Distribution of Pion, $E_{\gamma} < 600$	70
34 General COM Polar Angle Distribution of Dipion, $600 < E_{\gamma} < 1060$	71
35 Dipion COM Polar Angle Distribution of Pion, $600 < E_{\gamma} < 1060$	72
36 Dipion COM Azimuthal Angle Distribution of Pion, $600 < E_{\gamma} < 1060$	73
37 General COM Polar Angle Distribution of Isobar, $600 < E_{\gamma} < 1060$	74
38 Isobar COM Polar Angle Distribution of Pion, $600 < E_{\gamma} < 1060$	75

39	Isobar COM Azimuthal Angle Distribution of Pion, $600 < E_{\gamma} < 1060$	76
40	General COM Polar Angle Distribution of Dipion, $E_{\gamma} > 1060$	77
41	Dipion COM Polar Angle Distribution of Pion, $E_{\gamma} > 1060$	78
42	Dipion COM Azimuthal Angle Distribution of Pion $E_{\gamma} > 1060$	79
43	General COM Polar Angle Distribution of Isobar, $E_{\gamma} > 1060$	80
44	Isobar COM Polar Angle Distribution of Pion, $E_{\gamma} > 1060$	81
45	Isobar COM Azimuthal Angle Distribution of Pion, $E_{\gamma} > 1060$	82
46	Dipion Mass Distribution for Three Regions of Momentum Transfer ($600 < E_{\gamma} < 1060$)	85
47	Total Energy Distribution for Three Regions of Momentum Transfer ($600 < E_{\gamma} < 1060$, $360 < \text{Dipion Mass} < 480$)	87
48	Dipion Angular Distributions ($600 < E_{\gamma} < 1060$, $360 < \text{Dipion Mass} < 480$)	90

APPENDICES

A I-1	Bremsstrahlung Energy Spectrum in Target	98
A V-1	Data Analysis Program Logic Flow	154
A V-2	Bubble Chamber Optics Calculation Schematic Views	159
A V-3	Track Segment Description Schematic	175
A VI-1	Background Event Parameter Distributions	215
A VII-1	Multiple Scattering Range Effect Schematic	220
A VII-2	Hidden Material Traversal Schematic	224

A VII-3	Multiple Scattering Momentum Measurement	227
A IX-1	Accepted Event Origin Distribution.	240

LIST OF TABLES

Table	Text	Page
1	Yield and Total Cross Section for this Experiment	34
2	Chamber Detection Efficiency	36
3	Parameters from Model Fit to Data	42

Appendices

A II-1	Comparison of Counter Telescope and 40 MC Probe	110
A II-2	Percent Downstream Gamma Beam Absorption	112
A II-3	Beam Passing Through Hydrogen Target	119
A IV-1	Scanning Comparison Efficiencies	133
A IV-2	Film Region Scanning Efficiencies	134
A IV-3	Scanning Identification Accuracy	139
A V-1	Gamma Energy Errors for Analyzed Generated Events	191
A V-2	Average Parameter Measurement Errors for Valid Events	197
A VI-1	Background Event Acceptance Summary	202
A VI-2	Chamber Detection Efficiency	205
A VI-3	Approximate Pion Photoproduction Yields	205
A VI-4	Event Acceptance Rates	208
A VI-5	Scanned Event Prong Distributions	208
A VI-6	Possible Electronic Contribution in Scanning	212
A IX-1	Average Minimum Projected Track Length for Valid Events	246

I. INTRODUCTION

With the success of counter telescope and magnetic spectrometer techniques in studying single pion photoproduction processes, and the discovery of resonance phenomena associated with their production, attention naturally focused on the photoproduction of pion pairs as the next step up the ladder of complexity in pion photoproduction. The old techniques were not so easily applied to this problem, and they often led to low counting rates. Since its advent into the family of particle detectors, the bubble chamber has been recognized as an especially useful tool in high energy reactions with more than two particles in the final state. This thesis reports work done on the photoproduction of charged pion pairs from hydrogen, using the Caltech heavy liquid bubble chamber.

Charged pion pair photoproduction has been under study for the past twelve years¹⁻²⁷⁾. Early work was directed toward measurement of negative pion yields from photoproduction in hydrogen, with charge conservation implying pion pair production¹⁻⁶⁾. Then the negative pion was detected in a magnetic spectrometer together with the positive pion in a counter telescope⁷⁾. This study corroborated earlier indications that, in the general center-of-momentum system, the π^- went forward with low energy, while the π^+ was isotropic with higher energy, inferring the intermediate production of a doubly charged pion-nucleon isobar. However, counting rates were low and coverage of all available reaction phase space would be very difficult with this procedure.

The first attempt to study large solid angles in this reaction

employed a hydrogen-filled diffusion cloud chamber^{8,9)}. These results gave the above picture, with the exception that π^- energies were no longer peaked toward low values for gamma energy (E_γ) in the range $700 < E_\gamma < 1000$ MeV as they had been in the range $500 < E_\gamma < 700$. They concluded that the first pion-nucleon resonance, $N_{33}^*(1238)$, was indeed present, but that $\gamma + P \rightarrow N^* + \pi$ was probably not the only mechanism for pion pair photoproduction in this energy region.

Forward photoproduction of negative pions from hydrogen was measured with a magnetic spectrometer¹⁰⁾ in an attempt to discover whether such peripheral interactions could be explained by the one-pion-exchange model of Drell¹¹⁾. Angle and energy distributions agreed in shape with Drell's theory, but the cross-section came out roughly a factor of two higher, indicating that this was probably not the only process contributing¹²⁾.

Discovery of the ρ meson in π - π interactions¹³⁾ led to a search for its presence in pion pair photoproduction. The proton and one of the pions were detected in magnetic spectrometers so set up that $P\pi$ invariant masses in the region of the N_{33}^* would be avoided¹⁴⁾. The ρ was indeed found to be present.

Desirability of a π - π resonance in the neighborhood of 400 MeV invariant mass (so-called σ meson) to explain energy spectra and branching ratios of K and η meson decay¹⁵⁾ and the $K_1 - K_2$ mass difference¹⁶⁾ as well as indication of its existence in π - π spectrum from $\pi^- - p$ collisions¹⁷⁾ led to a search for its presence in pion

pair photoproduction. Del Fabbro et al., using spark chambers and counters^{18,19)} found some evidence for such a resonance.

Recent work by the Cambridge Bubble Chamber Group^{20,21)} and the DESY Bubble Chamber Group²²⁾ has extended pion pair photoproduction up to incoming gamma energies of 5.5 GeV by passing a photon beam directly through a hydrogen bubble chamber. They find that up to 1200 MeV N_{33}^{*++} production dominates the reaction; above this energy N^* production decreases and neutral ρ production dominates the process. In N^* production they find disagreement with the one-pion-exchange model of Drell¹¹⁾, but their results agree with the one-pion-exchange model of Stichel and Scholz²³⁾, who modified Drell's model to include corrections for gauge invariance. However, the sharp peaking of the N^* production cross section in the region of total system invariant mass approximating that of the N_{13}^{**} (1512) and N_{15}^{**} (1688) pion-nucleon resonances suggests that perhaps the N_{33}^* might be produced via these resonances. Neutral ρ production at higher energy and low momentum transfer to the proton agrees better with the diffraction model of Berman and Drell²⁴⁾ than the one-pion-exchange model. Primary features of the ρ^0 production are that the cross-section remains relatively constant (in the neighborhood of 12 μ barns) at high energy, and that the angular distribution of the ρ is strongly peaked forward in the total center-of-momentum system.

Theoretical predictions have enjoyed limited success in understanding pion pair photoproduction. At low energy, the theory of Cutkosky and Zachariasen²⁵⁾ assumes that the only important

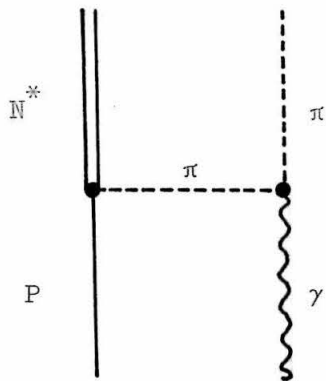
contribution comes from having one pion produced in an S state and one in a P state. Carruthers and Wong²⁶⁾ take this P state to be the obvious N_{33}^* , and find fairly good agreement with the results of Chasan et al.⁹⁾ below 1000 MeV. S-wave photoproduction of an N^* and a pion gives rise to the abrupt rise in the cross-section at the N^* threshold, similar to the rapid rise in cross-section at threshold for $\gamma + P \rightarrow N + \pi^+$.

In the region of 1200 MeV, the Drell calculation of the one-pion-exchange model¹¹⁾ gave qualitative but not quantitative agreement with the data of Kilner, Diebold and Walker¹⁰⁾. Itabashi¹²⁾ added the interaction current diagram to Drell's pion current diagram (see Figure 1), and the static Chew-Low model yielded agreement with the results of Kilner et al. More recently, Stichel and Scholz²³⁾ have made a gauge-invariant extension of Drell's process which contains contributions from all four diagrams of Fig. 1. They point out that their results correspond to those of Itabashi in the static limit, so that their model is a relativistic generalization of the static theory. The DESY group²²⁾ find that the energy dependence of the N^* photoproduction cross-section and the angular distribution of the N^* decay agree with the model of Stichel and Scholz for gamma energies below 1500 MeV; above that value N^* production is overshadowed by ρ^0 production.

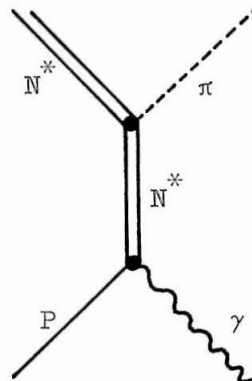
For the ρ^0 production dominating pion pair production at high energy, the primary models considered have been one-pion-exchange model^{24,27)} and the diffraction production model²⁴⁾ (Feynman diagrams

in Fig. 2). Consideration of the CEA²⁰⁾ and DESY²²⁾ results indicates disagreement of one-pion-exchange with the data for the ρ^0 decay distribution and the dependence of the cross-section on gamma energy and momentum transfer. The diffraction model fits the momentum transfer and gamma energy dependence somewhat better. Corrections to one-pion-exchange allowing for absorption in the final state may improve the momentum transfer dependence agreement with the data, but still give much too low a value for the total cross-section^{20,22)}.

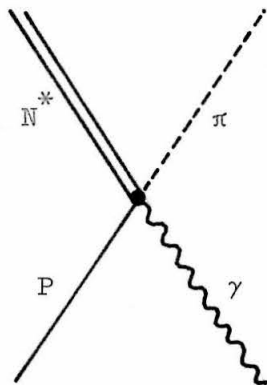
The primary objective of this experiment was to obtain added information on the total cross-section and cross-sections differential in energy and angle for charged pion photoproduction in the region below 1500 MeV. In addition there was a search for whatever resonant states might be present in pion-nucleon or pion-pion systems: N^* , ρ^0 , and σ might be anticipated. The N^* was expected to figure prominently in the data since this energy region is just the one dominated by the N^* . It was hoped that if the N^* was produced in significant quantities from one of the higher isobar resonances that this fact would be obvious from the data; otherwise, angular distributions could be compared to the theoretical predictions mentioned above. Although ρ^0 production is important above 1200 MeV, the most that was expected of it from this experiment was to see its presence, since our configuration was not sensitive to its forward-peaked angular distribution.



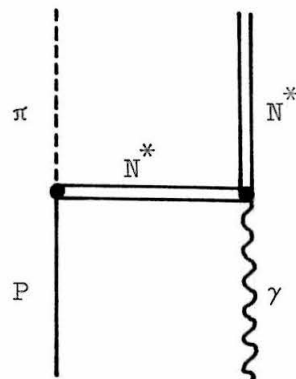
One Pion Exchange



Intermediate N^*



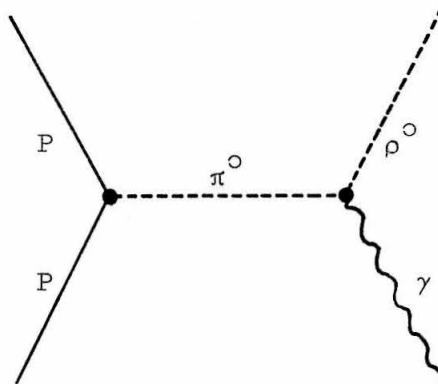
Interaction Current



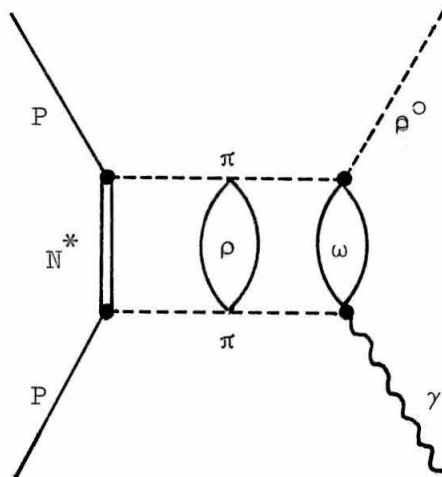
Exchange Cross Term

Figure 1

Feynman Diagrams for N_{33}^* Photoproduction



One Pion Exchange



Diffraction Mechanism

Figure 2

Feynman Diagrams for ρ^0 Photoproduction

II. EXPERIMENTAL METHOD

The basic technique for studying pion pair photoproduction in this experiment was similar to that of most bubble chamber experiments: pass a beam of particles through the center of the bubble chamber, take photographs of the resultant interactions, scan the photographs for the desired configurations, and analyze the event candidates in a computer to select the valid events. Novelty introduced by the desire to maximize the amount of beam per picture were the use of a heavy sensitive liquid in the chamber, and absence of a magnetic field surrounding the chamber. Motivation for this large beam content per picture was the necessity of economy in chamber construction and execution of the experiment, and the uncertainty of the lifetime of the chamber.

The traditional approach of passing a particle beam through a hydrogen bubble chamber surrounded by magnetic field is unworkable for high intensity photon beams because the copious supply of low momentum, forward-going electrons produced by photon interactions in the hydrogen would be bent throughout the volume of the bubble chamber by the magnetic field, obscuring the desired high momentum, wide angle processes. Thus, the use of a high-intensity photon beam dictates that there be no magnetic field on the bubble chamber^{*)}, so

*) One might conceive of using a magnetic field parallel to the photon beam, but bending of the desired pions and protons into the "shadow" of the photon beam would probably produce considerable identification difficulties, along with the loss of low-energy particles. Track reconstruction from stereoscopic views would
(Footnote continued on following page)

that products of electromagnetic interactions may continue in the forward direction characteristic of high-energy electronic interactions and leave the majority of the chamber volume unobscured.

Loss of magnetic field momentum and charge sign measurement leaves the hydrogen bubble chamber experimenter with only the particle direction measurement, giving no kinematical constraints on a non-coplanar pion pair production (a coplanar process is undetermined). Thus, it was felt to be desirable to use a heavy liquid chamber, with the promise of energy measurement on the particles that could be made to stop in the chamber, and the added constraint of some degree of qualitative particle identification based on bubble density and multiple scattering in the liquid.

Use of the heavy liquid itself as the photon target was undesirable for two reasons. The larger atomic number of the heavy liquid would lead to greatly increased showering and electronic multiple scattering compared to that in hydrogen, obscuring much more of the chamber volume. The presence of considerable proton internal energy within the heavy nucleus would make event analysis more difficult, seriously reducing the number of constraints on the kinematical system. Therefore, the approach used in this experiment was to fill the Caltech 12-inch bubble chamber with freon (CF_3Br),

Footnote continued from previous page

become more difficult. This approach also would have made the chamber considerably more expensive.

using a high pressure gaseous hydrogen target contained within a central beam tube²⁸⁾ surrounded by the sensitive liquid (See Appendix I). Detailed discussion of the resulting background is left to Appendix VI; general features are that obscuring background throughout the chamber volume at the average beam intensity of 3.1×10^5 equivalent quanta per picture was sufficient to be a nuisance though not a serious drawback, and that the background rate (largely from coincidence of single and double pion production) was 9.1 percent of the total event rate.

Figure 3 shows the experimental arrangement in the beam area. Since plenty of intensity was available from the synchrotron, the beam diameter was kept small (about 1/16 inch at the chamber), allowing the beam tube to be relatively small and providing a weak constraint on event origin location. A well-shielded primary collimator removed most of the unwanted beam as close as possible to the synchrotron source. "Beam hardeners" containing lithium hydride surrounded by a pulsed magnetic field removed most of the worst background-causing gamma radiation below 10 MeV while passing half the higher energy incident radiation. A second collimator removed the wider angle radiation produced in the beam hardener and defined the circular beam shape; subsequent sweeping magnets deflected any charged particles produced at the second collimator. A large lead scraper blocked passage of charged particles and gamma rays into the chamber away from the beam line; any particle passing through the scraper would not find metal to interact in until it had

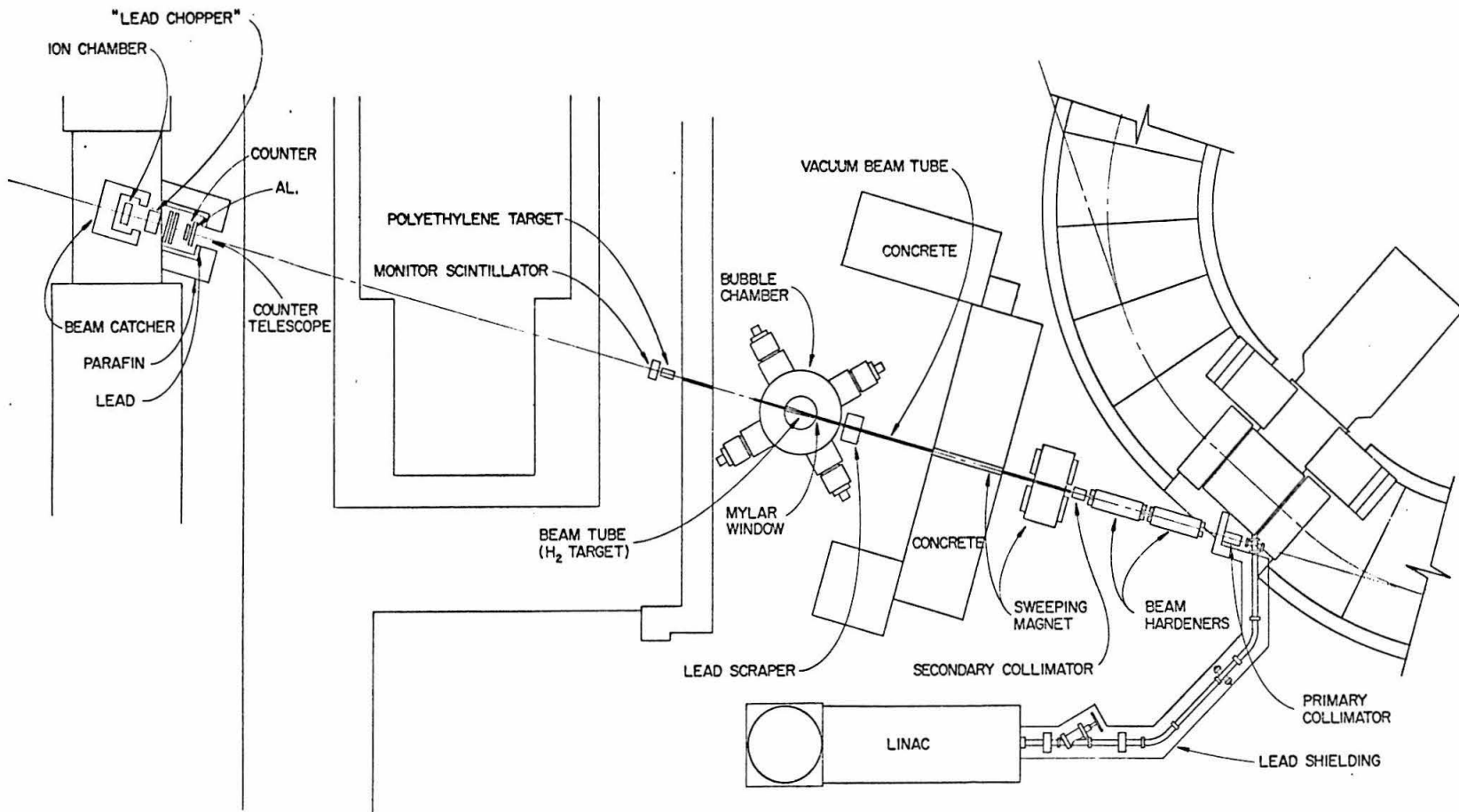


Figure 3

Experimental Arrangement and Beam Area

passed through the beam tube. After passage through the central beam tube hydrogen target, the beam intensity was monitored by a counter telescope looking at a polyethylene target in the beam. The telescope was itself continually calibrated against an ion chamber during the run. Further details of the beam line components and how they were aligned are given in Appendix I. Beam monitoring is discussed further in Appendix II. Details of bubble chamber construction and operation are available elsewhere^{29,30,31}).

One of the most difficult aspects of this experiment was the laborious task of scanning the film for the three-prong events that might be candidates for pion pair production. Scanner training times ranged from one to four months, and scanning efficiencies ranged from 50 percent to 96 percent, with the result that much of the film had to be multiply scanned (see Appendix IV for a more thorough discussion of scanning techniques and efficiencies). Scanning rates were also low; most of our people averaged between five and ten pictures per hour. In one year's time and running an average of two to three shifts on the two scanning machines available to this experiment (one of which was used part-time for analysis - see Appendix III for details concerning these machines) we were able to adequately scan about 13,000 pictures. An upper limit to what might be expected from fully trained personnel (assuming double-scanning on the average) is about 100 pictures per machine shift per week. One machine run three full shifts could then turn out at most 15,000 pictures (about 2,000 good events) per year.

An equally serious limitation on this experiment is the analysis time required, particularly in view of the fact that only the one machine is set up to do analysis. In general, three event candidates were accepted at the scanning table for each valid event. An average of 2.5 measurements were required per event candidate. About nine months were spent analyzing the 5,700 pictures considered in this thesis, but that is not a representative rate, since we had to learn how to do the analysis (Appendix IV contains more detail on analysis procedures). A reasonable upper limit to the analysis rate may be obtained from the average event candidate measurement rate of four per hour. Three full shifts of analysis could then produce up to 60 valid events per week, or about 3,000 per year. Thus the analysis table could keep pace with the 1 1/2 scanning tables, and even with experienced personnel it would require 2 1/2 years to scan and analyze the 52,000 pictures taken in two week's running time with the bubble chamber.

The major portion of event processing expense occurs in running the event analysis program in the IBM 7094 (see Appendix V for details of performance and speed). The total cost of scanning, analysis, and computation comes to about thirty dollars per valid event. Thus some of the economy in the high beam intensity inside the central beam tube is lost from the more complicated scanning and analysis procedures required.

A very serious limitation to this experimental procedure is the number of events that are lost due to chamber detection, scanning,

and analysis inefficiency, with increased chance of systematic errors creeping in. Average chamber detection efficiency for pion pair production is only about 20 percent, with the low momentum transfer processes that are often of theoretical interest being completely lost because all the reaction products go in the forward direction down the beam tube. Scanning efficiencies are low, as noted above, and this makes their inevitable daily fluctuations more serious. Some scanning biases can be allowed for (minimum average detectable track length, for example; see Appendix IX), but with low efficiencies there is more chance for undetected systematic bias. Analysis and computer processing efficiency (about 95 percent) should contribute the least error of the three, since it has the highest efficiency and a relatively good correction can be applied for what is lost.

Since the final accuracy of an experiment like this one is so strongly dependent on the quality of work performed by scanners and, analyzers, it was necessary to develop analysis procedures that monitored human performance as well as evaluating equipment and analysis method accuracy. Procedures used in this experiment are described in the next chapter.

III. EXPERIMENTAL PROCEDURES

Although an earlier bubble chamber run in the spring of 1964 had yielded 80,000 pictures at a synchrotron end point energy of 1350 MeV, this thesis reports work done on part of 105,000 pictures taken in early September, 1964 at 1500 MeV.

Immediately after completion of chamber and beam component lineup, the data run was begun, and it required approximately two weeks. Checks performed before, during, and after the run indicated that chamber operation, beam component lineup, and beam monitoring setup remained stable during that time. The run itself simply consisted of taking the pictures and recording beam intensity data, with beam calibration data being taken at the end of the run. Beam measurement and configuration stability are discussed in Appendix II.

Scanning techniques had been developed on earlier film, so that serious scanning could begin the moment the film was developed. Scanners were trained by simply having them scan film; when it appeared that their work was becoming good, they were assigned a test region to check their scanning efficiency. Only after this efficiency exceeded approximately 75 percent were they considered competent to scan film for this experiment; then the number of scanners assigned to a given region of film depended on their efficiencies.

Five 240-picture regions from four rolls of film were set aside as scan comparison regions: these were regions scanned by many people and analyzed very thoroughly to establish confidence in their accuracy as scanning efficiency evaluators. Scanning efficiencies

were based primarily on work done and these comparison regions, though some comparison between individuals was also done in other film areas.

Scanning was directed toward finding any configuration of three or more tracks that might be pions or protons coming from one origin region on the beam line. Scanners assigned qualitative particle identifications to tracks and indicated whether or not tracks stopped in the lit chamber volume, though these decisions were open to question in later analysis. Details of scanning method, scanning efficiencies, accuracy of qualitative identifications and other questions dealing with general film scanning efficiency are discussed in Appendix IV. Scanning equipment description may be found in Appendix III.

Pictures of typical good event configurations as they were accepted by the scanner are shown in Figures 4 to 7. In Fig. 6 it may be seen that the three tracks in the valid event line up well together, while the other track, probably from nearby single pion or pion pair production (indicated by dashed line) yields a worse lineup but was accepted in the scanning as a possibility. Figure 7 shows one of several cases of two pion pair production events occurring so close that they were written up together.

Analysis equipment and procedural details are split between Appendices III and IV, respectively. Analysis consisted of measurement of track coordinates and reference fiducial marks in each stereo view, with several points in general being taken along each track. Since there was no magnetic field on the chamber, the purpose

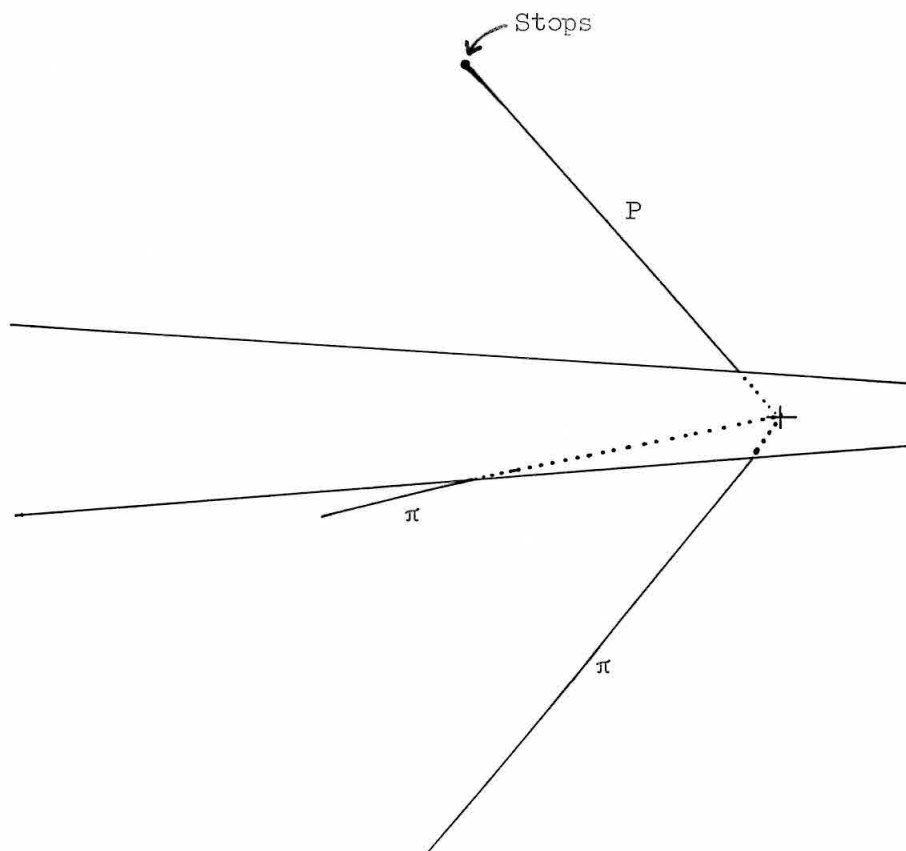
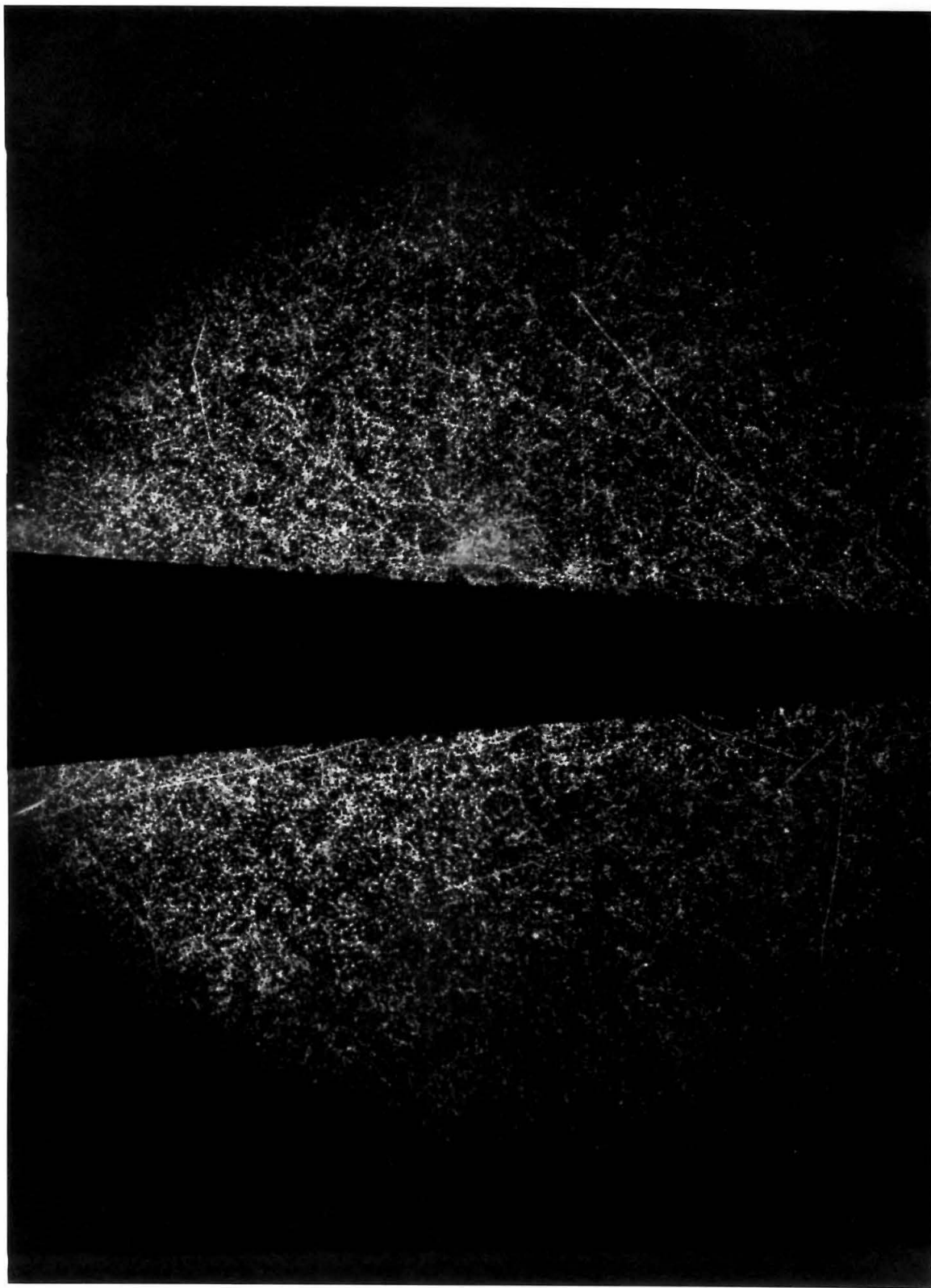


Figure 4

Pion Pair Event



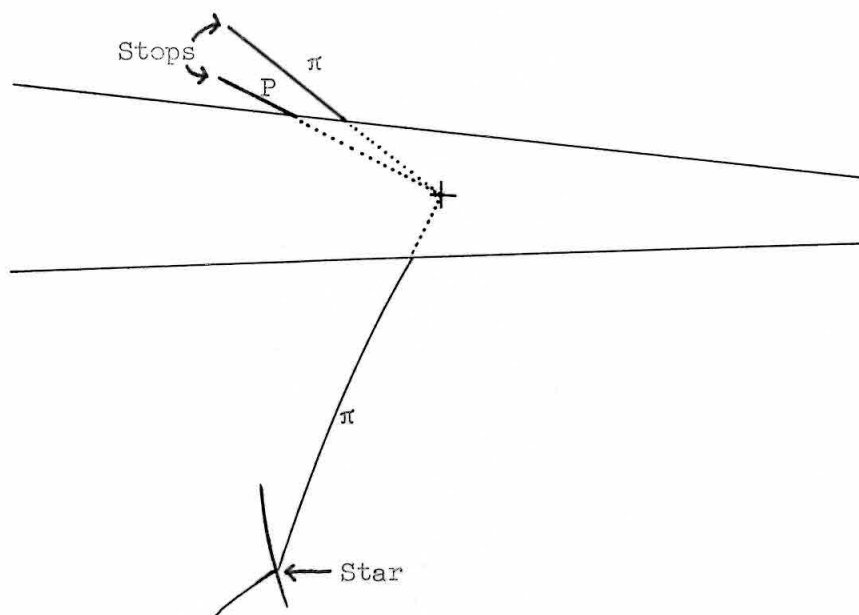
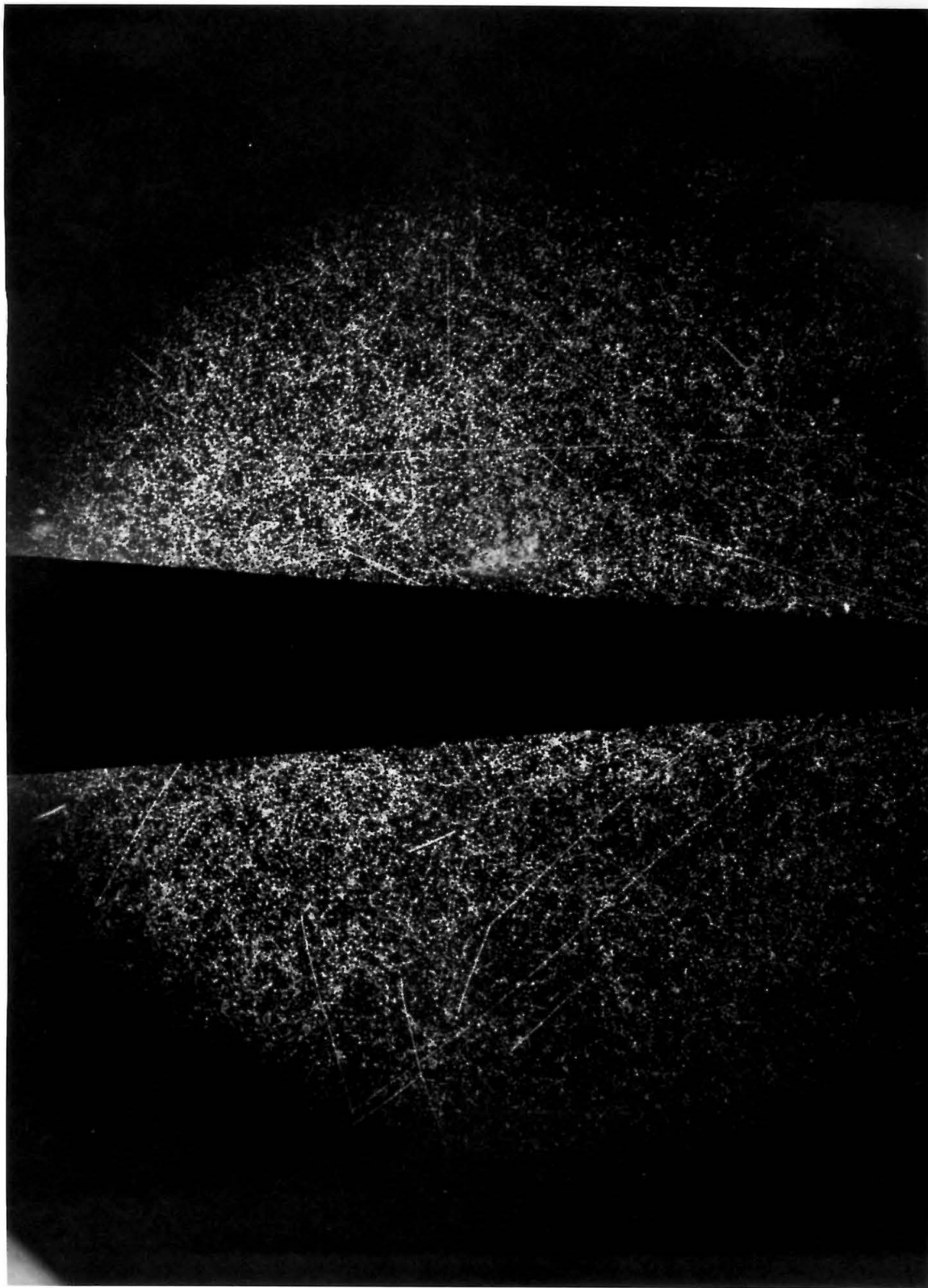


Figure 5

Pion Pair Event with Pion Star



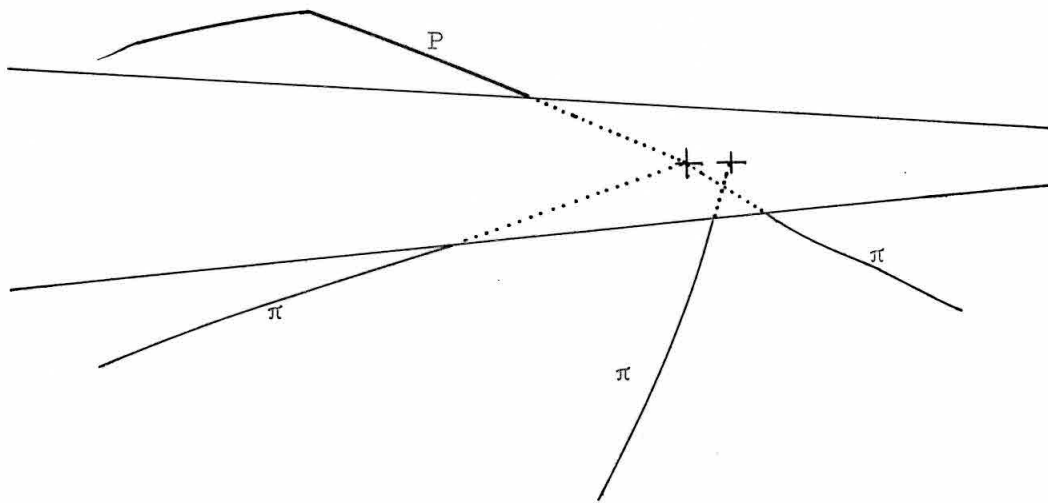
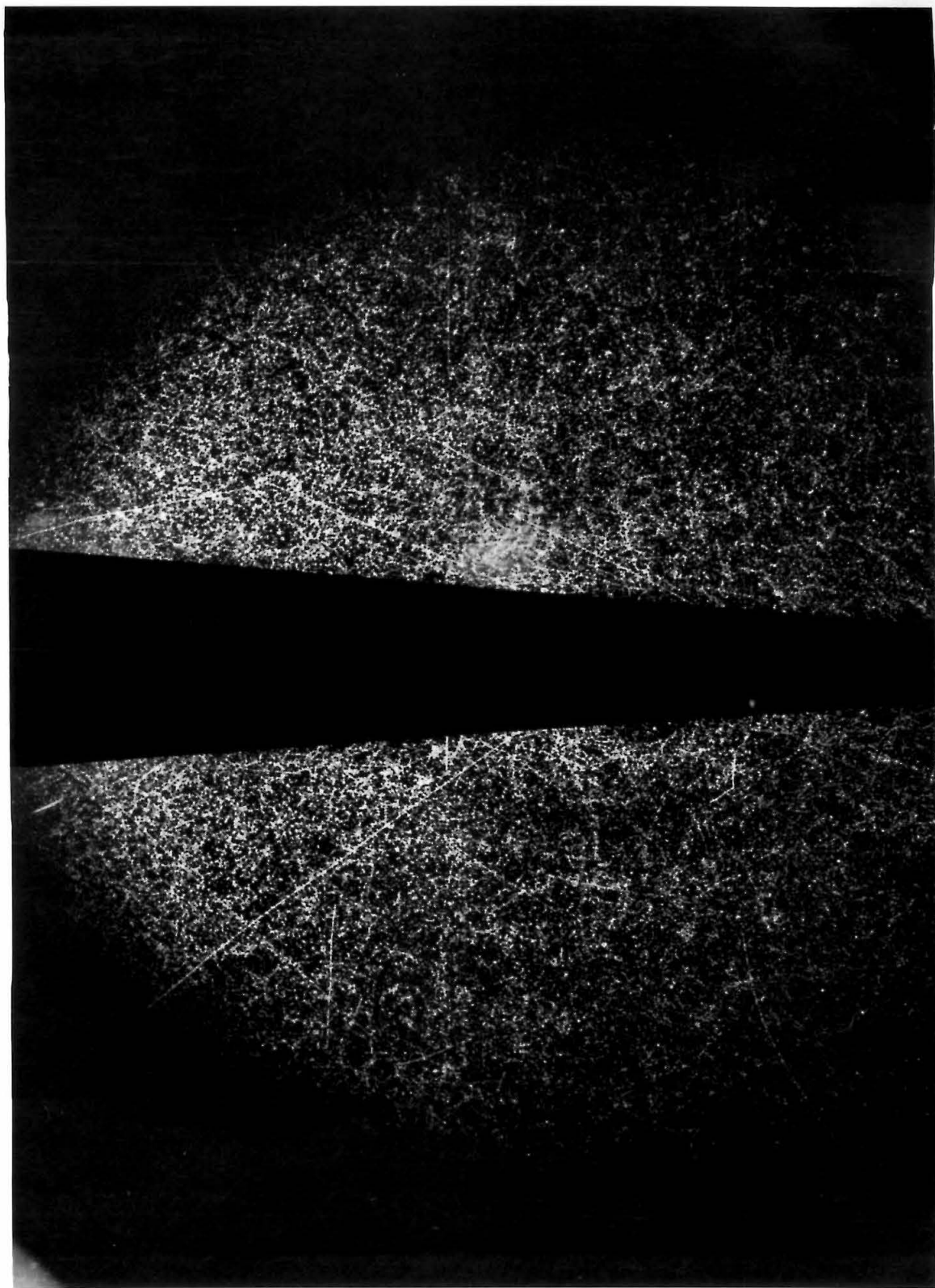


Figure 6

Pion Pair Event with Background Track



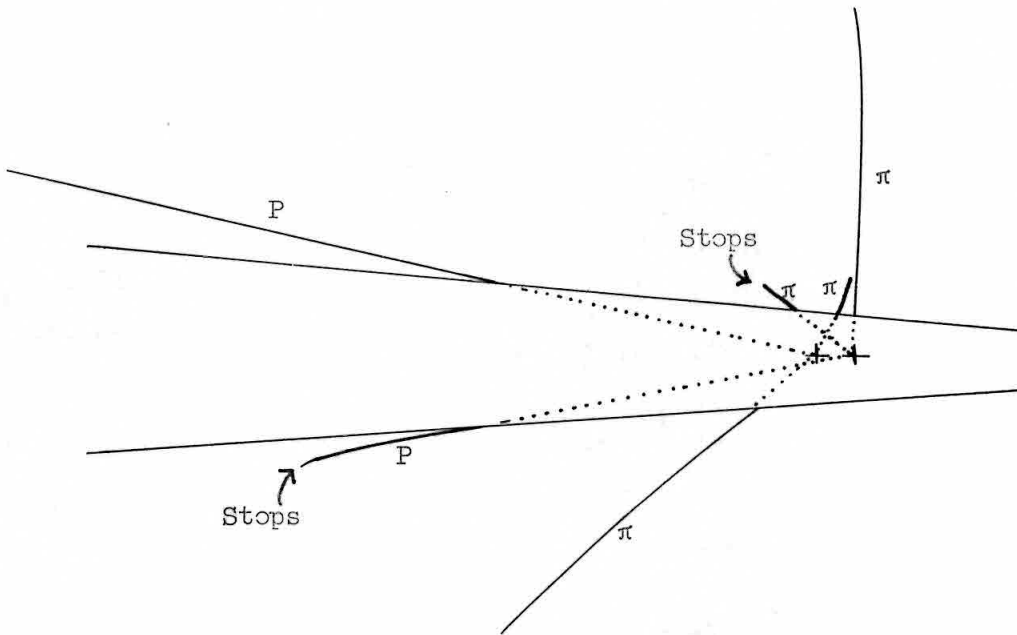
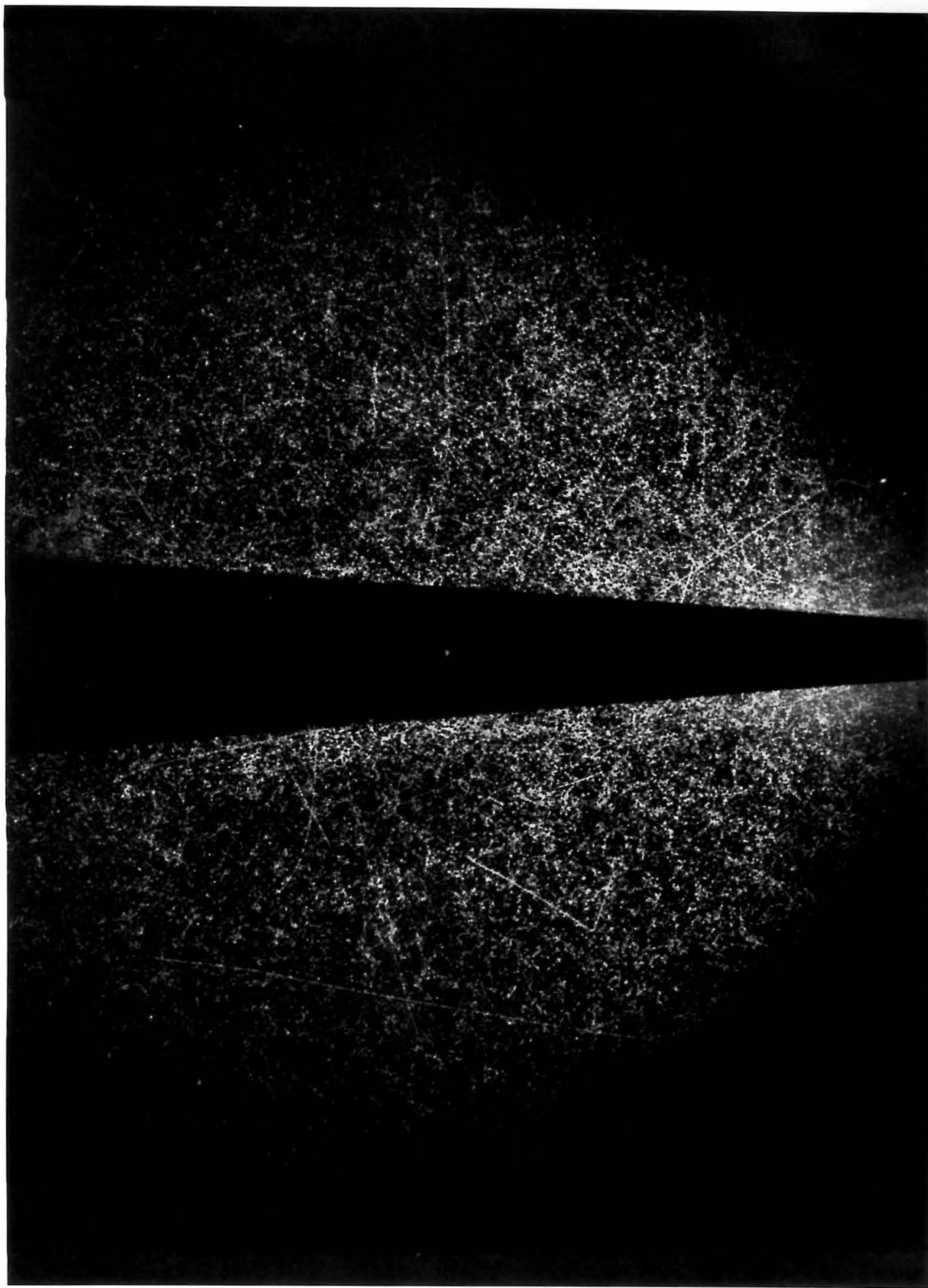


Figure 7

Two Pion Pair Events within Scanning Resolution



of the measurements was to determine the location of the first visible point on the track, track direction at that point, visible track range, and particle multiple scattering.

Analysis training was accomplished by having the analyzer repeat the analysis setup measurements (Appendix IV) where the answers were known until his work became careful and accurate. Training time was considerably shorter than that for scanning; we wonder if that is not related to the fact that those measurements were so boring to perform. Analysis of scanned data was begun in March, 1965, but had to be restarted in June after it was discovered that the digitized protractor being used to measure initial track direction led to such large errors that valid events were being lost and invalid ones accepted. Replacement of this technique with determination of track direction from the second measured point on the track is discussed in Appendix IV.

The computer program written to generate event hypotheses in the IBM 7094 from the digitized measurements is described in some detail in Appendix V. It reconstructed three-space track coordinates given corresponding or almost-corresponding^{*)} point measurements in the two stereo views by means of a corresponding point generating procedure. Then, using the Maximum Likelihood Method^{32,33)} implemented

*) Corresponding points are the two images on the film of a single bubble in the chamber. Almost-or pseudo-corresponding points are two points on the film (one in each view) that are close to corresponding points from a bubble on a particle track. Assumption that two almost-corresponding points are corresponding will usually lead to a calculated chamber "source bubble" position close to an actual bubble on the track.

by the Variable Metric Minimization Method³⁴⁾, it investigated all reasonable hypotheses for pion pair photoproduction from the tracks present in the event, in general allowing any combination of three tracks, and changing of particle identification and stopping criteria. Summaries of all acceptable hypothesis parameters (acceptance based on chi square probability being greater than 0.1 percent and gamma energy within 20 percent of being possible) were printed out and punched onto cards.

Computer output was examined by specially trained personnel to determine which of the hypotheses candidates were in fact possible. Since poor measurement could result in incorrect hypotheses, the computer output was examined for several possible indicators of trouble (see Appendix IV for details). Questions of particle identification and stopping changes were resolved by re-examining the event on the scanning table before a decision was made. If doubt remained, the event was remeasured. Total event failure also resulted in several remeasurements to ascertain that failure was not due to poor measurement. This analysis check at the scanning table occasionally turned up scanning errors and missed tracks, which were then incorporated into analysis.

After roughly fifty events had been accepted, it was realized that their origin distribution was not coming out centered on the beam line. In the belief that the center of the event origin distribution should accurately reflect the center of the beam line and that the discrepancy must be due to a combination of the measurement error in

the beam line depth measurement and errors in the medium indices of refraction (which was consistent with the known errors), the beam line location was changed by 0.135 cm, and the original data re-processed. When 246 events had been accumulated, this spacing was changed further by 0.060 cm. Later re-analysis of all events then showed the origin distribution to be centered on the beam line to better than 0.01 cm.

With event analysis about 80 percent complete, analysis of a group of computer-generated events showed that the computer data analysis program was biasing the results in such a way as to yield too high a value for gamma energy, π - π system invariant mass, and P - π system invariant mass on some events (notably those with little or no constraint from stopping particles). Analysis was halted until the difficulty was located. There were two important contributors to the biasing effect: (1) the measurement error associated with the first visible point was not included in the analysis of track scattering in the hidden regions of the beam tube (it had been included in the observed track direction error), and (2) the multiple scattering momentum measurement had been treated in a manner analogous to the range-energy momentum measurement in the likelihood function. The point measurement error had not been included since, for most events, the direction measurement error and hidden region multiple scattering represent much larger contributions to the uncertainty in track production direction than the point measurement error. Its contribution may be small, but it is important for some events. The other

difficulty arises because the error in the multiple scattering momentum measurement is comparable to the quantity itself, and is really a function of the true value rather than the measured value. Present (corrected) treatment of these two effects is handled in Appendices VIII and VII, respectively; the final form is exhibited in Appendix V.

Of course, event analysis could be completed with the corrected program, but re-processing of all the data already handled would have been far too expensive in time and money. The one ray of hope was that the old program had returned the correct hypothesis almost 90 percent of the time on the generated events; it had even given the correct numbers on over half of those. Thus it was decided to re-process all accepted events, forcing the computer to consider only the hypothesis that had been accepted; this procedure cut analysis time and cost by more than a factor of 15. Room for error was still left in those cases where there were several hypothesis possibilities, so all formerly accepted events having a chi square probability of less than 1 percent or making particle identification or stopping changes were re-processed (several measurements each) in a fashion allowing all hypotheses. In addition, events in the scan comparison regions having any reasonable possibility of hypotheses, particle identification or stop change were re-processed in detail. From this last set of data, the number of valid events remaining where the wrong hypothesis might have been taken is estimated to be about 0.9 percent of the total accepted events, and the number of invalid events accepted that should have been rejected is estimated to be about 0.4 percent of

the total accepted events.

Besides the acceptance of incorrect hypotheses, there is the possibility of valid events being rejected. A category of questionable failures had been kept, and these were automatically re-processed. Formerly accepted events that failed under the new program were re-processed several times (re-analyzing, if necessary) before being discarded. Finally, an area consisting of the scan comparison regions plus another 400-picture region was selected for failure investigation; all events that were felt to have any reasonable chance of being valid were re-processed. Results of this last run lead to the estimate that 3.0 percent of the valid events were lost from having failed with the old program and not being re-run with the new one.

Combining the figures above, it appears that the accepted event count should be augmented by 2.6 ± 3.0 percent due to difficulties caused by the initial analysis program being incorrect. Among the events in question there appeared to be no tendency toward clustering around any energy or mass value, so it will be assumed that these difficulties have not changed the event parameter distributions. More details relating to the effect of the program change may be found in Appendix IV.

The degree of acceptance of valid events and the inclusion of background events as valid by the current version of the data analysis program are discussed in Appendices V and VI, respectively. In summary it may be said that the analysis program appears to accept about 96 percent of all valid events, and at the average beam

intensity run in this experiment 9.1 percent of the total event rate is due to background. In all cases coplanar events with no stopping particles are not included, since those configurations are kinematically underdetermined. There appears to be no effect on parameter distributions among good events due to the lost valid events or the included background events.

IV. RESULTS

The results of this experiment are two-fold in nature: an analysis procedure has been devised for a heavy liquid bubble chamber equipped with a central beam tube, and cross sections and contributing processes for charged pion pair photoproduction have been investigated up to 1500 MeV gamma ray energy.

As mentioned above, the beam line configuration used (Appendix I) proved adequate for this type of experiment. The largest source of error in the experiment came from inefficiency in scanning; had the beam intensity accelerated by the synchrotron been reduced by a factor of two or three from that used in this experiment, the background due to the many single-bubble tracks in the chamber plus the accidental coincidence of nuclear events would have been considerably reduced, with consequent gain in scanning efficiencies. The computer analysis program, containing a track reconstruction section and an event synthesis section, was found to be approximately 96 percent efficient (Appendix V). The event synthesis section, which was peculiar to this experiment, was responsible for that 4 percent event loss. Considering the statistics of the test, one would then expect that the track reconstruction section should be at least 99 percent efficient when given good measurements. This section could be used in any experiment having a bubble chamber geometry similar to ours, and in particular will be used by Donald Coyne in his analysis of $\gamma + n \rightarrow K^0 + \Lambda$, done with the Caltech chamber.

In this experiment, the yield Y may be calculated from an equation of the form

$$Y = nQt \int \frac{\epsilon(k) \sigma(k)}{1 - b(k)} B(k, E_0) \frac{dk}{k}$$

where k is the photon energy, n is the density of target hydrogen nuclei, Q is the number of equivalent quanta passed through the target, t is the target length, ϵ is the over-all detection efficiency, σ is the total cross section, b is the fraction of the total counting rate due to background events, and $B(k, E_0)$ is the bremsstrahlung energy spectrum shape function discussed in Appendix I. Yield and total cross section for this experiment are shown as a function of gamma energy in Table 1.

Total cross sections were obtained by solving the relationship above for $\sigma(k)$; because of the limited statistics, the procedure adopted was that of replacing the integration by the function evaluated at the middle of the energy bin times the bin width (bin widths were 100 MeV). Since n, Q, and the part of ϵ coming from the scanning efficiency (Appendix IV) all varied during the course of the run, they were individually computed for small enough regions that they could be considered constant, then their products were summed over all the film analyzed. All events but one were found to occur between - 13.0 cm and + 7.0 cm along the beam line, so this 20 cm interval was the target length used for t, and was also the visible section for event generation in investigating chamber efficiency and background (Appendix IX). The value of $n Q t \epsilon_{\text{scan}}$ for this experiment was

$75.08 \pm 6.45 \times 10^{30}$ protons/cm², the error reflecting the root-mean-square folding together of the relative errors in the components.

After ϵ_{scan} is removed, the remaining contributions to $\epsilon(k)$ come from analysis efficiency and chamber detection efficiency. Analysis efficiency was assumed to be independent of energy; its components were 4.3 ± 2.1 percent event loss by the analysis program (Appendix V), 2.6 ± 3.0 percent event loss from improper re-analysis after the analysis program change (Chapter III), and 0.5 ± 0.5 percent event loss from the event chi square limit set. No correction was made for the possibility of repeated bad analysis of an event leading to its rejection. It is believed that this effect could be at most a fraction of a percent for four reasons: 1) nearly all event failures were measured by at least two and usually three different people to remove any one person's biases; 2) most event failures had at least three measurements, some having eight or ten; 3) a small sample of event failures were remeasured several times to see if any of them would yield acceptable hypotheses, and none of them did; 4) if the best hypothesis found, though unacceptable, looked like it could lead to something reasonable, or examination on the scanning table showed a possibility of difficulty in measurement, the event was remeasured one or two more times than it might have been otherwise. Thus the analysis efficiency was taken to be 92.6 ± 3.7 percent.

Chamber detection efficiency was a function of gamma energy, and it was computed from the results of a Monte Carlo event generation computer program (Appendix IX). Four possible models contributing to

Table I

Yield and Total Cross Section for this Experiment

Gamma Energy	Yield(events)	Total Cross Section (μ -barns)
450	18	17.2 ± 5.1
550	105	56.5 ± 9.9
650	142	86.6 ± 14.9
750	114	75.5 ± 13.9
850	87	65.0 ± 13.0
950	75	63.0 ± 13.7
1050	63	59.3 ± 14.0
1150	58	67.3 ± 17.1
1250	35	45.2 ± 13.2
1350	38	52.9 ± 16.1
1450	17	26.2 ± 9.7

pion pair photoproduction were included: phase space production, N_{33}^* isobar production, σ meson production, and ρ^0 meson production (a more detailed discussion of the model generation will be given below). For each model, the chamber efficiency was computed as a function of energy by drawing a smooth curve through efficiencies calculated every 100 MeV of gamma energy (the efficiency was the fraction of events generated in that bin that were actually visible in the chamber). At each energy the relative contribution of each model to pion pair photoproduction was estimated from our data and that of CEA³⁵⁾ and DESY²²⁾ (also to be discussed below). Then the chamber efficiency was taken to be the average of the model efficiencies, weighted according to the relative contributions of the models at each energy; the results are shown in Table 2. A relative error of 10 percent was assigned to each value (except the first, which was 20 percent), reflecting statistical errors and probable error in the relative contribution of the various models.

As discussed in Appendix VI, the background event contribution was taken to be 9.1 percent, independent of gamma energy. Since $B(k, E_0) \frac{dk}{k}$ was so slowly varying over most of the range of interest, it was evaluated at the mid-point of each bin except for the bin from 1400 to 1500 MeV, where a rough hand integration was performed.

In addition to the statistical and systematic uncertainties taken into account above or in the appendices, there are several other sources of systematic error that affect the total cross section. The uncertainty in the synchrotron end point energy (affecting the number of

Table 2

Chamber Detection Efficiency

Gamma Energy Efficiency (%)

450	5.8
550	13.2
650	14.4
750	15.8
850	16.2
950	16.4
1050	16.3
1150	14.5
1250	14.1
1350	14.1
1450	14.1

equivalent quanta per energy interval) was estimated to be 0.9 percent.^{*)} The bremsstrahlung energy spectrum shape function $B(k, E_0)$ as calculated by BPAK³⁷⁾ is probably accurate to 2 percent. Hydrogen target contamination is less than 1 percent. Uncertainty in the lit chamber radius leads to a chamber detection efficiency relative error of 3 percent.

By far the largest systematic uncertainty comes from the energy dependence of the scanning efficiency. It is obvious that high energy, low bubble density tracks are harder to see than low energy, high bubble density tracks, and the shorter the visible track length becomes the worse the effect is. Originally, the Monte Carlo program was run with the constant minimal projected track lengths shown in Table A IX-1. Then distributions were run on accepted event tracks, which showed that there was a cutoff in the location of the ends of tracks 0.4 cm from the beam tube in the plane of sight, and that the average minimum seen projected track lengths for non-stopping particles was an appreciable function of track energy. Inclusion of these effects into the Monte Carlo program reduced the chamber detection efficiency from 22.5 percent to 15.5 percent at 1250 MeV gamma energy.

Considering the minimum visible length to be a function of particle velocity (hence also bubble density) does not solve the whole problem;

*) This uncertainty comes from a probable 10 MeV error in the setting of the end point energy, 0.3 percent error in the beam energy meter calibration³⁶⁾, and estimated synchrotron orbit radius uncertainty of 2 inches leading to $\Delta E/E = (1 - n)\Delta R/R = 0.5$ percent (n is synchrotron field index). The end point energy was not even corrected to the radiator radius used because it was known that the electron orbit inside the synchrotron was quite eccentric.

for instance, an event with one low energy track and two high energy tracks is far more apt to attract attention than one where all three tracks have high energy. This was borne out in the distribution of minimal track length vs. particle velocity, where it was observed that a proton with chamber exit velocity $\beta = 0.7$ required about 0.5 cm more visible track length than a pion of the same exit velocity. One might expect the reverse to be true since the proton would then have heavier bubble density in the chamber. This effect is no doubt due to the fact that the heavier bubble density proton was usually the first track to be found in event scanning. If the event proton had already been found one might see a short, dim pion coming from the same origin, but if all three tracks were faint they all might have been overlooked in the selection of tracks for scanning (we have observed in Appendix IV that a low bubble density track is much easier to find when its direction is known). We could think of no reasonable way to take this bubble density correlation effect into account without danger of seriously biasing the data; therefore, it was not included. Since the different proton and pion treatment at the same velocity partially takes this effect into account, we believe that the remaining error from the correlation effect and from not having fit the individual track distribution correctly is approximately equal to the variation in chamber efficiency obtainable by varying the fit to the observed minimum length distribution over all reasonable values. This variation vanishes at gamma energy equal to 500 MeV, is approximately 4 percent in absolute chamber efficiency (25 percent relative change in efficiency)

at 1500 MeV, and appears to be roughly linear with gamma energy in between. This error estimate was therefore added to the list of errors discussed above.

Figure 8 shows a comparison of our total cross-section results to those of CEA³⁵⁾, DESY²²⁾ and Cornell⁹⁾. Errors shown for our data are statistical plus systematic, errors being combined by the root-mean-square method. Our values appear low at higher energies, which is very probably due to the minimum-length-to-energy correlation effect between tracks discussed above. There might also be some effect due to a small downward gamma energy bias in the data since the last point appears to be somewhat lower than the others.

A very crude attempt to estimate the relative importance of various models that might contribute to pion pair photoproduction was made by investigating the dipion and isobar invariant mass spectra. Events were generated by the Monte Carlo computer program under the assumption of four basic models: phase space pion pair production (constant matrix element), $N_{33}^*(1238)$ isobar resonance formation, neutral ρ meson production, and neutral σ meson production. In generating the last three resonant states the resonant diparticle invariant mass probability distributions used were the phase space resonant enhancement ones of Jackson³⁸⁾, exhibited in Appendix IX. The variation of resonance width with energy was taken to be that resulting from the angular momentum state of the two particles comprising the resonance, without resort to the empirical modifications for the individual resonances discussed in the appendix of Jackson's article. Resonance energy and

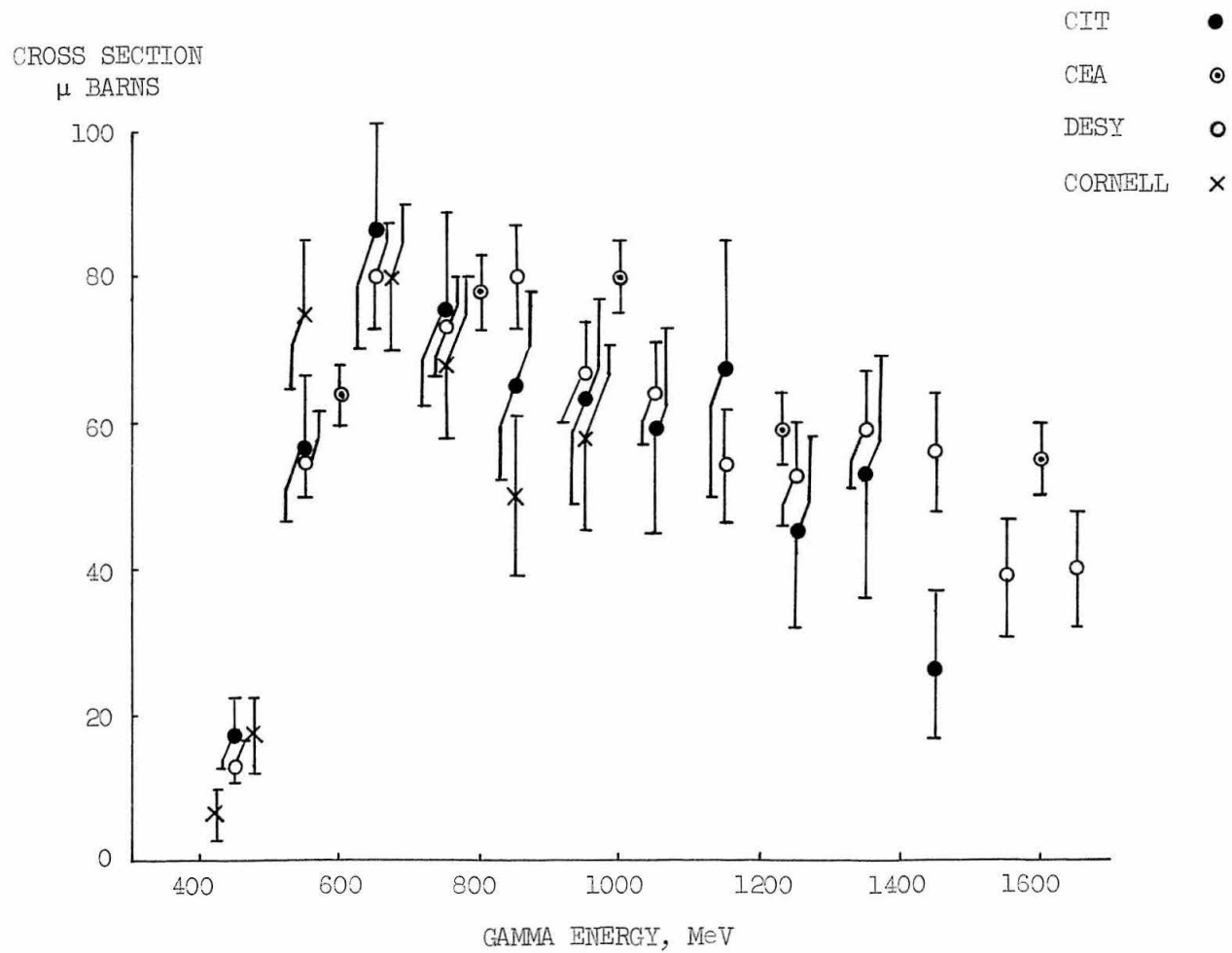


Figure 8

Total Cross Section Compared to Other Experiments

width values used were: $N_{33}^*(1233, 125)$, $\rho(740, 115)$, $\sigma(420, 100)$. Center-of-momentum angular distributions were taken to be simple numerical approximations to the empirical distributions obtained by CEA and DESY.

For comparison with our data (and for chamber detection efficiency calculation) 2500 visible events each were generated for phase space, N^* and σ ; 500 ρ 's sufficed. The generated events were sorted into dipion and isobar mass spectrum bins 40 MeV wide, separated into three regions of gamma energy: $E_\gamma < 600$ MeV, $600 < E_\gamma < 1060$ MeV, and $E_\gamma > 1060$ MeV. Data from our accepted events were similarly sorted (note that the 40 MeV bin width is somewhat larger than the average invariant mass measurement errors, shown in Table A V-2). Then a computer least-squares fit (using program MIN, the variable metric minimization method³⁴) attempted to match combinations of the generated spectra to the data in each energy region (isobar and dipion spectra were fitted simultaneously). The fitting procedure included statistical errors in the generated events as well as the data. Background was then subtracted from phase space after fitting.

Parameters resulting from fitting all four models to the data (the ρ is allowed only in the highest energy region) and from limiting the fit to only phase space and N^* are shown in Table 3. It is clear that the data cannot be fit without including the ρ meson. The case for the σ meson is dubious; the fit significantly improves in the central energy region when it is added, but within our limited statistics the fit is quite acceptable without it.

Table 3

Parameters from Model Fit to Data

<u>Four Model Fit</u>	<u>Percentage Contribution</u>		
	$E_Y < 600$	$600 < E_Y < 1060$	$E_Y > 1060$
Phase Space	4.80 ± 19.6	40.0 ± 11.4	63.1 ± 16.1
N_{33}^*	61.1 ± 22.5	40.5 ± 9.3	-12.6 ± 12.9
σ	-9.1 ± 13.0	19.5 ± 7.8	14.1 ± 7.9
ρ	----	----	35.4 ± 7.3
Fit χ^2	12.4	15.8	37.5
Degrees of Freedom	8	21	31
χ^2 Probability	13%	77%	19%

<u>Two Model Fit</u>	<u>Percentage Contribution</u>		
	$E_Y < 600$	$600 < E_Y < 1060$	$E_Y > 1060$
Phase Space	47.1 ± 19.3	56.5 ± 9.6	110.4 ± 13.1
N_{33}^*	52.9 ± 19.3	43.5 ± 9.6	-10.4 ± 13.1
Fit χ^2	13.5	20.6	59.1
Degrees of Freedom	8	21	31
χ^2 Probability	10%	49%	0.1%

Figure 9 shows a comparison of the four model fit to similar fits (excluding the σ meson) obtained by CEA and DESY. The CEA fitting procedure did not fit the dipion and isobar distributions simultaneously; in order to include their results in the comparison we have assumed that a resonance reflected into the other system would look like phase space production, and have assigned to phase space the fraction of the total rate not attributed to N^* or ρ in each energy region.

There is poor agreement between our relative assignment of N^* and phase space contributions and theirs. We believe that a combination of several factors makes our assignments unreliable. At low energy the curves for the two models look almost identical, making the relative contribution assignment strongly dependent on accidents of statistics and model assumptions made in the generated events (for instance, taking the N^* center-of-momentum angular distribution flat instead of matching the CEA data changed the N^* contribution from about 50 percent to 100 percent below 600 MeV gamma energy). In fact, we question whether anyone has good enough statistics to make a reliable estimate at 600 MeV. Even at higher energies, our curves are qualitatively similar for the two models, an unfortunate consequence of the fact that we cannot tell the π^+ from the π^- and therefore have to lump both possible isobar distributions together. The data of the other groups do not suffer from this limitation. With models so close there is certainly a strong effect from the choice of chamber shape parameters and the treatment of the scanning efficiency energy bias;

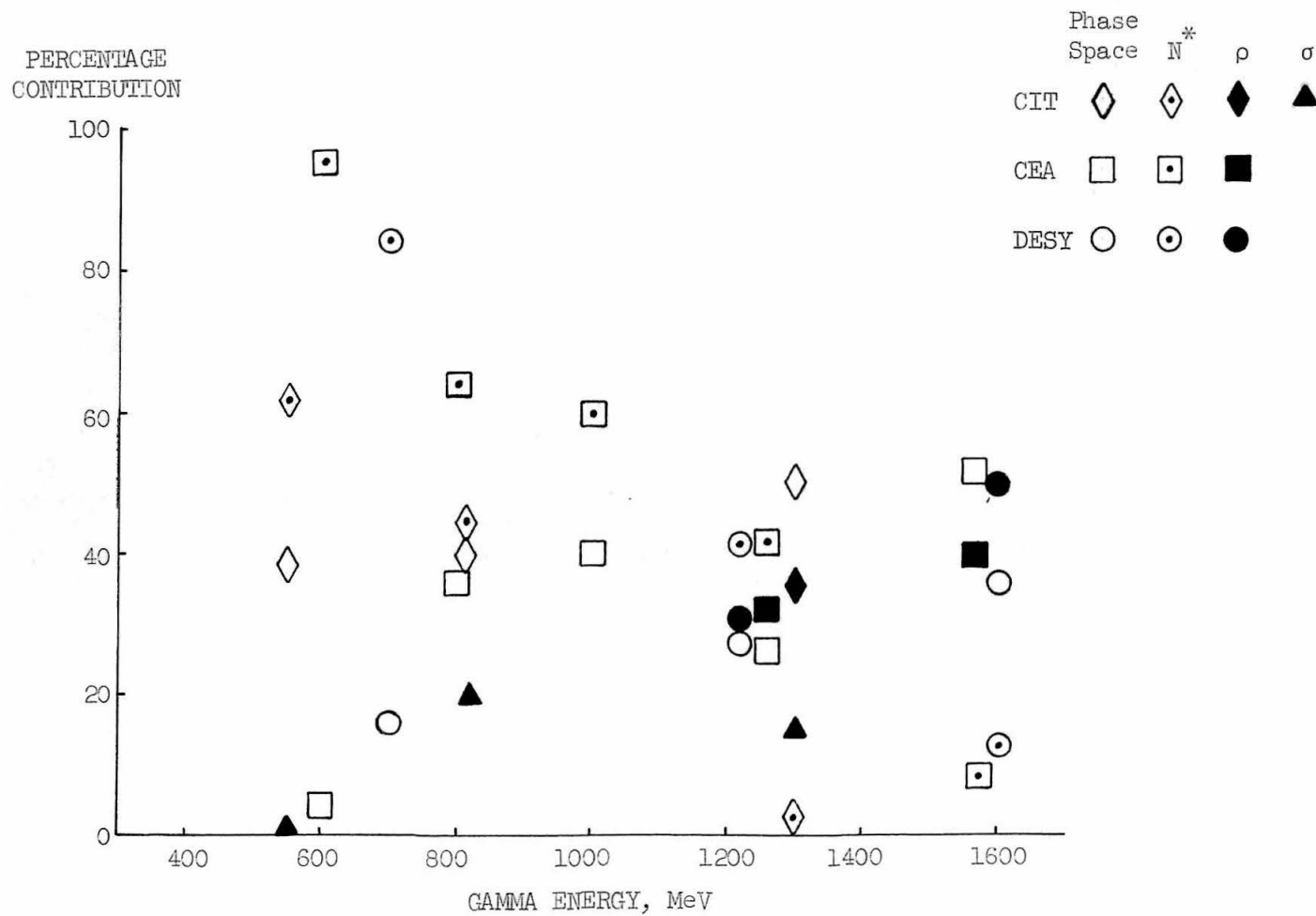


Figure 9

Model Contributions Compared to Other Experiments

indications were that reasonable changes in some of these quantities could make a change in the N^* contribution of the order of 20% to 30%, even in the range $600 < E_Y < 1060$. Since we were forced to generate a limited number of events for economic reasons, statistical errors in the generated histograms can affect the fit even though those errors are taken into account. We believe that these statistical variations are responsible for the fact that two of the fit coefficients went negative (though were within the probable error of being zero). For Figure 9 these negative values were subtracted from the phase space contributions and the negative models assigned zero contribution. A more serious difficulty with event generation was that we could not leave the resonance shape parameters free to be determined by the data; therefore, small biases in the data can change the fit appreciably (we used 1233 instead of 1238 for the N^* mass because our isobar peak seemed to be of the order of 5 MeV low). Thus we conclude that the CEA and DESY experiments are much more reliable in determining the relative contribution of N^* and phase space, and we adopted their values in determining our chamber efficiency.

The situation with the ρ meson is not quite so unfortunate. Even though our ρ detection efficiency is low due to its forward-peaked distribution, our data for its relative contribution is in good agreement with the other experiments. This is no doubt the case because the ρ curves do not resemble the N^* or phase space curves, so that model changes would not tend to mix the relative contributions as much. A similar independence exists for the σ meson, though it is much

closer to the phase space and N^* dipion peaks than the ρ , with increased loss of statistical confidence compared to that for the ρ .

Our dipion and isobar mass data histograms for the three gamma energy regions are shown in Figures 10-15. The smooth curves indicate the result of the computer fit to the generated data. It must be emphasized again that the fit was done to the generated histograms; after the fit a curve smoothing technique was applied so that the generated curves could be presented unambiguously with the data histograms (occasional curve irregularities are the result of smoothing and computer curve plotting problems rather than peculiarities in the original generated histograms). Figures 16-21 show the generated dipion and isobar histograms for phase space, N^* , and σ , with $600 < E_\gamma < 1060$, Figures 22-23 show the same curves for ρ with $E_\gamma > 1060$. In Figures 24-27 we show the generated dipion and isobar curves for phase space and N^* with $E_\gamma < 600$, so that the reader may see how slight the differences are.

Figures 28-45 show the data angular distributions in the three energy regions. Angular distributions are presented for the dipion and isobar systems; plotted are the cosine of the polar angle of the diparticle in the general center-of-momentum (COM) system, the cosine of the polar angle of a component pion in the diparticle COM system, and the azimuthal angle (in units of π) of that pion in the same system. Directions in the diparticle COM system are references to that of the appropriate initial state particle: gamma ray for the dipion system and proton for the isobar system (zero azimuthal angle is in the

FIT TO DATA

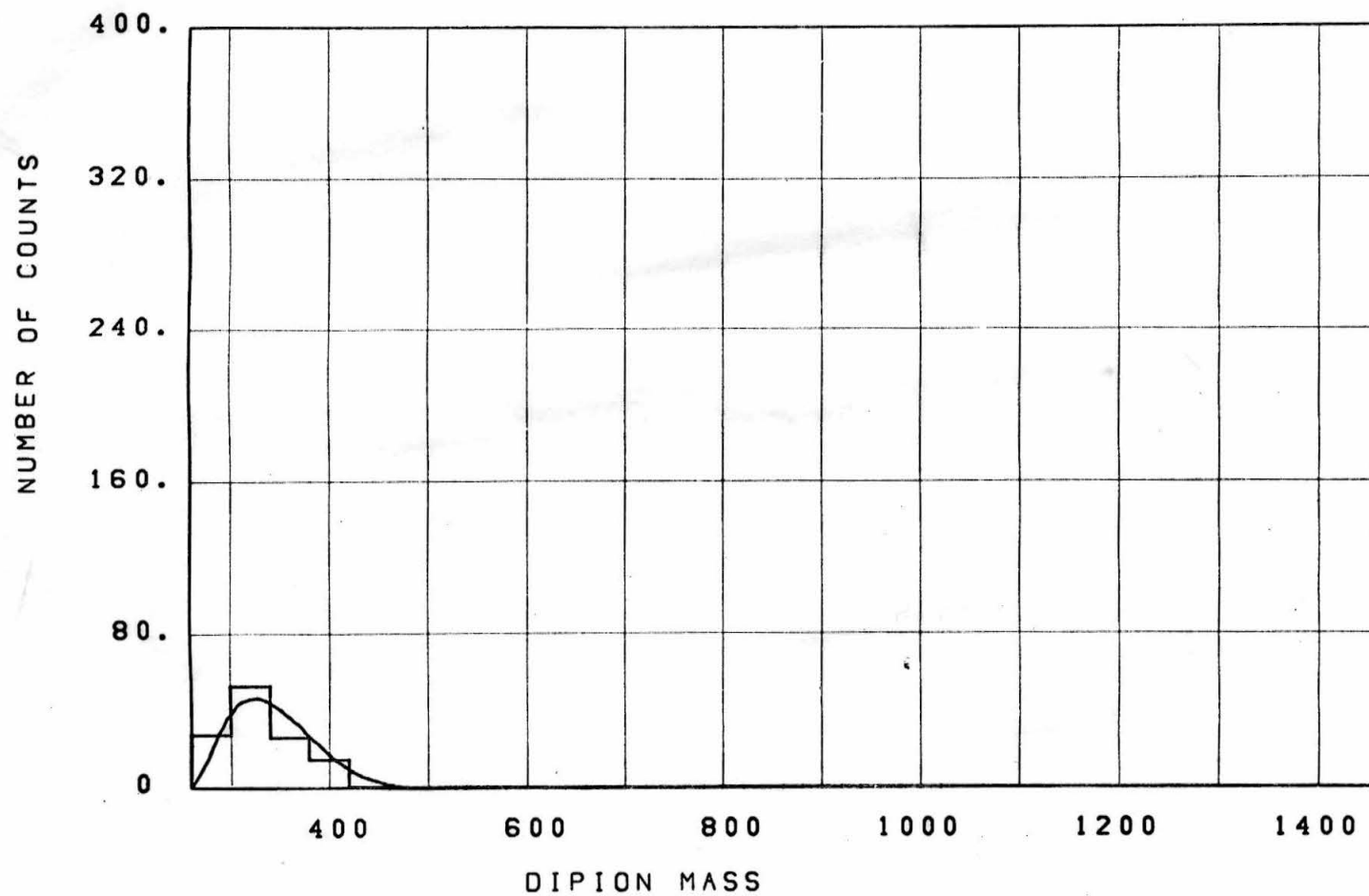


Figure 10

Data Dipion Mass Distribution, $E_\gamma < 600$

FIT TO DATA

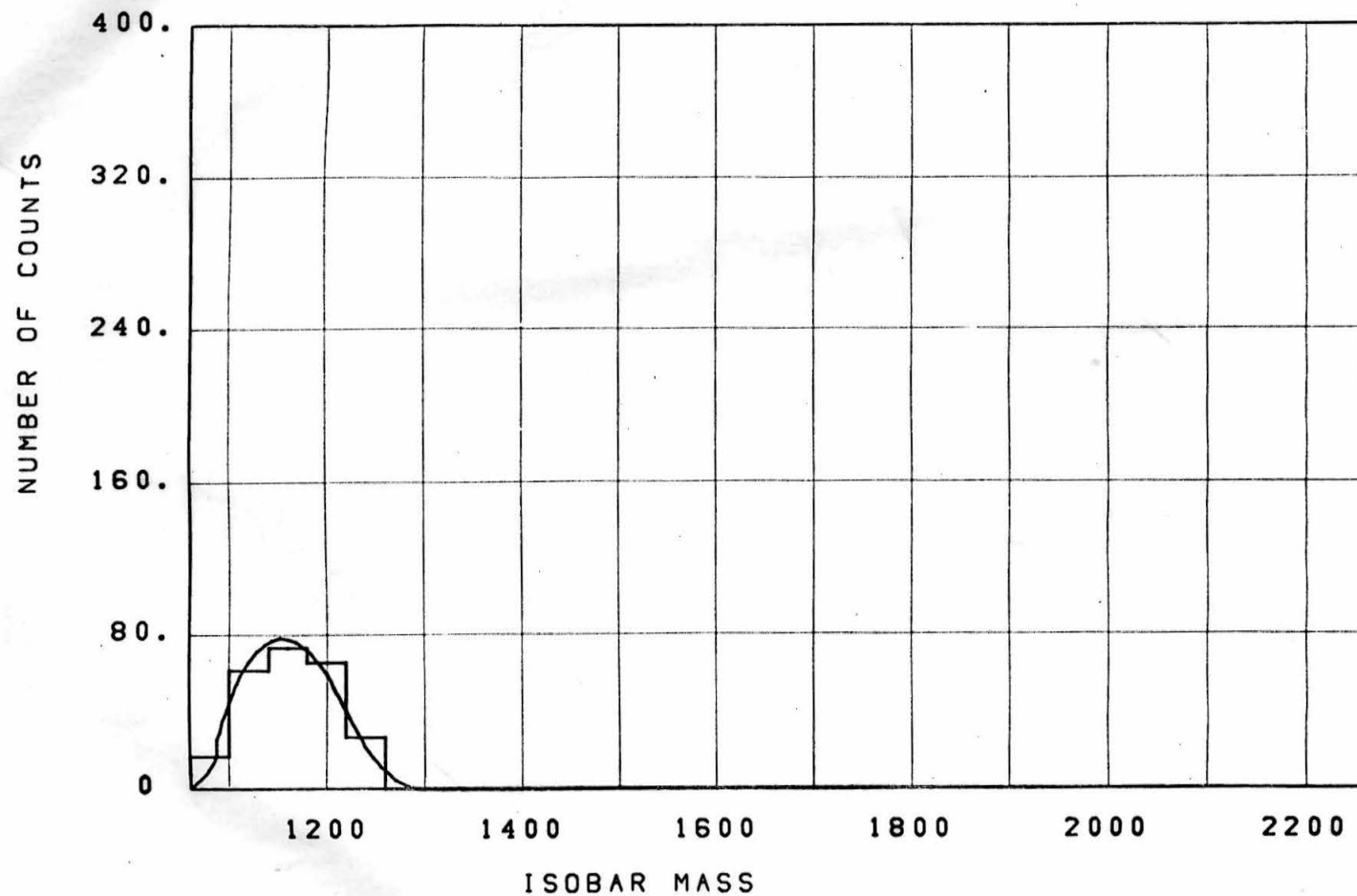


Figure 11

Data Isobar Mass Distribution, $E_{\gamma} < 600$

FIT TO DATA

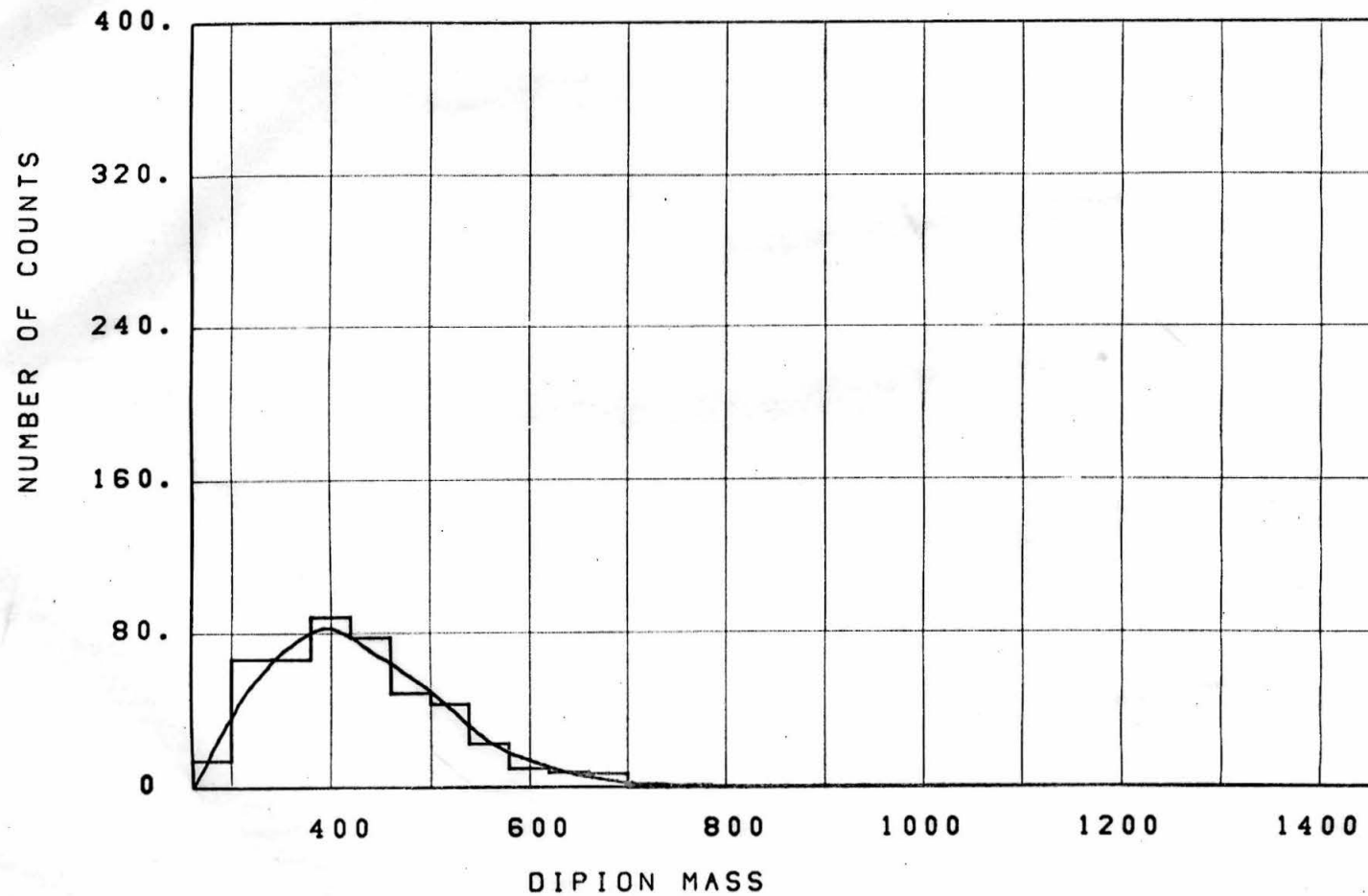


Figure 12

Data Dipion Mass Distribution, $600 < E_{\gamma} < 1060$

FIT TO DATA

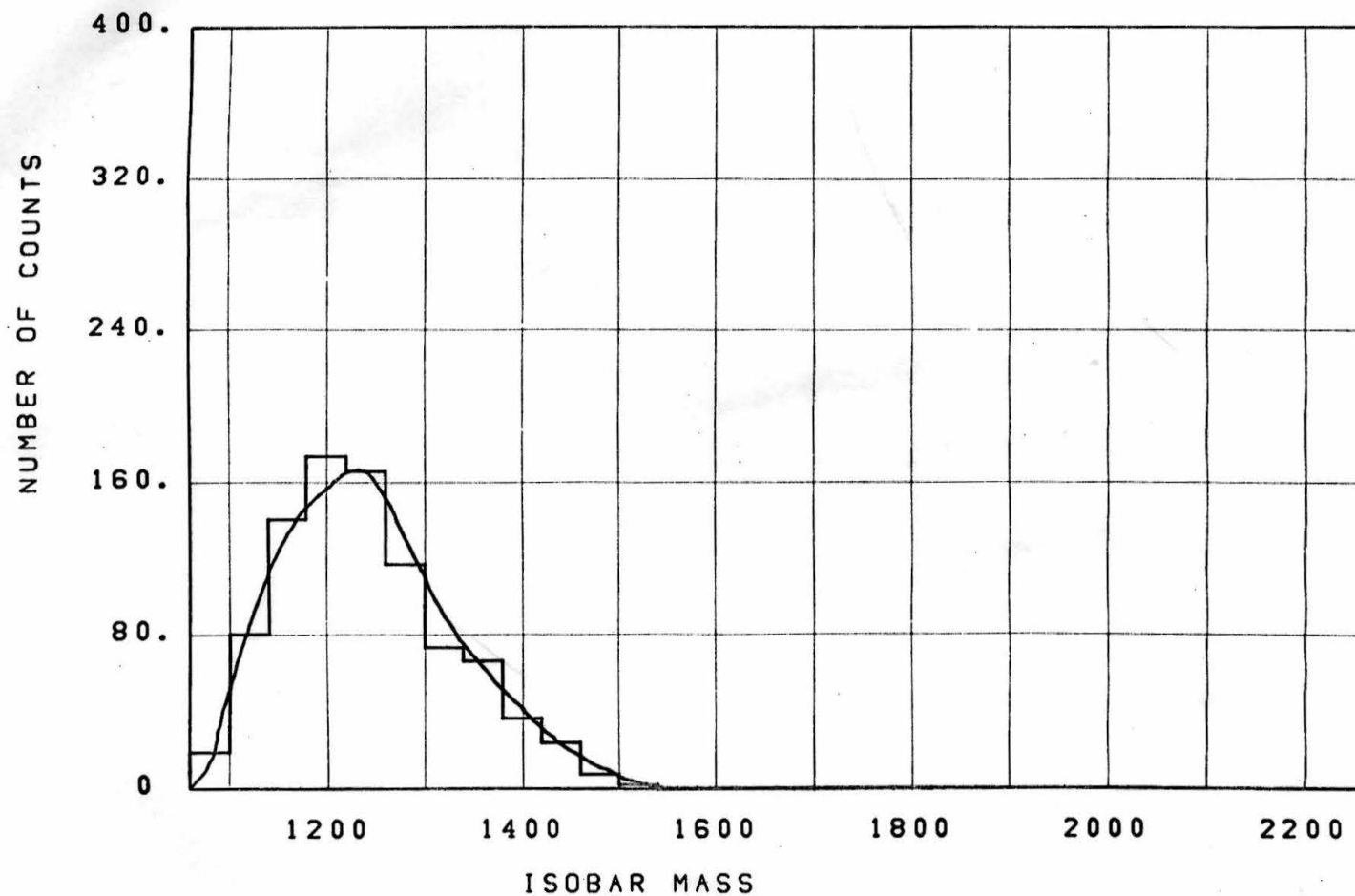


Figure 13

Data Isobar Mass Distribution, $600 < E_{\gamma} < 1060$

FIT TO DATA

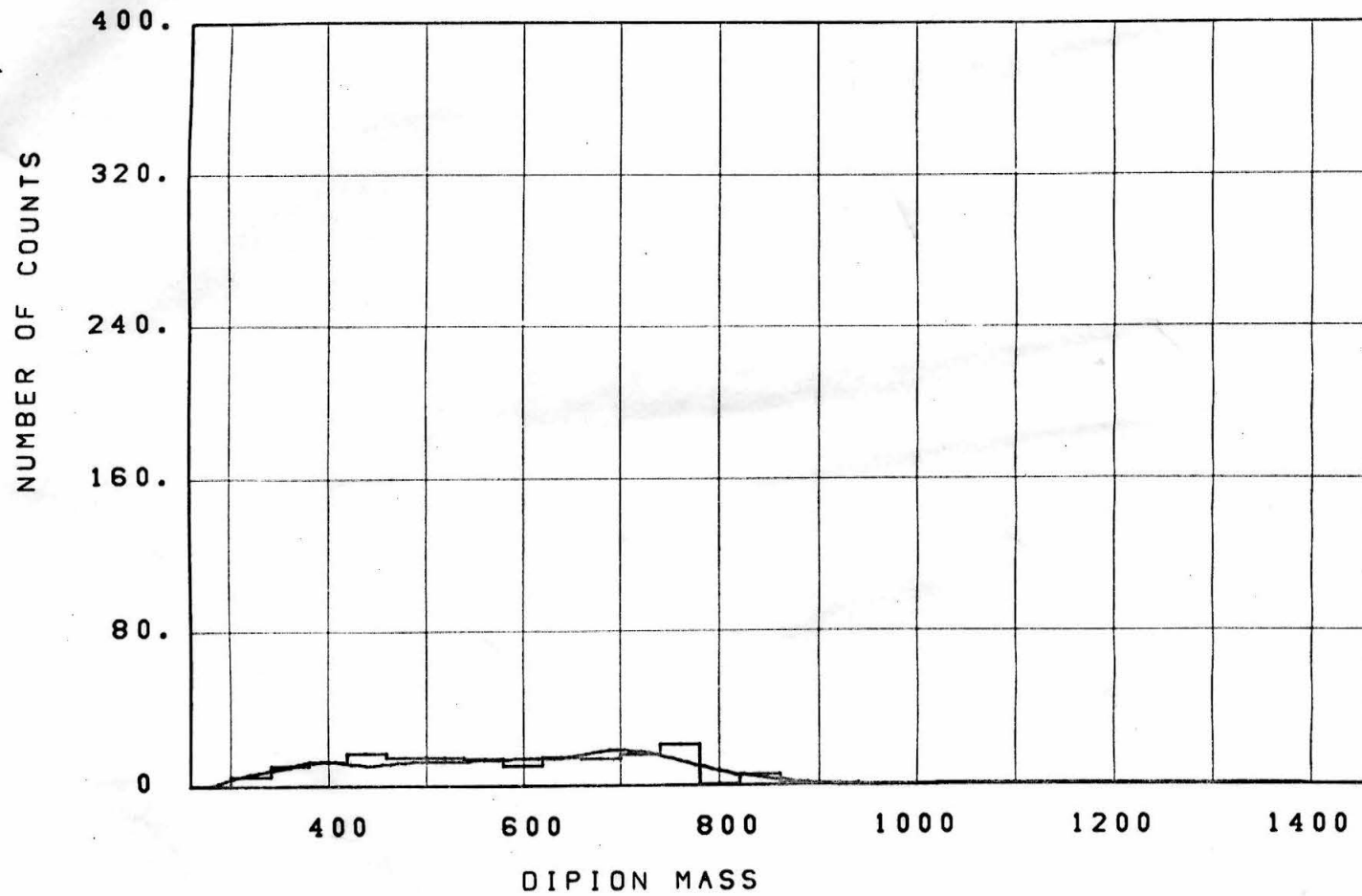


Figure 14

Data Dipion Mass Distribution, $E_\gamma > 1060$

FIT TO DATA

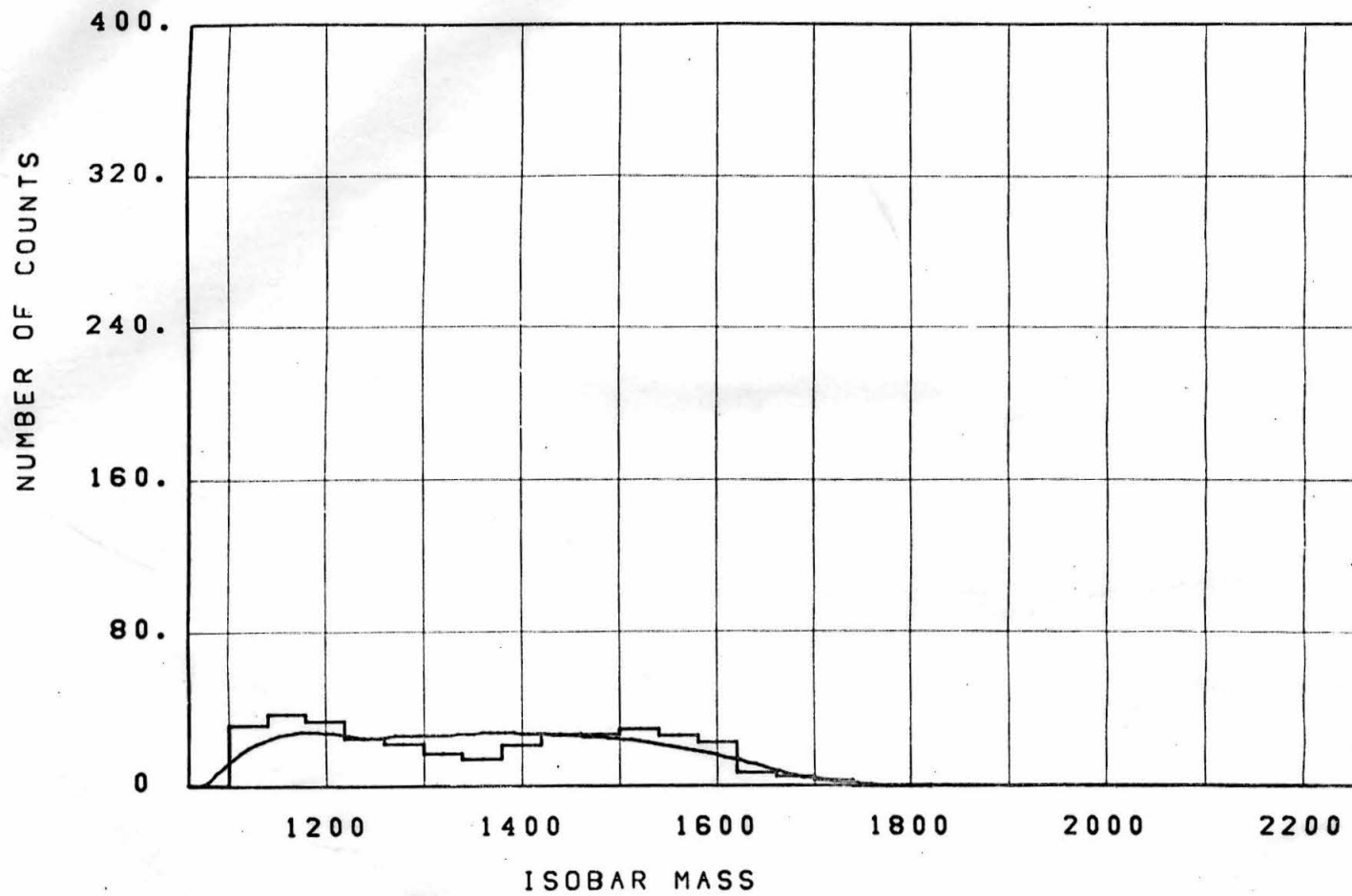


Figure 15

Data Isobar Mass Distribution, $E_\gamma > 1060$

PHASE SPACE GENERATION

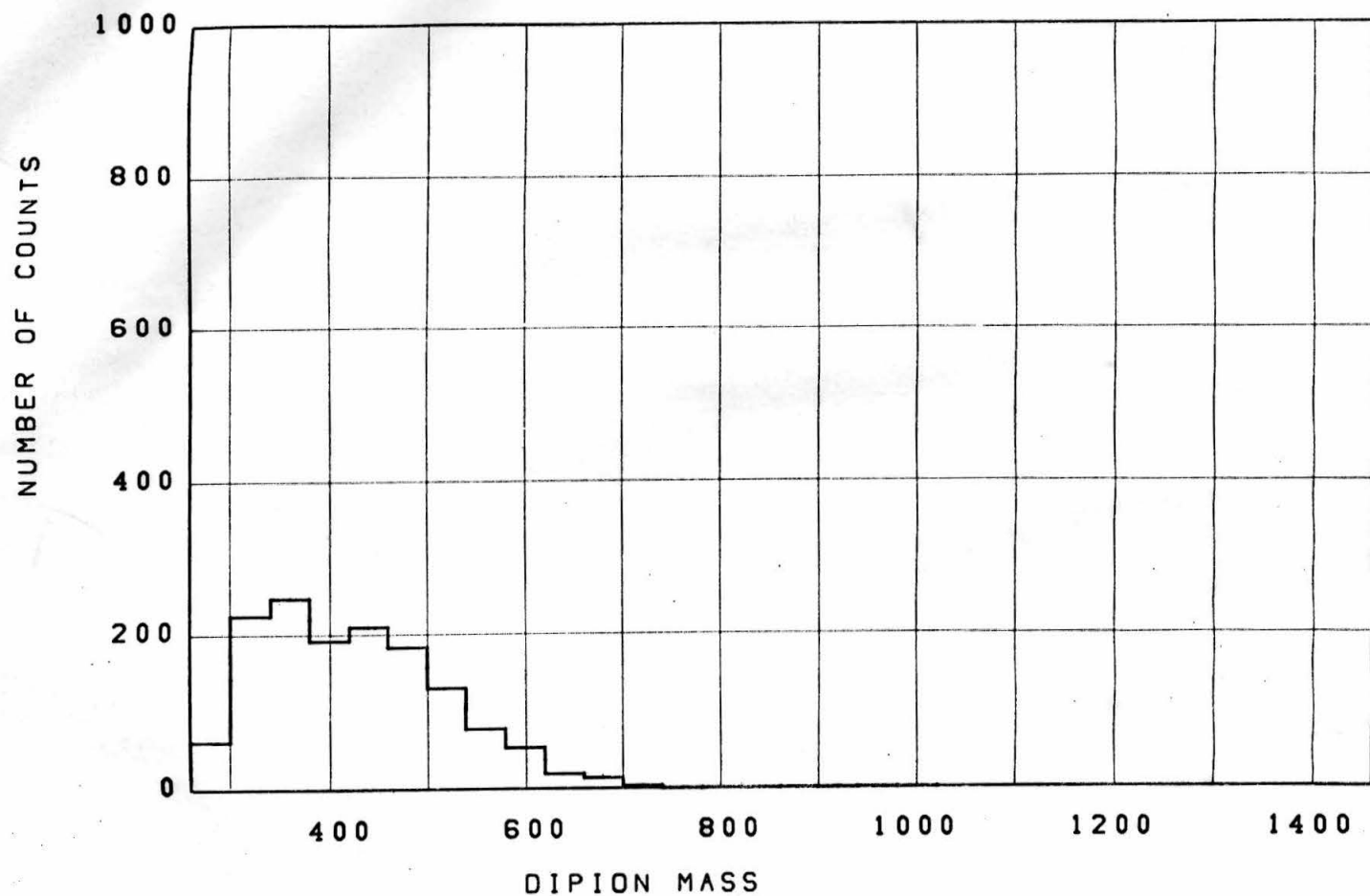


Figure 16

Generated Phase Space Dipion Mass Distribution, $600 < E_{\gamma} < 1060$

PHASE SPACE GENERATION

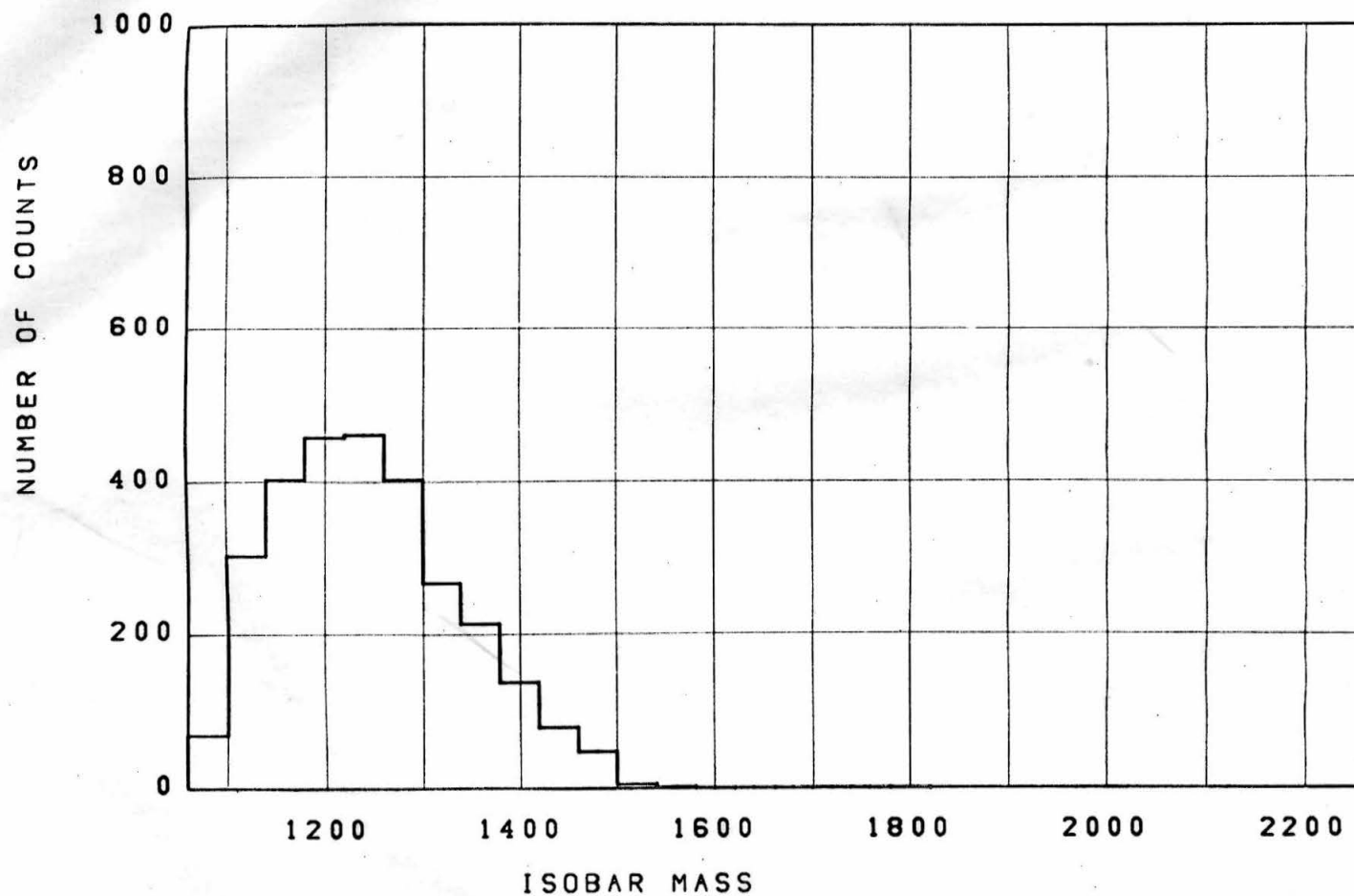


Figure 17

Generated Phase Space Isobar Mass Distribution, $600 < E_{\gamma} < 1060$

N-STAR (1238) GENERATION

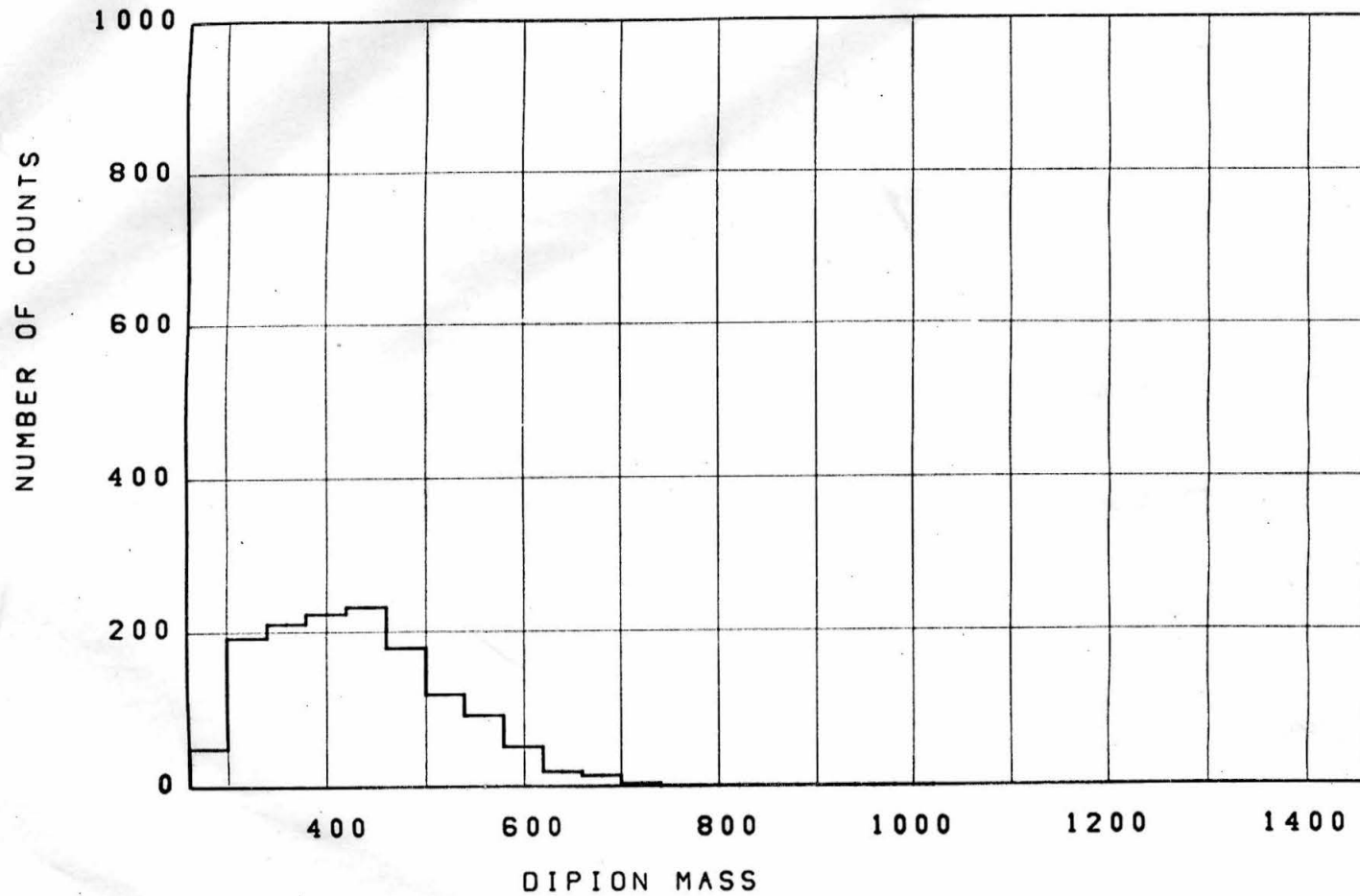


Figure 18

Generated N_{33}^* Dipion Mass Distribution, $600 < E_\gamma < 1060$

N-STAR (1238) GENERATION

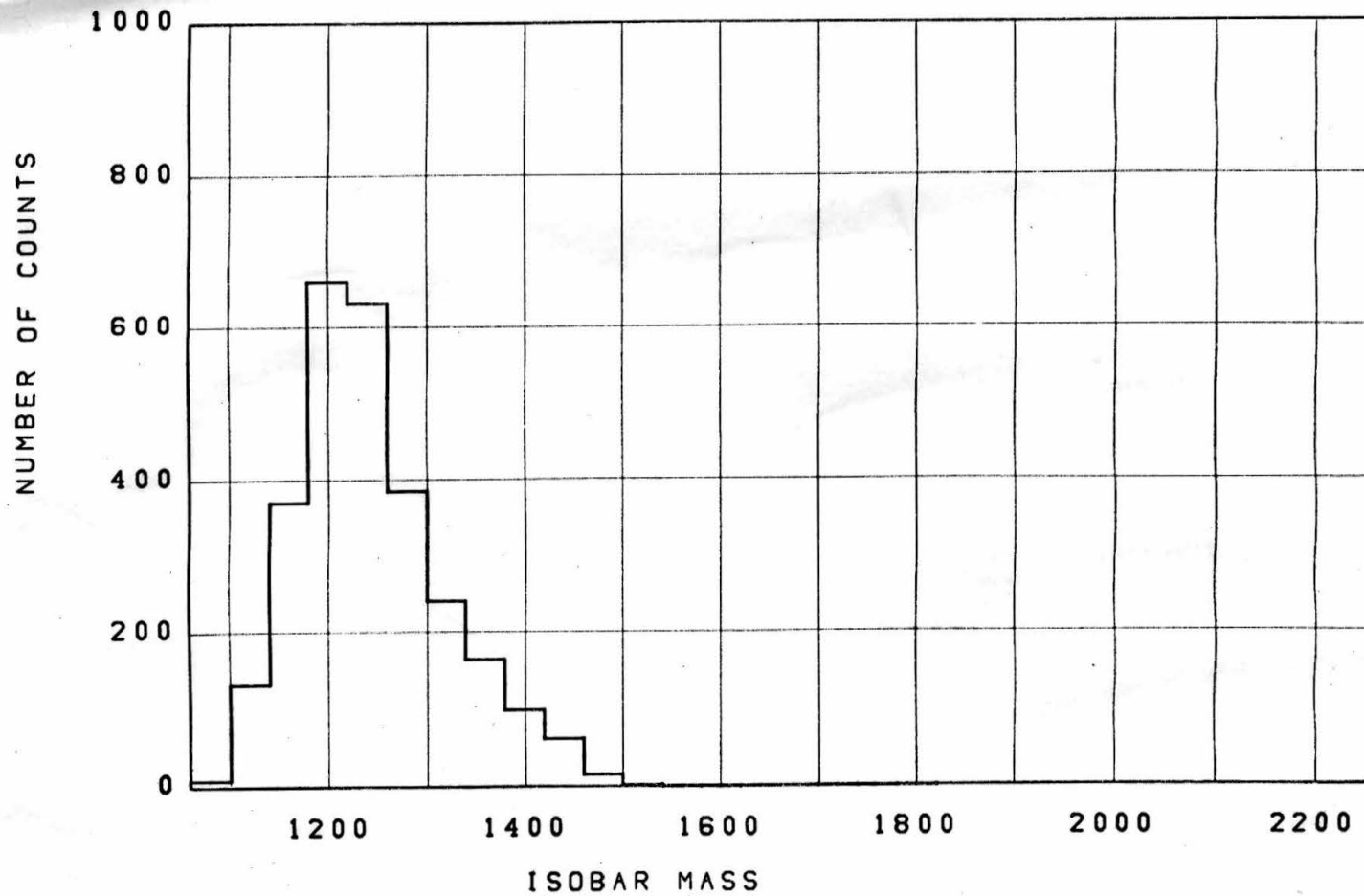


Figure 19

Generated N_{33}^* Isobar Mass Distribution, $600 < E_\gamma < 1060$

SIGMA MESON GENERATION

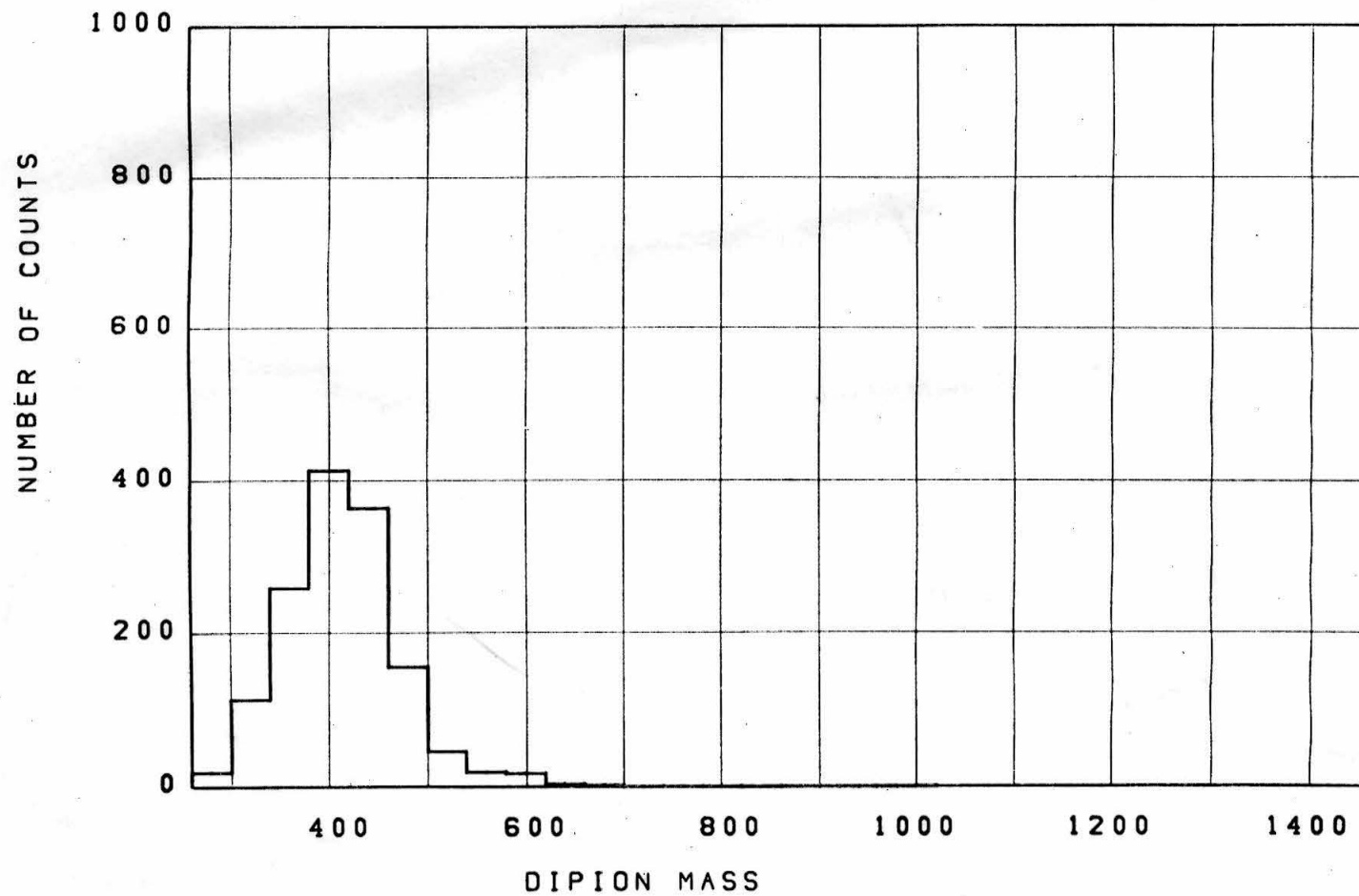


Figure 20

Generated σ Dipion Mass Distribution, $600 < E_{\gamma} < 1060$

SIGMA MESON GENERATION

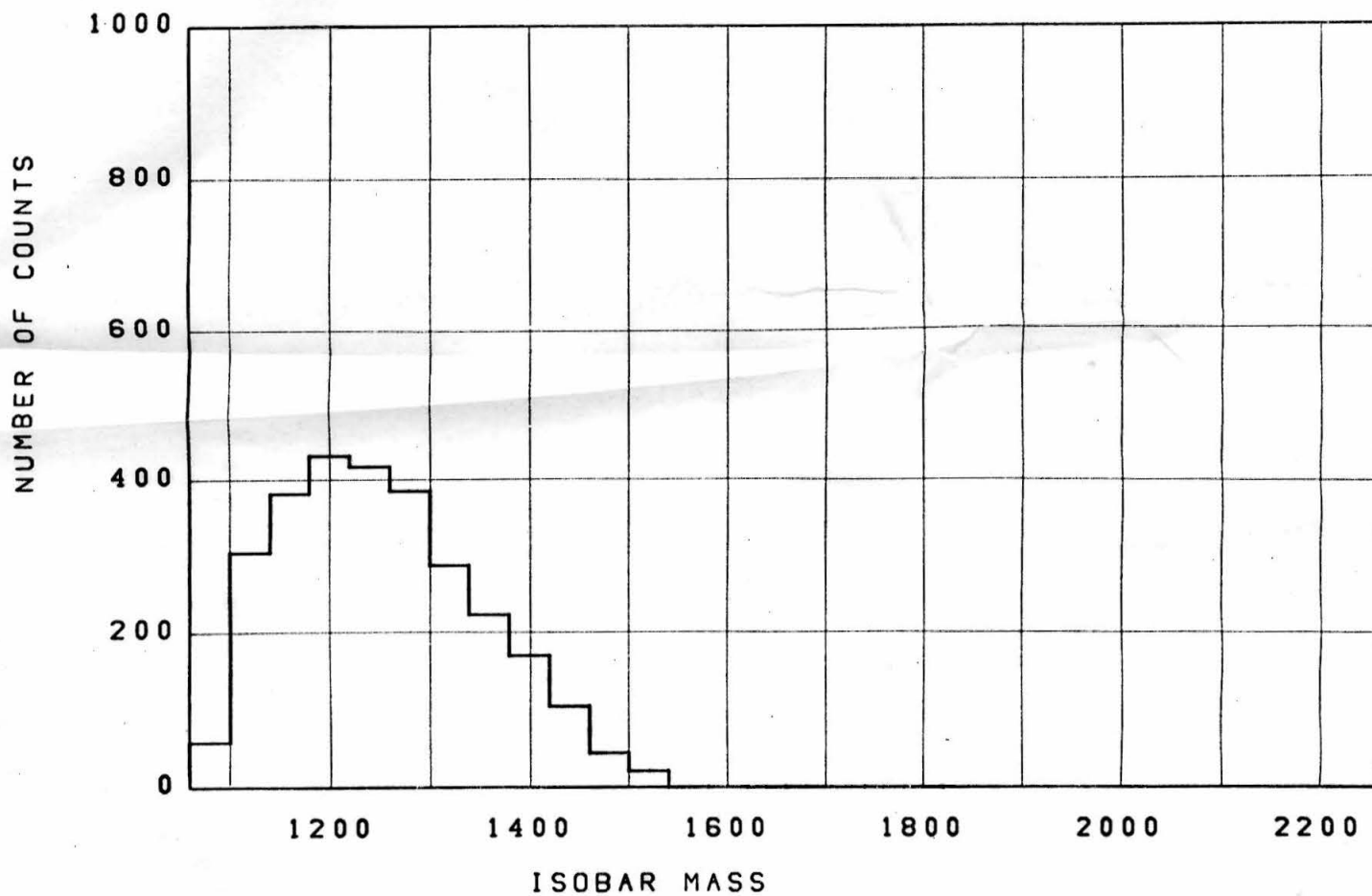


Figure 21

Generated σ Isobar Mass Distribution, $600 < E_{\gamma} < 1060$

RHO MESON GENERATION

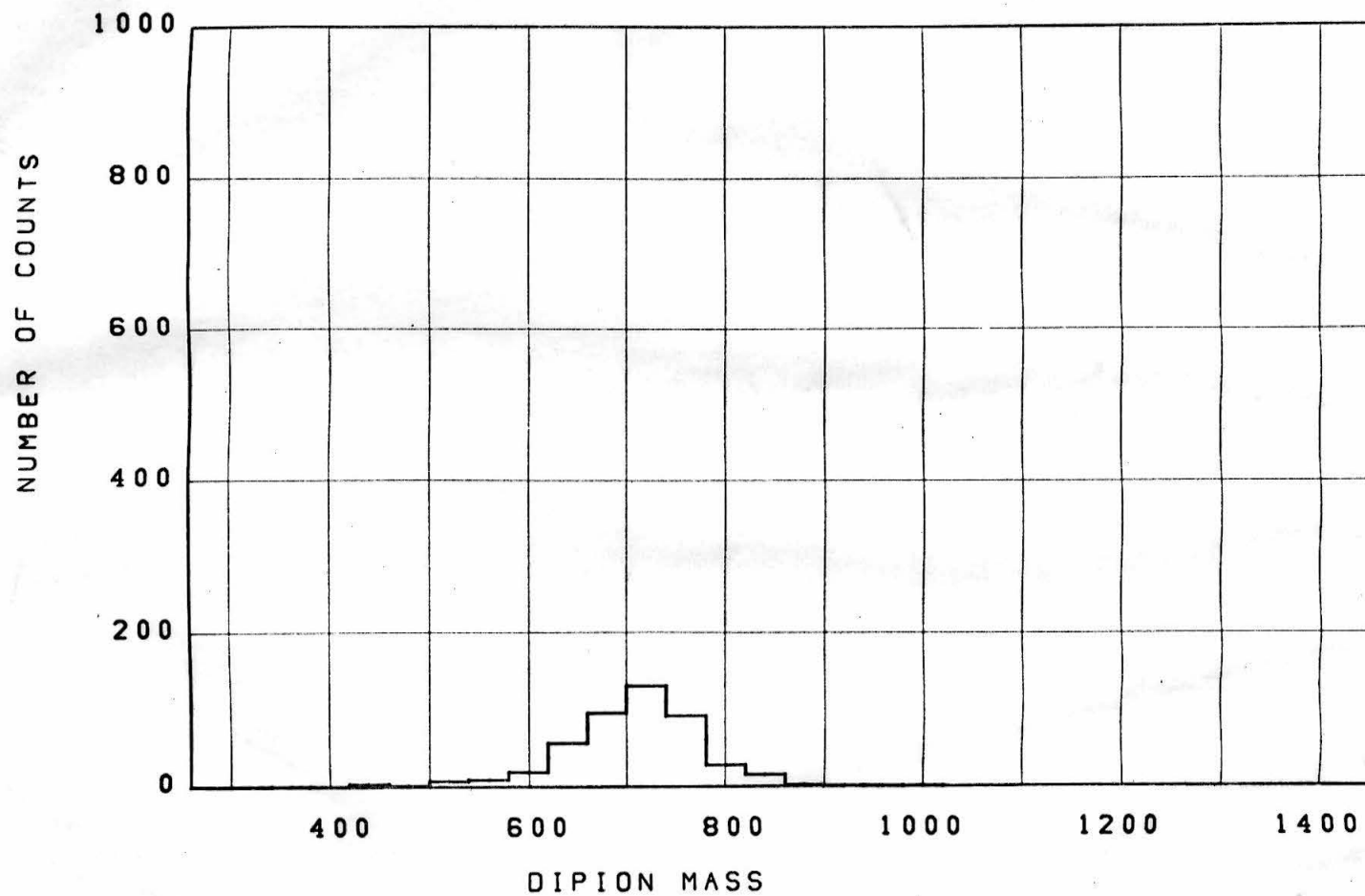


Figure 22

Generated ρ Dipion Mass Distribution, $E_\gamma > 1060$

RHO MESON GENERATION

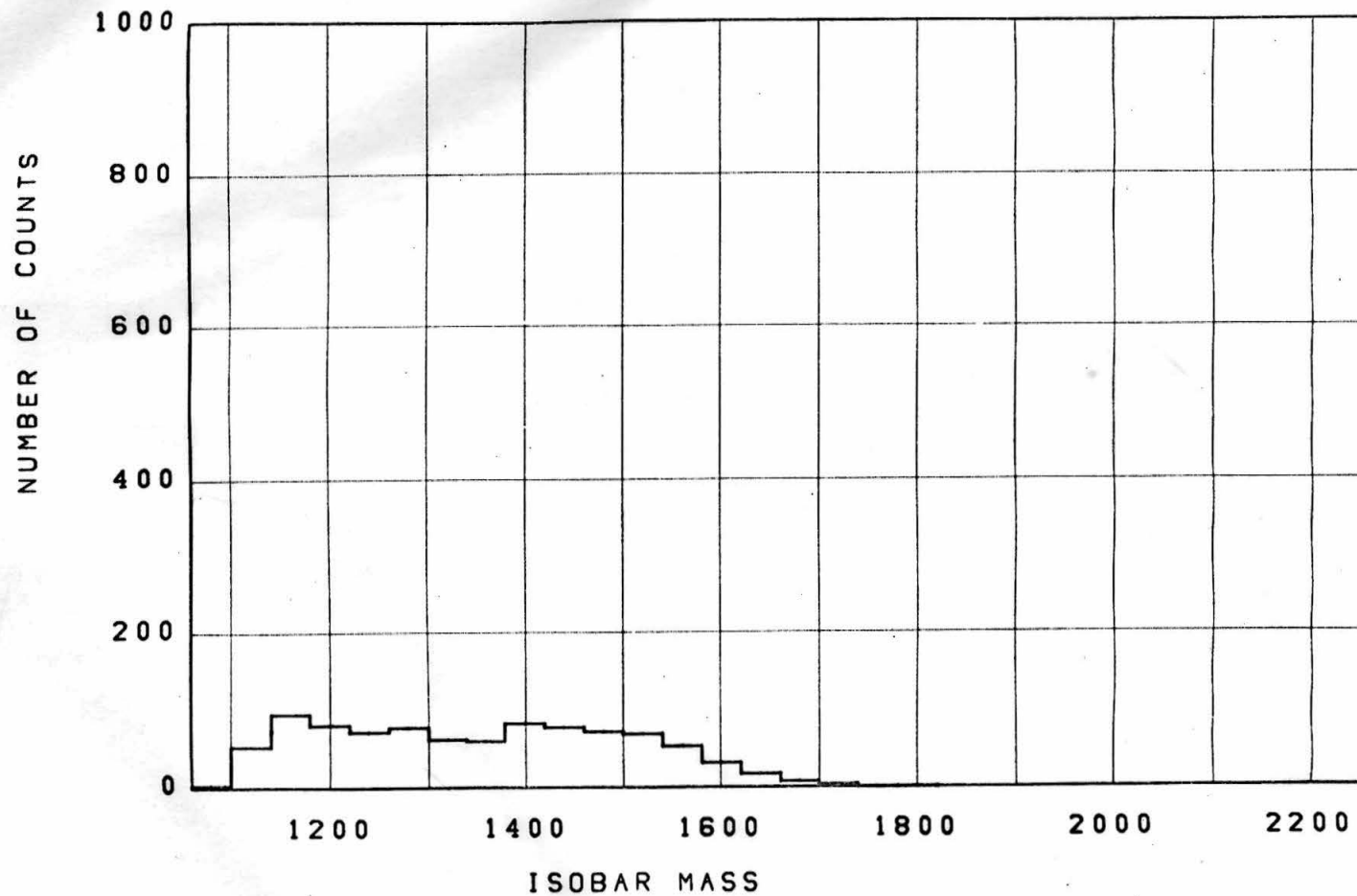


Figure 23

Generated ρ Isobar Mass Distribution, $E_\gamma > 1060$

PHASE SPACE GENERATION

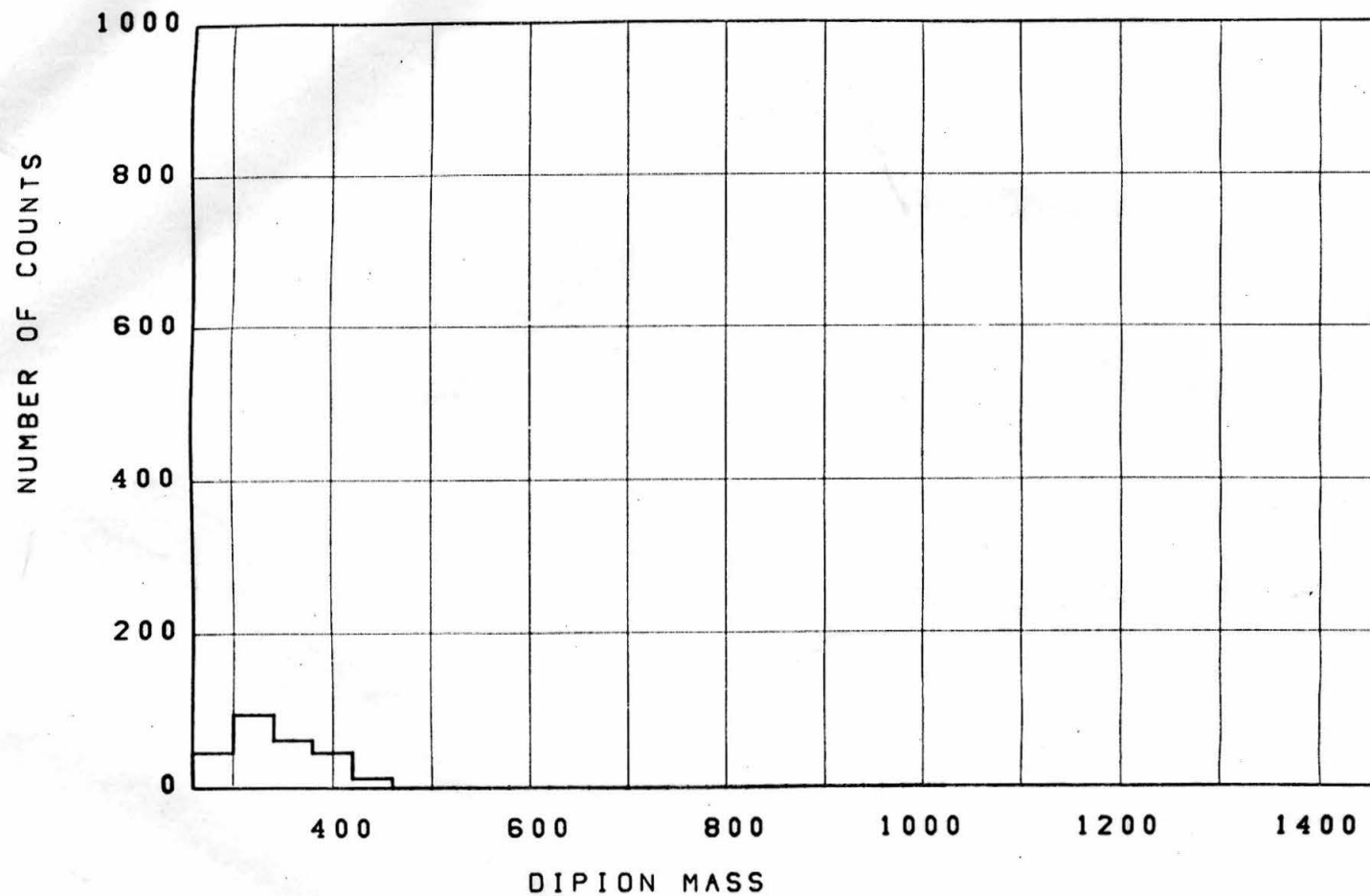


Figure 24

Generated Phase Space Dipion Mass Distribution, $E_\gamma < 600$

PHASE SPACE GENERATION

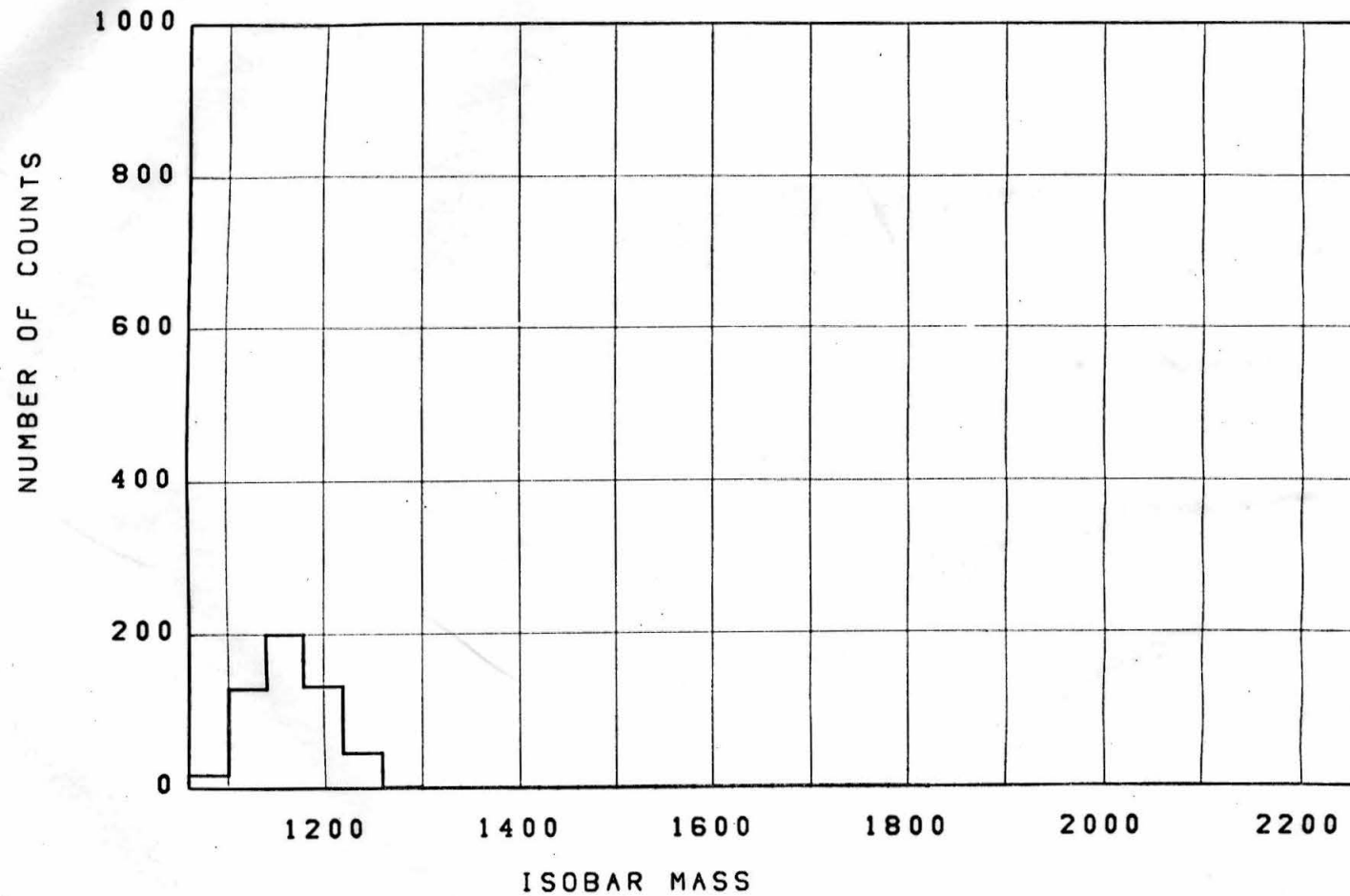


Figure 25

Generated Phase Space Isobar Mass Distribution, $E_\gamma < 600$

N-STAR (1238) GENERATION

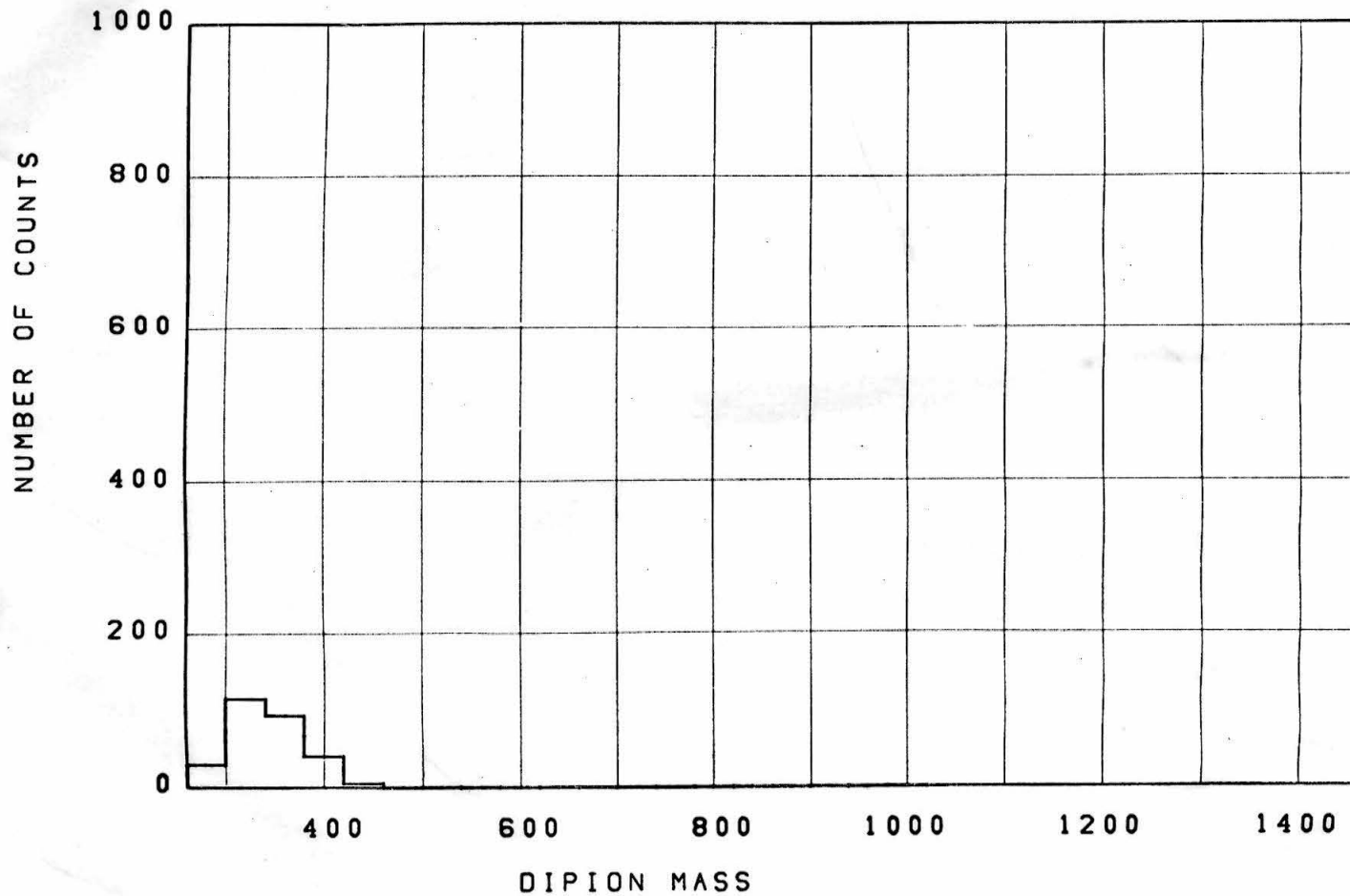


Figure 26

Generated N_{33}^* Dipion Mass Distribution, $E_\gamma < 600$

N-STAR (1238) GENERATION

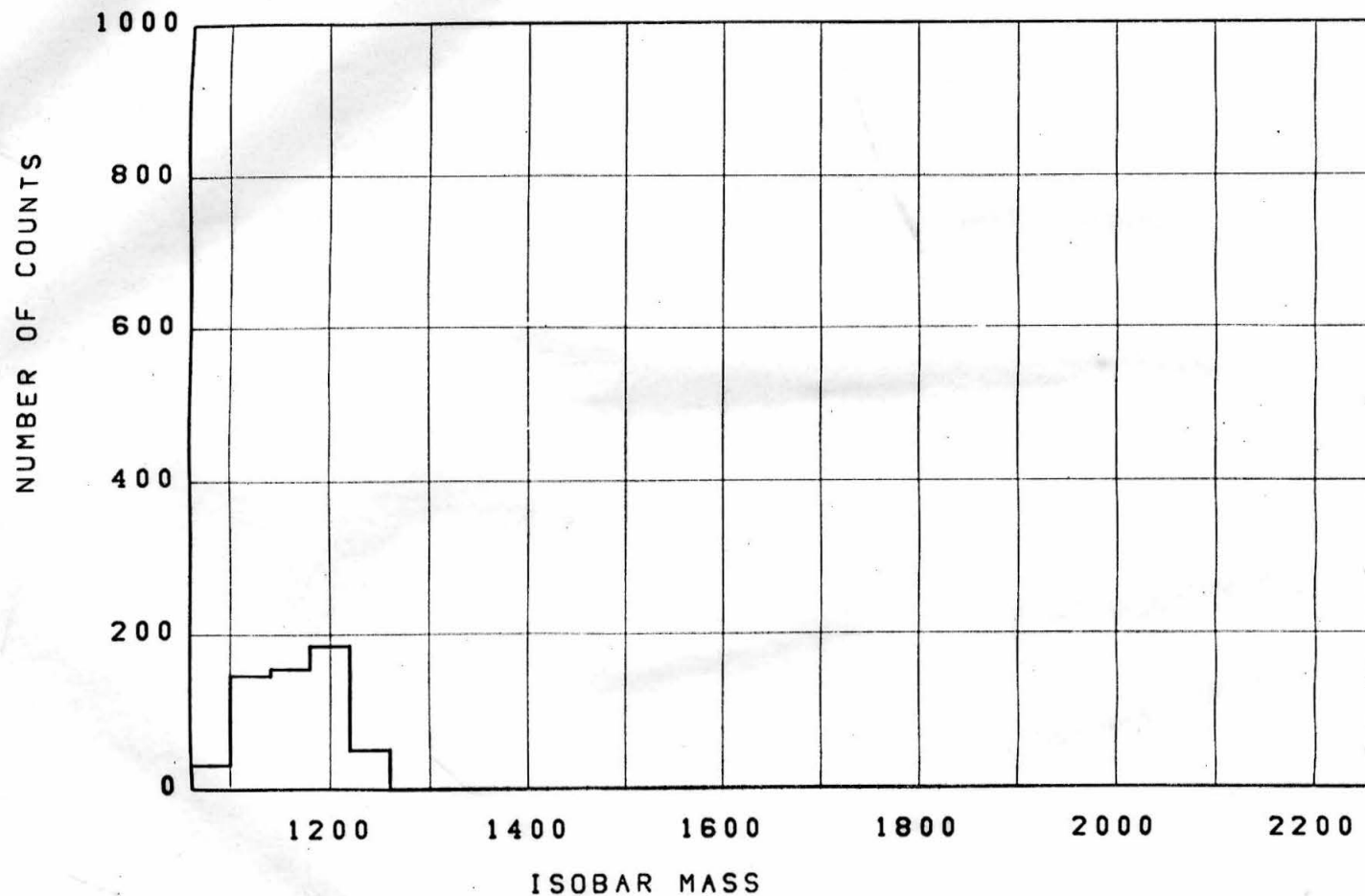


Figure 27

Generated N_{33}^* Isobar Mass Distribution, $E_\gamma < 600$

DIPION SYSTEM

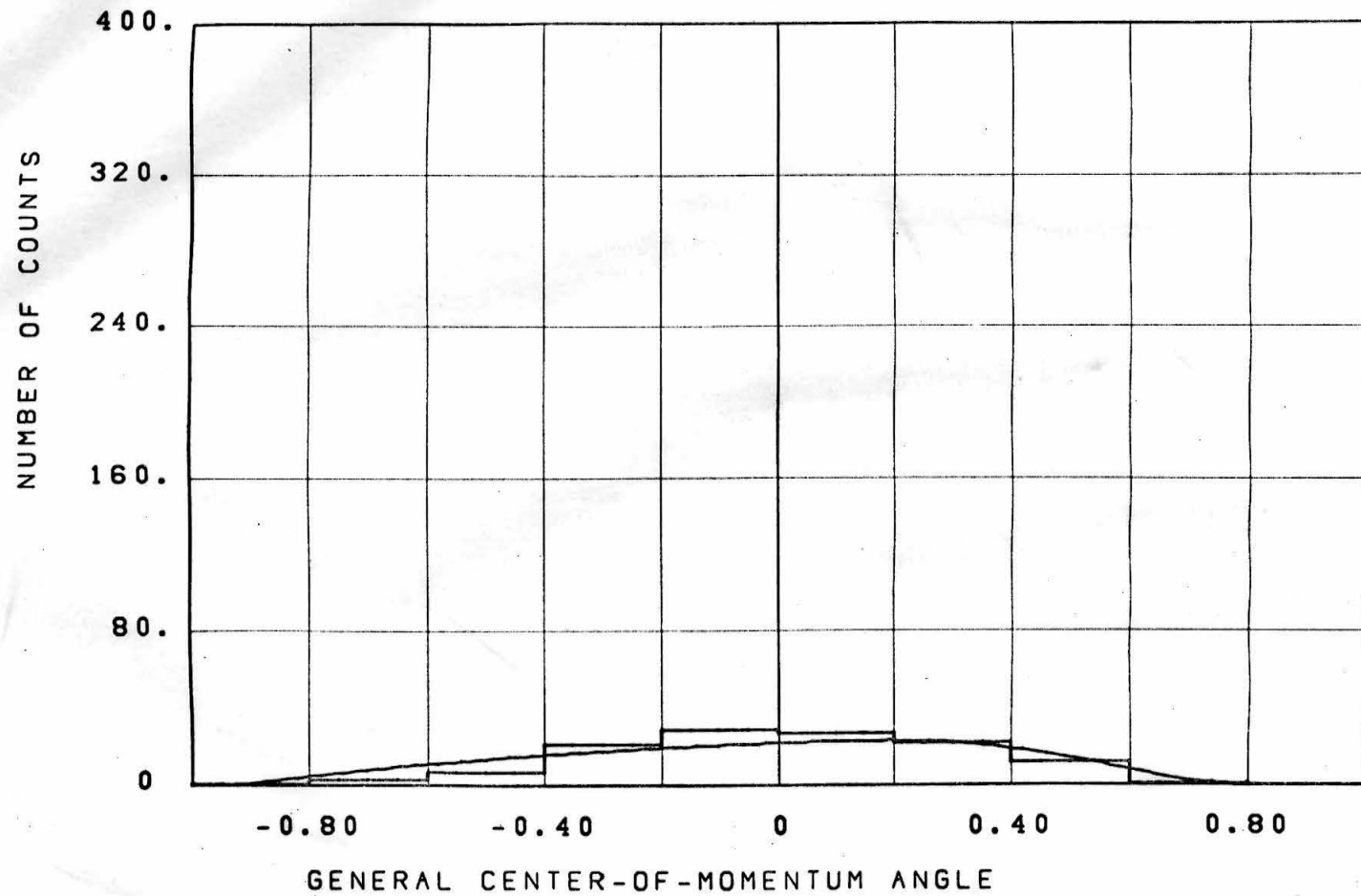


Figure 28

General COM Polar Angle Distribution of Dipion, $E_\gamma < 600$

DIPION SYSTEM

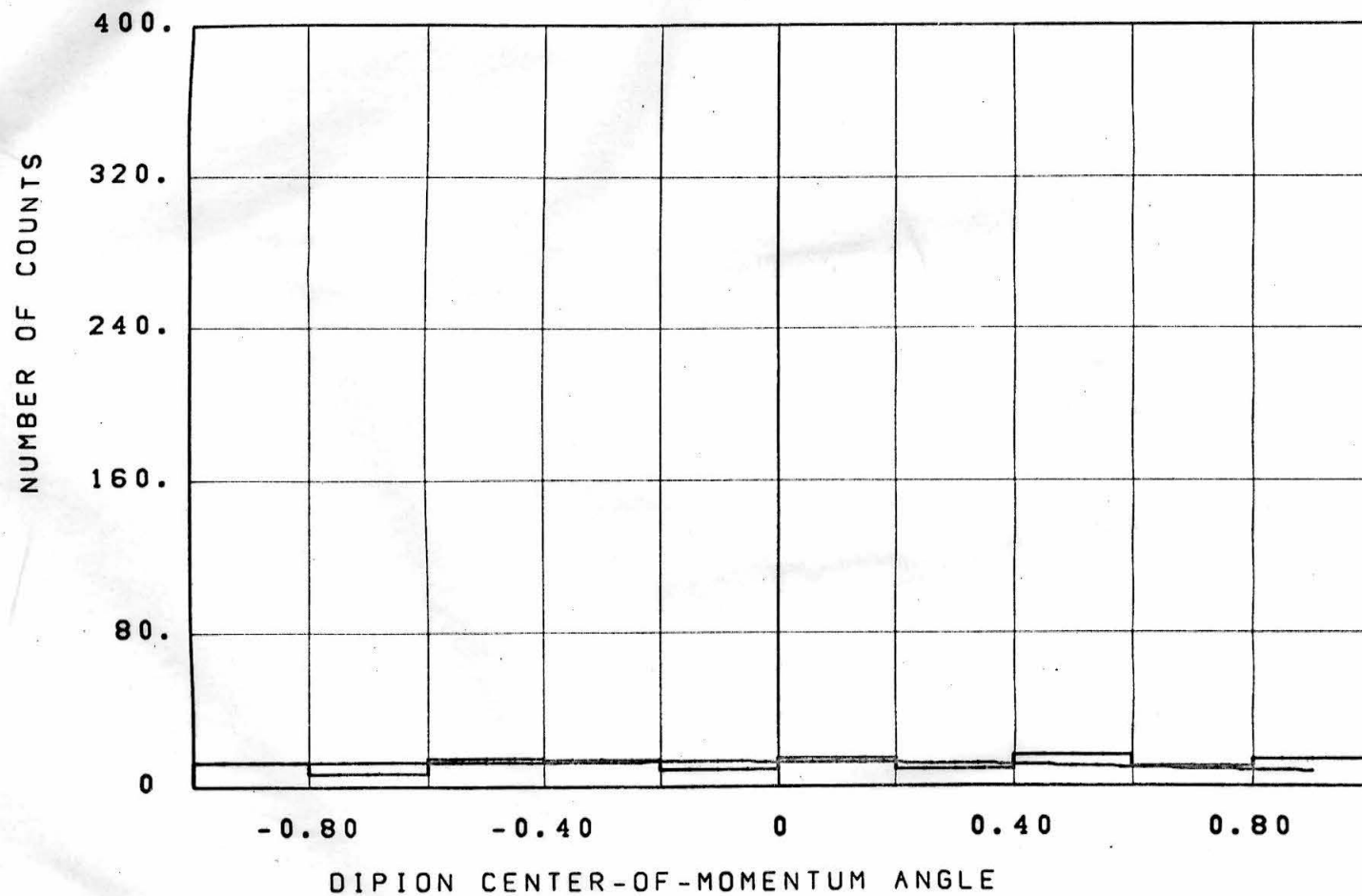


Figure 29

Dipion COM Polar Angle Distribution of Pion, $E_\gamma < 600$

DIPION SYSTEM

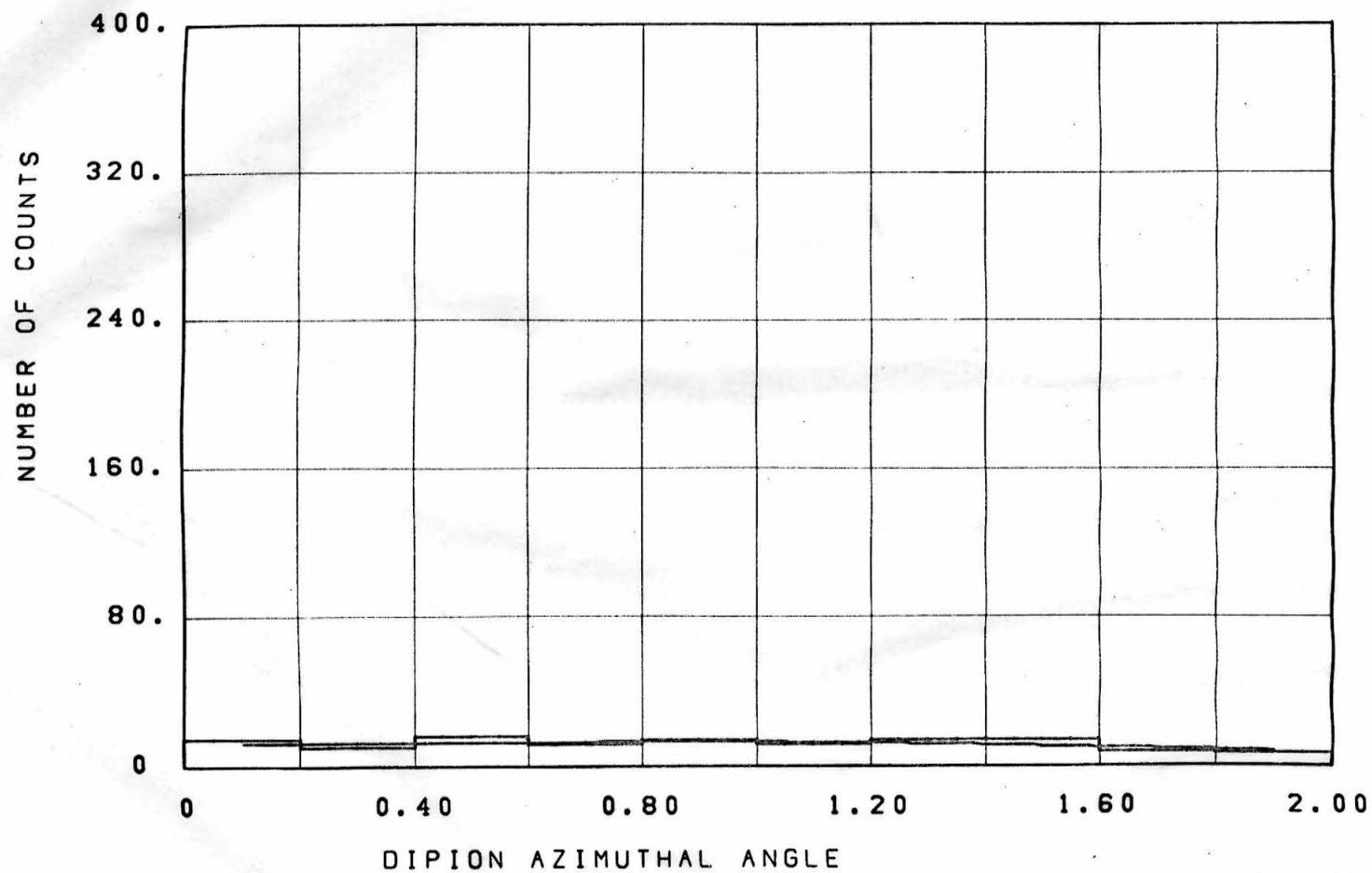


Figure 30

Dipion COM Azimuthal Angle Distribution of Pion, $E_\gamma < 600$

ISOBAR SYSTEM

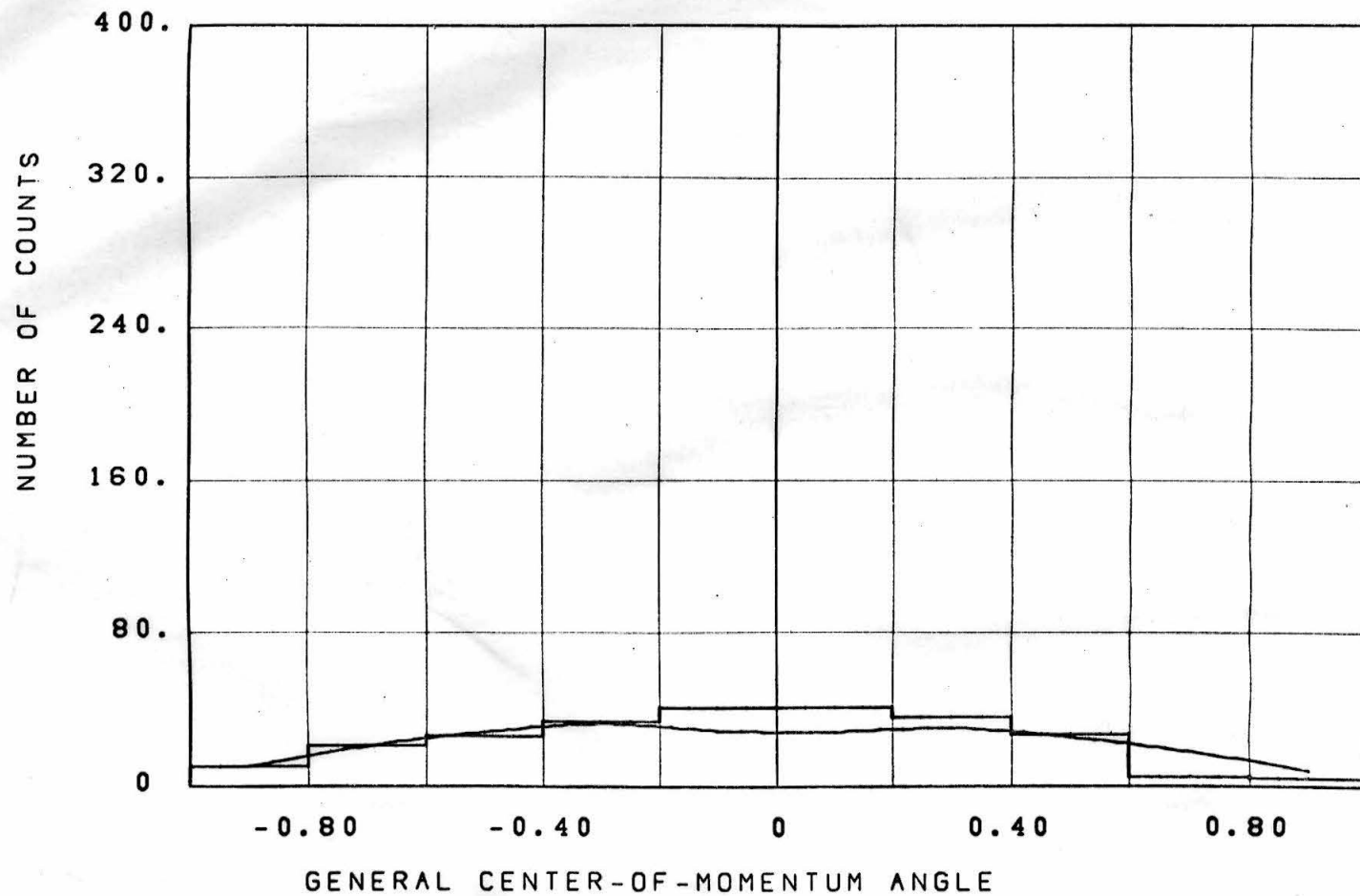


Figure 31

General COM Polar Angle Distribution of Isobar, $E_\gamma < 600$

ISOBAR SYSTEM

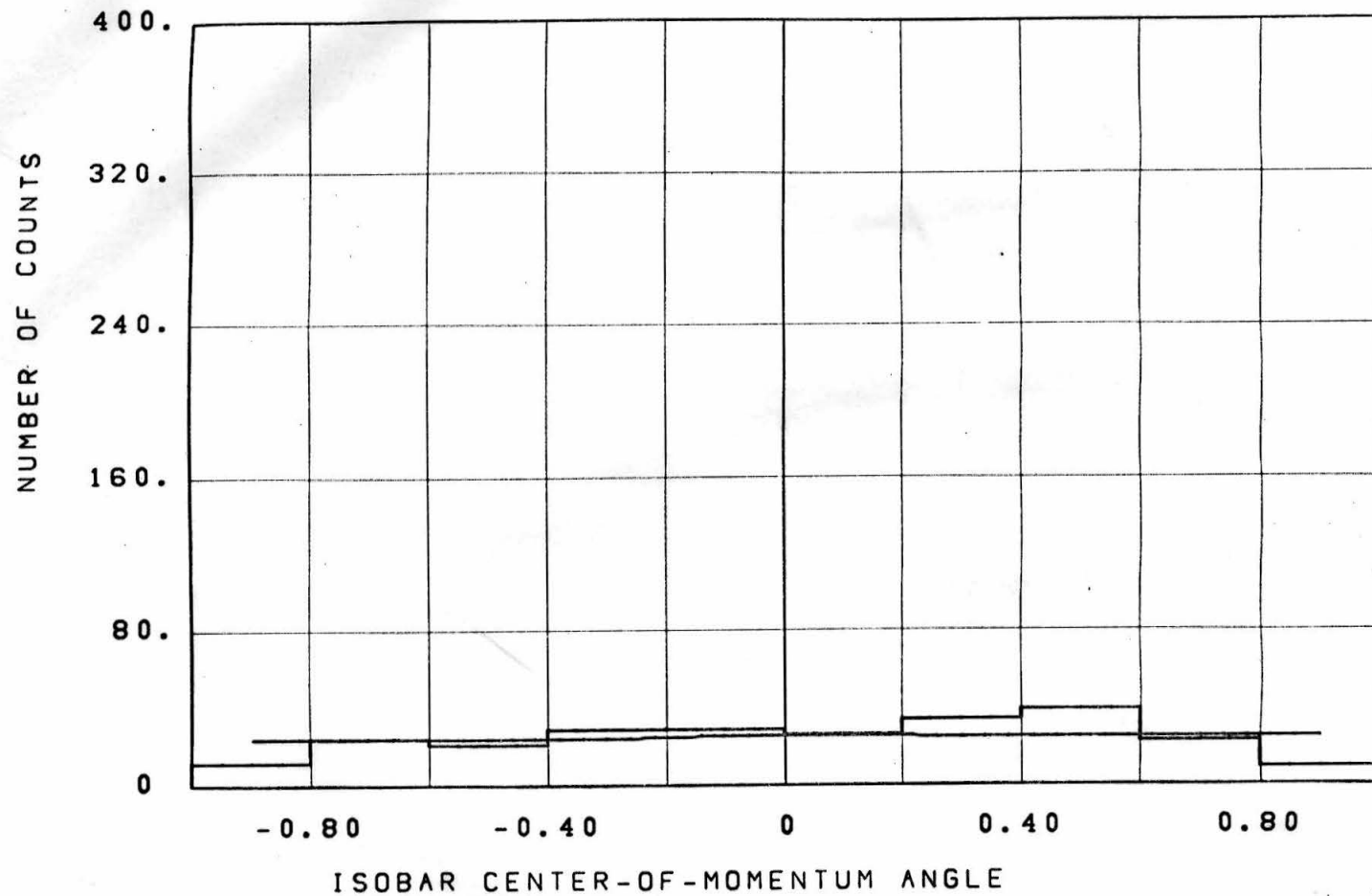


Figure 32

Isobar COM Polar Angle Distribution of Pion, $E_\gamma < 600$

ISOBAR SYSTEM

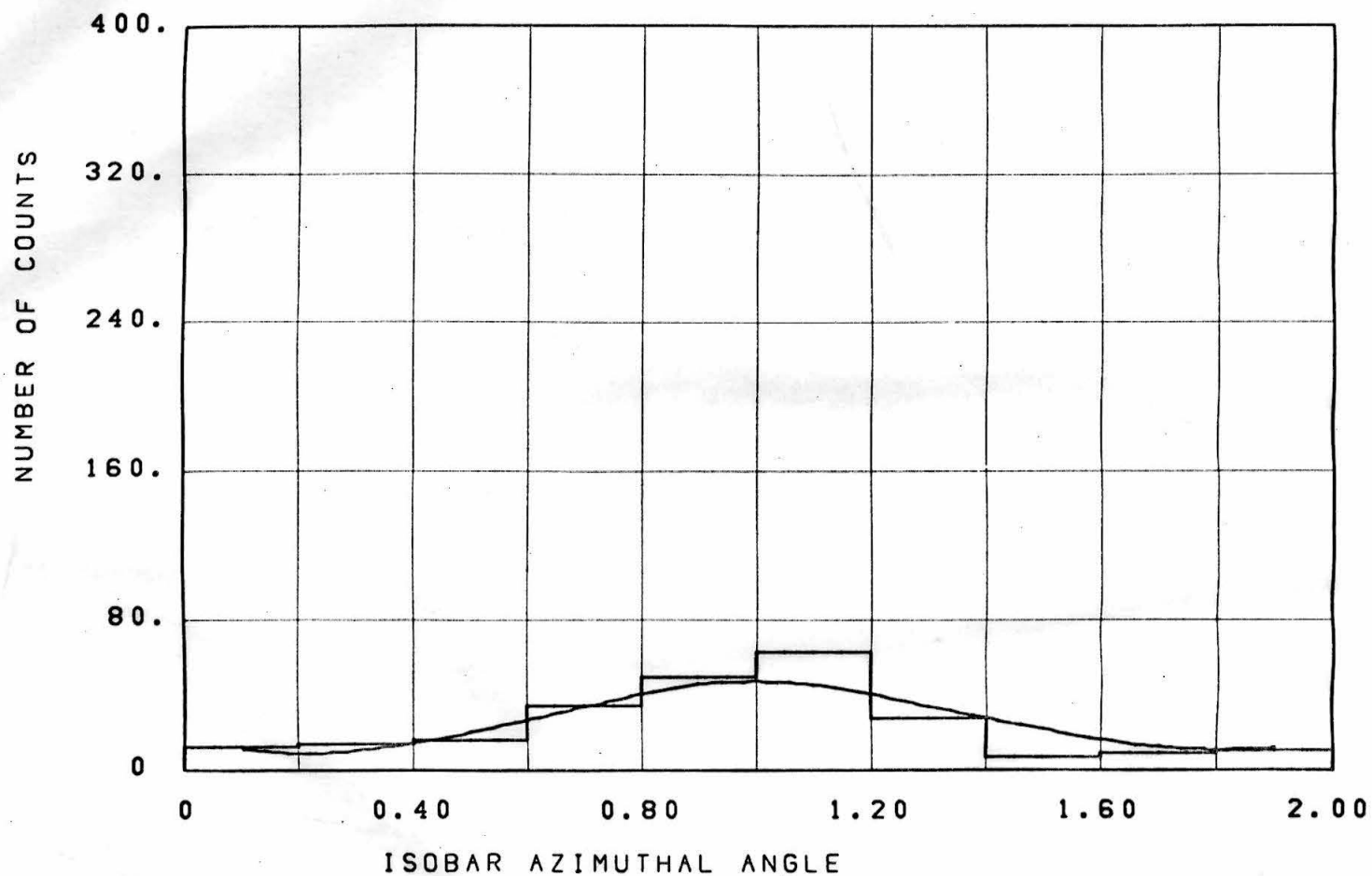


Figure 33

Isobar COM Azimuthal Angle Distribution of Pion, $E_\gamma < 600$

DIPION SYSTEM

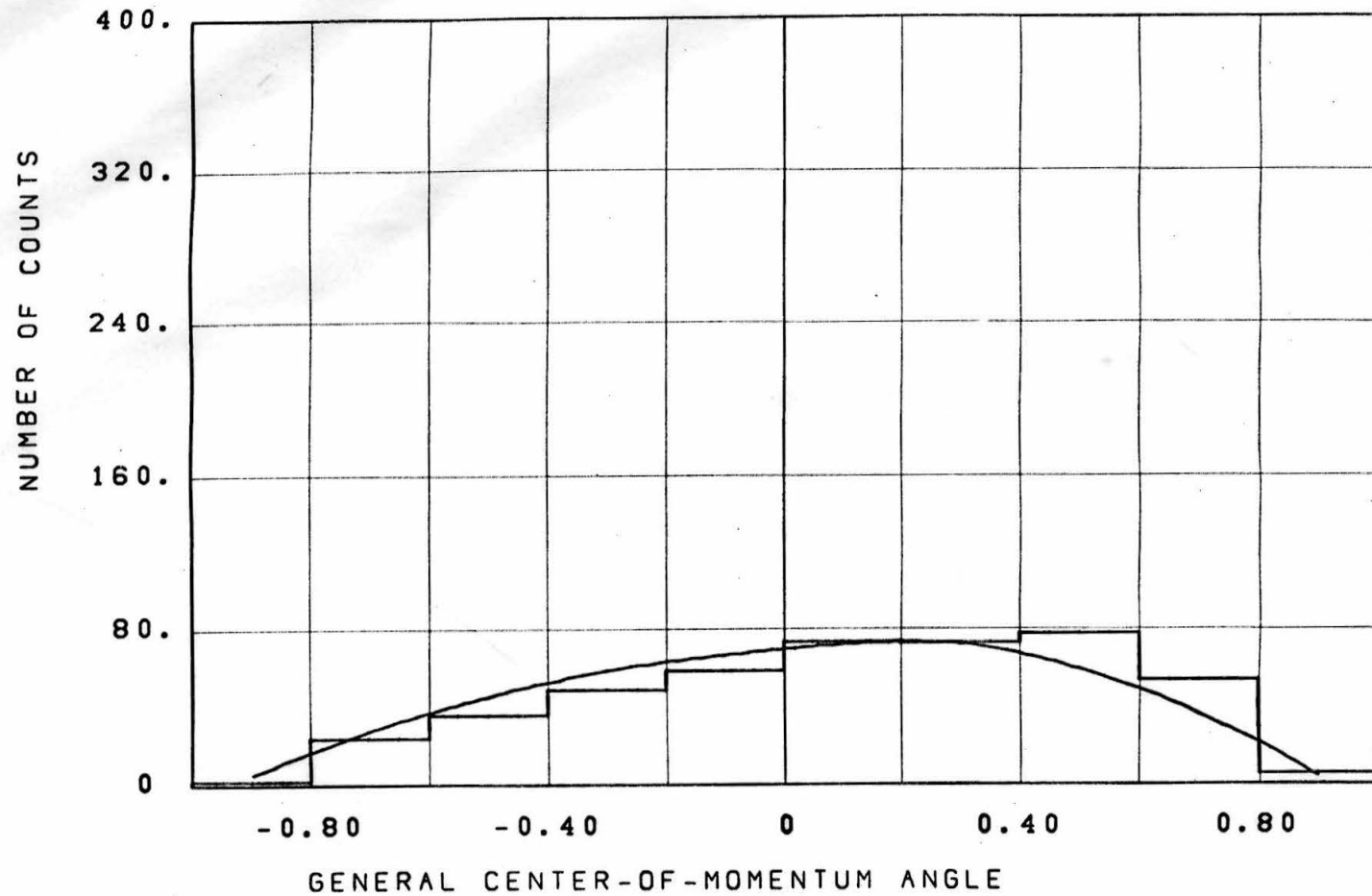


Figure 34

General COM Polar Angle Distribution of Dipion, $600 E_\gamma < 1060$

DIPION SYSTEM

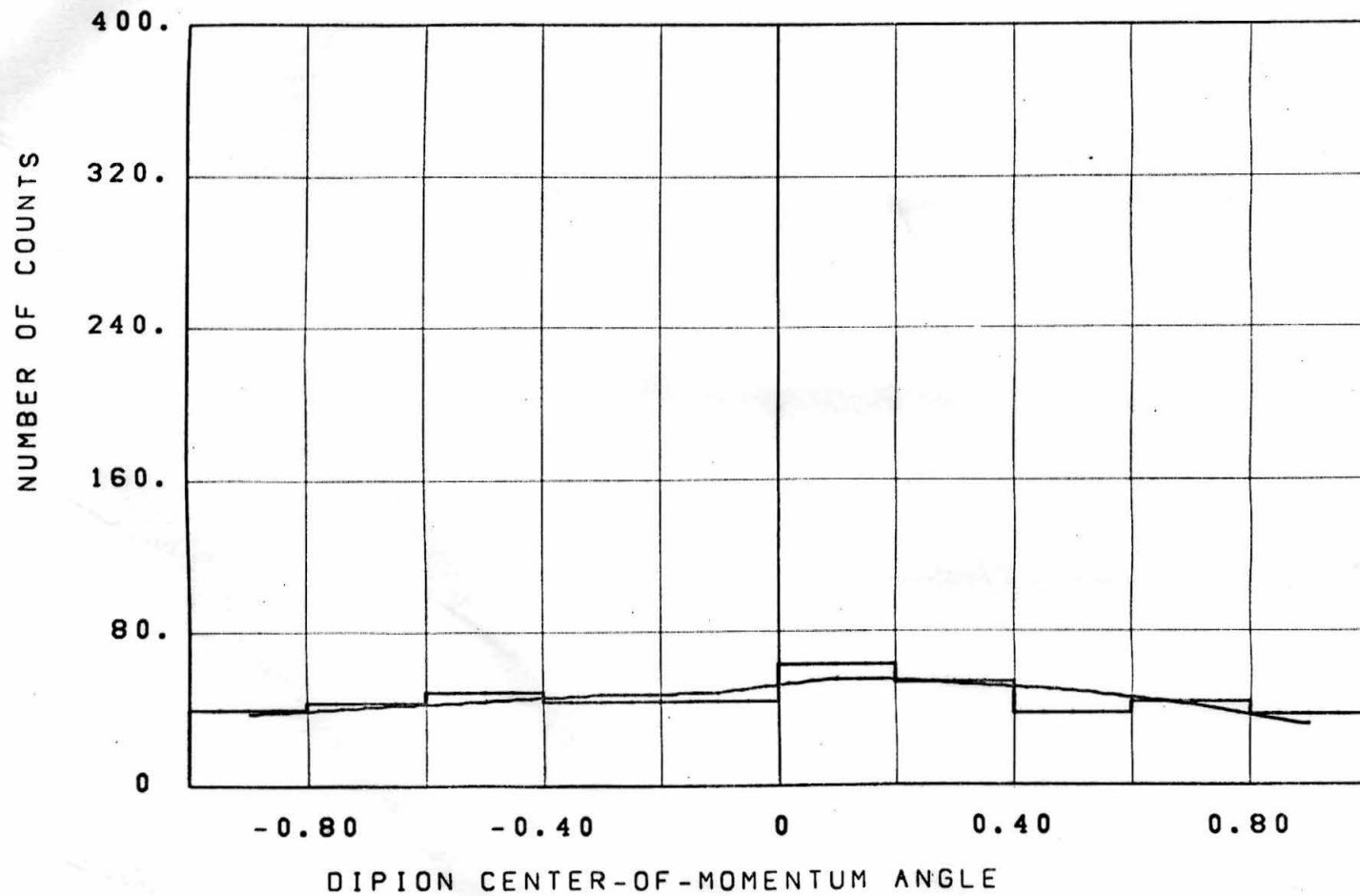


Figure 35

Dipion COM Polar Angle Distribution of Pion, $600 < E_{\gamma} < 1060$

DIPION SYSTEM

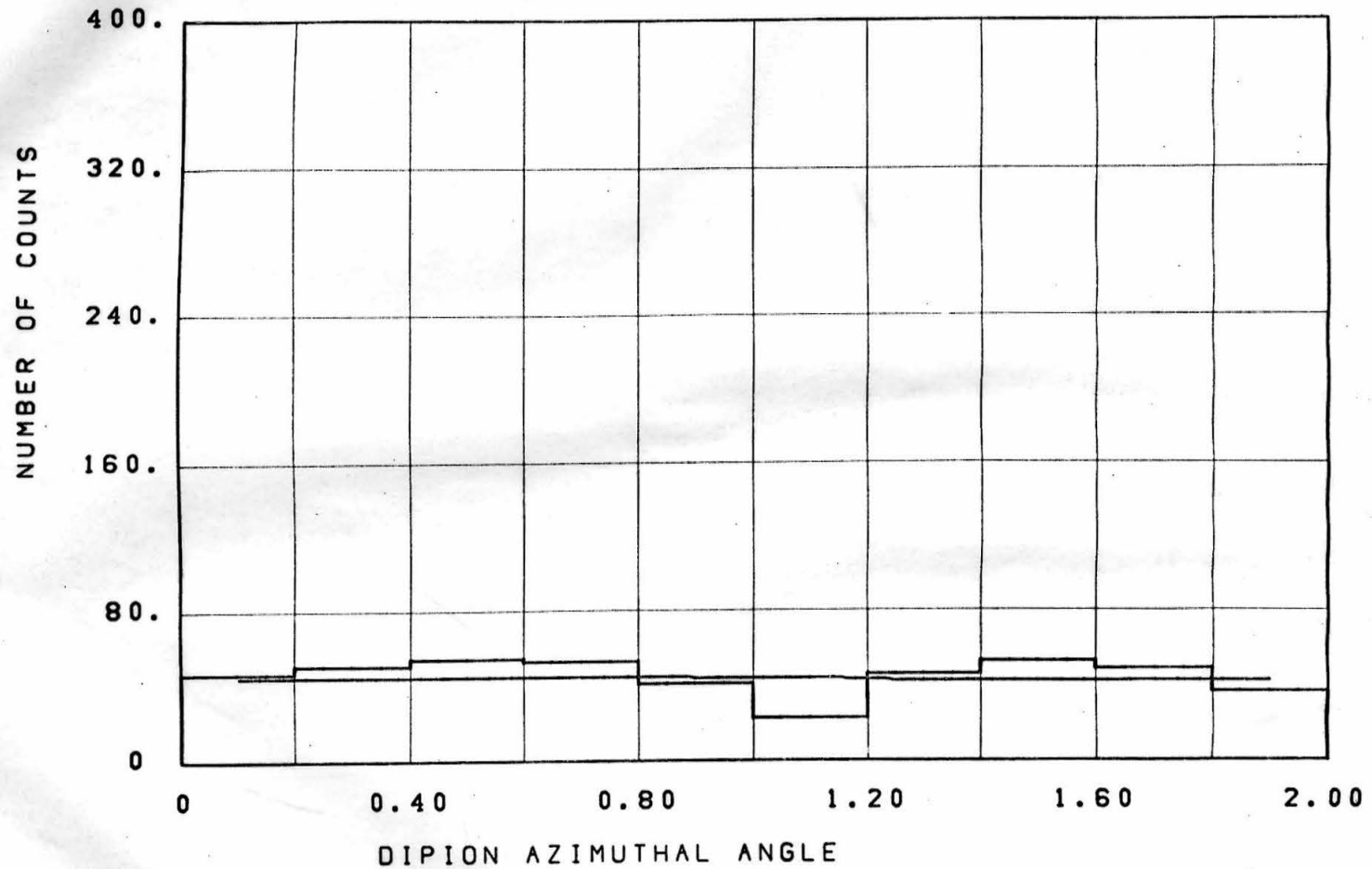


Figure 36

Dipion COM Azimuthal Angle Distribution of Pion, $600 < E_{\gamma} < 1060$

ISOBAR SYSTEM

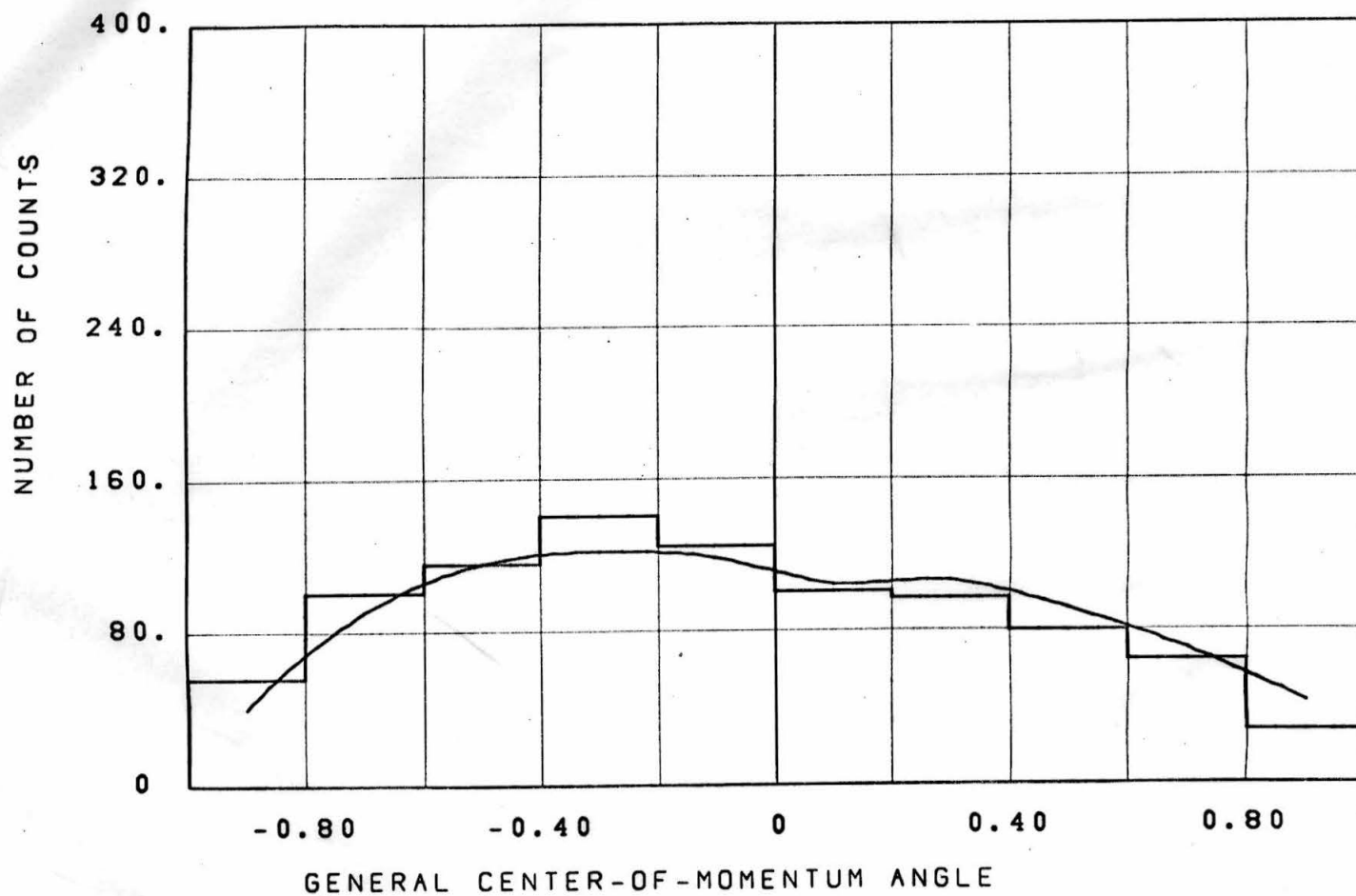


Figure 37

General COM Polar Angle Distribution of Isobar, $600 < E_{\gamma} < 1060$

ISOBAR SYSTEM

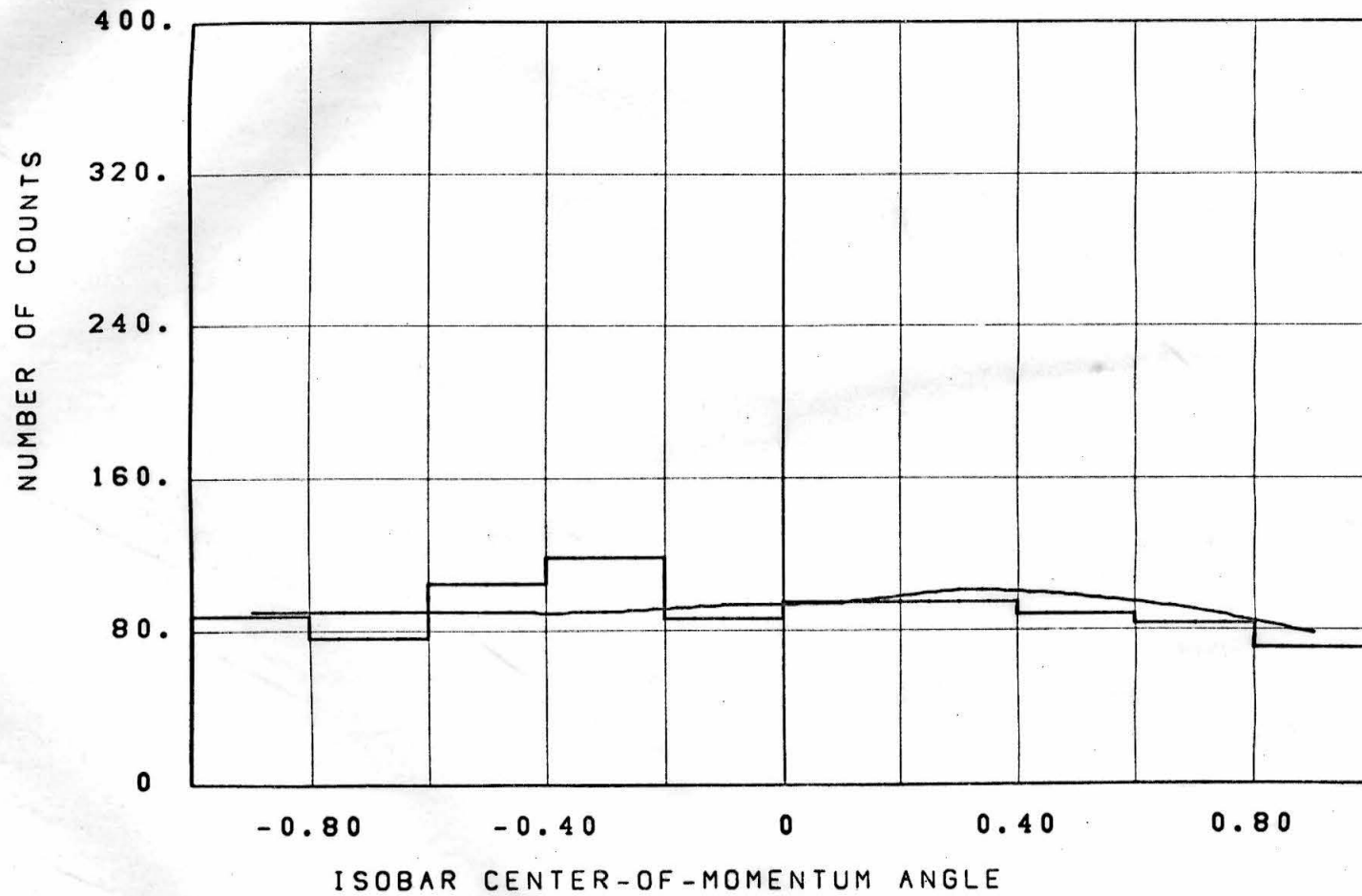


Figure 38

Isobar COM Polar Angle Distribution of Pion, $600 < E_{\gamma} < 1060$

ISOBAR SYSTEM

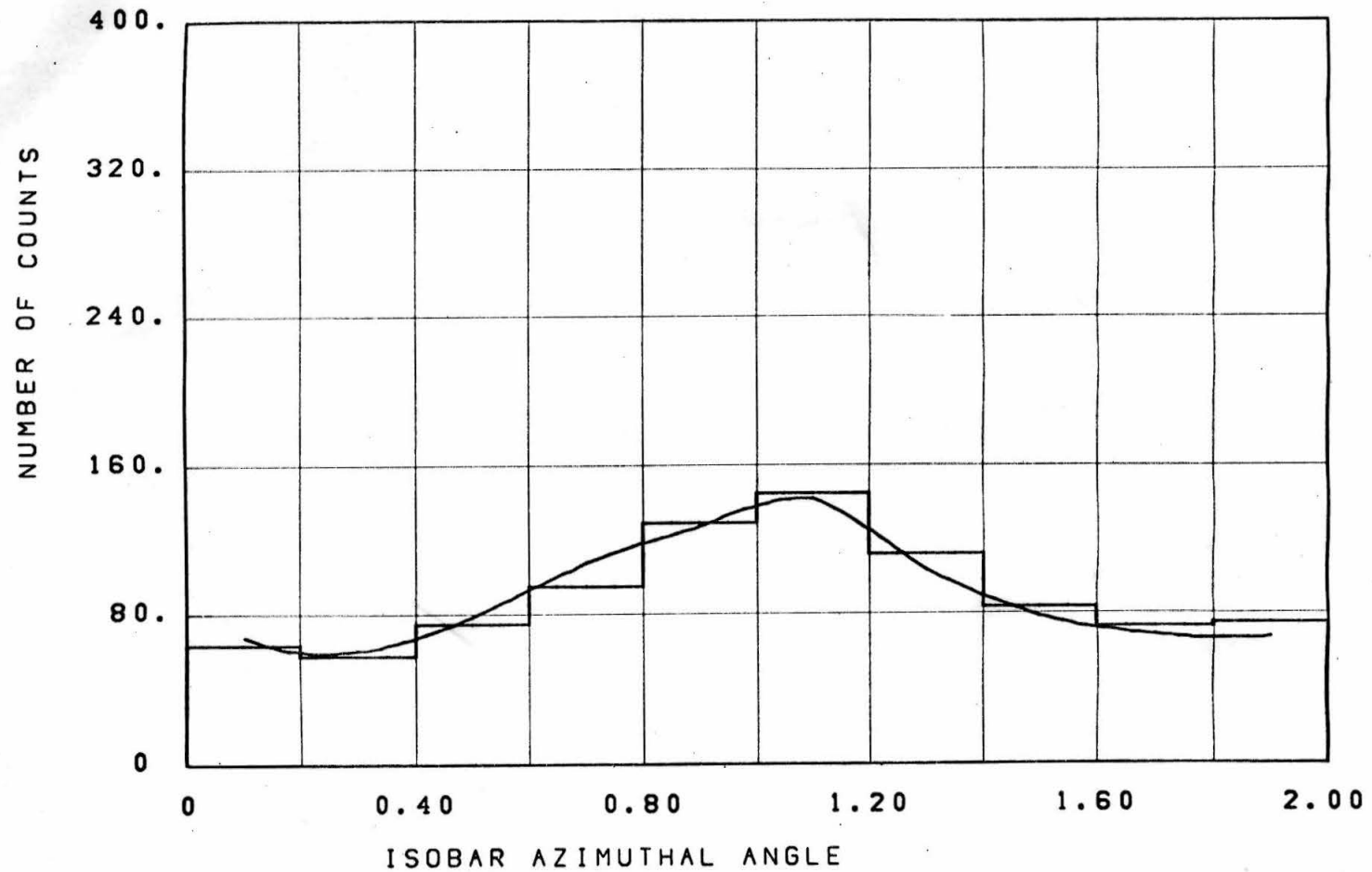


Figure 39

Isobar COM Azimuthal Angle Distribution of Pion, $600 < E_{\gamma} < 1060$

DIPION SYSTEM

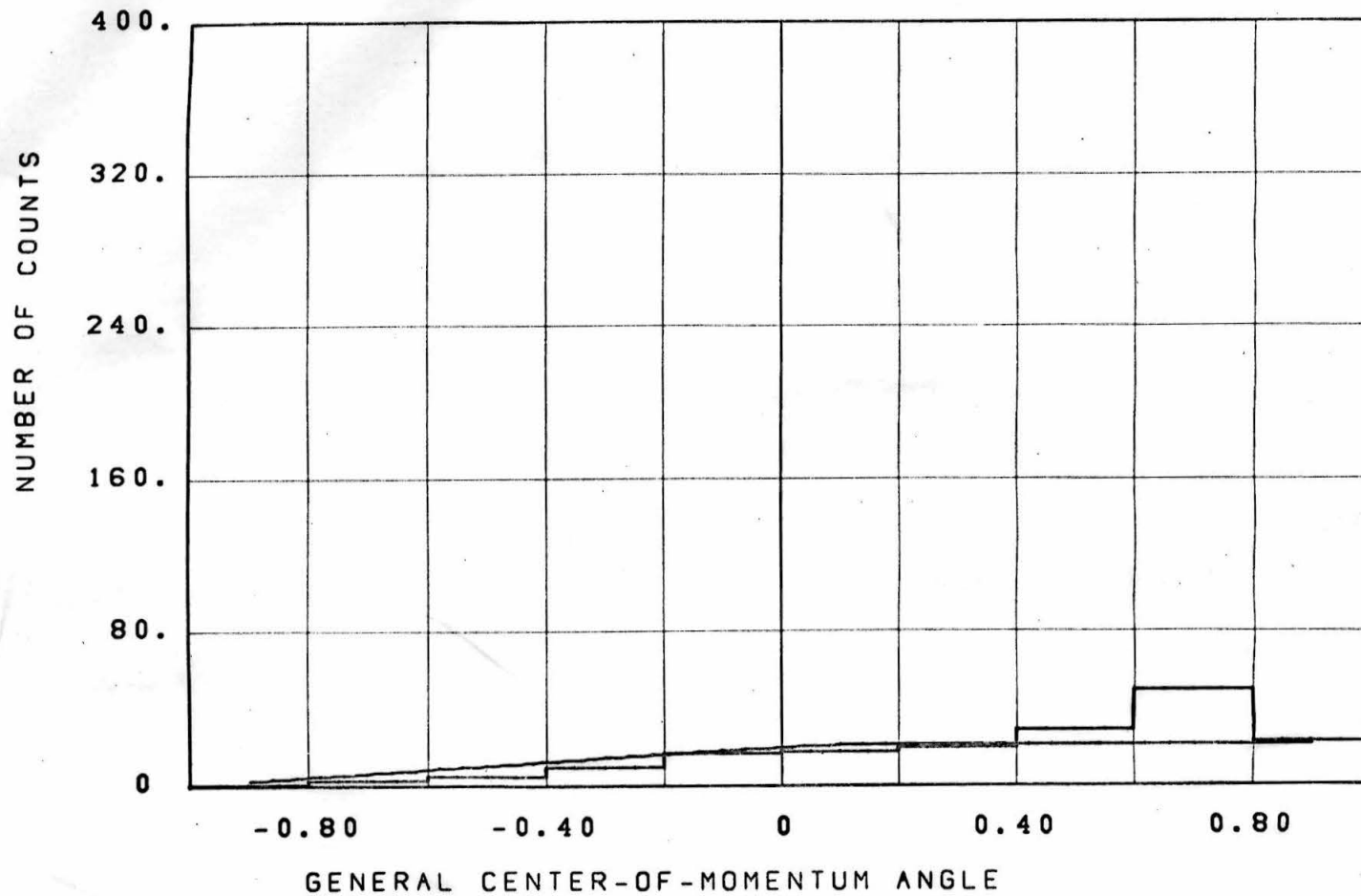


Figure 40

General COM Polar Angle Distribution of Dipion, $E_\gamma > 1060$

DIPION SYSTEM

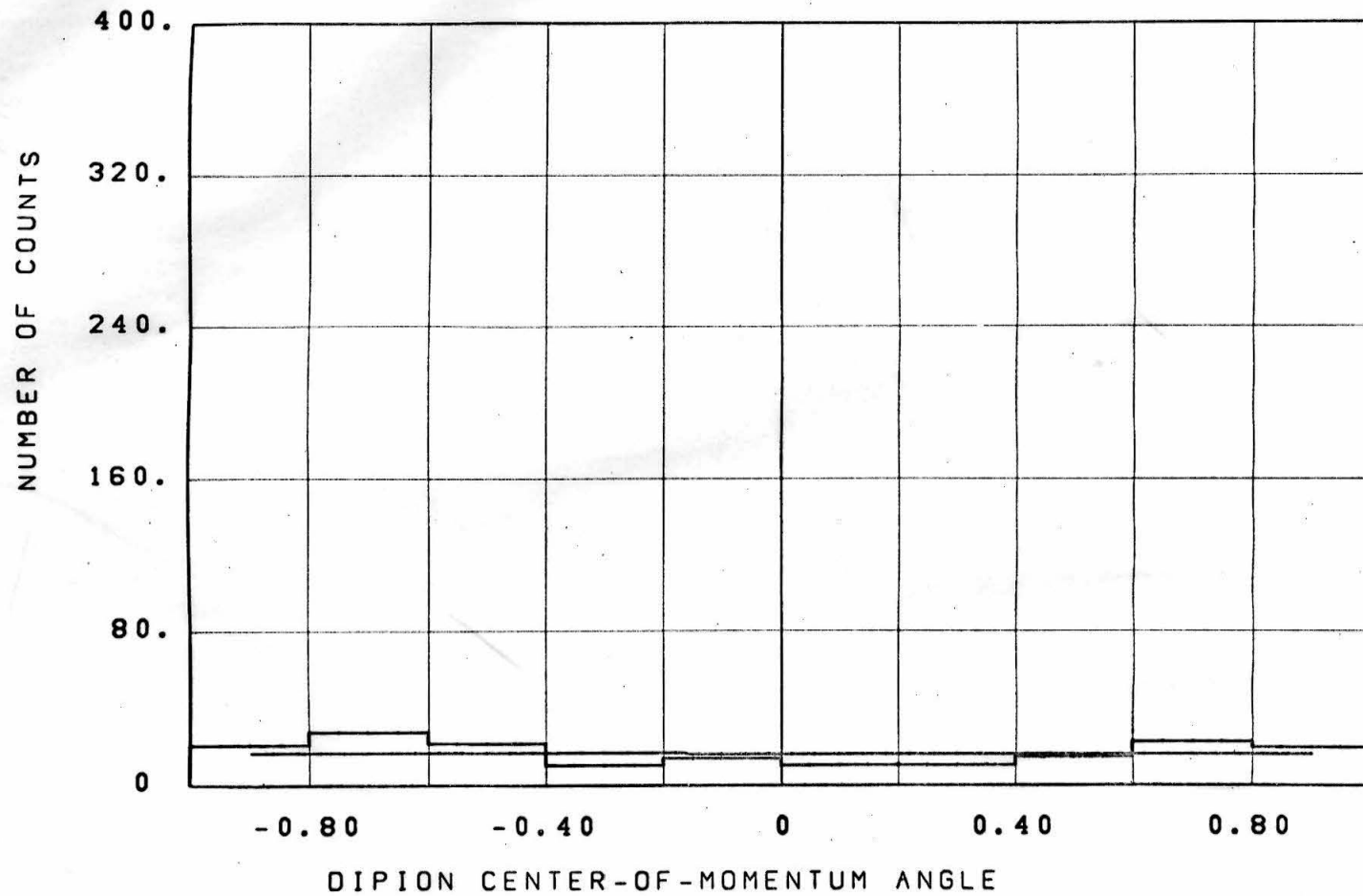


Figure 41

Dipion COM Polar Angle Distribution of Pion, $E_\gamma > 1060$

DIPION SYSTEM

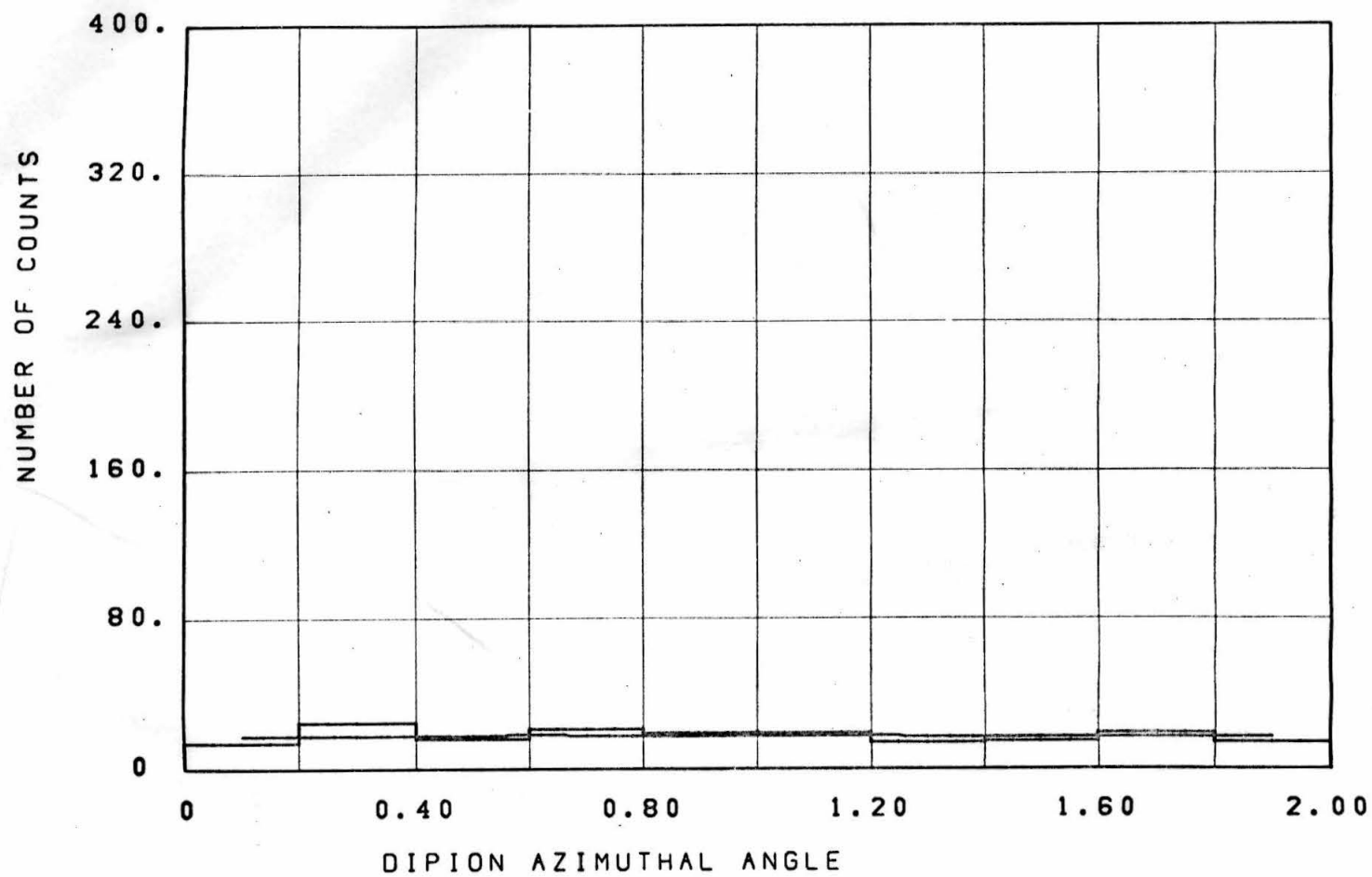


Figure 42

Dipion COM Azimuthal Angle Distribution of Pion, $E_\gamma > 1060$

ISOBAR SYSTEM

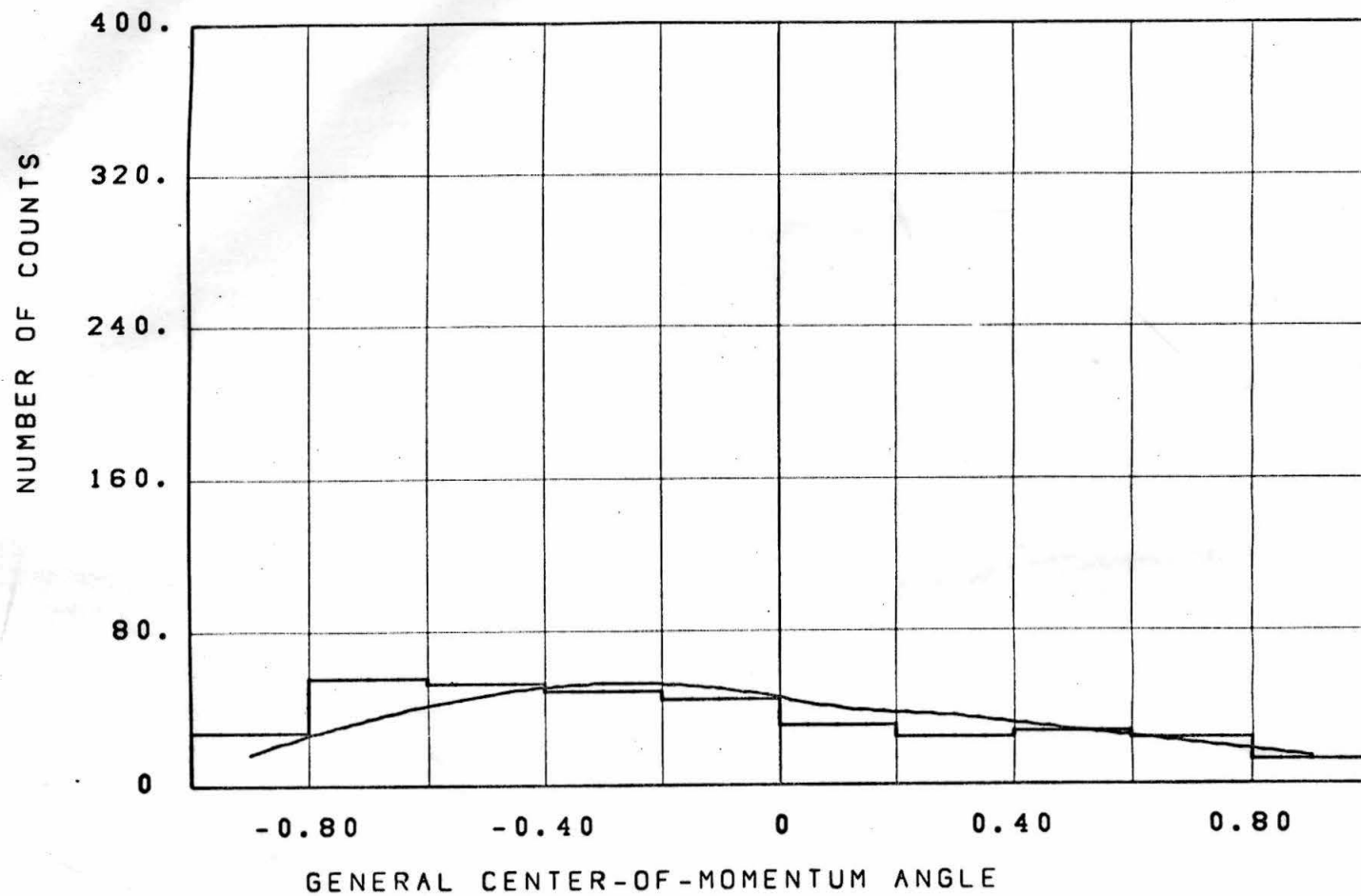


Figure 43

General COM Polar Angle Distribution of Isobar, $E_{\gamma} > 1060$

ISOBAR SYSTEM

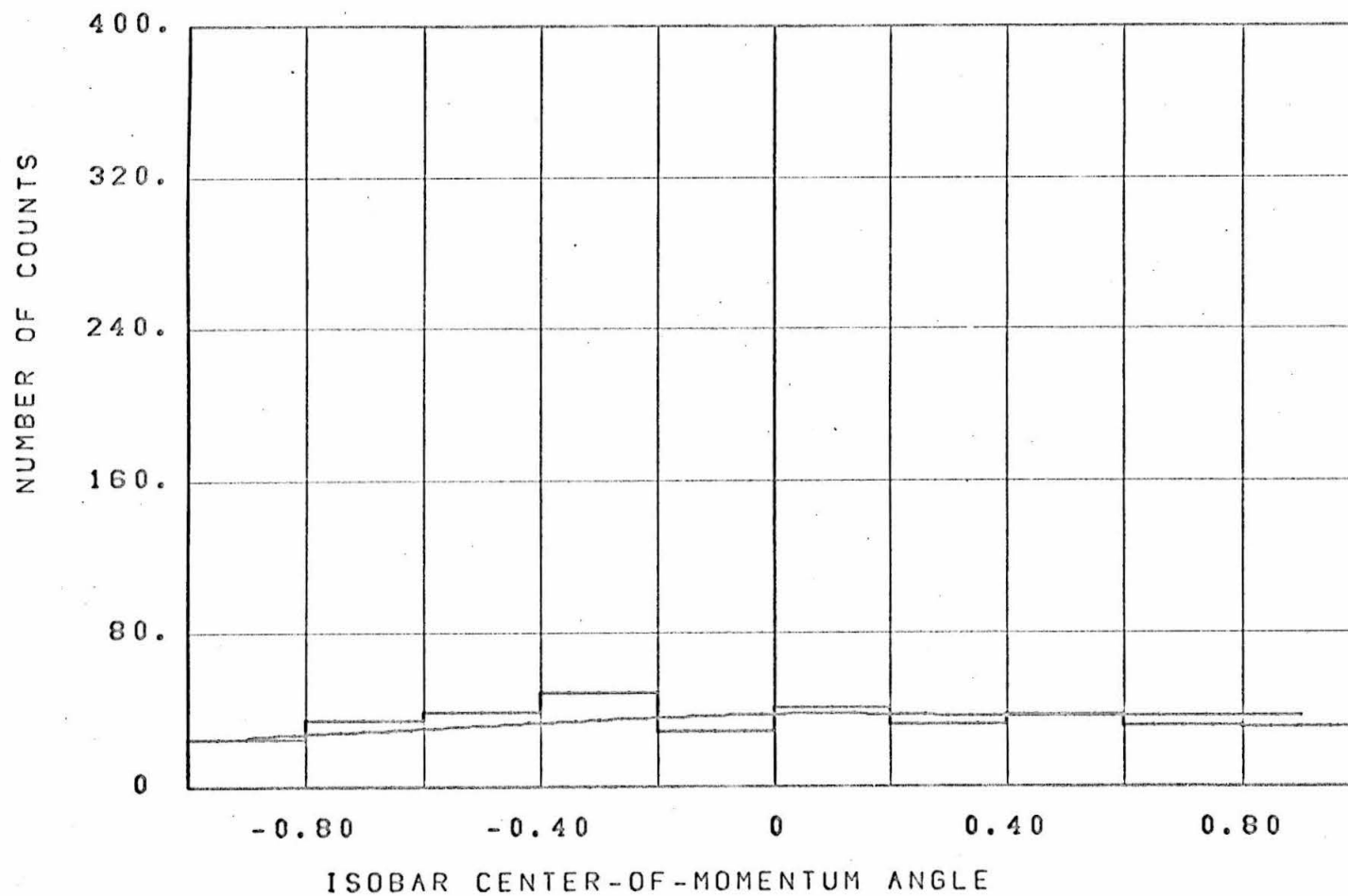


Figure 44

Isobar COM Polar Angle Distribution of Pion, $E_\gamma > 1060$

ISOBAR SYSTEM

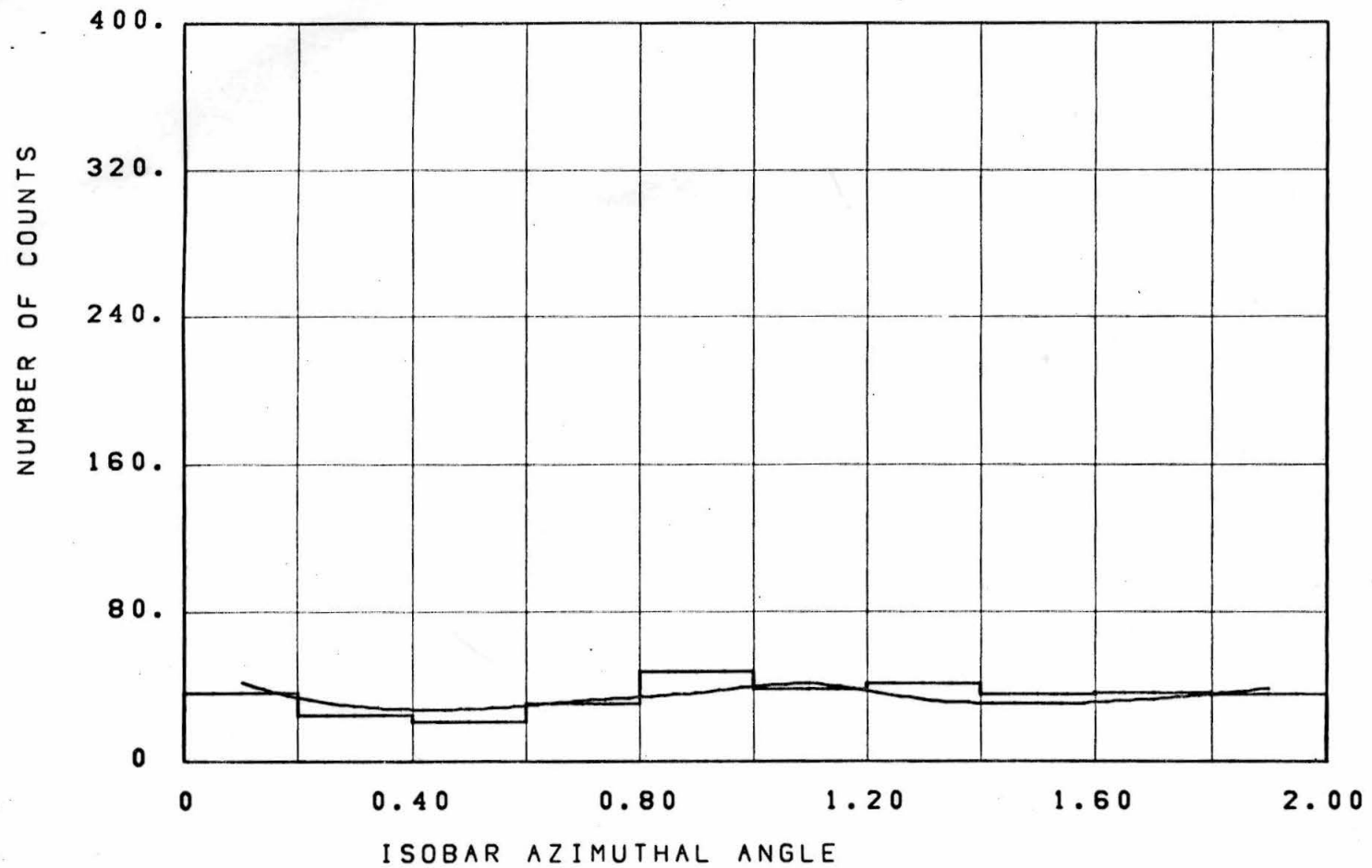


Figure 45

Isobar COM Azimuthal Angle Distribution of Pion, $E_{\gamma} > 1060$

production plane). The smooth curves again represent the generated data, model contributions taken in accord with the results of the dipion and isobar mass fit described above. Discrepancies between curves and histograms, though not serious, are an indication of the crudity of the assumptions in the event generation angular distributions and the drawback of not having these parameters free in performing the fitting. These discrepancies could have been used to modify the generated angular distributions and the fitting procedure could have been rerun, but this would have been an expensive, time-consuming operation and was not done.

The model fitting procedure used here can only be taken as an indication of what might be occurring in pion pair photoproduction. Aside from the difficulties noted above with the assumption of chamber and scanning parameters, this procedure does not take into account interference effects, except as they are included phenomenologically in generated event distributions. Also, as we noted above, it would be highly desirable to have resonance parameters free in the fitting. In order to perform the integrations necessary to such a procedure, one would need an algebraic representation of the chamber detection efficiency (including the energy-dependent scanning effects) as a function of the five model-dependent parameters required to determine an event (see Appendix IX). Such a function fit was attempted on the IBM 7094 in the hope that a few obvious dependences could be put in explicitly (such as the doubling of the average chamber efficiency at very low dipion masses), and that the remaining functional dependence

on the five variables might be simple. However, as the number of coefficients approached 100 (with monstrous increase in computer time required) the functional discrepancy from generated event efficiencies was still more than twice the 3 percent it should have been and there was no evidence that a reasonable number of terms would provide a good enough fit, so the project was abandoned. More insight into the correlative effects of the five parameters might have provided a workable function with few enough terms, but with the limited statistics inherent in the data and the large scanning uncertainties we did not feel that the added labor was justified.

Although our fitting procedure can say nothing definite about the existence of the σ meson, there are a few observations from the data that we would like to make if we were to assume that it existed.

Figure 46 shows the dipion mass plot for gamma energy limited to $600 < E_\gamma < 1060$, with a breakdown into three regions of invariant momentum transfer to the proton: $|t| < 0.14$, $0.14 < |t| < 0.32$, $|t| > 0.32$ ($|t|$ less than 0.1 is not seen because of the central beam tube). It can be seen that the " σ bump" in the region of 400 MeV occurs primarily in the middle region, and in particular seems to be absent in the low momentum transfer region. Thus one might conclude that σ meson photoproduction does not proceed primarily through a peripheral interaction.

In Figure 47 we see a plot of the total energy in the γ -p system for the three regions of Figure 46, with the additional restriction that the dipion mass be in the interval 360 to 480 MeV. In the two

Figure 46

Dipion Mass Distribution for Three Regions of Momentum Transfer

$$600 < E_{\gamma} < 1060$$

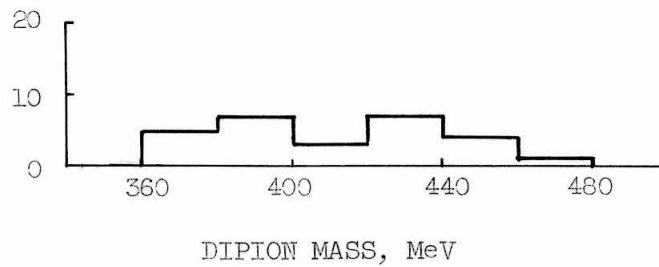
A. $|t| < 0.14$

B. $0.14 < |t| < 0.32$

C. $|t| > 0.32$

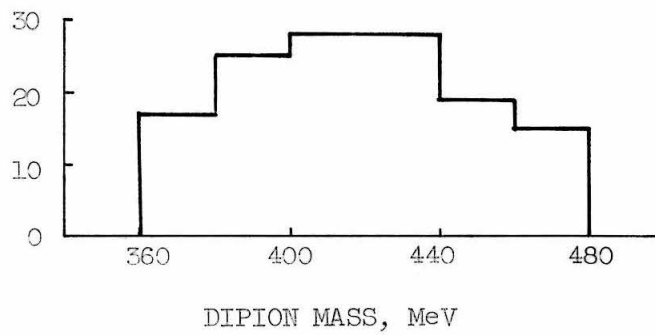
EVENTS

A.



EVENTS

B.



EVENTS

C.

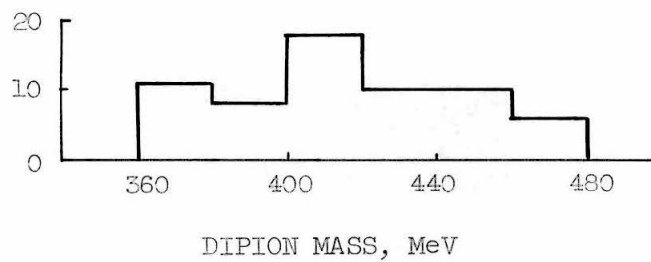


FIGURE 47

Total Energy Distribution for Three Regions of Momentum Transfer

$$600 < E_{\gamma} < 1060$$

$$360 < \text{Dipion Mass} < 480$$

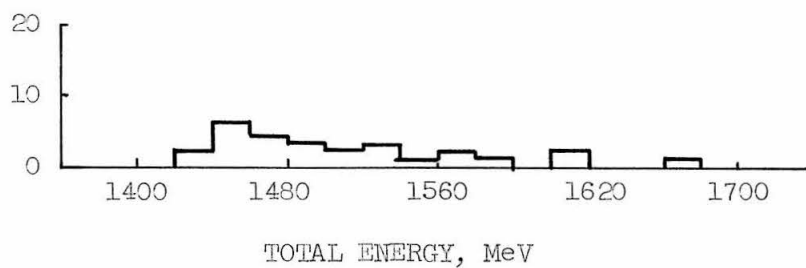
A. $|t| < 0.14$

B. $0.14 < |t| < 0.32$

C. $|t| > 0.32$

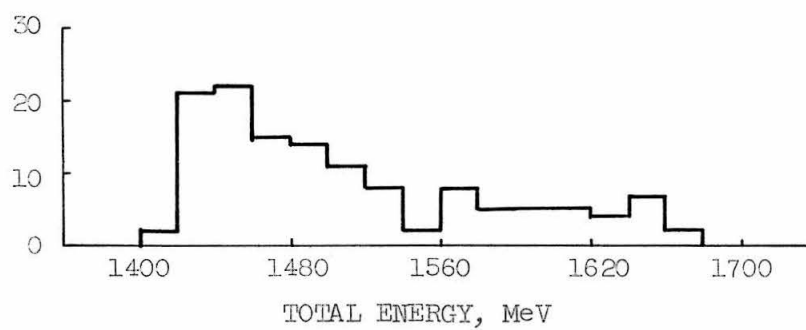
EVENTS

A.



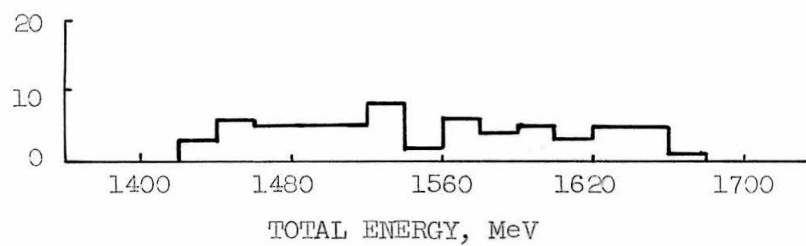
EVENTS

B.

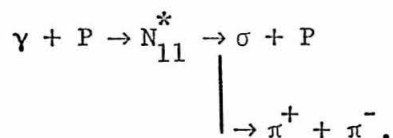


EVENTS

C.



regions where the σ peak was not prominent the distributions are flat, but in the central region (which showed the σ peak) a definite peak in total energy appears. The location of this peak corresponds to the mass of the N_{11}^* (1425 MeV). The lower energy part of this peak is sliced off by the 600 MeV gamma energy restriction; σ investigation was not extended to lower energies because 600 MeV is the approximate threshold for dipion mass 440 MeV as limited by the chamber's central beam tube. Thus we speculate that the σ meson might be photoproduced via an N_{11}^* intermediate state:



Of course higher energy σ production (900-1000 MeV E_γ) would have to proceed via a different mechanism.

Dipion angular distributions for $600 < E_\gamma < 1060$ and $360 < \text{dipion mass} < 480$ are shown in Figure 48. The angular variables and ranges are the same as described above. Within statistics the dipion decay parameters are consistent with isotropy. The dipion general COM polar angle appears to be peaked in the vicinity of $\cos \theta = 0.2$. Examination of generated events from the fitting procedure above showed the σ and phase space to lead to distributions peaked at $\cos \theta = 0$, and N_{33}^* to a distribution peaked at $\cos \theta = 0.3$. The curve shown against the histogram was calculated using a best guess for the three model contributions at 750 MeV based on our σ data and CEA and DESY N_{33}^* data: σ 21 percent, N_{33}^* 74 percent, phase space 5 percent. Although

FIGURE 48

Dipion Angular Distributions

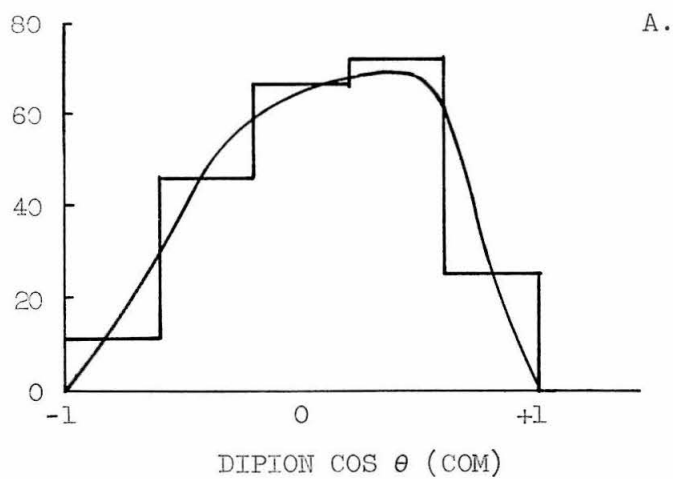
$$600 < E_{\gamma} < 1060$$

$$360 < \text{Dipion Mass} < 480$$

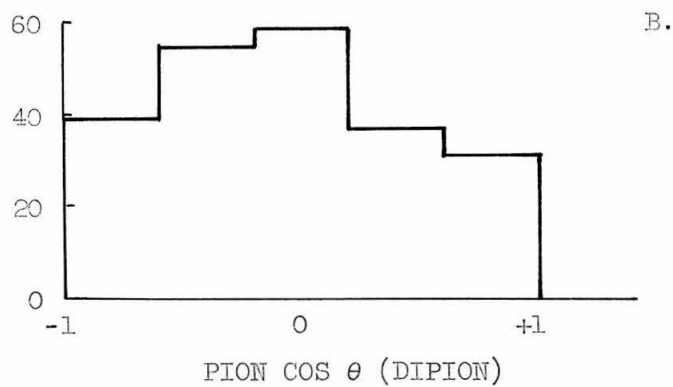
- A. Cosine of Polar Angle of Dipion in General COM System
- B. Cosine of Polar Angle of Pion in Dipion COM System
- C. Azimuthal Angle of Pion in Dipion COM System

EVENTS

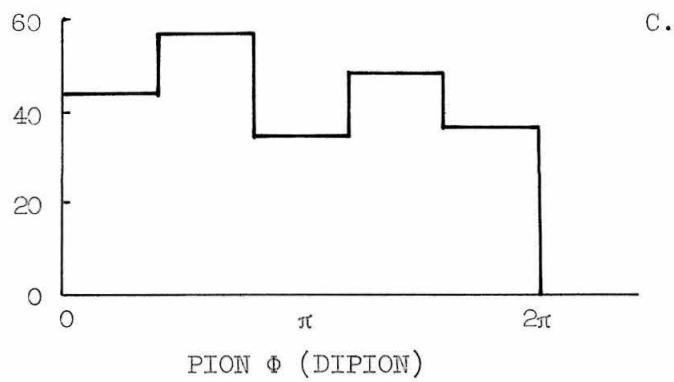
- 91 -



EVENTS



EVENTS



this comparison is not strictly valid since the generated events were not restricted to fall in the 360-480 MeV dipion interval, it does perhaps indicate that the peak observed in $\cos \theta$ does not need to imply anything other than isotropy in σ production. Thus our angular distributions are consistent with (but in no way prove) σ production from an N_{11}^* intermediate state, with σ spin being zero.

With the crudeness of our fitting techniques, little could be said about a σ production cross section except that it appears to decrease as one goes above about 1050 MeV gamma energy. Interestingly enough, this is just the ρ meson photoproduction threshold. If one believes that σ meson production accounts for about 20 percent of total pion pair production below 1000 MeV, it may not be unreasonable that the sum of the σ and ρ production cross sections remains roughly constant as one moves up in gamma energy across the ρ threshold. Much more experimental and theoretical work will have to be done before this can be removed from the realm of pure conjecture.

The σ meson has been an elusive creature since Samios, et al. first reported it in 1962¹⁷⁾. Their experiment was π^- plus proton going to four charged mesons incident on a hydrogen bubble chamber. It was also seen in a similar CERN bubble chamber experiment done with a 4 GeV π^- beam³⁹⁾. In both experiments its statistical significance was not good. The same experiment was done with a 10 GeV π^- beam by Biswas et al.⁴⁰⁾; there may be the vaguest indication of something at 400 MeV dipion mass in their data, but it is certainly reduced from that of the other experiments if it is there at all, so in π -p inter-

actions it may also disappear at higher energies. Thus far the σ has only been seen in the $\pi^+\pi^-$ system, implying isotopic spin zero. Experiments done with $\pi^- + P \rightarrow n + \pi^- + \pi^+$ have failed to show any conclusive evidence of the σ in the $\pi^+\pi^-$ system⁴¹⁻⁴³; whether this may be the result of a final state interaction is not known, at least to the author. We mentioned above that σ photoproduction has previously been reported by a Frascati group; the CEA and DESY experiments made no mention of it. Certainly if our experiment is any indication, its appearance is not large, even away from the low momentum transfer interactions and in the limited gamma energy region between its threshold and that of the ρ . Thus it might easily have been missed in the other experiments, and a much better experiment than ours (in statistics and systematic errors) will have to be performed before anything conclusive can be said regarding the σ .

In conclusion it may be said that this experiment has not answered any basic questions in physics; rather, it may have raised one more. Use of a heavy liquid bubble chamber in a central beam tube configuration with a gamma ray beam has been shown to be possible, though serious analysis difficulties resulted, especially from the large energy content of the beam run in this experiment. Our results on pion pair photoproduction appear to be consistent with those previously reported. We see a statistically insignificant indication of a "bump" in the dipion mass spectrum around 400 MeV. The speculations given above on the existence of the σ meson and modes of its production were not intended to be an experimental result, but rather a stimulus to

further investigation, experimental and theoretical, and a possible indication of what regions of investigation might prove fruitful.

APPENDIX I

BEAM LINE CONFIGURATION

There are several properties of an incoming particle beam that the experimenter would like to optimize. The beam should be as well defined as possible, implying both that it should be physically as small as possible, consistent with getting enough beam into the experiment, and that the edge of the beam should be well defined, with a minimum of radiation outside its limits. The beam should contain a minimal contamination of particles other than the one desired, and as few particles as possible of the desired variety with energies outside the usable region, both effects leading to undesired background events. The operator needs a monitoring scheme to make sure that his beam properties are not changing during the course of the run. Finally, he needs a stable, accurate detection system for measuring the amount of usable beam put through the target.

The gamma ray intensity from the synchrotron was more than adequate for the 2.5×10^5 equivalent quanta desired per pulse, allowing attenuation of the beam from beam hardening, and collimation down to a very small beam size. Figure 3 shows the gamma-ray beam defining and measurement system used in this experiment. Because of previous troubles with electromagnetic background radiation, beam definition and sweeping were done more thoroughly than was absolutely necessary.

A. Radiator Placement and Beam Orbit

Prerequisite to setup of a beam-defining system is the choice

of synchrotron internal radiator position, which establishes the position and direction of the gamma ray flux. Intimately tied to this choice is the choice of RF accelerating frequency, which determines the equilibrium electron orbit inside the synchrotron. Objectives of these choices were threefold: that the beam be going through the bubble chamber at a convenient place, that the beam cross-section be as circular as possible, and that early beam dump be a minimum.

If the radiator is placed too close to the equilibrium orbit the electrons start hitting the radiator from the time it is pulsed into position and objectionable early beam dump results. Too large a radius (low frequency) for the equilibrium orbit will encounter regions of bad magnetic field at high energy as portions of the magnet start to saturate, and lead to bad early beam dump just before dump time. Too small a radius value for the radiator (or beam orbit, for that matter) encounters a resonance in the magnetic field parameters, causing vertical blow-up of the beam.

The parameters finally chosen were $\rho = 670.0$, $\theta = 1871.8$ on the mechanical counters at the north beam radiator (the servo control was not trustworthy). This corresponds to a radius of about 146.4 inches. The RF accelerating frequency was run at 40.17 Mc, corresponding to a radius of 148.6 inches.

B. Beam Hardening

"Hardening" of gamma-ray beams by passing them through lithium hydride in order to reduce low energy background radiation has been described elsewhere^{30,28,44}). In this experiment, two sections of

lithium hydride beam hardener surrounded by pulsed magnetic fields of the type described by Alyea³⁰⁾ were used.

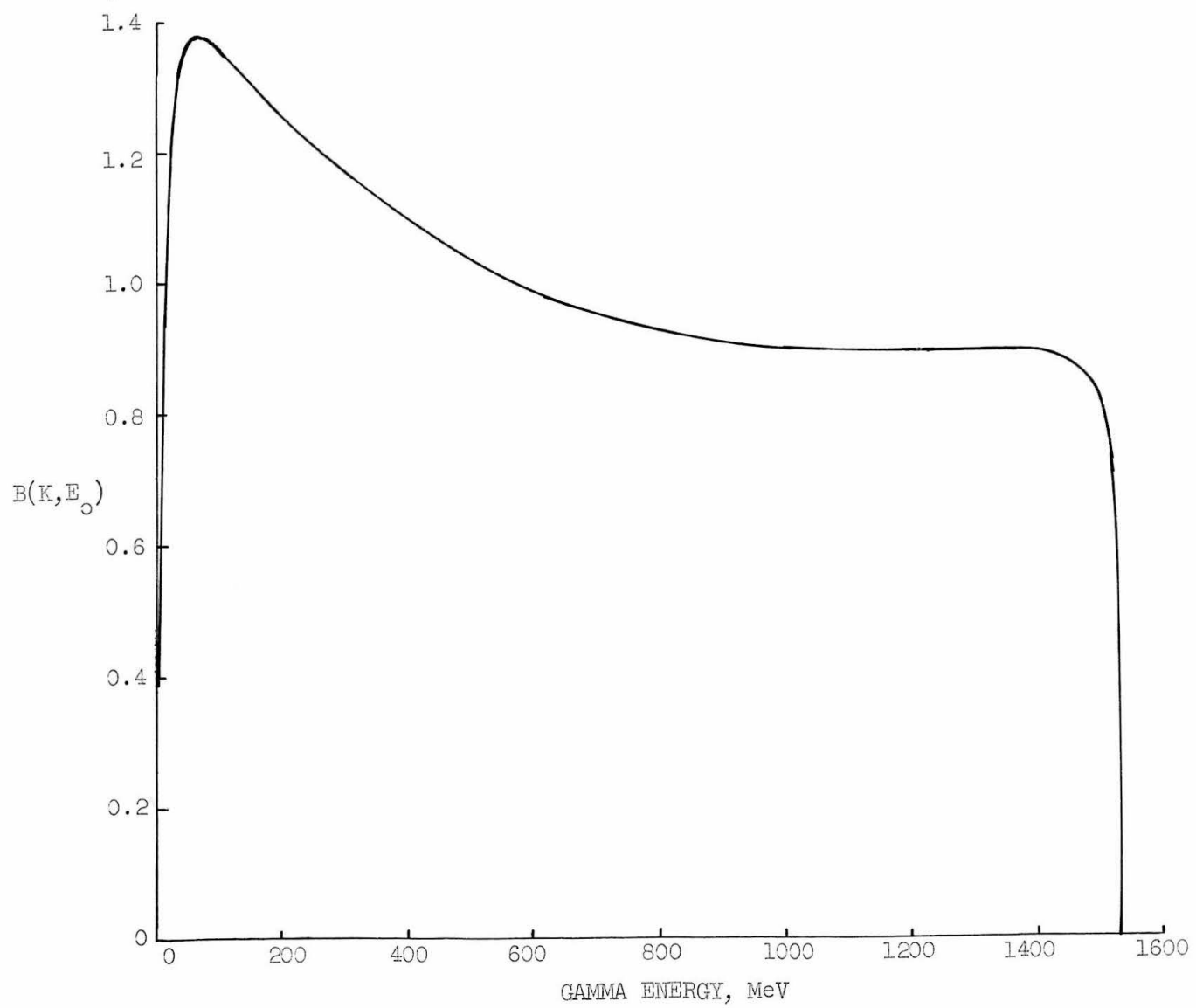
Since the beam is used and measured downstream from the beam hardener, the only important effect of the beam hardener is to alter the bremsstrahlung spectrum. Integral beam attenuation by the hardener was measured to be 0.488 and 0.520 at end point energies of 1350 and 1500 MeV, respectively. Frank Wolvertson's BPAK computer program³⁷⁾ was utilized to calculate the effect of the hardener on the bremsstrahlung spectrum, taking into account electronic and nuclear pair production and Compton scattering in the LiH. The amount of LiH in the beam was found iteratively by requiring that the integral spectrum attenuation match the measured value. This yielded 74.0 gm/cm^2 , in good agreement with Alyea's value of 37.7 gm/cm^2 per section.

The resultant spectrum is shown in Figure A I-1. The results are in good agreement with the calculation of Hart and White⁴⁴⁾. They observe experimentally a photon enhancement below about 300 MeV which they attributed to showering in the LiH. They decided that they could not limit this enhancement with collimation, no doubt due to the small development angles in the shower. However, in this experiment that enhancement should not be present due to the combination of magnetic field in the LiH and subsequent collimation; an approximate calculation^{*)} using this configuration indicates less than

*) This calculation assumed electron bremsstrahlung in the LiH to be uniform into a cone of half-angle m/E (m is electron mass, E electron energy), took electron energies to be half their parent
(continued on following page)

FIGURE A I-1

Bremsstrahlung Energy Spectrum in Target



than 0.005 percent of the incident beam energy should be passed on through the secondary collimator as a result of showering in the LiH. Thus the spectrum resulting from surrounding the hardener by magnetic field is "harder" (less low energy component) than that produced by collimation alone, as well as being more amenable to calculation.

C. Collimation, Scraping, Sweeping and Shielding

Gamma ray beam definition was done in several stages (see Figure 3). A primary collimator consisting of a thirteen-inch thick cylinder of lead with a cylindrical hole through the center 0.024 inches in diameter was placed about eight feet from the tantalum bremsstrahlung target (0.2 radiation length thick) inside the synchrotron. Following the beam hardener described above was situated a secondary collimator, an eight-inch-thick slab of lead with an 0.035-inch diameter hole through the center. This collimator served to render the beam shape more circular, and to remove radiation produced in the beam hardener. Finally, a one-foot-thick block of lead located just before the bubble chamber acted as a scraper. The hole through the scraper cleared the beam by about 1/16 inch, and was made in three conical sections tapered to remove gamma rays produced at the second collimator by primary beam interactions.

(continuation of footnote from previous page)

gamma ray energies, and integrated the acceptance into the solid angle subtended by the collimator over the gamma energy bremsstrahlung spectrum and position along the beam line inside the hardener. Electron radiating lengths were limited to 1.3 mm so that the electron would still be within an angle m/E of its original direction in the 13 kilogauss field.

Massive shielding proved to be an important part of this experiment. A concrete wall three feet thick and twelve feet high was built around three sides of the bubble chamber, the concrete wall to the power room forming the fourth side of the cave. An eight-inch timber partial roof with a thin layer of lead on top was suspended above the chamber. Re-radiation from the primary collimator, a troublesome source of background both for the bubble chamber and the counter telescope beam monitor, was greatly reduced by lead and copper shielding surrounding as much of the primary collimator as possible. The bubble chamber itself was surrounded by lead and paraffin wherever practical. All this shielding was done in an effort to reduce the omni-directional flux of neutrons and/or gammas that fills the room at dump time. Despite the large improvement effected, the vast majority of the background radiation remaining in the bubble chamber appeared to come from this source rather than beam-line-associated sources, and the resulting pictures would have been easier to scan and analyze had it been practical to spend more time completing the shielding to reduce this background further.

After passing through the secondary collimator, the beam entered a vacuum beam tube through a thin aluminum window. The beam then continued in vacuum until it reached the mylar entrance window to the hydrogen gas target. It was never clear that the vacuum beam tube did much good, but it was a safety precaution against breakage of the mylar window.

Sweeping of unwanted charged particles out of the gamma ray

beam was done in three steps. The beam hardener was surrounded by a 13 kilogauss pulsed magnetic field. Behind the secondary collimator, the vacuum beam tube passed through 14 inches of 8 kilogauss D.C. magnetic field (the so-called "cosmic ray magnet"). Then in its three-foot passage through the concrete wall the beam was surrounded by a 4 kilogauss D.C. magnet designed and built by A.D. McInturff. Sweeping probably would have been adequate with any two of these magnetic fields, but all three were left in.

The scraper hole size was chosen so that any gamma that was produced at the secondary collimator or farther from the bubble chamber and that cleared the scraper would not encounter any metal in the chamber in which it could shower until it had gotten to the far side of the chamber, at which point a shower would pose no problems. To see whether the scraper was actually necessary after the double collimation scheme, the chamber was pulsed once with the scraper removed. The resulting picture left no doubt. So many bubbles had been formed that light couldn't even get through the chamber in the vicinity of the beam tube.

X-ray pictures taken downstream with only the primary collimator in place gave a good picture of how the electrons in the synchrotron were striking the tantalum target, for the tiny hole in the collimator acted as a pinhole camera. Since this gamma source was not circular, the secondary collimator was required to make the beam cross-section much more circular, compatible with the scraper and bubble chamber geometry downstream. The chamber was never pulsed with

either collimator removed, but it is believed that radiation background would have been much worse had not the portion of the synchrotron beam being collimated out been stopped as soon as possible.

D. Target

The beam target in this experiment was a high pressure (50 atmospheres) hydrogen gas target, located approximately in the center of the bubble chamber. Hydrogen used was the usual grade of target hydrogen at the laboratory, with impurities not exceeding 0.5 percent.

The target container, known as the central beam tube, is a conical device made of steel with the narrow end toward the synchrotron. This geometry was chosen in the hope that shower development would remain at small angles to the original beam direction in the hydrogen, not getting out into the steel walls or freon liquid where the angular development would widen and event tracks might be obscured. Based on shower development calculations, a cone half-angle of about 4.5 degrees was chosen. The tube is 0.030 inches thick at the small end and 0.080 inches thick at the large end in an attempt to keep unseen multiple scattering and energy loss as low as possible. As it turned out the design was conservative. Very little shower development was seen at the edge of the beam tube, and the opening angle of the beam tube could probably have been made somewhat smaller, with a considerable gain in chamber detection efficiency.

The beam entered the beam tube through a mylar window, 0.008 inches thick and 0.25 inch in diameter, preformed to a spherical shape to better stand the pressure differential. The beam left the target

through a thin stainless steel window outside the bubble chamber. Since the radiation damage to the mylar was unknown, a safety device was built into the vacuum system upstream of the mylar window by Coyne and McInturff, which fortunately was never needed.

E. Beam Monitoring Equipment

A short distance behind the bubble chamber was placed a cylindrical polyethylene target one inch in diameter and four inches thick. It was viewed at close range by a scintillator (for studying predump and setting dump timing) and at a distance by a counter telescope (for beam measurement). The counter telescope consisted of two half-inch-thick plastic scintillators viewed by 6810 photomultipliers. Each scintillator was preceded by a half-inch plate of aluminum to reduce singles counting rates. A lead house surrounding the telescope was itself surrounded by paraffin. The telescope was about twenty feet from the polyethylene target at an angle of about twenty degrees from the beam direction.

The beam reached the Cornell type ion chamber housed in the lead beam stopper about thirty feet behind the bubble chamber after passing through a device known as the lead chopper. The lead chopper was a cylinder of lead two inches in diameter and four inches long mounted as a pendulum that could block the beam just before the ion chamber or be swung out of the way on alternate synchrotron pulses. Lead walls with holes 0.5 inches in diameter before and after the lead chopper prevented radiation coming in somewhat near the beam line or scattered out by the lead chopper from reaching the ion chamber.

F. Component Alignment

After the radiator position inside the synchrotron had been chosen as described above, the beam component alignment was done. The small beam size necessitated considerable lineup accuracy. Indications are that the bubble chamber lineup was good to about 0.03 inch, the scraper to about 0.005 inch, and the collimator lineups each to about 0.002 inch. The accurate collimator lineup was possible thanks to stable bases and reproducible screw-driven movements with the angular and position motions decoupled.

Collimator and scraper alignment was accomplished by maximizing the beam passed through the device for a given circulating beam size inside the synchrotron. Mullins' new stable 40 MC probe circuit was used to monitor the synchrotron circulating beam. It was sampled just before beam dump and a charge proportional to the circulating beam intensity integrated on a standard laboratory integrator (model 4) as described in Alyea's thesis³⁰). Beam passed through to an ion chamber*) was simultaneously integrated on another integrator channel. Then the ratio of the two integrations was plotted as a function of the parameter being varied and the center of the resulting curve chosen as the optimum value. This ratio proved reasonably stable as a function of time, reflecting the improvements that had been made in the 40 MC probe and the RF accelerating system by Mullins and Maloy.

The primary collimator was lined up first with the other components removed. Its position was chosen to be centered on the peak

*) The traditional "Cornell type air chamber".

intensity of the bremsstrahlung intensity from the radiator, and to give a reasonable beam location downstream. Then its angular orientation was optimized. Then the secondary collimator was installed and its position and angular orientation optimized.

The bubble chamber was lined up using X-ray pictures. Plugs were made to define the locations of the ends of the beam tube. Double exposures were made using the synchrotron as a source of illumination and alternating between the plugs and the collimated beam (the collimator inserts could be easily removed and accurately replaced). Finally, the scraper position and direction were determined, again using the 40 MC probe ratio method.

Lineup of the other beam line components (beam hardeners, sweeping magnets, polyethylene target, lead chopper, and ion chamber) was much less critical; they were optically centered on the beam position, as determined by X-ray pictures.

APPENDIX II

BEAM MONITORING

A. Beam Monitoring Logic

Because of the possibility of saturation effects^{*)} and early beam dump, the standard laboratory beam measuring device (Cornell-type ion chamber) was not used directly in this experiment. Instead a counter telescope (described in Appendix I) was used to monitor the beam intensity. Since bubble chamber operation was limited to one expansion for every three beam pulses, the two pulses following a bubble chamber pulse were used for continuous telescope calibration against an ion chamber throughout the experiment.

On a chamber pulse the lead chopper (see Appendix I) prevented the beam from reaching the ion chamber. The same pulse that initiated the fast beam dump in the synchrotron was used to gate on the scaler used to monitor the counter telescope during fast dump, thus preventing early beam dump (to which the bubble chamber is not sensitive) from being counted.

Immediately after the bubble chamber pulse the lead chopper was moved out of the beam. The next two synchrotron pulses were taken with slow dump (10 milliseconds duration) so that saturation effect would be negligible. The counter telescope was monitored

^{*)} With large gamma-ray beams, the fast dump used for the bubble chamber can result in appreciable saturation effects due to ion recombination before collection³⁰⁾. In this beam configuration there was no appreciable saturation, probably due to the small size of beam used.

on a second scaler for these two pulses. The slow dump scaler was gated on 50 milliseconds before dump time, since early beam dump would be picked up by the ion chamber (both scalers were gated off 30 milliseconds after start of their beam dump).

After the two calibration pulses, the lead chopper was moved back in to block the beam, and the bubble chamber could again be pulsed. Due to beam size variation from pulse to pulse it had been found desirable to set a window on the beam size that would be acceptable so that pictures would not be empty or flooded with beam. This was accomplished by monitoring the signal from the 40 MC probe about 50 milliseconds before dump time. If it fell within the preset window, chamber expansion and fast dump would be initiated. If not, the chamber waited for the next pulse. In this case the beam was blocked from the ion chamber by the lead chopper and both sets of scalers were left gated off, so that beam measurement and calibration were not lost.

The lead chopper was the least reliable part of the beam monitoring system. Microswitches monitored the lead chopper position and controlled the scaler gating action. If the lead chopper was in the wrong position or in transit at any time during either a slow or fast dump beam gate, an alarm was sounded and chamber pulsing automatically stopped. This happened a few times in the course of the run.

On pulses accepted by the bubble chamber the 40 MC probe was also integrated as described above (see Component Alignment , Appendix I). This was intended as a secondary beam measurement should the counter telescope system fail for some reason, and as a

check against loss of the delicate system lineup (which would change the ratio of 40 MC integration to accepted beam integration). It was monitored throughout the run, though neither difficulty ever arose. Table A II-1 shows the variation of the ratio of 40 MC integration to fast dump beam integration as indicated by the counter telescope system. The largest deviation from average is still within the errors expected from variations in the 40 MC probe signal and the beam characteristics, as well as the beam measurement error itself.

B. Early Beam Dump

Due to limitations in the RF beam accelerating system and the finite size of the accelerated electron beam, some fraction of the beam was observed to come out before beam dump time. This early beam dump, called predump, was observed to begin about the time the synchrotron internal radiator was pulsed into position (about 70 milliseconds before dump time), and it continued more or less at a uniform rate up to dump time.

Predump was checked continually throughout the run, and it was found to run $7 \text{ percent} \pm 3 \text{ percent}$ of the total beam intensity. Worse predump than this was the result of synchrotron mis-timing; it was always possible to keep the predump within these approximate limits during picture taking.

To monitor the predump, the output of the scintillator located near the polyethylene was integrated with a long time constant (10 seconds) and displayed on an oscilloscope. The voltage on the photomultiplier tube was run sufficiently low that no saturation occurred. The scintillator was placed as close as practical to the

Table A II-1

Comparison of Counter Telescope and 40 MC Probe

Roll	Region	40 MC/Chamber Beam *)
45	1	0.808
	2	0.817
46	1	0.826
	2	0.809
47	1	0.800
	2	0.753
48	1	0.752
	2	0.760
49	1	0.768
	2	0.786

*) Arbitrary units. Chamber beam is corrected beam through hydrogen target, based on counter telescope readings.

polyethylene target consistent with clearing the beam, since it was found that the scintillator itself appeared to saturate when placed directly in the beam.

Predump correction to beam monitoring on fast dump pulses was not done. The bubble chamber is sensitive for only about one millisecond before dump time. The fast dump beam scaler was turned on .25 milliseconds before beam dump, and the beam accepted by the chamber during the remaining .75 milliseconds would have represented a correction of 0.1 percent at most. Unfortunately, a predump correction was required on the beam calibration pulses. Due to occasional erratic behavior the internal radiator timing had been moved earlier, and the slow dump beam gate was not moved to cover it. Thus the first 25 milliseconds of predump was integrated by the ion chamber but not by the slow dump scaler. Since the predump was checked much more often than it was recorded, and since it could vary reasonably fast, a constant correction of 2.5 ± 1.0 percent was used for the entire run rather than attempting to follow local variations.

C. Beam Absorption

Between the target and the ion chamber were several media whose beam absorption must be taken into account. Table A II-2 gives a summary of the absorption measurements taken at the conclusion of the run, and comparison with calculated values. The most important process contributing to this energy loss is electron pair production, followed by multiple scattering sufficient to cause the electrons to

Table A II-2

Percent Downstream Gamma Beam Absorption

Material	Measurement	Calculation
Target hydrogen	0.6 ± 0.6	0.34 ± 0.2
Steel target exit cap	3.1 ± 0.9	3.3 ± 1.0
Polyethylene target	15.4 ± 0.8	12.9 ± 1.5
Air Path	-----	1.4 ± 0.5

miss the half-inch aperture to the ion chamber at the lead chopper. Range energy loss by the electrons produced was a negligible effect. Compton scattering and other processes contributed significantly in elements with low atomic number and for low energy gamma rays, and were included in the calculations for hydrogen and polyethylene. They were not included in the air calculation since the effect itself was so small. For beam correction the measured value was used for steel, an average value for polyethylene, and the calculated values for air and hydrogen since measurement was less accurate or impossible.

Beam absorption in the lead pendulum of the lead chopper was not complete. Beam transmission was found to be 0.36 percent, so this fraction of the beam taken by the bubble chamber (with the beam blocked by the lead chopper) was subtracted from the total ion chamber integration to determine the beam passed on the calibration pulses. The effect of possible beam pulses passed by was not included. These beam pulses missed were of low intensity or they would have been accepted for a chamber picture, and they did not occur very often (perhaps once every few chamber pulses). If the beam tuning became poor enough that many pulses were lost, the experiment was shut off until it improved.

D. Calibration of Ion Chamber

Since the duration of the experiment was only two and a half weeks, the ion chamber was calibrated once against the laboratory standard quantameter. This was done in the south beam at the conclusion of the experiment, using slow beam dump and the thin-

wall chamber as a reference monitor. The calibration constant C is defined as

$$C = \frac{\frac{\text{Thin chamber}}{\text{Ion chamber}}}{\frac{\text{Thin chamber}}{\text{Quantameter}}} \frac{(P/T) \text{ Ion Chamber}}{(P/T) \text{ Quantameter}}$$

with P the gas pressure in the ion chamber measured in mm, Hg and T its absolute temperature. The average of several measurements yielded $C = 1.267 \pm 0.003$, with the error reflecting the measurement fluctuations.

The ion chamber integrator was also calibrated at the end of the run. As the integrator puts out a pulse after accumulating a fixed charge, beam measurement during the experiment was taken in terms of these Beam Integrator Pulses (called Bips). The calibration value for the integrator (used on scale I) was $4.70 \pm 0.01 \times 10^8$ Bips/Coulomb.

The absolute ion chamber calibration⁴⁵⁾ is

$$U = 13.10 \times 10^{18} \frac{C}{(P/T) \text{ Ion Chamber}} \text{ MeV/Coulomb,}$$

with the relative error in the constant being 3 percent⁴⁶⁾. Thus for this experiment the total energy in the beam is given by

$$W = 3.53 \pm 0.11 \times 10^{10} (T/P) \text{ MeV/Bip.}$$

E. Counter Telescope Electronics

The counter telescope electronics consisted mostly of circuitry designed by Professor Alvin Tollestrup. Used were two 1B limiters, one TC5 coincidence circuit, one TM4 multiplexor, two TG2 gate circuits, and two sets of scalers, each with one decade of 10 MC scalers and three decades of 1 MC scalers. Additional circuits designed by Dr. Mullins were a synchrotron beam gate translator, a "predump cheater" which determined the gate-on time for fast dump counting, and a lead chopper error display circuit.

Timing curves were run just before and just after data taking, and agreed to about 1 nsec. At the delay corresponding to the peak on the timing curve both scaler channels showed the same counting efficiency; variation in this relative efficiency at other timing settings leads to the assignment of 0.0 ± 0.5 percent for the efficiency difference between channels.

Single counting rates in the two scintillators were measured to be approximately 0.4×10^6 and 1.1×10^6 counts per second, respectively, during fast dump, and of course much less during slow dump or predump. An expected accidental coincidence rate may be calculated from

$$C = \frac{AB}{N} \frac{\tau}{T},$$

where

A = Counts per bip in counter A

B = Counts per bip in counter B

C = Accidental coincidence per bip

τ = Resolving time of coincidence circuit

T = Dump duration

N = Number of dumps per bip.

Using the observed singles rates, the measured width of the timing curve (12 nsec, full width at half maximum), and a fast dump time of 100 μ sec, one would expect an accidental coincidence rate of 8.4 ± 5 counts/bip. A measurement was taken by setting the timing 25 nsec from the correct value (corresponding to the time difference between electron bunches in the synchrotron) which yielded 2.3 ± 0.6 counts/bip. The agreement is not terribly good; this may in part be due to unequal population of the four bunches of electrons being accelerated.

An attempt to measure the saturation of the ion chamber during fast dump by comparing the counter telescope and the ion chamber gave 0.9 ± 2.0 percent more counts per bip on slow dump than fast. Using the measured accidental coincidence rate (1.6 percent) would give an ion chamber "saturation" of -2.5 ± 2.1 percent. Since there seemed to be no plausible explanation for the ion chamber being more efficient on fast dump than slow, the effect could either be attributed to a saturation effect in the counter telescope system or to statistics in the measurement. (Measurements by MacInturff⁴⁸) tend to confirm the belief that for this small beam size and intensity, ion chamber saturation effects are negligible). Professor Walker suggested that the saturation effect might be due to dead time of the scalers used; however, the measured 2.5 percent "saturation"

with the average count rate of 4.7 counts per beam dump would lead to a dead time of 0.5 μ sec per count, whereas the actual scaler dead time is about 0.1 μ sec per count. Since the scaler dead time was better known than the "saturation" effect, the remaining 2.0 ± 2.1 percent was attributed to statistical error. Since a window had been set so that pulses accepted by the bubble chamber were of approximately equal beam intensity, and since the saturation measurement was taken at the same average beam intensity as the bubble chamber pictures, the scaler readings were corrected by the measured accidental coincidence rate and the known scaler dead time (giving a net decrease of 1.1 percent in the fast dump scaler readings), and the uncertainty assigned to this value was taken to be the 2.0 percent of the "saturation" measurement.

F. Beam Correction Summary

To summarize the corrections described in this Appendix, define W = total beam through hydrogen target in units of 10^{10} MeV, I = ion chamber integrator reading in Bips (scale 1), F = number of fast dump scaler counts, S = number of slow dump scaler counts, T = absolute ion chamber temperature in degrees Kelvin, and P = ion chamber pressure in mm Hg. Then

$$W = F_1 F_2 F_3 F_4 F_5 F_6 F_7 F_8 F_9 I.$$

The terms are:

- 1) Ion chamber and integrator calibration

$$F_1 = (3.53 \pm 0.11) \frac{T}{P}$$

- 2) Slow dump scaler predump correction

$$F_2 = 0.975 \pm 0.01$$

- 3) Scaler channel relative counting efficiency

$$F_3 = 1.000 \pm 0.005.$$

- 4) Counter telescope saturation and accidentals

$$F_4 = 0.989 \pm 0.020.$$

- 5) Fast/Slow count ratio and Lead Chopper transmission

$$F_5 = \frac{R}{1.0 \pm 0.0036R}, \text{ with } R = \frac{F}{S}$$

$$\text{Relative error is } \frac{1}{F} + \frac{1}{S}.$$

- 6) Air path absorption

$$F_6 = 1.014 \pm 0.005.$$

- 7) Polyethylene target absorption

$$F_7 = 1.144 \pm 0.008.$$

- 8) Steel target exit cap absorption

$$F_8 = 1.031 \pm 0.009.$$

- 9) Hydrogen target absorption

$$F_9 = 1.003 \pm 0.002.$$

Combining these factors,

$$W = 4.225 \frac{T}{P} \frac{R}{1.0 \pm 0.0036R},$$

$$\text{with a relative error } E = \sqrt{.001586 + \frac{1}{F} + \frac{1}{S}}.$$

Table A II-3 shows the beam through the hydrogen target for the five rolls of film analyzed for this thesis.

TABLE A II-3

Beam Passing Through Hydrogen Target

Roll Number	Number of Pictures	Beam in 10^{10} MeV	Equivalent Quanta ^{*)}
45	2627	117.63 ± 4.92	76.78 ± 3.21
46	2630	125.09 ± 5.22	81.65 ± 3.41
47	2620	127.01 ± 5.37	82.91 ± 3.51
48	2632	127.34 ± 5.30	83.12 ± 3.46
49	2634	127.87 ± 5.32	83.47 ± 3.47

*) The number of equivalent quanta in the beam is defined as the total energy in the beam divided by the bremsstrahlung end point energy. The numbers quoted here are in units of 10^7 .

APPENDIX III

SCANNING AND ANALYSIS EQUIPMENT

A. The First Scanner

One film scanning machine used in this experiment has already been described in some detail³⁰⁾. It is an overhead projection scanner capable of handling 1000 foot rolls of 65 mm perforated film, with a slow single-frame advance or a high-speed drive variable up to about 300 feet of film per minute, both drives being bi-directional. A dual projection system permits either of the two stereo views (spaced a fixed distance apart on the same roll of film) to be projected onto the table in front of the operator. A presettable frame counter follows the film frame numbers backwards or forward. Control and transport sections have been rebuilt for more dependable operation, but functionally it is the same machine Alyea used.

B. The Analyzing Scanner

Patterned mostly after the scanner described above, a second machine was built to serve both as a scanning machine and an analyzing machine. Film transport and control are almost identical to the other machine. The frame is much heavier and the glass mirrors thicker (one inch), providing the stability required for the extra precision in analysis. Schneider Componon lenses, f:5.6, 210 mm focal length were used to provide sharper focus from better flatness of field than the Xenar. Vacuum backing was used in addition to the pressure fronts to hold the film steady during measurement. Change-

over between scanning and analysis is easily accomplished by removing the scanning table from the machine and installing the analysis table.

Like the scanning table, the frame of the analysis table basically consists of a table top and four legs equipped with rollers to facilitate moving and minimize vibration damage to the delicate encoders. When in position the table rests on four locked bolts bearing upon metal plates glued to the floor rather than resting upon the flexible rollers. It is joined to the main frame by two vertical tapered bolts, providing a lateral placement reproducible to better than $1/32$ inch.

Atop the analyzing table rests the analyzer itself, an aluminum table with a long precision roller at each edge and two .005 inch mylar belts mounted orthogonally over the rollers. Each belt loop is completed by a network of 18 small springs to provide constant tension. The belts are hand-driven, one roller for each belt, being coupled through a friction clutch to a hand wheel accessible to the operator. The top belt is clear mylar with a scribed, ink-filled line on the lower surface. The bottom belt is frosted mylar painted white with the white side up. A black band painted on the back shows through a groove scribed through the white surface as a black line. Both lines are about 0.003 inch wide, and are made to be as perpendicular to the direction of belt motion and to each other as possible, although any lack of perpendicularity is automatically taken into account by the analysis set-up procedure used (see Appendix IV). This arrangement of white viewing surface and black lines being essentially coplanar was

chosen to reduce parallax errors, which had been a considerable problem when the table surface under the lower mylar belt had been used as a viewing surface.

To make a measurement, the operator moves the belts until the lines cross at the point to be measured. Belt motion is translated into roller rotation, which in turn can be digitized. Each roller not driven by a hand wheel is connected to a Datex CG703A-1 encoder by means of anti-backlash gears. This encoder has 1000 counts per turn and counts 100 turns. The result of the gearing is to give about 36,000 counts across the 18 inch table, yielding a resolution of 0.0013 cm on the table or 0.00015 cm on the film.

In the belief that the direction of a bubble track could be determined more accurately by placing a line tangent to the track at a given point than by measuring point locations along the track, an angle measuring device was constructed for use with the analysis table. It consisted of an arrangement very similar to an ordinary drafting machine, with a plastic circle containing a cross at its center and a line emanating from the cross. A sprocket wheel around the plastic circle was joined to a single turn Datex encoder (C 711-1, 1000 counts per turn) by two chain links, with sprocket wheels centered on the arm pivot points. The line could be rotated to lie along the track direction, which could then be read by the encoder. This device was not used in event analysis for reasons discussed in Appendix IV.

In addition to the encoder readings, various parameters are required to describe the data taken. Most of these are entered on a

parameter board located to the right of the operator. Infrequently changed numbers like operator and analysis date are entered on rotary switches. Frequently changed numbers (track number, particle identification, stopping indicator, etc.) are entered into more convenient push-button switches. Various mode options are controlled by toggle switches. The Event Start push-button and normal Record push-button (which is paralleled by a foot switch) are also located on this board.

Many steps were taken to prevent operator errors, resulting in a considerable saving of analysis time. A panel of color-coded indicator lights mounted on the parameter board indicated the position of the mode switches, so that an amber or red light could remind the operator of a forgotten switch before much data was lost. A few of the least used but most troublesome of these also operated a soft buzzer while on. The presettable Neuron film frame counter was directly digitized, the only operator action required being to set it correctly at the start of a roll of film. The view identifier was set directly by the switch that selected the view. Lights in the Event Start and Record push-buttons reminded the operator of the sequence of operations (after advancing film to the desired frame the Event Start was lit and Record off. Once Event Start was pushed it went out and Record came on for the remainder of the event.).

C. The Data Recorder

The intermediary between the encoder and switch outputs and the IBM 026 card punch was a data recorder built by Ransom Research. It served two principal functions: translation and storage of encoder

readings, and programming of information fed to the card punch.

The encoders were not continuously followed as the belts moved. When Record was pressed, the data recorder interrogated the encoders, translated the cyclic decimal code used by the encoders to decimal, and stored the reading in a display on the front of the data recorder. This storage allowed the operator to be moving the belts to the next point while the information was still being punched out.

Card format consisted of an identification field followed by some number of data fields. Identification field length, data field length, and number of data fields per card were variable by means of thumb switches located on the front of the data recorder. The identification field was made up of parameter information (frame number, event number, analysis date, etc.); the data field contained parameter information (track number, particle identification, etc.) followed by ten encoder digits. Pressing Event Start caused a new card to appear at the punching station and the identification field to be punched. Pressing Record caused a data field to be punched. After the allowable number of data fields was placed on a card, that card was automatically released and the identification field placed on the next card. Information was fed to the card punch serially at the rate of fifteen digits per second.

D. Scanning Aids

1. Scanning Board. Each scanning table had a movable scanning board on top which acted as the viewing surface and contained the location of the fiducial crosses and the beam tube outline in both

views. Both views could be lined up simultaneously by using the two lens motions and moving the board appropriately to make the fiducial crosses in the pictures match the correct locations on the board. This line-up was chosen so that points on the gamma ray beam line were at the same place on the board in both views, which facilitated checking out tracks of particles produced by the beam.

2. Ray Tracer. The Ray Tracer was a device built to test the line-up of tracks tracing back into the hidden region of the beam tube. It consisted of three thin plastic arms pivoted at a common point with scribed lines emanating from that point. Given one or two tracks that might have come from the beam line, it was used to determine the origin on the beam line in order to search for additional tracks related to that origin. After an event had been found it could be used as an indicator of track initial direction, so that an operator could decide whether the track's line-up was good enough, taking into account the observed multiple scattering of the track.

3. Epsilon Limiter. Since picture line-up was chosen to superimpose the two views of an event occurring at the depth of the beam line, events occurring at the chamber windows would have a fixed separation in the two views. The epsilon limiter was simply a piece of plastic with these two distances scribed on it and color coded to identify which windows the marks corresponded to. It was used to help decide whether or not a track stopped in the chamber.

4. Track Starter. The track starter was a cardboard cut-out of the beam tube shape with numbers along the edge to aid in identifying a

track. This feature was later added to the scanning board itself. With the large number of tracks per picture the track starter was invaluable for knowing which track the operator had intended, and for comparing several operators' work in multiply scanned regions.

E. Operation and Stability for Analysis

Proper film environment is essential to film stability for analysis. Film was stored in the room with the machines. The air temperature was controlled to $73^{\circ} \pm 3^{\circ}$ Fahrenheit, and the relative humidity was not allowed to drop below 55 percent (fortunately it seldom exceeded 60 percent). Some film creep in measurement was observed during analysis setup; since it varied in different parts of the picture, did not correlate with the film drive direction, and would finally cease after about half an hour, it was attributed to temperature and humidity change of the film itself rather than failure of the vacuum backing to hold well enough. It was discovered that air supplied to the pressure fronts was fairly warm; passing it through a heat exchanger to bring it to room temperature reduced film creep considerably. Considerable film motion was still observed during machine warm-up, about one half hour after turn-on. After the machine had been on for an hour a little film creep was still observable, but it was of the order of the measurement errors in the length of time required to analyze an event, so no further attempt was made to reduce the effect.

Tests done to look for slippage of the mylar belts on the rollers gave no indication of slippage, even under harsher conditions

than normal analysis. When the table was properly installed, normal handling did not produce any observable motion of the table relative to the main machine. Combination of human vision limitations and the finite line width on the belts resulted in measurement reproducibility of two or three encoder units (about 0.003 cm on the table) when measuring a fine object. Actual track and fiducial measurement errors were larger than this, as discussed in Appendix V.

APPENDIX IV

SCANNING AND ANALYSIS PROCEDURES

A. Scanning Procedure

Scanning the bubble chamber pictures for event candidates was the most time-consuming operation in this experiment. Pictures were examined sequentially for possible event candidates, and these candidates were recorded on scan cards for later analysis. Because of the difficulty of scanning this set of pictures, the overhead projection scanning machines and hand tools used (which have been described in Appendix III) were designed with a view toward keeping the operation as simple as possible. Separation of proton, pion and electron tracks based on qualitative track characteristics in the chamber freon was quite good in the energy range of this experiment, as will be discussed below. Thus, the operator was faced with the task of investigating all pion and proton tracks in the chamber, and selecting any grouping of three or more such tracks that might have come from the beam line (hidden inside the beam tube shadow).

First the two stereo views were lined up properly with respect to each other on the scanning board. Then each proton or pion track emanating from the beam tube was checked to see if it came from the beam line (which required that it have approximately the same origin location in both views). If it did, the ray tracer was used to see whether there were any other tracks coming approximately from the same origin. Upon finding a second track, the operator relocated the ray

tracer origin for a best simultaneous fit to both, and continued the search for a third. This process was continued to however many tracks (3 or more) could be found in the entire field of view, since other events having nearby origins could contribute tracks that appeared to line up. This scan for additional tracks from the same origin was performed in both views, since lighting and background variations in the chamber might show up a track much better in one view than the other. Possible track origins were investigated sequentially, starting at the small end of the beam tube.

This scanning technique was important to finding the very high energy and very low energy tracks in an event. High energy pions and protons had low bubble density and would not be apparent in a region of heavy background. However, when one sighted out from the approximate origin location, the straight-line collection of bubbles would suddenly become very obvious. Low-energy tracks which stopped after going a short distance into the visible region of the chamber were quite obvious because of the heavy bubble density. However, the location of their origins was doubtful because of the short visible length for determining direction and because of the probability of considerable multiple scattering in the unseen regions, and it was usually necessary to find these as the second or third track of an event.

Recognition of a given track's mate in the other stereo view was based on similar bubble density and multiple scattering characteristics, common beam line origin, and occurrence of charac-

teristic features (beginning, end, kinks, etc.) at approximately equal distances from the beam line (which was also the line between camera optical axes). It was also necessary that the separation between all corresponding points on a track be within the appropriate limits prescribed by the epsilon limiter in order for them to correspond to a physical bubble in the chamber, and this fact could be used to limit the region where one might look for a missing track mate in a region of poor lighting or confusing background tracks. Lighting and background bubble variation in different parts of the chamber rendered apparent track darkness untrustworthy as a criterion.

Additional criteria imposed upon tracks were that they trace all the way back to the limits of the lighting imposed by the beam tube shadow and the lighting cutoff at the edge of the chamber, and that the tracks have passed through only the straight-line regions of the beam tube (since hidden region matter traversal could not be calculated for the oddly shaped parts of the beam tube). These criteria proved so restrictive at the small end of the beam tube that it was not necessary to add an additional restriction that the event origin be well away from the mylar window at the beam tube entrance.

With the large number of tracks per picture it might be expected that extremely short tracks would go unnoticed. This turned out to be the case, the minimum seen projected length in the chamber averaging about 0.5 cm for stopping tracks, and 1.5 and 2.0 cm respectively for non-stopping protons and pions.

Identification of stopping particles was based primarily on the length of the region of very heavy bubble density: about 1 cm for a pion and about 5 cm for a proton in the chamber. Non-stopping tracks were identified largely on the basis of bubble density and multiple scattering. Any backwards-going tracks were necessarily pions. Although high-energy pions and protons may look alike, many such cases were resolved by the fact of the other tracks in the event having obvious identifications. In the remaining cases, taking the most likely proton candidate as the proton gave the correct answer most of the time. Another particle indicator of limited usefulness was the π - μ -e decay of a stopping positive pion. It was used wherever found, but the relatively small number of pions stopping in the chamber coupled with the difficulty of seeing the μ and the electron against the sea of background tracks rendered these events rare. Scanning particle identification was used primarily as an aid in analysis interpretation since the computer program in general tried all possible particle indentifications anyhow.

Tracks exhibiting the bubble density increase described above and terminating well within the lit region of the chamber were assumed to stop. If there was any doubt that the termination might be due to lighting failure or a window exit, the particle was not called stopping. Tracks that ended within the lit chamber volume but showed no major increase in bubble density at the end were assumed to have suffered a nuclear interaction in flight and thus were considered non-stopping. Any track that suffered a major kink or produced a

nuclear star without obviously stopping first was considered non-stopping at that point. All of these criteria were directed toward avoiding called a track stopping when it wasn't, and thus making a false energy measurement on the track.

B. Scanning Evaluation

The largest single source of error in this experiment was inefficiency in scanning. Scanning efficiencies were low because of the large amount of visual background present, and thus the short term variations caused by how people were feeling or what else was going on in the room were much more serious. Five scan comparison regions were set aside for special study of scanning and analysis; scanning efficiencies in those regions are shown in Table A IV-1. The low values in that table are not representative of actual film scanning since they represent training periods for some people, and a few never qualified for film scanning. Final film regional efficiencies are shown in Table A IV-2.

From looking at the events on the scanning table it was clear that some events were harder to find than others. Thus we checked on the correlation of events found by different people in the scan comparison regions and found that Alyea's assumption³⁰⁾ of scanning efficiencies being independent for different scans did not describe our data; the independent efficiency model would predict much higher efficiency for several people scanning a region than was actually the case. Denoting two people's scanning efficiencies by x and y , it was found that the efficiency of the two combined could be described

TABLE A IV-1

Scanning Comparison Efficiencies^{*)}

Personnel ^{**)}	Scan Region				
	Roll 45-I	Roll 45-II	Roll 46	Roll 47	Roll 49
02	65.18	62.78			
12	96.30	93.33	79.59	80.90	
13	64.45	64.44		60.00	
14	57.04				
17	62.96	82.78	80.62	62.73	83.41
18	68.89				
20	61.48	51.07	80.00	55.45	82.44
21	65.93	76.67	77.14		
24	63.70		69.39	60.91	79.51
28	71.85				
31		75.0			

^{*)} Efficiencies above are percentage found of total number of events in the region.

^{**)} Scanner Identification Numbers

TABLE A IV-2

Film Region Scanning Efficiencies

Roll	Region	Personnel Contributing **)	Number Pictures	Scan Efficiency	Probable Error
45	1*)	02,12,13,14,17,18,20 21,24,28	243	99.6	2.7
	2	02,13,14,17,20	279	89.2	5.8
	3	12	630	90.8	5.4
	4*)	02,12,13,17,20,21,31	241	97.5	3.5
	5	12	1235	84.4	6.7
46	1	02,12,13,14,17,20,21	47	98.7	3.1
	2	02,12,13,14,17,20,21	109	89.7	5.7
	3	02,13,14,17,20	33	86.7	6.3
	4	02,12,13,14,17,20	100	97.5	3.5
	5	02,13,14,17,20	200	90.6	5.5
	6	02,13,14,17	120	83.6	6.9
	7	02,13,17	360	80.6	7.4
	8	02,13,17	120	86.0	6.4
	9	13,17	480	82.2	7.1
	10	17	120	77.4	7.9
	11	24,31	200	83.9	6.8
	12*)	12,17,20,21,24	240	96.4	3.9
	13	12	503	80.7	7.4
47	1*)	12,13,17,20,24	241	95.4	4.2
49	1*)	17,20,24	240	94.7	4.4

*) Denotes Scanning Comparison Region

**) Scanner Identification Numbers

by our equation of the form

$$E(x,y) = 1 - [(1 - x)(1 - y) + axy(1 - x)(1 - y)] . \quad (A \text{ IV-1})$$

This form was chosen to be symmetric in the variables, and to return (approximately) the higher efficiency when a high efficiency was combined with a low one. The constant a was a slight function of which region of film was chosen (since it naturally relates to scanning difficulty), but was apparently not a function of who was doing the scanning. The value $a = 1.5 \pm 0.5$ described all comparison regions but roll 49 (which gave 0.7, but that value is suspect because so few people scanned the region). Best averages actually used were 1.6 on roll 45 and 1.8 on roll 46. The formula above also adequately described combinations of more than two people; it was used to compute the number of events missed by everyone in the scan comparison regions, and to calculate the scanning efficiency in multiply scanned regions. All scanning efficiencies were computed only on the basis of finally accepted events.

Whether a person found all three tracks of an event was not an accurate gauge of scanning efficiency, because if someone found two out of the three, the third would often be found during the course of analysis or subsequent event examination on the scanning table. This effect was estimated by taking a single scanner region surrounding a scan comparison where the scanner found 70 valid events, 6 of which contained prongs added later which contributed to the valid event. Checking against her scanning efficiency in that comparison, this

corresponded to 60 ± 20 percent of the events where she found only two prongs of the correct three actually being accepted. Since these tracks picked up were more a function of the later processing than the original scanning and all non-comparison regions were handled approximately the same, it was felt that this correction could be safely employed in all scanning efficiencies. The effect is not large: the 20 percent error quoted above represents a 2 percent effect in scanning efficiencies on the average. Thus each person's scanning efficiency was computed by adding 60 percent of the number of events where he found only two of the three tracks to the number of events where he found all three, then dividing by the total number of events in that region^{*)}.

Since scanned events in general consisted of more than three prongs because of background nuclear events close by, there was some question whether the scanner might not look hard for three prongs, then tend to give up more easily on looking for others in the belief that he had found "the event". Certainly there was some tendency for this observed in the work of individual scanners. However, the consistency of the observed prong multiplicity rate with the calculated one (shown in Table A VI-5) indicated that selection of the most complete card for event analysis in multiply scanned regions plus the addition of tracks during analysis processing adequately supplied the missing tracks, so such an effect should not be present in the final data.

*) The total number of events in a scan comparison region included a correction for the number of events missed by everyone, computed from Eq. (A IV-1).

One possible source of final event bias (in energy or diparticle mass) resulting from scanning could have been the loss of low-energy tracks due to multiple scattering in the hidden regions of the beam tube causing them to fail to line up with the actual event origin. However, the fact that the effective scanning origin resolution width is more than twice the equivalent analysis width (details are given in Appendix VI) would indicate that such events would be lost by the analysis program rather than in the scanning; thus this effect should have already been included in the analysis program efficiency calculation (Appendix V).

Table A IV-2 shows the final regional efficiencies computed from Eq. (A IV-1) in regions of multiple scanning. The error was computed from

$$\Delta E = \frac{\sqrt{N(1 - E) + 1}}{N} \quad (\text{A IV-2})$$

with the square root representing a statistical error in the number of events missed in a comparison region with the total number of events in the region, N , being taken to be 40. Scanning efficiencies were computed as a function of time for each person by drawing a smooth curve that roughly fit his performance on scan comparisons: then each film regional efficiency was found from the curve at the time he scanned that region. Since the curves average the results of several comparisons ranging in length from 22 to 49 events, it was felt that the statistical accuracy associated with a 40-event measurement should best describe the average confidence at any point on the

curve; any more accurate procedure is simply not justified in the light of the crude assumptions that have already been made. In multiply scanned regions an attempt could have been made to combine individual errors in a manner compatible with Eq. (A IV-1); however, the basic confidence in the measurement depends upon the number of events missed in the scanning, so it was felt that use of Eq. (A IV-2) with E the regional efficiency still gave the most reliable error estimate.

In some cases scanners were not aware that regions they were scanning were comparison regions, but a good fraction of the time they were. Since there was the possibility that they might work harder on regions they knew would be evaluated, a few local checks were performed in non-comparison regions on the work of the people that figured most prominently in the scanning efficiencies. In general there was reasonable agreement (to about 8 percent) with the scanning efficiency curves.

Particle identification and stopping designation accuracy are shown in Table A IV-3. The true situation is taken to be that given by the finally accepted computer output; the scanning results are those of the initial scan, independent of comments added later in event checking. As can be seen from the table, a good fraction of the incorrect particle identifications had the other possibility also mentioned on the scan card. Many of the ones that did not, are attributable to laziness on the part of the scanner in writing such things down rather than not realizing the possibility. From this data it may be concluded that particle identification is about

Table A IV-3

Scanning Identification Accuracy

Error	Total Percentage Incorrectly Assigned	Percentage with Alternate not Mentioned
Called proton, was pion	2.7	2.1
Called pion, was proton	10.8	7.1
Called stopping, was going out	0.2	0.1
Called going out, was stopping	1.5	1.3

Percentages are based on the number of tracks of the appropriate type (proton, pion) among all the accepted events. For the stopping errors, the total number of tracks was used.

90 percent accurate in this energy range for this type of experiment. A check of accepted events indicated that pions could be "definitely" identified (confidence estimated to be greater than 95 percent) up to a particle momentum of about 250 MeV/C, and protons up to about 750 MeV/C, about 5 cm of visible projected length in the chamber being minimal for these decisions on non-stopping particles. Stopping particles could be identified with 1.5 cm projected chamber length seen. The high efficiency quoted above implies that even in energy regions where identification is not definite, qualitative identification can still be made with considerable confidence. The preponderance of stopping particles called non-stopping represents those cases of particles stopping in regions of lighting cutoff where the scanners were instructed to be overly cautious.

C. Analysis Calibrations

Before event analysis could be undertaken, it was necessary to know the location (relative to the film in the camera) of the fiducial marks on the big chamber window, the beam line through the chamber, the beam tube, and the various optical surfaces in the chamber. Also required was a knowledge of the optical distortions introduced by the projection and measuring system. Camera distortions were neglected since the camera lenses should have produced no measurable distortion (Goerz Rectagon lenses used at approximately f:32) and the various indices of refraction were explicitly taken into account by the computer program.

A glass-backed emulsion plate was ruled with a grid of 21 lines

each way in the field of view. Measurements of the relative location of all 441 intersections were repeatedly taken on a microscope until consistency was achieved. Then this grid was placed at the film location in each view, and all intersections in the resultant images measured on the analysis table. A computer program made a least squares fit to a general linear transformation (6 parameters) mapping the microscope data onto the table data. Differences between the transformed microscope data and the table data could then be examined for measurement error and secular variations. Repeated measurements were taken and checked for consistency. With the initial 1/4 inch-thick glass mirrors, secular variations of the order of .05 cm on the table were observed; when these were replaced by better quality 1 inch-thick mirrors the variations decreased to about .005 cm and appeared to be randomly distributed (the measurement error is about .005 cm on a single intersection). This it was concluded that all remaining distortions due to projection lenses, lack of mirror flatness, lack of line perpendicularity in the mylar belts on the measuring table, lack of perpendicularity in the mirrors, and lack of parallelism between film plane and image plane were adequately corrected by the linear transformation, and this transformation was then applied to all data taken on that table. This measurement was repeated a few times during the course of data measurement to guard against machine or mirror motion; long term variation in the relevant parameters did not exceed the short term variation from one measurement to the next (a few parts in 10^5), and no secular change was observable.

Bubble chamber optical spacings were carefully measured directly. The distance from the big chamber window to the beam tube was also measured directly. However, since this measurement of beam tube and beam line location are somewhat less accurate, this measurement was later modified as described below.

To obtain the location of the fiducial marks on the outer surface of the big chamber window, use was made of the fact that the two surfaces of that window were very close to being parallel. Two crosses made up of 13 ball bearings each in the shape of a cross were mounted beneath the big window at positions orthogonal to the camera lenses. The reflections of these crosses in the two surfaces of the big window were then photographed simultaneously with the chamber fiducial marks. Since lines joining corresponding image points will all intersect the camera axes (defined to be the lines dropped from the center of the camera lenses perpendicular to the big window), all the fiducials and all the ball bearing images were measured on the analysis table, and the common intersection points of lines joining corresponding ball bearing images (again from a computer least-squares fit program) were taken to be the camera axis locations relative to the fiducials. The spacing between camera lens axes was in excellent agreement with the known measured value. Multiple measurements were taken, and an average of six good measurements was chosen to determine the fiducial locations.

Since the beam tube had good circular symmetry about its axis and the chamber lineup was done with respect to plugs placed in the

beam tube, the beam position was assumed to center on the beam tube axis. The beam tube location in the plane of sight was determined by measurement of its outline on the analysis table, calculation of the resultant shape and position in true space by the computer, and hand fit to the actual beam tube shape as measured by Don Coyne. Its depth in the chamber was determined by the spacing measurement from the big window as described above. As event analysis proceeded, a study of the distribution of valid event origins in the plane perpendicular to the beam line showed no bias in the plane of sight, but a definite bias in depth. The amount of this discrepancy was compatible with the original measurement errors, so the beam tube depth was changed by an amount calculated to destroy the beam origin bias, and these early events were re-analyzed. The final event origin distribution shows no appreciable bias.

D. Direction Measurement Technique

Since event origins are hidden inside the beam tube, it is important to have a good measurement of particle direction at the first observable point in order to determine the event origin and kinematics well. Appendix III describes an angle measuring device intended to make this track tangent measurement, and in Appendix V are included the calculations for turning this angle measurement into a three-space direction measurement. Why this technique did not work satisfactorily will now be investigated.

In the absence of indices of refraction, one may imagine such a direction measurement line on the film plus the center of the camera

lens to determine a plane in each view. Then the line intersection of these two planes gives the true particle direction in three-space. Indices of refraction distort these planes a bit, but the principle is the same. It is clear that the technique fails as the film directions become parallel to the line between camera axes, for the two planes approach coincidence and fail to determine a line well. The camera lenses were placed on the beam line just so that tracks emerging from the beam tube would be going at an appreciable angle with respect to this line, minimizing this difficulty.

Event analysis was begun using the angle encoder device and the errors involved in point and direction measurement were evaluated. It was found that the direction determination was poor enough that some difficulty was encountered in finding an initial event parameter guess for the minimization procedure, and often several hypotheses could fit an event well because of the large directional uncertainties. Direction measurement errors were compared with those that would arise from simply using the second measured point on the track to determine track direction, including point measurement errors and multiple scattering effects; of course this requires that the spacing between the first and second track points be reasonably chosen, based on the observed multiple scattering of the track. For tracks moving perpendicular to the beam line the two methods were found to have roughly equal errors; as the tracks approached the beam line direction the angular technique became decidedly worse. Since the angular technique was also more difficult and time-consuming, requiring

the device to be continually moving into and out of the field of view, it was abandoned at that point, and all analyzed events had track directions determined by the second point on the track.

One contributor to the additional error in the angular measurement technique might be that measurement of three widely separated fiducial points provides a better rotational reference than lining up the line on the angular protractor with a reference line on the picture; this effect is most likely responsible for the fact that the angular technique is no better than the point technique for tracks perpendicular to the beam line. The major effect at smaller angles must be the fact that the point technique can take advantage of finding or generating corresponding points where the angular technique cannot. Of course, a track moving almost parallel to the beam line with no recognizable corresponding points is in trouble with the point technique too, but fortunately there were not many of these.

In the computer, the direction measurement error was broken down into the contributions from multiple scattering and point measurement error. Comparison of the two would indicate whether the person analyzing was choosing his second point too far out or too far in, or whether he was handling some types of tracks correctly and others incorrectly. This type of feedback was used to train the analyzers on the proper choice of the second point, about two weeks being required for one to develop good judgment in this choice.

E. Analyzing Table Procedure

An event was measured as rapidly as was consistent with good accuracy in order to minimize film creep during measurement, which was of the same order of magnitude as the measurement errors in the time required to measure an event. Three fiducial marks were measured in each view before and after data point measurement so that any gross film movement during measurement would show up as inconsistency in the fiducial measurements.

Tracks were measured by choosing a sequence of corresponding or pseudo-corresponding (close to corresponding) points along the track. The first clear point of beam tube shadow emergence initiated the track, and the last clear point on the track or the point where the track stopped terminated the track, except for any sharp kinks in the track which might have been inelastic events and were therefore considered to be the end of the track. Both views of a given point were measured before progressing to the next point in order to make it easier for the operator to find corresponding points. The second point on the track was chosen as far as possible from the first point, consistent with this point still being along the original track direction. As mentioned in the section above, computer feedback was used to train operators in making this choice. Except for extremely short tracks, a minimum of three points were measured along a track. A curving stopping pion might require eight or ten points, choice of points after the second being governed by the resultant chords being a good approximation to track length and scattering.

F. Computer Output Processing

The output of the event reconstruction computer program was carefully examined to ascertain as far as possible that events accepted were indeed reasonable and that events rejected were not valid. This work required considerable understanding of scanning and analysis techniques, with the result that not all the scanners could have been trained to do it. Lenore Fretwell handled most of this work, with the rest being performed by Phyllis Nilsson and the author.

In order to be accepted by the computer an event had to have a chi square probability of at least 0.1 percent. Event acceptance was considered dubious if this probability was less than about 1 percent. Incoming gamma-ray energy was required to be less than 1540 MeV, the approximate bremsstrahlung limit of the synchrotron. If the hypothesis accepted by the computer required any track to have a different particle identification than the one given it by the scanner, or if it claimed the track stopped or had bubble density more than about six times minimum at the end of the visible region of the track when the scan card indicated the track to be non-stopping, the event was re-examined on the scanning table and the hypothesis was considered acceptable only if these changes seemed reasonable. Other quantities examined for having reasonable values were the event origin location, agreement of observed track direction with calculated production direction, agreement of calculated particle production momenta with measured values determined by multiple scattering and range-energy measurements, magnitude of the error in the observed direction measurements, mode of

exit from the minimization routine, and the error messages printed during analysis that indicated various parameters outside expected tolerances or potentially troublesome conditions present. Acceptance criteria here varied from event to event (for example, one would expect a much worse direction measurement on a short, stopping pion than on a high-energy proton); the primary purpose of these checks was to ascertain that poor measurement technique had not given rise to such large allowable errors that an incorrect hypothesis could yield a low value of chi square, or that a valid event had not been carelessly measured. Questionable events were remeasured several times until the truth became obvious.

When the computer found no acceptable hypothesis, the best one found was printed out; it was examined on the basis of the criteria discussed above (primarily chi square and the error messages) to attempt to decide whether failure might be the result of poor measurement of a valid event. All event failures were measured at least twice (except for obvious momentum conservation failures); if it seemed that there might be a valid event present or that the previous measurements had not been correctly performed, the event was remeasured as many times as necessary to provide a reasonably clear pattern of failure^{*)}. Event failures were often re-examined on the scanning table, as occasional failures were attributable to incorrect track selection in the two views or inelastic processes occurring along a track that had been overlooked. Re-examination of an event on the scanning table included searching for additional prongs, and

*) The average number of measurements is discussed in Chapter II.

prongs found in this way contributed significantly to the good event rate. Since post-scanning examination was bringing to light additional tracks, there arose the question whether it might not be a good idea to rescan the events found for additional prongs. A limited region was rescanned this way; however, in the region where the event re-examination had already taken place so few additional prongs were found that were part of valid events upon subsequent analysis that the project was soon abandoned.

If an event yielded several acceptable hypotheses, the event was very carefully examined for criteria to distinguish between them (bubble density, confidence in particle identification, etc.). In general, the hypothesis with lowest chi square was accepted. Here remeasurement was almost guaranteed in order to establish confidence in the hypothesis and chi square pattern.

G. Analysis Evaluation

Errors in the analysis phase of this experiment (including measurement, computer processing, and computer output processing) may be considered in terms of three general classifications:

(1) Events accepted that are not valid, (2) Events rejected that are valid, and (3) valid events accepted with incorrect parameter values. As far as the computer program itself is concerned, point (1) is covered in the background discussion of Appendix VI and the other two points are discussed in the section on program accuracy in Appendix V. Since part of the purpose of the computer output processing routine was finding bad measurements, the remainder of

this evaluation devolves upon how well that processing was done.

The largest contribution to this error must come from the fact that the analysis program was incorrect when the majority of the data was first processed, as discussed in Chapter III. After program correction, all previously accepted events had their same hypothesis re-calculated. The 27 events that failed were thoroughly re-measured and re-calculated before being discarded. Events that gave acceptable hypotheses might still have had another hypothesis that was better, so all that had a χ^2 probability of less than 1 percent or made stopping or particle identification changes from what had originally been specified were reprocessed to look for such alternate hypotheses. Scan comparison regions were scrutinized more carefully, events having any indication of being suspect being checked out on the scanning table, then re-analyzed if necessary. Altogether 26 events from comparison regions and 48 events from non-comparison regions were re-analyzed; 15 failed and 8 gave other hypotheses more acceptable. In the comparison regions 6 of the events rerun would not have been selected on the basis of χ^2 or particle identification or stopping change; of these 3 were accepted the same as before, 1 failed, and 2 yielded alternate (improved) hypotheses. Assuming that this ratio also holds in the equivalent non-comparison areas, we would expect that 0.4 percent of the total event rate would have failed and 0.9 percent would have given alternate hypotheses had this same check been performed on the non-comparison regions as well.

Events rejected under the old program and not rerun under the

new one represent a more serious error. A special category had been kept for marginal failures; all of these were re-processed. In an area consisting of the scan comparisons plus a 400-picture region, all event failures were carefully examined, and any with a remote chance of giving an acceptable hypothesis were rerun. This analysis yielded 17 good events, of which 10 were not in the automatic re-processing category. Extrapolation of this result to the non-processed areas implies that 3.0 percent of the total event rate was lost by not re-processing all failures. Because of the uncertainty in this extrapolation we take the error also to be 3 percent rather than the statistical error.

Direct human error in output processing is difficult to assess. All failures under the new program were double-checked by the author, which eliminated several mistakes. Accepted events were spot-checked at random in addition to the checks done on dubious acceptances described above. It is believed that remaining errors in event count and hypothesis choice are negligible compared to the other errors in the experiment. Under the old program there may have been some processing errors, but corrections for these have automatically been included in the corrections above since processing and computer error would have been indistinguishable at that point. Errors in mechanical card handling should have been negligible since duplicate records were kept during analysis (scan cards and analysis summary sheets) and an accepted event record was kept on magnetic tape at the computing center; these were continually cross-checked for

discrepancies.

As far as possible error in the technique itself is concerned, it should be noted that 5.8 percent of the accepted events had alternate hypotheses involving other tracks that would have been acceptable, although they were not as good as the one taken. 0.7 percent had competing hypotheses involving different particle assignments for the same three tracks. All particle and stopping conditions were allowed if they seemed at all reasonable. Considering the result of the event generation study (Appendix VI) that the correct hypothesis always looked best, it seems unlikely that wrong hypothesis choices could have been made in as much as 1 percent of the data, so no correction will be applied for wrong choices.

APPENDIX V

EVENT RECONSTRUCTION

This appendix contains a discussion of the data analysis techniques used in event reconstruction, and the IBM 7094 computer program written to perform them. The complete program consists of 40 subroutines coded in Fortran IV, and 12 subroutines coded in Map language. With the necessary IBSYS and library routines, it occupies all but 1709 of the computer's 32,768 word memory. Thus no attempt will be made to describe the subroutine structure in detail, but only to give the guiding lines around which it was built.

A. Program Logic

A general block diagram of the logic flow in this program is shown in Figure A V-1. The main program is only entered once, and is used for constant setup purposes. Events are processed by two subroutines which call each other, so that control is never returned to the main program: NEXTEV, which reads in the next event, and SEQUOR, which controls the operations performed on the event. As difficulties are encountered in data processing, subroutine ERROR is called to give a record of the error condition on an alternate output unit. ERROR has two calling sequences, depending on the seriousness of the error condition detected: if the error is so serious that the event being processed should be abandoned, ERROR turns control over to NEXTEV; otherwise only a warning is intended, and control is returned to the point where the error was found.

Figure A V-1

EVENT RECONSTRUCTION PROGRAM LOGIC FLOW

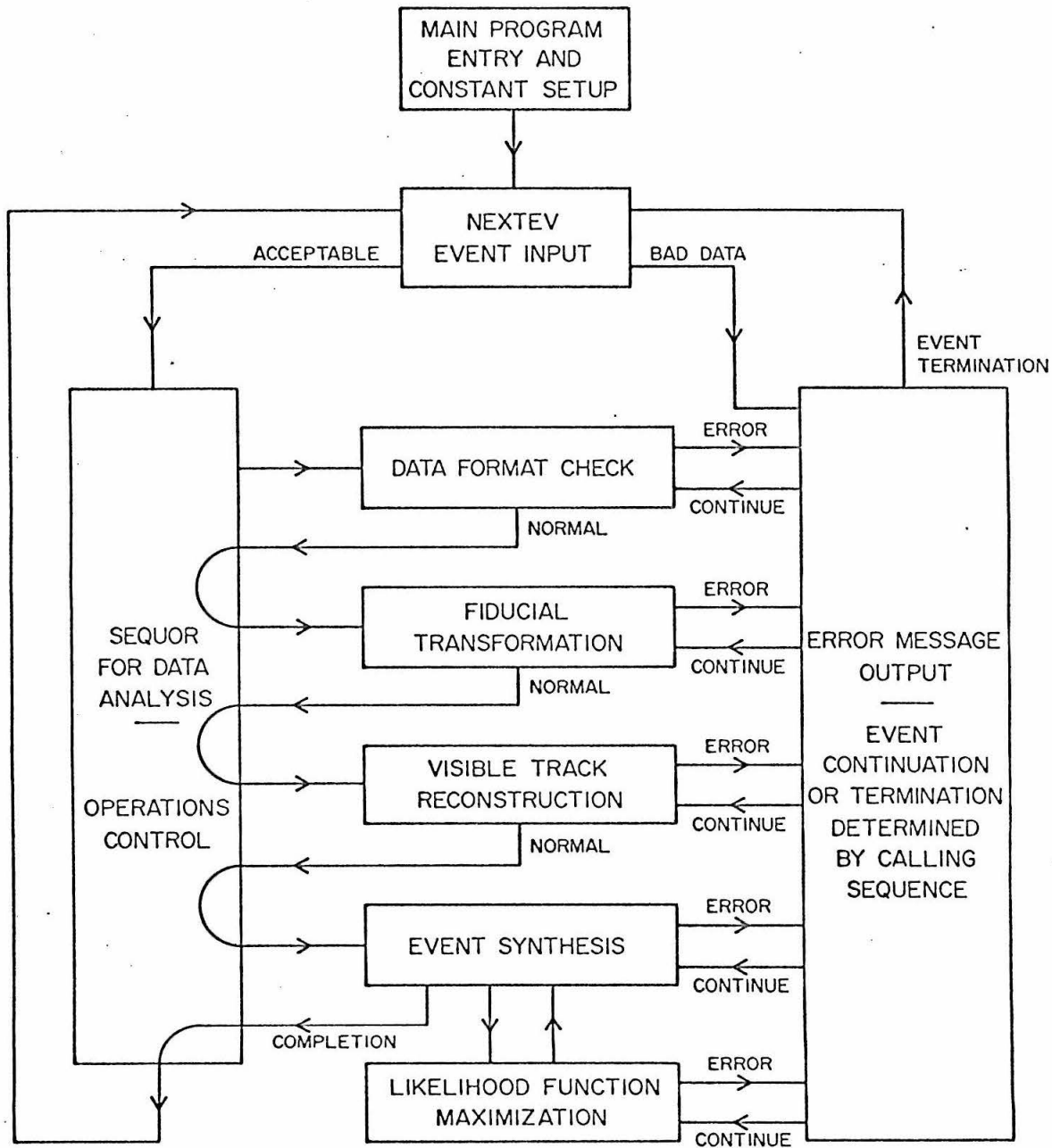


Figure A V-1

During data read-in, NEXTEV does some rudimentary checking on the input data format. If it is acceptable, SEQUOR calls another subroutine which performs a more careful format check. The vast majority of the careless switch settings on the parameter board of the analysis machine (discussed in Appendix III) are found by one of these two subroutines. Next, the fiducial transformation subroutines reduce the encoder readings to the actual film coordinates, and establish the logic of the measured points. The visible track reconstruction subroutines then reconstruct the particle tracks in the bubble chamber. Finally, the event synthesis subroutines investigate the possible hypotheses for the event (assuming charged pi pair photo-production), find the optimized parameters, and handle the output. At the conclusion of analysis, SEQUOR returns control to NEXTEV to read in the next event.

B. Data Format

The data card consisted of five fields of 16 columns each. The first field on the card, known as the event identification field, contained film frame number, event number, measurement number (tag), analysis date, and operator code. This field would remain the same for all cards comprising one event, and that was the basis of event discrimination by subroutine NEXTEV since events varied in length. The other four fields on a card were data fields, containing a code for particle stopping and forcing of stopping or particle identification; the weight factor assigned that measurement; particle identification code; a code giving view measured and whether the measurement

was data point, direction, fiducial, or an error flag; vertex and track identification numbers; and ten encoder digits. It was not required that all data fields on an intermediate card be used, but the requirement of no blanks or non-numeric characters in a used field pointed up most of the data recorder and punch errors.

The measurement procedure is described in detail in Appendix IV. The analysis program expected at least two separate fiducial measurements in each view. It checked for parameter consistency between two corresponding view measurements. The requirement that points be taken sequentially along a track precluded recurrence of a given set of vertex and track numbers after another set had occurred, and this check found many of the operator switch setting errors.

C. Visible Track Reconstruction

1. Bubble Chamber Optics Calculation

The problem of coordinate transformation between two stereo views on the film and real space in the bubble chamber has three aspects treated here. They are the calculation of true space bubble coordinates given the film image coordinates, the calculation of true space direction from a bubble given the film image bubble coordinates and the film image directions, and the calculation of film image coordinates given the true space bubble coordinates. The analysis will proceed under the assumption that the bubble images considered in the two views correspond to the same physical bubble in the chamber.

a. Chamber Position Calculation

Given points x_L, y_L, x_R, y_R on the film of corresponding bubble images (Fig. A V-2), the true space bubble position calculation can be taken in two steps:

- (1) Locating the $Z = 0$ points (where imaginary light rays from the bubble images enter the chamber liquid), and finding the light ray direction vectors at those points.
- (2) Finding the point lying on the mutual perpendicular to the lines representing the two light rays in the chamber liquid, placed so that its distance from the light rays is inversely proportional to the weighting factors assigned in the original film measurements.

(1) Points in $Z = 0$ Plane

Let X_L, Y_L, X_R, Y_R denote left and right view light ray intersections with $Z = 0$ plane. The distance between the $Z = 0$ light ray intersection and the camera lens axis for a given view is seen from Fig. A V-2c to be

$$R = \sum_i h_i \tan \theta_i \quad (\text{A V-1})$$

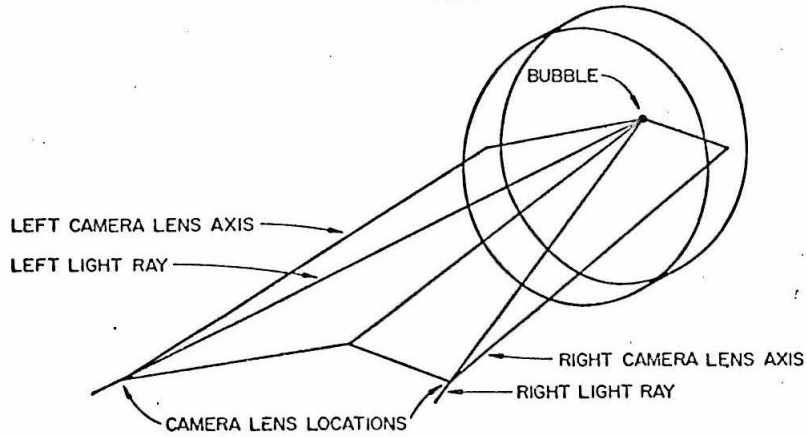
where the sum is taken over all indices of refraction except, of course, the chamber liquid^{*)}.

*) This calculation assumes that all medium interfaces are flat and parallel. Deviation from parallelism was at most 0.001 inch for the big chamber window and the viewing ports. Displacement and magnification change due to optical distortion can be ignored, since the fiducial set up procedure used (Appendix IV) automatically compensates for these. The major distortion due to a wedge-shaped window would be an apparent depth change across the chamber; an 0.001 inch deviation would produce a depth change of 0.013 mm across the chamber, which is
(footnote continued on following page)

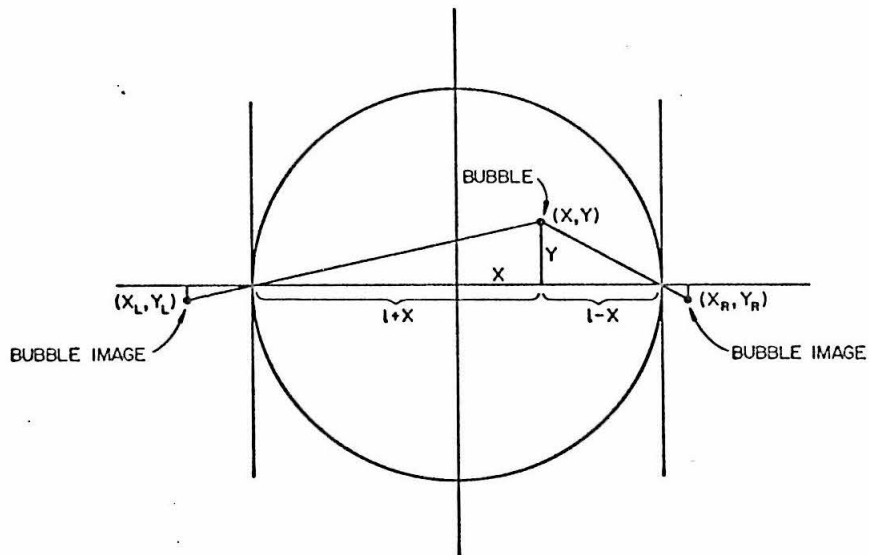
Figure A V-2

Bubble Chamber Optics Calculation Schematic Views

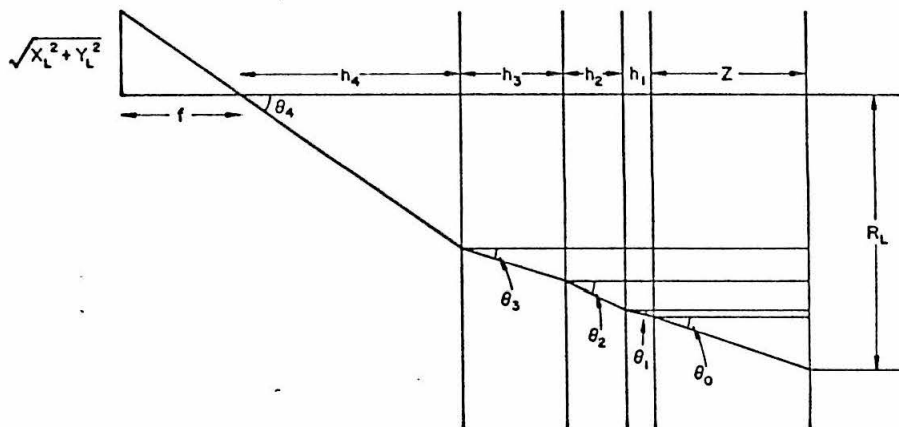
- A. No-Index Approximation General View
- B. Plane of Sight
- C. Plane of Light Ray



(A)



(B)



(C)

Figure A V-2

Now,

$$\tan \theta_i = \frac{n_j \tan \theta_j}{n_i \sqrt{1 + \tan^2 \theta_j (1 - n_j^2/n_i^2)}} \quad (\text{A V-2})$$

$$\tan \theta_{\text{air}} = \frac{\sqrt{x_{L,R}^2 + y_{L,R}^2}}{f_{L,R}}.$$

From Fig. A V-2 B,

$$X_L + \ell = \frac{-x_L R_L}{\sqrt{x_L^2 + y_L^2}},$$

with similar expressions for Y_L , X_R , and Y_R . Thus the light ray intercepts at the chamber liquid entrance are given by:

$$X_L = -\ell - X_L \sum_i \frac{h_i}{n_i \sqrt{f_L^2 + (1 - 1/n_i^2)(x_L^2 + y_L^2)}}$$

$$Y_L = -Y_L \sum_i \frac{h_i}{n_i \sqrt{f_L^2 + (1 - 1/n_i^2)(x_L^2 + y_L^2)}} \quad (\text{A V-3})$$

Footnote continued from previous page

completely negligible compared to measurement errors. The effect of viewing port tilt with respect to the big window can be described by a change in window thickness independent of light ray angle and a change in index of refraction dependent upon light ray angle. Again ignoring displacement and magnification changes, a 1° tilt in a viewing port would make a lateral distortion of 0.003 mm across the chamber, again negligible since the actual tilt cannot appreciably exceed 1° .

$$X_R = \ell - X_R \sum_i \frac{h_i}{n_i \sqrt{f_R^2 + (1 - 1/n_i^2)(x_R^2 + y_R^2)}} \quad (\text{A V-3})$$

$$Y_R = - y_R \sum_i \frac{h_i}{n_i \sqrt{f_R^2 + (1 - 1/n_i^2)(x_R^2 + y_R^2)}} .$$

Looking at Fig. A V-2, one can see that the light ray direction cosines into the chamber liquid are given by

$$i_z = - \cos \theta_0$$

$$i_x = \sin \theta_0 \cdot \frac{-x_{L,R}}{\sqrt{x_{L,R}^2 + y_{L,R}^2}} \quad (\text{A V-4})$$

$$i_y = \sin \theta_0 \cdot \frac{-y_{L,R}}{\sqrt{x_{L,R}^2 + y_{L,R}^2}}$$

with subscript zero denoting chamber liquid. Thus

$$i_{x_L} = \frac{-x_L}{n_0 \sqrt{f_L^2 + x_L^2 + y_L^2}}$$

$$i_{y_L} = \frac{-y_L}{n_0 \sqrt{f_L^2 + x_L^2 + y_L^2}}$$

$$i_{z_L} = \frac{-\sqrt{f_L^2 + (1 - 1/n_0^2)(x_L^2 + y_L^2)}}{\sqrt{f_L^2 + x_L^2 + y_L^2}} \quad (\text{A V-5})$$

$$i_{x_R} = \frac{-x_R}{n_0 \sqrt{f_R^2 + x_R^2 + y_R^2}}$$

$$i_{y_R} = \frac{-y_R}{n_0 \sqrt{f_R^2 + x_R^2 + y_R^2}}$$

$$i_{z_R} = \frac{-\sqrt{f_R^2 + (1 - 1/n_0^2)(x_R^2 + y_R^2)}}{\sqrt{f_R^2 + x_R^2 + y_R^2}}.$$

(2) Closest Point to Two Lines in 3-Space

Given points P_1 and P_2 , and unit vectors \vec{V}_1 and \vec{V}_2 , find the location of the point P on the line segment perpendicular to \vec{V}_1 and \vec{V}_2 whose distances from \vec{V}_1 and \vec{V}_2 are proportional to W_2/W_1 , W_1 and W_2 being weighting factors assigned to the point and unit vector measurements.

Let \vec{P}_1 and \vec{P}_2 denote vectors from the coordinate system origin to P_1 and P_2 . \vec{P} will denote the vector from the origin to P .

Any point along the line of vector \vec{V}_1 will be given by

$$\vec{r}_1 = \vec{P}_1 + s_1 \vec{V}_1 \quad (\text{A V-6})$$

for some S_1 .

Any point along the line of \vec{V}_2 will be given by

$$\vec{r}_2 = \vec{P}_2 + S_2 \vec{V}_2 \quad (\text{A V-7})$$

for some S_2 .

The segment containing P will be perpendicular to both \vec{V}_1 and \vec{V}_2 ; its direction is therefore given by $\vec{V}_1 \times \vec{V}_2$. Now let \vec{D}_2 be the vector from the coordinate system origin to the intersection of \vec{V}_2 with the plane containing \vec{V}_1 and the mutual perpendicular. Similarly, let \vec{D}_1 be the vector from the origin to the intersection of \vec{V}_1 with the plane containing \vec{V}_2 and the mutual perpendicular. Find \vec{D}_1 and \vec{D}_2 , and then P will be chosen appropriately along $\vec{D}_2 - \vec{D}_1$.

Any point in the plane containing \vec{V}_1 and the mutual perpendicular will be given by

$$\vec{q}_1 = \vec{P}_1 + a_1 \vec{V}_1 + b_1 \vec{V}_1 \times \vec{V}_2 \quad (\text{A V-8})$$

for some a_1 and b_1 .

Any point in the plane containing \vec{V}_2 and the mutual perpendicular will be given by

$$\vec{q}_2 = \vec{P}_2 + a_2 \vec{V}_2 + b_2 \vec{V}_1 \times \vec{V}_2$$

for some a_2 and b_2 .

Now

$$\vec{D}_2 = \vec{q}_1 = \vec{r}_2, \quad \vec{D}_1 = \vec{q}_2 = \vec{r}_1$$

so that using Eqs. (A V-7) and (A V-8)

$$\vec{P}_1 + a_1 \vec{V}_1 + b_1 \vec{V}_1 \times \vec{V}_2 = \vec{P}_2 + s_2 \vec{V}_2$$

or

$$\vec{P}_1 - \vec{P}_2 = -a_1 \vec{V}_1 + s_2 \vec{V}_2 - b_1 \vec{V}_1 \times \vec{V}_2. \quad (\text{A V-10})$$

Using (A V-6) and (A V-9),

$$\vec{P}_2 + a_2 \vec{V}_2 + b_2 \vec{V}_1 \times \vec{V}_2 = \vec{P}_1 + s_1 \vec{V}_1 \quad (\text{A V-11})$$

or

$$\vec{P}_1 - \vec{P}_2 = -s_1 \vec{V}_1 + a_2 \vec{V}_2 + b_2 \vec{V}_1 \times \vec{V}_2.$$

Comparison of (A V-10) and (A V-11) shows that $a_1 = s_1$, $a_2 = s_2$,

$b_2 = -b_1$, so that one must simply solve the system of equations

$$-a_1 \vec{V}_1 + a_2 \vec{V}_2 + b_2 \vec{V}_1 \times \vec{V}_2 = \vec{P}_1 - \vec{P}_2 \quad (\text{A V-12})$$

for a_1 , a_2 , and b_2 .

Then

$$\vec{P} = \frac{w_1}{w_1 + w_2} \vec{D}_1 + \frac{w_2}{w_1 + w_2} \vec{D}_2.$$

Using (A V-8) and (A V-9)

$$\vec{P} = \frac{w_1}{w_1 + w_2} \vec{P}_1 + \frac{w_2}{w_1 + w_2} \vec{P}_2 + \frac{w_1}{w_1 + w_2} a_1 \vec{V}_1 + \frac{w_2}{w_1 + w_2} a_2 \vec{V}_2. \quad (\text{A V-13})$$

The length of $\vec{D}_2 - \vec{D}_1$ is obtained from (A V-6) and (A V-8):

$$\vec{D}_1 = \vec{r}_1 = \vec{P}_1 + a_1 \vec{V}_1$$

$$\vec{D}_2 = \vec{q}_1 = \vec{P}_1 + a_1 \vec{V}_1 + b_1 \vec{V}_1 \times \vec{V}_2$$

$$\vec{D}_2 - \vec{D}_1 = b_1 \vec{V}_1 \times \vec{V}_2$$

$$|\vec{D}_2 - \vec{D}_1| = |b_1| \sqrt{1 - (\vec{V}_1 \cdot \vec{V}_2)^2}. \quad (\text{A V-14})$$

This quantity is used as an estimate of the error in correspondence of the points chosen on the film.

b. Chamber Direction Calculation

Given points x_L, y_L, x_R, y_R on the film and direction vectors $\Delta x_L, \Delta y_L$, and $\Delta x_R, \Delta y_R$ on the film, it is necessary to find the direction vector of the corresponding track in the chamber. This will be done in two steps:

- (1) Find the track direction for each view in the $Z = \text{constant}$ plane corresponding to the approximate Z depth of the bubble in the chamber.
- (2) Using each view's $Z = \text{constant}$ track direction and light ray direction from the $Z = 0$ point into the chamber (which was found in Section I) to determine a plane, calculate the true space direction by finding the direction of the intersection line of these two planes.

(1) $Z = \text{Constant}$ Track Direction

Imagining the Δ 's to describe a point infinitesimally removed from the original point along the track direction on the film, from Eq. (A V-3), the $Z = \text{constant}$ passage of that point's light ray is

$$X^* = \pm \ell - (x + \Delta x) \sum_i \frac{h_i}{n_i \sqrt{f^2 + (1 - 1/n_i^2)(x + \Delta x)^2 + (y + \Delta y)^2}}$$

$$Y^* = - (y + \Delta y) \sum_i \frac{h_i}{n_i \sqrt{f^2 + (1 - 1/n_i^2)((x + \Delta x)^2 + (y + \Delta y)^2)}}.$$

Track direction will be given by $X^* - X$ and $Y^* - Y$, so that

$$\begin{aligned} \Delta X_L = - \Delta x_L \sum_i \frac{h_i}{n_i \sqrt{f_L^2 + (1 - 1/n_i^2)(x_L^2 + y_L^2)}} + \\ x_L \sum_i \frac{h_i (1 - 1/n_i^2) (x_L \Delta x_L + y_L \Delta y_L)}{n_i (f_L^2 + (1 - 1/n_i^2)(x_L^2 + y_L^2))^{3/2}} \end{aligned}$$

$$\Delta Y_L = - \Delta y_L \sum_i \frac{h_i}{n_i \sqrt{f_L^2 + (1 - 1/n_i^2)(x_L^2 + y_L^2)}} + \quad (A \ V-15)$$

$$y_L \sum_i \frac{h_i (1 - 1/n_i^2) (x_L \Delta x_L + y_L \Delta y_L)}{n_i (f_L^2 + (1 - 1/n_i^2)(x_L^2 + y_L^2))^{3/2}}$$

$$\Delta X_R = - \Delta x_R \sum_i \frac{h_i}{n_i \sqrt{f_R^2 + (1 - 1/n_i^2)(x_R^2 + y_R^2)}}$$

$$\begin{aligned}
 & + x_R \sum_i \frac{h_i (1 - 1/n_i^2) (x_R \Delta x_R + y_R \Delta y_R)}{n_i (f_L^2 + (1 - 1/n_i^2) (x_R^2 + y_R^2))^{3/2}} \\
 \Delta Y_R = - \Delta y_R \sum_i & \frac{h_i}{n_i \sqrt{f_R^2 + (1 - 1/n_i^2) (x_R^2 + y_R^2)}} \\
 & + y_R \sum_i \frac{h_i (1 - 1/n_i^2) (x_R \Delta x_R + y_R \Delta y_R)}{n_i (f_L^2 + (1 - 1/n_i^2) (x_R^2 + y_R^2))^{3/2}} .
 \end{aligned}$$

Equations (A V-15) will obviously give the same straight line whether the Δx and Δy are infinitesimal or not , so one may relax that restriction on them and use the measured film direction cosines for Δx and Δy . Then ΔX and ΔY , although not the components of a unit vector, will nevertheless be components of a true direction vector in the $Z = \text{constant}$ plane.

(2) Chamber Track Direction

The chamber direction is given by the intersection of two planes containing the light rays and the $Z = \text{constant}$ track directions. First form the two plane normals by taking the cross product of light ray direction and $Z = \text{constant}$ direction. The perpendicular to both plane normals, or their cross product, will then lie in both planes and hence will be along their intersection. Care must be taken as to which direction is chosen along the intersection; the way this was done was to multiply the resultant triple

cross product by the sign of the dot product of itself with one of the $Z = \text{constant}$ track direction vectors. Then the result may be re-normalized to yield a unit vector.

c. Film Image Calculation

This calculation is the inverse of the chamber position calculation. Given x , y , and z in the chamber, one wants to find x_L , y_L , x_R , and y_R on the film. The direct solution of this problem is impossible, so an iterative process will be used.

The variable iterated will be $\tan \theta_0$, called m . Defining $h_0 = -z$, we may write (combining Eqs. (A V-1) and (A V-2))

$$R = \sum_i h_i n_0/n_i \frac{m}{\sqrt{1 + (1 - n_0^2/n_i^2)m^2}} \quad (\text{A V-16})$$

where the sum is taken over all indices of refraction including the chamber liquid, and R is the distance between the chamber bubble and the camera axis (the iteration is done separately for each view).

Splitting up the m -dependence of Eq. (A V-16), define

$$A \equiv h_{\text{air}} n_0$$

$$B(m) \equiv Z + \sum_{\substack{i \neq 0 \\ \text{or air}}} \frac{h_i n_0/n_i}{\sqrt{1 + m^2 (1 - n_0^2/n_i^2)}}$$

$$C \equiv n_0^2 - 1.$$

Then (A V-16) is rewritten in iterative form

$$m = \frac{R}{B(m) + \frac{A}{\sqrt{1 - m^2 C}}} \quad (\text{A V-17})$$

Since x , y , and z are known, R is given by

$$R = \sqrt{(\ell + x)^2 + y^2} \quad (\text{left view})$$

$$R = \sqrt{(x - \ell)^2 + y^2} \quad (\text{right view})$$

So, in Eq. (A V-17), R , A , and C are constants, and B is a slowly varying function of m . Expanding Eq. (A V-17),

$$A^2 m^2 = R^2 - 2 BRm + (B^2 - R^2 C)m^2 + 2 BRCm^3 - B^2 Cm^4$$

$$F(m) = B^2 cm^4 - 2 BRCm^3 + (A^2 - B^2 + R^2 c)m^2 + 2 BRm - R^2 = 0.$$

(A V-18)

Newton's method is used to find the root of $F(m) = 0$.

To get a starting value for m , (A V-17) is approximated by

$$m(0) = \frac{R}{Z + \sum_{i \neq 0} h_i n_0/n_i} \quad (\text{A V-19})$$

Having found a value of m that satisfies (A V-18), one may calculate $\tan \theta_{\text{air}}$ from (A V-2). Then, denoting left view $\tan \theta_{\text{air}}$ by m_L and right view $\tan \theta_{\text{air}}$ by m_R ,

$$x_L = \frac{-m_L f_L (\ell + x)}{R}$$

$$y_L = \frac{-m_L f_L y}{R}$$

$$x_R = \frac{m_{R,R}^f (\ell - x)}{R} \quad (\text{A V-20})$$

$$y_R = \frac{-m_{R,R}^f y}{R} .$$

2. Corresponding Point Generation

The optics calculations above assume that the measurements given in the two views correspond to the same physical bubble in the chamber. Often this can be the case. However, heavy bubble density on stopping particles or background bubbles against a minimum ionizing track can render recognition of corresponding bubbles impossible. In these cases one would like to measure points that approximately correspond, without being constrained to spend the time necessary to find exactly corresponding points. One would also like to use corresponding points where they can be found. The corresponding point generation procedure developed for this analysis program meets both of these needs.

Two properties of corresponding points are important to this procedure. One is that the Y values (see Fig. A V-2b) are nearly equal in the two views (in the no-refractive-index approximation they are equal). Thus it is possible for the analyzer, aided by track characteristics, to choose points that are close to corresponding if not actually corresponding (these are called pseudo-corresponding points). The other property is that, in a local region of the chamber at constant depth, the difference of X values and the difference of

Y values between the two views are slowly varying as the source bubble moves. In addition, one must remember that the track is represented by straight line segments joining the measured points, the analyzer choosing the points so that the representation is a good one.

Corresponding point generation is the responsibility of a subroutine called XYZPT. First, it calls optics subroutine XRAY, which provides the point locations where light rays from the measured film points first enter the chamber liquid (defined to be $Z = 0$; Fig. A V-2c), and the light ray direction vectors at those points. This gives in each view a description of the tracks in terms of line segments joining pseudo-corresponding $Z = 0$ points.

Now the calculation proceeds point by point. First, taking the pseudo-corresponding points as if they were corresponding, XYZPT calls subroutine LININT to find the corresponding "bubble" location in the chamber closest to the two light rays. XYZPT also checks the distance between these light rays; if it is small enough (the points really were corresponding) it has found the desired chamber point.

If correspondence was not sufficiently good, XYZPT calls subroutine XYZINV, the inverse optics calculation, to find the $Z = 0$ intersections of light rays joining this calculated "bubble" position to its film images. These two $Z = 0$ points are not on the track image in general, but they are corresponding points. Maintaining the X and Y separation of these two points so that they

will remain almost corresponding, XYZPT moves them in such a way as to obtain the best fit to the original points and the nearby track segments. The quantity minimized is the sum of the distance squared from the new point to the measured point in each view plus the distance squared from the new point to the track segments in each view. If the point under consideration is in an intermediate position along the track, the distances to both track segments are included. Here XYZPT has found almost corresponding points lying close to the track images. Next, these points are projected onto the track segments; in the case of intermediate points on the track, the segment closer to this new point is chosen. Now XYZPT has an improved pair of pseudo-corresponding points. Now XYZINV provides the light ray vector direction at these points. LININT finds the corresponding "bubble" location in the chamber, and XYZPT again checks the correspondence error. If correspondence is still not sufficiently good, this process is repeated again.

The correspondence requirement imposed in data analysis was that the distance between the two light rays be less than 0.01 cm, and up to twenty iterations were allowed to accomplish this. If the iteration limit was exceeded before the required accuracy was obtained, the last point obtained was used in the analysis, and an error message was printed out indicating the magnitude of the error. Whether satisfactory correspondence was obtained or not, the remaining correspondence error was included as part of the point measurement error. Serious correspondence errors did not occur often, and most

of the ones that did arise were cured by remeasurement.

For a derivation of the distance minimization equations, consider first Fig. A V-3a. The line through points 1 and 2 may be described by

$$x \cos \theta + y \sin \theta = \pm a \quad (\text{A V-21})$$

where a is the distance from the origin to the line. Passing through (x_1, y_1) and (x_2, y_2) , this line must also satisfy

$$x(y_2 - y_1) - y(x_2 - x_1) = x_1 y_2 - x_2 y_1. \quad (\text{A V-22})$$

Putting Eq. (A V-22) in the form of Eq. (A V-21), one has

$$X \frac{y_2 - y_1}{\sqrt{(x_2 - x_1)^2 + (y_2 - y_1)^2}} - Y \frac{x_2 - x_1}{\sqrt{(x_2 - x_1)^2 + (y_2 - y_1)^2}} = \frac{x_1 y_2 - x_2 y_1}{\sqrt{(x_2 - x_1)^2 + (y_2 - y_1)^2}}. \quad (\text{A V-23})$$

Comparing (A V-23) and (A V-21), one sees that

$$a^2 = \frac{(x_1 y_2 - x_2 y_1)^2}{(x_2 - x_1)^2 + (y_2 - y_1)^2}. \quad (\text{A V-24})$$

To obtain b , one imagines the coordinate system origin shifted to (x_3, y_3) , where (A V-24) immediately yields

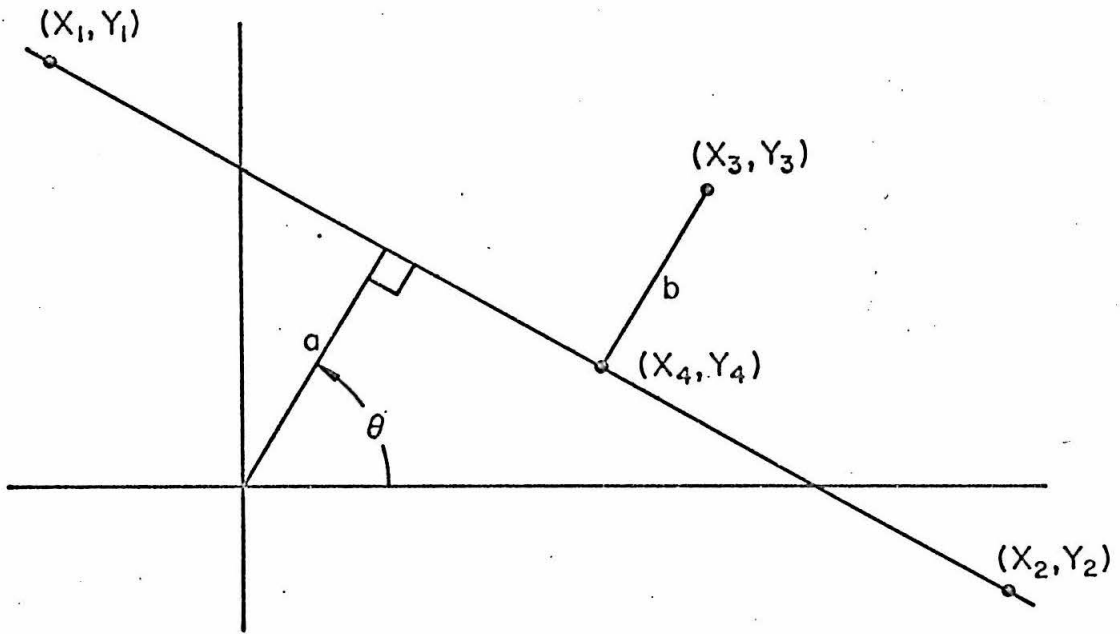
$$b^2 = \frac{[x_1 y_2 - x_2 y_1 + y_3(x_2 - x_1) - x_3(y_2 - y_1)]^2}{(x_2 - x_1)^2 + (y_2 - y_1)^2}. \quad (\text{A V-25})$$

Figure A V-3

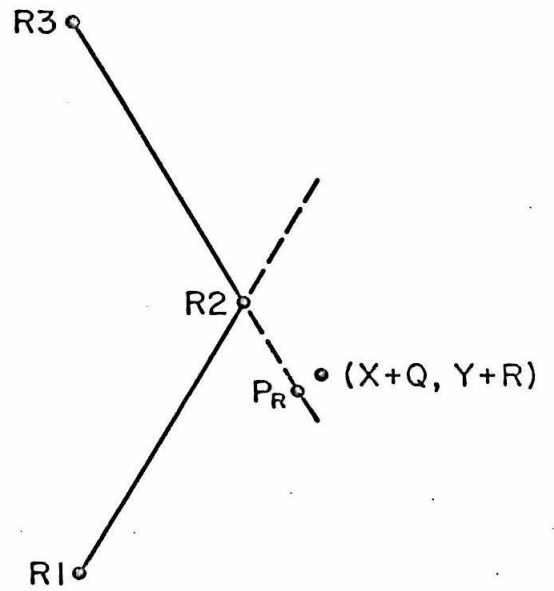
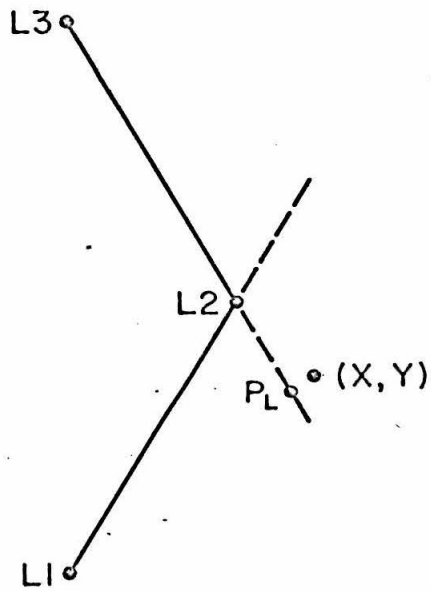
Track Segment Description Schematic

A. Line Description

B. Track Segment Notation



(A)



(B)

Figure A V-3

Point 4 at the foot of the perpendicular from point 3 to the line joining points 1 and 2 is found by examining the equation for the perpendicular, which is of the form

$$x \cos \theta' + y \sin \theta' = \pm b.$$

Since

$$\theta' = \theta \pm \frac{\pi}{2},$$

$$x \sin \theta - y \cos \theta = \pm b.$$

Again comparing (A V-21) and (A V-23),

$$x(x_2 - x_1) + y(y_2 - y_1) = \text{constant} = x_3(x_2 - x_1) + y_3(y_2 - y_1)$$

since (x_3, y_3) lies on the perpendicular. To be on this perpendicular, (x_4, y_4) must satisfy

$$x_4(x_2 - x_1) + y_4(y_2 - y_1) = x_3(x_2 - x_1) + y_3(y_2 - y_1).$$

To be on the original line, (x_4, y_4) must satisfy

$$x_4(y_2 - y_1) - y_4(x_2 - x_1) = x_1y_2 - x_2y_1.$$

Simultaneous solution yields

$$x_4 = \frac{x_3(x_2 - x_1)^2 + y_3(x_2 - x_1)(y_2 - y_1) + (y_2 - y_1)(x_1y_2 - x_2y_1)}{(x_2 - x_1)^2 + (y_2 - y_1)^2}$$

$$y_4 = \frac{y_3(y_2 - y_1)^2 + x_3(x_2 - x_1)(y_2 - y_1) - (x_2 - x_1)(x_1y_2 - x_2y_1)}{(x_2 - x_1)^2 + (y_2 - y_1)^2} \quad (\text{A V-26})$$

Now, referring to Fig. A V-3b, imagine that point 2 is to be iterated. Points L2 and R2 were input to LININT; from that chamber point XYZINV returned corresponding points (x', y') and $(x' + Q, y' + R)$ for left and right view light rays, respectively. The problem is to minimize the sum of the squares of the distances from (x, y) to L2, (x, y) to both line segments for left rays, $(x + Q, y + R)$ to R2, and $(x + Q, y + R)$ to both line segments for right rays.

Let D_{ij} denote the distance from corresponding point i to the line joining points ij and $i(j + 1)$. From Eq. (A V-25), we have

$$D_{ij}^2 = (y_i U_{ij} - x_i V_{ij} + W_{ij})^2$$

where

$$\begin{aligned} U_{ij} &= \frac{x_{ij+1} - x_{ij}}{\sqrt{(x_{ij+1} - x_{ij})^2 + (y_{ij+1} - y_{ij})^2}} \\ V_{ij} &= \frac{y_{ij+1} - y_{ij}}{\sqrt{(x_{ij+1} - x_{ij})^2 + (y_{ij+1} - y_{ij})^2}} \\ W_{ij} &= \frac{x_{ij} y_{ij+1} - x_{ij+1} y_{ij}}{\sqrt{(x_{ij+1} - x_{ij})^2 + (y_{ij+1} - y_{ij})^2}} \end{aligned} \quad (\text{A V-27})$$

The distance squared from corresponding point i to point ij being $C_{ij}^2 = (x_{ij} - x_i)^2 + (y_{ij} - y_i)^2$, and assigning weights H_L and H_R to the two view measurements, one finds the function F to be minimized,

$$F = \sum_{i=L}^R \sum_{j=1}^2 D_{ij}^2 + \sum_{i=L}^R C_{i2}^2 \quad (\text{A V-28})$$

Remembering that $X_R = X_L + Q$, $Y_R = Y_L + R$, one obtains for minimum F:

$$\begin{aligned}
 & X_L \sum_{i=L}^R H_i \left(1 + \sum_{j=1}^2 V_{ij}^2 \right) + Y_L \left(- \sum_{i=L}^R \sum_{j=1}^2 H_i U_{ij} V_{ij} \right) \\
 & = \sum_{i=L}^R \sum_{j=1}^2 H_i V_{ij} W_{ij} + \sum_{j=1}^2 H_R (R U_{Rj} - Q V_{Rj}) V_{Rj} + H_L X_{L2} + \\
 & \quad H_R (X_{R2} - Q) \\
 & X_L \left(- \sum_{i=L}^R \sum_{j=1}^2 H_i U_{ij} V_{ij} \right) + Y_L \sum_{i=L}^R H_i \left(1 + \sum_{j=1}^2 U_{ij}^2 \right) \\
 & = - \sum_{i=L}^R \sum_{j=1}^2 H_i U_{ij} W_{ij} - \sum_{j=1}^2 H_R (R U_{Rj} - Q V_{Rj}) U_{Rj} + H_L Y_{L2} \\
 & \quad + H_R (Y_{R2} - R) .
 \end{aligned}$$

(A V-29)

Simultaneous solution yields (x_L, y_L) and $(x_L + Q, y_L + R)$ as the almost corresponding points. These are substituted into Eqs. (A V-26) as points 3 to yield points 4, which are the improved pseudo-corresponding points. If the point under consideration had been a vertex or track end instead of an intermediate point, the $j = 1$ or 2 terms respectively in Eq. (A V-29) would have been omitted.

D. Event Synthesis

If one knows which particle is the proton, the kinematics of charged pi pair photoproduction is determined by knowledge of the

three-particle production directions for non-coplanar events. The track reconstruction procedure described above provides a measurement of the first observation point and direction for each track, and a procedure to be described below provides an initial guess at particle production direction (hidden inside the beam tube) that is somewhat improved over the observation direction. In addition, a very rough measurement of each particle's momentum is provided by using the points measured along the track^{*)} to compute the track multiple scattering. The range-energy relationship provides a good additional constraint on particle energy for any stopping particles (about 65 percent of the events have at least one stopping particle). Finally, the location and size of the gamma ray beam inside the target is known, and this is included as a constraint on the production origin location. Thus the degree of constraint varies from event to event, but in general there are at least three constraints on an event.

The likelihood function maximization procedure used in this program makes improvements on an initial guess at the relevant parameters, and taking some care in choosing this initial approximation was found to be highly desirable. The spatial location of the event origin and the production three-momenta of two particles were chosen as the independent variables of the problem. This choice of

*) Anywhere from three to six or seven points may be measured along a track, three being the most common number. On extremely short tracks, only two might be taken.

variables**) seemed to lead to the simplest formulation of the likelihood function and energy-momentum conservation.

Track direction at the observation point was taken to be the direction from the observation point to the second point on the track. Justification for this procedure rather than a direct angular measurement and criteria for choice of the second point are discussed in Appendix IV.

1. Starting Parameter Estimation

The initial origin location was found by tracing back into the beam tube the three track directions from the observation points and finding the point lying closest to these three lines. Distance from the three lines was weighted according to the observation point measurement error, the direction measurement error, and the angular error that could have been introduced by multiple scattering in the freon hidden by the beam tube and in the steel beam tube itself. Multiple scattering estimates were based on the observed track multiple scattering, and the hidden distances were calculated assuming the particle observation direction. No attempt was made here to constrain this origin to the known beam location.

Following the origin choice, an improved production direction was calculated for each particle. The direction chosen was the most

**) This scheme may be extended to photoproduction of more than three particles: for production of N particles of known mass, one may use the event origin and the momenta of $N-1$ particles.

likely one for the particle to have left the estimated origin position, undergone multiple scattering in the steel beam tube and hidden freon, and appeared at the first observed point going in the observed direction. The multiple scattering parameters used were the same ones used in the origin calculation. At the conclusion of the production direction calculation, the distances of hydrogen, steel and hidden freon traversed by each particle were recalculated on the basis of the new trajectories.

Using the improved hidden distances, the observed track lengths, and the assumed particle identifications, the production momenta of all particles were calculated using the range-energy relationship under the assumption that the particles actually stopped at the last observed points in the chamber. For stopping particles this provided a good measurement of the production momentum; for non-stopping particles it provided a lower limit on the magnitude of the particle momentum. A value of momentum for each track was also calculated using the multiple scattering measurement and particle identification. This value was assumed to hold at the mid-point of the observed region of the track, and the range-energy relationship was again applied to obtain the production momentum estimate, allowing for energy loss in hidden and observed regions. Because of the large errors involved (typically 30 percent), the multiple scattering momentum measurement was mostly useful in obtaining initial momentum estimates, although it did provide a weak constraint in the likelihood function. The treatment of multiple scattering and the range-

energy relationship are described in Appendix VII.

The final step of the event set-up procedure was to calculate the actual particle production momenta. The two particles having the most accurate measurements of the magnitudes of their momenta were chosen, and their three-momenta calculated from these momentum magnitudes and their calculated production directions. Then energy-momentum conservation was applied to calculate the vector momentum of the third particle, and this direction compared to its calculated production direction. If an approximate chi square based on the angular discrepancy and the probable error in the direction measurement was less than 100, the approximation was considered satisfactory. If not, the magnitudes of the momenta of the two given particles were changed separately in steps of 0.25 times the probable error in the momentum measurement and the procedure was tried again. A limited set of these changes was allowed such that the particle momenta could change by about a factor of three times the measurement error; if none of these trials proved satisfactory, that fact was recorded, and the set of numbers giving the lowest "chi square" was used anyhow. Analysis was abandoned at this point only if none of the combinations tried would conserve energy and momentum. Such an elaborate initializer was used since the likelihood function maximization procedure used could get into trouble if it was given a set of particle momenta that did not conserve energy and momentum, or if a particle production direction was grossly different from the observed direction.

2. Likelihood Function Maximization

The maximum likelihood method^{32,33)} was employed in obtaining optimized values for the parameters characterizing an event since the event configuration was overdetermined. Actually the negative logarithm of the likelihood function was minimized, the technique used being the variable metric method of minimization by W.C. Davidon³⁴⁾.

A few changes were made in the logic of the program (called MIN) as it was obtained from Argonne National Laboratory. Aside from input and output changes, they were principally changes directed toward continuing minimization where the original version would have given up. If the program found an answer but the chi square was not low enough, the required accuracy was doubled and the program continued operating. If a divide check or overflow condition was encountered, a random step in the parameters was taken and operation resumed. After a satisfactory chi square was obtained on an event, a small random step could be taken to obtain better information about the error matrix. To save computer time the combined number of the above procedures allowed was two per event, and two levels of iteration limiters allowed about seventy iterations per event.

The function minimized may be written as

$$W = Q + \sum_{i=1}^3 (R_i + S_i + T_i)$$

where the sum is taken over the three tracks. Term Q results from assuming a normally distributed beam shape about the

X axis^{*)}(which is defined to be the center of the beam). R_i and S_i relate the momentum of particle i to the range-energy and multiple scattering momentum measurements (if any) respectively; a normal distribution is assumed here also. T_i relates the observed particle position and direction to the event origin and production direction, allowing for multiple scattering in the hidden regions, as discussed in Appendix VIII. The actual functions used are shown below.

Define:

$\vec{X}(x,y,z)$: Particle production origin

\vec{P}_i : Particle i production momentum

\vec{a}_i : Particle i production unit vector

\vec{R}_i : Vector from origin to particle i observation point

\vec{U}_i : Observed particle i unit vector direction

t_{1i}, t_{2i} : Unseen particle i distances traversed through steel and freon, respectively

σ_0 : Standard deviation, origin distribution

σ_{Ri} : Standard deviation, range-energy momentum measurement

σ_{Si} : Standard deviation, multiple scattering momentum measurement

*) The actual distribution is unknown; with perfect collimation and a point gamma-ray source it would be uniform across a disk. The width of the normal distribution was taken larger than the expected disk size so as not to provide too severe a constraint on origins within the disk, while providing a constraint on origins for outside the disk resulting from track multiple scattering or invalid track combinations. Final event origin distribution was consistent with a normal distribution with a width about the expected disk size; effective widths in the y and z directions respectively were 0.06 and 0.09 cm, with the distribution function standard deviation having been 0.15 cm.

- σ_i : Standard deviation, observation direction measurement
 Δ_i : Standard deviation, observation point measurement
 P_{Ri}^* : Range-energy momentum measurement
 θ_{Si}^{*2} : Multiple scattering momentum measurement
 k_1^2, k_2^2 : Constants relating mean square multiple scattering per unit length to particle $(P\beta)^2$, in steel and freon, respectively
 ρ_i : $(k_2^2 t_{2i}^2 - k_1^2 t_{1i}^2)^2 + 4 k_1^2 k_2^2 t_{1i} t_{2i} (t_{1i} + t_{2i})^2 + 4(P\beta)_i^2 \sigma_i^2$
 $[k_1^2 (t_{1i} + t_{2i})^3 + t_{2i}^3 (k_2^2 - k_1^2)] + 4(P\beta)_i^2 \Delta_j^2$
 $[3 k_1^2 t_{ij} + 3 k_2^2 t_{2j}] + 12(P\beta)_j^4 \Delta_j^2 \sigma_j^2$.

Then

$$Q = \frac{1}{2\sigma_0^2} (y^2 + z^2)$$

$$R_i = \frac{1}{2\sigma_{Ri}} (|\vec{P}_i| - P_{Ri}^*)^2$$

$$S_i = \frac{(\theta_{Si}^2 - \theta_{Si}^{*2})^2}{2\sigma_{Si}^2 \left(\frac{3}{4} \frac{\theta_{Si}^2}{\theta_{Si}^{*2}} + \frac{1}{4} \frac{\theta_{Si}^4}{\theta_{Si}^{*4}} \right)}, \quad \theta_{Si}^2 = \frac{k_2^2}{(P\beta)_i^2}$$

$$\begin{aligned}
 T_i = 4 \frac{(P\beta)_i^2}{\rho_i} & \left\{ 3[\vec{R}_i \cdot \vec{R}_i - (\vec{a}_i \cdot \vec{R}_i)|\vec{a}_i \cdot \vec{R}_i|][k_1^2 t_{1i} + k_2^2 t_{2i} + \sigma_1^2 (P\beta)_i^2] \right. \\
 & - 3[\vec{u}_i \cdot \vec{R}_i - (\vec{a}_i \cdot \vec{u}_i)(\vec{a}_i \cdot \vec{R}_i)][k_1^2 (t_{1i} + t_{2i})^2 + t_{2i}^2 (k_2^2 - k_1^2)] \\
 & \left. + [1 - (\vec{a}_i \cdot \vec{u}_i)|\vec{a}_i \cdot \vec{u}_i|][k_1^2 (t_{1i} + t_{2i})^3 + t_{2i}^3 (k_2^2 - k_1^2)] + 3\Delta_j^2 (P\beta)_j^2 \right\} \\
 & + \ln \left(\frac{\rho_i}{(P\beta)_i^4} \right).
 \end{aligned}$$

The absolute value signs were inserted into the expression for T_i so that the function would continue to rise as \vec{a}_i became anti-parallel to \vec{R} and \vec{u} ; otherwise the small angle approximation inherent in the multiple scattering derivation (Appendix VIII) could have led to spurious solutions in the anti-parallel case.

Terms Q and R_i clearly represent normal distributions. S_i is a modification of a normal distribution as discussed in Appendix VII. If one defines $T_i' \equiv T_i - \ln (\rho_i / (P\beta)_i^4)$, T_i' can be shown to represent a normal distribution^{*)}. The logarithmic term is a normalization term slowly varying in the region of the solution, so $W' = Q + \sum_{i=1}^3 (R_i + S_i + T_i')$ should characterize the function W well in the region of the solution. Since for normal distributions, chi square is given by $-2 \times \ln$ (likelihood function), $2W'$ was used as a figure of merit for hypotheses obtained from the minimization procedure, and was treated as χ^2 .

To calculate the number of degrees of freedom, use was made of the fact that the number of degrees of freedom is given by the expectation value of χ^2 47). Q contributes two, each R_i and S_i term one, and each T_i term four degrees of freedom. Where there is no range-energy or multiple scattering momentum measurement for a particle, the corresponding term was simply omitted.

*) From the derivation (Appendix VIII), T_i' is seen to be a composite of two two-dimensional projections of the scattering, each of the form $a\theta^2 + b\theta y + cy^2$. This quadratic form may easily be transformed to the form $a'\theta'^2 + b'y'^2$, by a linear transformation. Since

(footnote continued on following page)

3. Alternate Hypotheses

For each event analyzed, several hypotheses were tried. Since particle identification might have been open to question, for every configuration of three tracks all three possible particle identification hypotheses were separately calculated. In cases where more than three tracks came close to a given origin and were analyzed as part of an event, the computer tried all possible combinations of three particles. The program could reset a non-stopping particle to stopping if its momentum came down to the range-energy momentum value for the observed track length. In the absence of particle stopping restrictions, there are in general two events kinematical solutions consistent with a given set of particle production directions. After one solution had been found, the other solution was attempted by allowing minimization to proceed after being given the same set of directions with momenta corresponding to the other solution. Finally, if an event failed to produce any hypotheses with sufficiently good χ^2 , all stopping restrictions were removed and the event tried again, in case a particle had been indicated as stopping when it should not have been.

The program also contained provision for forcing particle or stopping identification on a track to prevent the computer's options and save computer time. In particular, backwards-going particles

(Footnote continuation from previous page

the first form represents a probability distribution in (θ, y) , the second form represents a probability distribution in (θ', y') . The second form is obviously normal, so T_i' may be considered normal in the appropriate orthogonal variables.

were usually forced to be pions, since a photoproduced proton may not go backward in the laboratory system.

4. Output

A summary of the relevant parameters of every acceptable hypothesis was printed, and also punched on cards for handling by programs working with parameter distributions. Events providing no acceptable hypotheses had their best hypothesis printed (though not punched) for checking purposes. All error conditions found during analysis were printed on a separate unit.

E. Accuracy and Efficiency

Any computer program as complicated as the event reconstruction program must be checked out in a variety of ways before it can be assumed to be working properly. In this section we present a brief summary of the testing performed, and some of the program characteristics learned from these tests.

Each of the major program components was tested individually before being connected with the others. Most of these tests were trivial, except for XYZPT. XYZPT and XYZINV were checked for self-consistency on corresponding points. Then XYZPT was tested, given points in each view corresponding to equal y-values on a line segment. Finally, XYZPT was given points on line segments corresponding to points differing by 0.4 cm, in the chamber. In each case, satisfactory agreement between the final point and the true line segment was obtained. Studies of individual iterations within XYZPT

showed that when given non-corresponding points on a line segment it converged toward a point on the segment.

For purposes of testing whether the reconstruction program would accept valid events and whether it was introducing any bias into the final event parameters, the program was used to analyze 99 generated pion pair events (event generation is described in Appendix IX). It soon became obvious that whenever the gamma energy came out higher than the correct (generated) value, in general so did the dipion and isobar masses. Thus, only the gamma energy was studied as an indicator of bias, and the results are shown in Table A V-1 (the six coplanar events with no stopping particles were not included in this analysis, in analogy to actual data handling). There appears to be no significant bias (the ++ to -- majority among stopping events is not believed to be statistically significant since the + and - numbers are so nearly equal). Among the 93 events there were 4 that claimed to have particles stopping or almost stopping, which would have been rejected upon recheck at the scanning table had they been real events. Interpretation of this fact is difficult, since with actual data an event that looked reasonable except for a stop change would have been remeasured, and had the change been due to measurement error rather than track multiple scattering in the hidden region of the beam tube, the event should have yielded a reasonable hypothesis. For 10 out of the 12 relevant tracks, the expected multiple scattering contribution to the effective angular measurement error considerably outweighed the point

Table A V-1

Gamma Energy Errors for Analyzed Generated Events

	---	--	-	0	+	++	+++
One or more stopping tracks	0	2	16	13	18	8	0
No stopping tracks	1	4	13	3	12	2	1
Total	1	6	29	16	30	10	1

Column Code:

- 0 : Essential agreement with generated value
- (+, -) : (Above, Below) generated value, but within 1 standard deviation
- (++, --) : (Above, Below) generated value, between 1 and 2.5 standard deviations
- (+++, ---) : (Above, Below) generated value, outside 2.5 standard deviations

measurement error contribution. Thus it was concluded that the stop changes were probably due to multiple scattering effects which would not be changed upon remeasurement, and therefore 4 ± 2 percent of all valid events could be expected to be lost by the reconstruction program. The stopping restriction was not dropped to gain back the 4 percent because the background increase would have been far greater. One might expect a parameter bias due to this effect since the lower energy events should be the ones having particles nearly stopping. Of the four generated events that failed, one had gamma energy below 600 MeV, two were in the range 600 - 900 MeV, and one was in the range 900 - 1200 MeV. Of the --- and +++ accepted events, one was in the range 600 - 900 MeV and one was in the range 900 - 1200 MeV. The dipion and isobar masses also do not show any clustering at low values; the distribution appears consistent with phase space, within the very limited statistics (the highest energy dipion was 651 MeV, the highest energy isobar 1475 MeV, invariant mass). Although the very highest energy regions made no contribution to these losses, the approximate agreement of these distributions with phase space for the small percentage of events lost leads us to conclude that no event parameter bias should result.

To test invalid event acceptance by the program, 340 background events were analyzed. The results of this test are discussed in Appendix VI.

Because there might be some trait of generated data that would be different from that of real data and cause a different program bias, 34 accepted real events that had stopping particles were re-run with the stopping restrictions removed. Random measurement errors and multiple scattering effects should cause half of the events to have higher energy and the other half to remain about the same (since going to lower energy would bring the particle that stops inside its stopping momentum value) if stopping and non-stopping events are biased the same. Of the 34 events, 16 had higher energy and 18 stayed about the same, which is consistent with the evidence from generated events that no bias is present.

As noted above, the effective beam width was about half the size of the constraint, but it was still felt to be conceivable that any origin constraint might have a biasing effect on event parameters. Analyzing 33 valid events with and without the origin constraint gave a completely negligible net bias in gamma energy due to the origin constraint.

To obtain some idea of the origin resolution width of the program, ten generated pion pair events were chosen for a displacement test. Each track in turn was displaced from its original position in a direction anti-parallel to the beam direction until the hypothesis provided by the program was no longer acceptable. This mean displacement was 1.1 cm. Only two of the thirty tracks had displacements exceeding 2 cm, which is statistically consistent with the mean value. Thus 2 cm was chosen as the origin resolution width in the generation of multiple origin background events described in

Appendix VI.

Average program execution time on the 7094 was 13 seconds for a three-prong event. A six-prong candidate has twenty times the number of three-track combinations, requiring almost twenty times the execution time. Considerable analysis expense could have been saved had the beam intensity per picture been a factor of two smaller (as suggested in Appendix VI for background reasons), with attendant drastic reduction in higher prong multiplicity occurrence.

No program is without its shortcomings, and this one had its share. It was necessary to analyze an event at least two or three times before one could conclude that it was not valid. Whether the earlier failures that sometimes occurred on valid events were the fault of the analysis or the program was never determined, but it is believed that they must share the blame. Another difficulty, apparently basic to the way MIN (the variable metric minimization program) works, was that occasionally an hypothesis would be accepted with parameter errors that were clearly much too small. At these times, the number of iterations required to reach the answer was also unusually low. We believe that erratic error values were caused by MIN accidentally bouncing in to the correct value without having time to modify the error matrix by sampling the terrain close by. Starting with smaller initial metric guesses and requiring MIN to take two random steps in the region of the solution helped somewhat. Even so, four of the events in the ++ and -- categories in Table A V-1 had ridiculously small errors, and their assignment to these cate-

gories was based on what the errors reasonably should have been.

Another source of abnormally low errors was related to our usage of MIN. If a track was close to stopping, the process of minimization might bring its momentum inside the stopping point. At that point the range-energy relationship term would be turned on. This had the effect of making the error matrix think it had a stopping particle, with the result that it suddenly got smaller, tending to trap that particle momentum in a stopping or almost-stopping condition. Various attempts to beat this problem by changing the shape of the range-energy function inside the stopping point were unsuccessful. The only approach that seemed to help (which we did not adopt, since there was no physical justification for it) was to give the function a slight slope as particle momenta neared the stopping point from above.

Program accuracy is fundamentally tied to errors made in measurement. For well-determined points (vertices of V's or ends of stopping particles) the x and y average measurement errors were each about 0.007 cm in the chamber; because of the narrow stereo angle, the Z error was about four times that. These values were used in angular measurement error evaluation since the intermediate track point location uncertainty is along track direction, which does not appreciably affect direction or total track length measurement. Errors due to lack of correspondence in point measurement were folded into these. Implicitly, there were the errors due to multiple scattering. Errors involved in range-energy and multiple scattering momentum determinations are discussed in Appendix VII. Parameter

errors were then computed for each event from the error matrix after minimization was completed. Table A V-2 presents a summary of some of the average parameter errors as a function of the number of stopping particles (coplanar non-stopping events are not included).

Table A V-2

Average Parameter Measurement Errors* for Valid Events

		Gamma Energy	Dipion Mass	Isobar Mass
Number of Stopping Particles	0	82.2	22.1	27.8
	1	47.7	16.6	17.6
	2	19.9	6.4	7.2
	3	2.4	0.6	1.3
Gamma Below 900 MeV		36.7	12.5	14.7
Energy 900 - 1200 MeV		80.8	22.7	27.3
Range Above 1200 MeV		93.9	28.0	27.0
Over-all average		54.3	16.7	19.2

*) Errors above are in MeV.

APPENDIX VI

BACKGROUND

There are two general classifications of background that may occur in an experiment: obscuring background, which makes detection of the desired process more difficult, and process background, which produces apparently valid examples of the process studied from invalid constituents. Both types were present in this experiment to some degree.

A. Visual Background

The primary obscuration in this experiment was visual, as may be seen from Figures 4 - 7. Each chamber picture contained hundreds of short electron tracks (usually a single bubble in length) resulting from low-energy gamma and neutron radiation interacting in the chamber freon. Despite numerous cleanliness precautions, the inevitable small amount of dirt (ground glass from former windows, etc.) managed to collect on the windows of the chamber, causing a small occluded area. The lucite lens system used to illuminate the chamber caused some light scattering at small angles, with the result that the major lens is visible in each picture. Although none of this background resembled the proton and pion tracks being sought, it made finding low bubble density tracks considerably more difficult, led to occasional confusion where tracks crossed, and rendered finding corresponding bubbles for measurement much harder.

The most annoying of these background sources was the myriad of

electron tracks. Considerable effort was expended in reducing this background, as is discussed in Appendix I. The amount of this background was related to the amount of beam being accelerated in the synchrotron, and especially the amount dumped out in the north beam area (the one used in this experiment). Further reduction of this background would undoubtedly have made scanning and analysis more efficient had it been feasible. Beam intensity per picture was kept as high as seemed reasonable for economy in picture taking, processing, and scanning, and because no-one was certain how long the chamber would last and how long the delicate line-up would stay. Improvement in the general electron background would not have allowed more beam intensity per pulse, since the major source of analysis background already came from coincidence of nuclear events, as discussed below.

B. Analysis Background

Analysis background resulted from three particle tracks (not originating from a single pion pair production) occurring in such a configuration as to cause the event reconstruction computer program (described in Appendix V) to produce a satisfactory fit to a pion pair production hypothesis. This source of background was studied by using the Monte Carlo event generation program described in Appendix IX to generate events in various configurations, which were then fed into the event reconstruction program and treated in the same fashion as actual data^{*)}.

This type of background may be classified according to the

*) Computer output processing is described in Appendix IV, Section F.

number of distinct event origins that contributed tracks to the pseudo-event. Accordingly, several types of background event configurations were generated. Single origin contributions were studied by generating 10 six-prong events, each of which consisted of two pions pair productions at the same origin location, and by generating 20 four-prong events, equivalent to three pion photoproduction but with all particles considered charged. To evaluate the double origin contributions, 170 events consisting of a pion pair production with one track unseen joined by a single pion production with its origin within 2 cm^{**) of the pion pair's origin were generated. The triple origin contributions were represented by 120 events consisting of pion pair production with two tracks unseen, and two single pion productions, each having its origin within 2 cm of that of the pion pair event. In the single pion productions above, at least one prong was required to be seen, though if both were in the visible region of the chamber they were both included as being charged. Single pion generation was roughly based on experimental cross-sections with the bremsstrahlung spectrum folded in; double and triple pion production were taken to be phase-space-distributed, taking into account the bremsstrahlung spectrum (see Appendix IX).}

**) A track displacement procedure on generated pion pair events yielded an average origin resolution of 1.1 cm as described in Appendix V. Since 93 percent of all successful accidental hypotheses should then occur within an origin resolution of 2.0 cm, this resolution width was chosen in the generation of the single pion events.

Results from analysis of the 340 background events are shown in Table A VI-1. In the column labelled configuration are shown the particle configurations as they are generated; those coming from the same origin are written together, those from different origins being separated by + signs. Several interesting conclusions may be drawn from this data regarding particle identification:

(1) Out of 268 three-pion combinations generated in all configurations, none were accepted. Thus it appears that the combination of momentum conservation, range-energy restrictions, and particle identification based on bubble density in regions of confident identification render it extremely unlikely that a pion will be called a proton in a pion pair event hypothesis.

(2) In double and triple origin events, $2P + \pi$ acceptance is slightly greater than $2\pi + P$ acceptance, though this comparison is of dubious statistical significance. A probable explanation of such an effect (if real) may be found in the fact that six out of the twelve identification-changing events observed accomplished this feat by having a stopping proton so short (less than 1 cm) that positive identification is impossible, and these tracks were then called stopping pions. A short stopping pion could have suffered considerable multiple scattering in the hidden regions of the beam tube, with the result that its angular fit to the event origin is much less critical. The greater $2P + \pi$ acceptance would simply be due to the fact that there are more short stopping protons than pions resulting from pion photo-production in this energy range.

TABLE A VI-1

Background Event Acceptance Summary

<u>Run</u>	<u>Configuration</u>	<u>Possibilities</u>	<u>Accepted Events</u>	<u>Configuration Acceptance %</u>
6-prong,	$P\pi\pi$	40	2	5.0 ± 3.5
single origin	$P\pi\pi$	100	6	6.0 ± 2.5
	$\pi\pi\pi$	40	0	0.0
3 π ,	$P\pi\pi$	60	8	13.3 ± 4.7
single origin	$\pi\pi\pi$	20	0	0.0
Double origin,	$P\pi + P$	37	2	5.4 ± 3.8
two tracks from	$P\pi + \pi$	70	1	1.4 ± 1.4
pi pair	$\pi\pi + P$	43	2	4.7 ± 3.3
	$\pi\pi + \pi$	98	0	0.0
Triple origin	$P + P + \pi$	29	1	3.4 ± 3.4
	$P + \pi + \pi$	103	2	1.9 ± 1.3
	$\pi + \pi + \pi$	110	0	0.0
Double and triple,	$P\pi + P$	91	7	7.7 ± 2.9
two tracks from	$P\pi + \pi$	317	14	4.4 ± 1.2
single π				

Quoted errors are based on Poisson statistics

(3) Of even more dubious significance is the indication that this identification-changing acceptance enhancement may not be present in single origin events. One might expect this to be the case, since particle identification should make the identification-changing acceptance smaller, and there is not much to be gained in single origin events from the ability to fit a wide latitude of origin locations.

(4) Within statistics, the ratio of the identification-changing acceptance to the unchanged acceptance is roughly the same for all three categories of multiple origin events.

In all the events generated, no triple proton combinations were observed. Since the background contribution from such combinations should be quite small, it was estimated from the other data rather than explicitly generated^{*)}.

In the 6-prong event generation, although eight acceptable configurations occurred out of 140 possibilities (ignoring the 40 triple pions), in every event the hypotheses corresponding to the

*) The triple proton combination can only occur in triple origin events. Let A_{3p} , $A_{2p,\pi}$, and $A_{p,2\pi}$ represent the triple origin acceptances for the configurations indicated in the subscripts, and assuming $A_{2p,\pi} = K A_{p,2\pi}$ and $A_{3p} = K A_{2p,\pi}$, one obtains $K = 1.8$ and $A_{3p} = 6.1$ percent. Assuming that the same value of K also holds in the equivalent relationship for the two origin events, one obtains $K = 1.8$ and $A_{3p} = 6.2$ percent. Since half the identification changes are due to short stopping tracks, one quarter of these triple proton events will have both pseudo-pions short stopping tracks. Investigation of the resulting kinematics shows that only dipion masses between 280 and 310 MeV will occur, and only in those between 280 and 290 with incoming gamma energy (into $\gamma + p \rightarrow p + \pi^0$) greater than 390 MeV will the third proton be non-stopping. Since the kinematic constraints are so tight and the available phase space so small, these double-short events should not contribute to the background. Thus, $A_{3p} = 4.6 \pm 4.6$ percent will be used.

generated events were better. Thus it is concluded that the acceptance for background configurations where all three prongs of the valid event are seen is 0.0 ± 0.4 percent for two-origin configurations and 0.0 ± 0.3 percent for three-origin configurations. Since these quantities are considerable smaller than those for other competing processes, contribution of pi pair events to background will only be considered in cases where at least one prong of the π pair event is unseen.

Chamber detection efficiencies for single and double pion photoproduction are shown in Table A VI-2. The pion pair efficiencies were calculated based on 1000 generated events, which were than tested for visible prong distributions. Single pion efficiencies were calculated from the single pion events generated for the background studies. Since triple pion photoproduction produces the same prongs as pion pairs, only with slightly reduced energies, the triple pion efficiency was assumed equal to the double pion one.

Table A VI-3 shows the average yield per cm of target for the major processes contributing to the background. This yield was defined to be

$$Y = \int_{\text{threshold}}^{E_0} n \sigma(k) \bar{\epsilon} Q B(k, E_0) \frac{dk}{k}$$

where

$$n = \text{Nuclei/cc in target} = 2.41 \times 10^{21}$$

$\bar{\epsilon}$ = Average chamber detection efficiency for the process in question

$$Q = \text{Equivalent quanta per picture} = 3.2 \times 10^5, \text{ average value}$$

Table A VI-2.

Chamber Detection Efficiency

<u>Event Type</u>	<u>Prong</u>	<u>Generated</u>	<u>Seen</u>	<u>Efficiency</u>
$\gamma + P \rightarrow P + \pi^+ + \pi^-$	P $\pi\pi$	1000	207	20.7 ± 1.4
	P π	1000	150	15.0 ± 1.2
	$\pi\pi$	1000	228	22.8 ± 1.5
	P	1000	14	1.4 ± 0.4
	π	1000	237	23.7 ± 1.5
$\gamma + P \rightarrow P + \pi^0$	P	637	218	34.3 ± 2.3
$\gamma + P \rightarrow n + \pi^+$	π	637	469	73.6 ± 3.4

Table A VI-3

Approximate Pion Photoproduction Yield

<u>Event Type</u>	<u>Yield^{*)}/cm</u>
$\gamma + P \rightarrow P + \pi^+ + \pi^-$	0.0523
$\gamma + P \rightarrow P + \pi^+ + \pi^- + n \pi^0$	0.00583
$\gamma + P \rightarrow P + \pi^0$	0.1010
$\gamma + P \rightarrow n + \pi^+$	0.1440

*) Yield given is yield per cm of target per unit average chamber efficiency per chamber pulse for the process.

B = Bremsstrahlung spectrum shape function

K = Incoming photon energy

E_0 = Bremsstrahlung end point energy

σ = Total cross section for process^{20,22,58,59}.

A small but significant fraction of the gammas resulting from π^0 production will convert in the hidden regions of the beam tube, producing electrons of sufficiently high energy that they resemble pions. An approximate value of 0.32 is obtained for this fraction in Section C of this Appendix. Background pion rates were then augmented to take this effect into account. Change in the background due to this effect was 1 percent of the total event rate.

With R denoting acceptable event (or pseudo-event) rate per cm of target, and Y and A process yield and acceptance respectively, rates are given by:

(1) Single origin event

$$R = \sum_{\text{processes}} Y_i A_i.$$

(2) Double origin events

$$R = \sum_{\text{processes}} Y_{2 \text{ prong}} (Y_{1 \text{ prong}} \cdot 4 \text{ cm}) A_{2 \text{ prong} + 1 \text{ prong}}.$$

(3) Triple origin events

$$R = \sum_{\text{processes}} Y_{1 \text{ prong}} (Y_{1 \text{ prong}} \cdot 4 \text{ cm}) (Y_{1 \text{ prong}} \cdot 4 \text{ cm}) A_{1 \text{ prong} + 1 \text{ prong} + 1 \text{ prong}}.$$

Combining the results of Tables A VI-1, A VI-2, and A VI-3, rates for the single and double pion production processes considered so far are

given in Table A VI-4.

A variety of processes remain that contribute negligibly to the background.

They are:

(1) $\gamma + P \rightarrow P + \pi^0$; one gamma from π^0 converting into an electron pair in the hidden region of the beam tube.

This process was ruled out by requiring that the pions have a minimal separation of 1.5° between origin production directions.

(2) $\gamma + P \rightarrow P + \pi^+ + \pi^-$; one pi unseen, one of the other tracks producing a knock-on electron looking like a pion.

This process was also ruled out by requiring that tracks have a minimal separation of 1.5° between origin production directions. This also applies to proton and pion from other sources.

(3) $\gamma + P \rightarrow P + \pi^0$; both gammas from π^0 converting in the hidden region of the beam tube.

Investigation of accepted events showed average pion steel and hidden freon traversal to be 0.28 and 1.30 cm, respectively, representing 0.23 radiation length. Using the electron recognizability criteria described in Section C below but remembering that it is only necessary that one electron from each pair look like a pion, one obtains a rate of 0.000004 events/cm for this process, which is negligible compared to the other background sources.

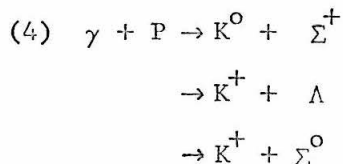


Table A VI-4

Event Acceptance Rates

		Rate (event/cm)
$\gamma + P \rightarrow P + \pi^+ + \pi^-$		0.01039 ± 0.00075
$\gamma + P \rightarrow P + \pi^+ + \pi^- + n \pi^0$		0.00016 ± 0.00006
Double Origin	{ 2 or 3 pion production, 2 prongs seen, plus single prong from 1, 2, or 3 pion production	0.00034 ± 0.00016
Triple Origin	{ Three single prongs from 1, 2, or 3 pion production	0.00055 ± 0.00028
Total Background		0.00105 ± 0.00033

Table A VI-5

Scanned Event Prong Distribution

Number of Prongs	Accepted Events		Rejected Events	
	Observed	Calculated	Observed	Calculated
3	337	337	1300	1375
4	280	284	572	579
5	128	127	192	168
6	66	58	66	53
7	22	18	13	15
8	2	4	1	3
TOTAL	835	828	2144	2193

Using median momenta of K^0 and Λ^0 , one finds that about 10 percent of K^0 's and Λ 's will decay via charged modes within 1.1 cm of the production origin (the average program resolution distance). With probably somewhat high total cross section estimates of 6 μb , 3 μb , and 2 μb , respectively, for the three reactions,^{49, 50, 51)} the regular two-pion chamber efficiency and the average single vertex acceptance, an approximate rate of 0.000005 events/cm is obtained for all three processes combined.

(5) $\gamma + P \rightarrow P + 4\pi$.

Negligible cross section below 1.5 BeV.²⁰⁾

C. Scanned Track Distributions

As a check on the assumptions made in deriving the analysis background rates above, one may use the same data to estimate various scanning distributions and compare them to the observed distributions.

Total number of events and scanning prong multiplicity distributions for valid and non-valid events are shown in Table A VI-5. The primary quantity yet needed for these calculations was the scanning origin resolution width, analogous to the 1.1 cm resolution width for analysis. This quantity (2.3 cm) was determined from the three-prong rate for good events, since this determination required the fewest assumptions and had the best statistical accuracy.

The calculation was carried out under the assumption that the contributing events obeyed a modified Poisson distribution in space, the modification being the fact that the effective resolution width decreases with increasing event multiplicity due to the necessity

that all contributing events lie within the resolution width of each other. This rate of decrease was calculated weighting all contributing events equally, and assuming a Gaussian acceptance probability distribution. Certainly a three-prong event demands a better fit than a single-prong event, but this refinement was not included since it was not clear how the weighting should be done.

A few comments can be made on these results. The scanning resolution width being more than twice the analysis resolution width helps validate the procedure used above to calculate the background rate, since all reasonable candidates for background contribution should have been included in the scanned data. Agreement between the observed and calculated prong distributions for good events is excellent. Agreement is good on the rejected event distribution; one would expect this prediction to be worse than the one for the accepted events because the higher multiplicity of processes required for the rejected events is more sensitive to the assumptions made in the calculation.

Another quantity amenable to calculation is the number of gammas from π^0 production that are converted to electron pairs in the hidden regions of the beam tube (gammas converting in the visible volume were not scanned for). A further restriction on these pairs is that the electrons must look like pions, since we were not interested in electromagnetic processes in this experiment. Since the proton chamber efficiency for $\gamma + P \rightarrow P + \pi^0$ matched that for $\gamma + P \rightarrow P + \pi^+ + \pi^-$ rather well, it was assumed that the π^0 decay

gamma efficiencies would also match the charged pion efficiencies (the two processes are kinematically the same except for the mass of the lighter particle).

Table A VI-6 gives a summary of the e pair and knock-on electron (koe) candidates found among the scanned data. Estimating the total number of protons to be 3149 and pions to be 7831 from the prong multiplicity data, one obtains a proton koe probability of 0.0022 per track. Since koe probability should be roughly proportional to $1/\beta^{2.52}$, we estimate a pion koe probability of 0.0007, which would indicate that of the 176 observed "electron pairs", 6 might be expected to be koe's from pions. Assuming the remaining 170 to be electron pairs, comparison with the accepted event rate indicates that the fraction Γ of converted electron pairs having both tracks high enough energy that they look like pions is 0.091. Feeling that this number might be a bit low, we did a rough calculation of the fraction of converting gammas from π^0 production that would give electrons each having an energy greater than 75 MeV (this seemed to be a reasonable discrimination point, based on bubble density and multiple scattering relationship for pions and electrons). The calculation included the bremsstrahlung distribution, cross section variation with energy, π^0 , gamma, and electron energy distributions, but ignored any chamber efficiency effects. The result was 0.128. One would expect the actual value to be a little lower than this, since the highest energy gammas would tend to go forward and be unseen. A similar calculation requiring that only one electron be above 75 MeV energy gave 0.455.

Table A VI-6

Possible Electronic Contribution in Scanning

<u>Contribution to Scanned Event</u>	<u>Accepted Events</u>	<u>Rejected Events</u>
Single "electron pair"	42	130
Two "electron pairs"	1	1
Both prongs of "electron pair" part of "accepted" event	28	---
One prong of "electron pair" part of "accepted" event	10	---
Proton with knock-on-electron possibility	3	4

Correcting this value by the ration of Γ observed to Γ calculated, we estimate the fraction of gammas giving at least one electron of energy above 75 MeV to be 0.32.

Calculation of the probability for simultaneous conversion of both gammas gave 0.0275; correction by the same Γ ratio yields 0.0195. Combining this result with the chamber efficiency for seen pion pair events gives an expected value of 1.2 double pairs in the experiment; 2 were observed. Using Γ , the single pion chamber efficiencies and the scanning origin resolution width, we would expect 5.1 single pair conversions associated with (but not part of) valid events; 5 were observed.

Although simultaneous conversion of both gammas represents a negligible background contribution as was shown in Section B, conversion of single gammas does produce a significant contribution to the pion background. Using the single electron acceptance factor of 0.32 since only one electron need resemble a pion to produce background, the gamma conversion contribution to $P\pi$ combinations gave a rate of 0.00368 and to single π a rate of 0.00821 events/cm. These rates were added to the rates from the processes discussed in Section B in computing the analysis background. Because of the uncertainty in the method of calculation of these figures, relative errors of 50 percent were assigned to them.

D. Background Error Evaluation

Since 9.1 percent of the event count rate is contributed by background, it is important to find what effect the background

will have on the gamma energy, dipion mass, and isobar distribution.

Figure A VI-1 shows the distribution of these quantities among the 24 generated background events that were deemed acceptable (events with two tracks from a single pion production were not included since they were not physically realizeable). It is clear that there is no tendency toward clustering around any one value, and within the limited statistics the distributions appear to match those for phase space production. There appeared to be no difference between the distributions for one-, two-, and three-origin events. Thus it was concluded that the background event parameter distributions would roughly match those for phase-space-generated events, and no special background correction was applied to those distributions.

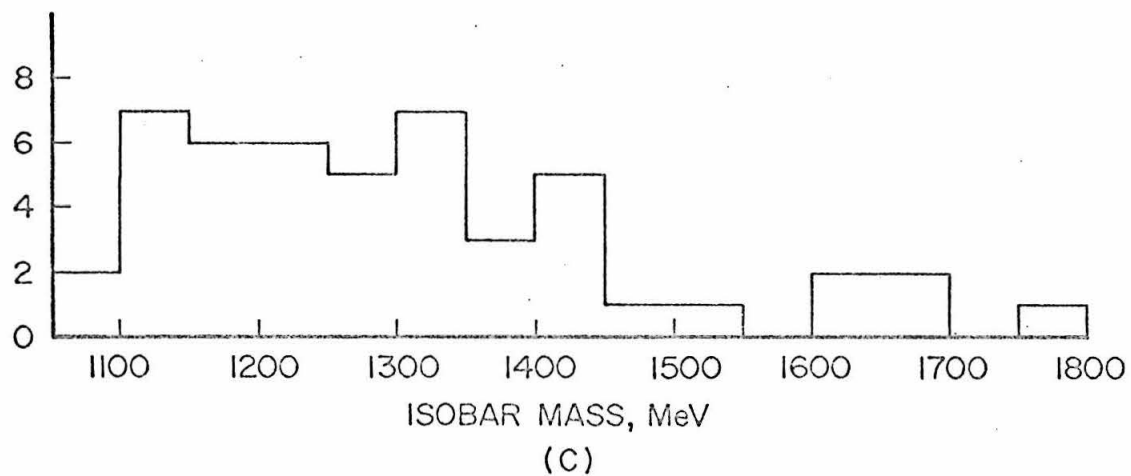
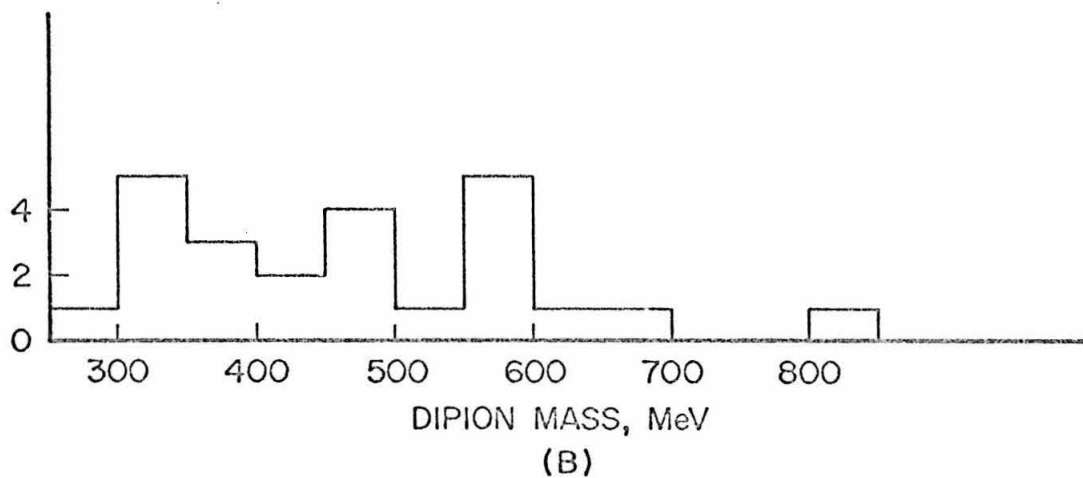
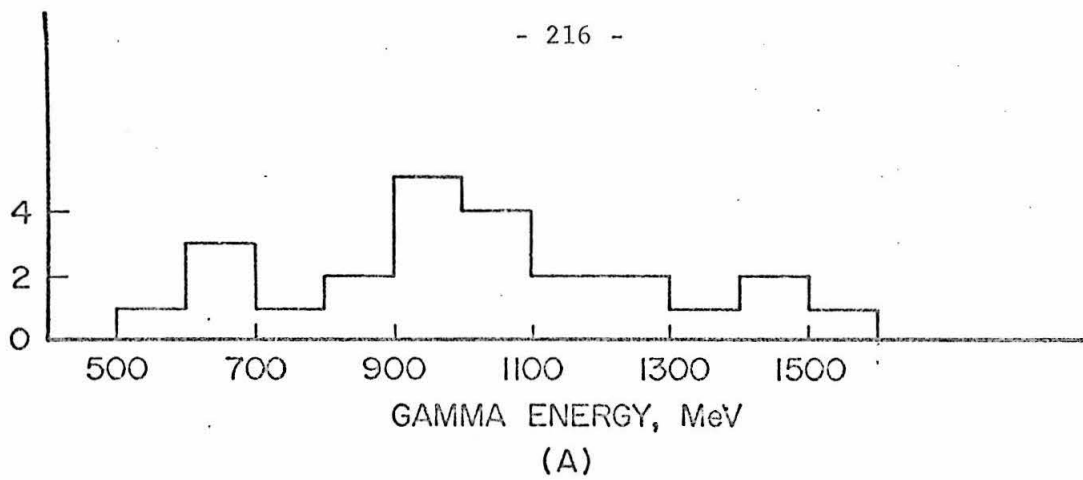
The increase in the background contribution as one moves toward higher contributing event origin multiplicity indicates that a higher beam intensity than the one used in this experiment would not have been desirable. In fact, about half our intensity would have roughly equalized the contributions from all three origin multiplicities, which may be an optimum condition for this type of experiment.

As is noted in Appendix IX, the manner in which the event generation program chose the track "measured" points may have caused the background estimate to be slightly high. Such an effect might have affected at most 5 of the single origin events, 1 of the double origin events, and none of the triple origin events accepted. Thus the background estimate may be high by at most ten percent.

Figure A VI-1

Parameter Distributions of 24 Generated Background Events

- A. Gamma Energy
- B. Dipion Mass
- C. Isobar Mass



APPENDIX VII

PARTICLE MOMENTUM MEASUREMENT

A. Range-Energy Relationship

In the event reconstruction computer programs described in Appendix V, the range-energy relationship was used to provide an accurate momentum measurement on any particle stopping in the bubble chamber, and to provide a lower limit on the magnitude of the momentum of a particle not stopping in the chamber. The purpose of this section is to discuss the approximation used and its errors.

For a homogeneous medium, the rate of energy loss for a heavy particle is given by⁵³⁾

$$K(\beta) = 4\pi N \frac{Z}{A} r_e^2 \frac{m_e C^2}{\beta^2} \left[\ln \frac{2m_e C^2 \beta^2}{(1 - \beta^2) I(z)} - \beta^2 \right] \quad (\text{A VII-1})$$

where K is Energy loss per gm cm^{-2} , N is Avogadro's number, Z and A are the charge and mass numbers of the material, r_e is the classical electron radius ($e^2/m_e C^2$), m_e the electron mass, β the particle velocity/ C , and $I(z)$ the average ionization potential of the atom.

Energy loss per unit length for molecules composed of several atoms is then given by

$$\frac{dE}{dx} = \frac{4\pi N r_e^2 m_e C^2 \rho}{\beta^2 \sum_i A_i} \left[\sum_i z_i \left(\ln \frac{2m_e C^2 \beta^2}{1 - \beta^2} - \beta^2 \right) - \sum_i z_i \ln I_i(Z) \right] \quad (\text{A VII-2})$$

where ρ is the liquid density (taken to be 1.485^{30}), since chamber operating conditions matched Alyea's), and the sum is taken over all

atoms in the molecule. Values used for the average ionization potential per unit charge, I/Z , for CF_3Br ^{54,55)} were 13.0 eV for carbon and fluorine, and 12.1 eV for bromine.

Equation (A VII-2) is not valid at very low energies (below 2 MeV for protons⁵⁴⁾). Since range behaves inversely as an average dE/dx , an approximation of the form

$$\text{Range} = \text{const.} \times \frac{A}{Z} \frac{1}{\ln 2m_e c^2 - \ln I - W} \quad (\text{A VII-3})$$

where $W = -\ln(\beta^2/1 - \beta^2) + \beta^2$ at some "average" value of β between 0 and 2 MeV for protons, was used to fit the 2 MeV proton range data⁵⁴⁾ for Al and Cu, and this value of W gave good agreement with the data for C. (A VII-3) was then used to find the range R_0 of a 2 MeV proton ($\beta_0 = 0.065$) in freon and yielded 0.0093 cm. The range-energy relationship was calculated by integrating (A VII-2) from β_0 to β and adding R_0 .

Chamber measurement error is of the order of R_0 , so errors in the approximation (A VII-3) were ignored. The density effect (due to screening of charged particle electric field by nearby atoms) was not included in (A VII-2); estimates of the effect⁵³⁾ indicated that it would be well below 1 percent for particles of energy low enough to allow stopping in the chamber.

Computer programs written by Donald Coyne and the author were used to find polynomial approximations to the range-energy relationship accurate to 0.1 percent in the region of interest, and this was the

form used in the event reconstruction program. Measurements were expressed in terms of momentum instead of energy as a matter of convenience in dealing with the momentum variables.

Additional error in the range-energy relationship application may be expected from five sources: (1) track multiple scattering, (2) straggling, (3) chamber point measurement error, (4) hidden distance traversal uncertainty, and (5) error in energy loss treatment in steel and hydrogen.

(1) Multiple Scattering

Chamber tracks are approximated as straight line segments, the segments being chords joining points that lie on the track. Multiple scattering causes the true path length to exceed the measured length. From Figure A VII-1, S is the true path length, T the measured chord, L the path projection on the initial direction, Y the perpendicular from the measured point to the original direction. The deviation of $R = S/T$ from 1 will show the amount of error introduced by multiple scattering. In this calculation particle velocity is assumed constant along the segment, and small angle approximations are used.

If $\text{Pr}(y)$ is the differential probability that the particle is at y within dy when it has gone an X-distance equal to L along its original direction, and if $\bar{S}(y)$ is the mean path length averaged over all possible paths,

$$R = \int_{-\infty}^{\infty} \frac{\bar{S}(y) \text{Pr}(y)}{\sqrt{L^2 + y^2}} dy \quad (\text{A VII-4})$$

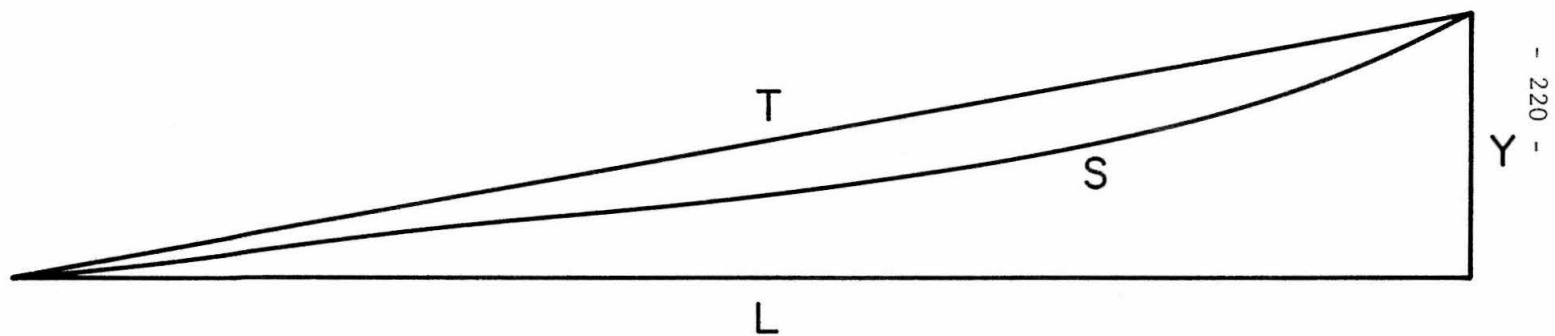


Figure A VII-1

Multiple Scattering Range Effect Schematic

Arc length (θ is angle from initial direction) is given by

$$\bar{S}(y) = \int_0^L \sqrt{1 + \theta^2(x)} \, dX,$$

again averaged over all possible paths. Let $P(Z, \theta, X)$ denote the differential probability of a particle being deviant a distance Z (within dZ) and an angle θ (with $d\theta$) from its original direction after going a distance along its initial direction equal to X . Let $P'(Z, X)$ represent $P(Z, \theta, X)$ integrated over all possible θ . Then R may be found from

$$R(L) = \int_{-\infty}^{\infty} \int_0^L \int_{-\infty}^{\infty} \int_{-\infty}^{\infty} \frac{\sqrt{1 + \theta^2}}{\sqrt{L^2 + Y^2}} P(Z, \theta, X) P'(Y - Z - \theta(L - X), L - X) d\theta dZ \, dx \, dy. \quad (\text{A VII-5})$$

Using the position and angular distributions given in Rossi⁵²⁾ and expanding the square roots, one obtains (to first order)

$$R(L) = 1 + \frac{\theta_s^2 L}{24} \quad (\text{A VII-6})$$

where θ_s^2 is the mean square scattering angle per unit length. This value of $R - 1$ is six times smaller than the one obtained by Alyea³⁰⁾; his value can be obtained if one compares S to L instead of T , and if one integrates arc length using the average scattering angle $\theta^2(x) = \theta_s^2 X$ instead of integrating over the θ probability distribution.

With the track segmentation procedure used in the analysis, a random sample of 300 tracks including the work of three analyzers

gave an average value of $\theta_s^2 L$ of 0.0081^{*)}; average of the pion sample alone was 0.0091. Thus, this effect was not considered large enough to be included in the range-energy momentum error evaluation.

(2) Straggling

Because of statistical fluctuation in energy loss, the r.m.s. fluctuation in range varies from 2.4 percent to 3 percent for pions and from 1 percent to 2 percent for protons stopping in the chamber⁵⁴⁾. Since the energy region of interest here is the straight-line region in Symon's plot⁵⁶⁾ of $f(E/mc^2)$ vs $\ln(E/mc^2)$ where f is a constant times the relative amount of straggling, a straight line was crudely fitted to that region of the plot and that relationship used to calculate the straggling contribution to the range-energy momentum error for each track.

(3) Chamber Point Measurement Error

The measurement error for the end point of the track was included in the range uncertainty. Errors in intermediate points would not contribute significantly because of the small angle between consecutive track segments. Errors in the first track point would

*) The largest value of θ_s^2 in this sample was 0.083 for a pion; even this case represented an error of only 0.3 percent. A few cases have been observed with $\theta_s^2 L$ ranging from 0.2 to 0.4; in every case investigated, the particle had suffered a single scattering, and the operator had erroneously measured the first observed point, the kink point, and the end of the track. Although this led to a misleading multiple scattering measurement and therefore a slightly worse χ^2 than otherwise might have been obtained, the chord approximation to track length was much better than $\theta_s^2 L$ would seem to indicate, so that the track range measurement was still a good one.

change the ratio of visible and hidden distances, but not affect the total distance.

(4) Hidden Distance Traversal Uncertainty

Usually the largest contribution to the range error came from the uncertainty in the precise path taken through the steel beam tube and the hidden freon by the particle. Because of the beam tube symmetry and the fact that a valid event origin is very near the center of the beam tube, the major contributor to this error is the uncertainty in the X component (beam direction) of the observation direction unit vector.

Considering the simplification shown in Figure A VII-2, let S be the distance from the observed point to the intersection point of the traced-back observed direction with the inner surface of the beam tube. It is easily shown that

$$\frac{dS}{d\alpha} = S \cot (\beta - \alpha). \quad (\text{A VII-7})$$

Since the two beam tube surfaces are nearly parallel, the hidden freon and steel distances should scale proportionately, so Eq. (A VII-7) was used to evaluate the direction uncertainty contribution to the range error, with S being the equivalent freon unseen path length, and $d\alpha$ the two-dimensional part of the observed direction uncertainty.

The total range uncertainty was taken as

$$\Delta R = \sqrt{(\Delta R_2)^2 + (\Delta R_3)^2 + (\Delta R_4)^2 + (0.002)^2} \quad (\text{A VII-8})$$

with ΔR_2 being the straggling range uncertainty, ΔR_3 the measurement

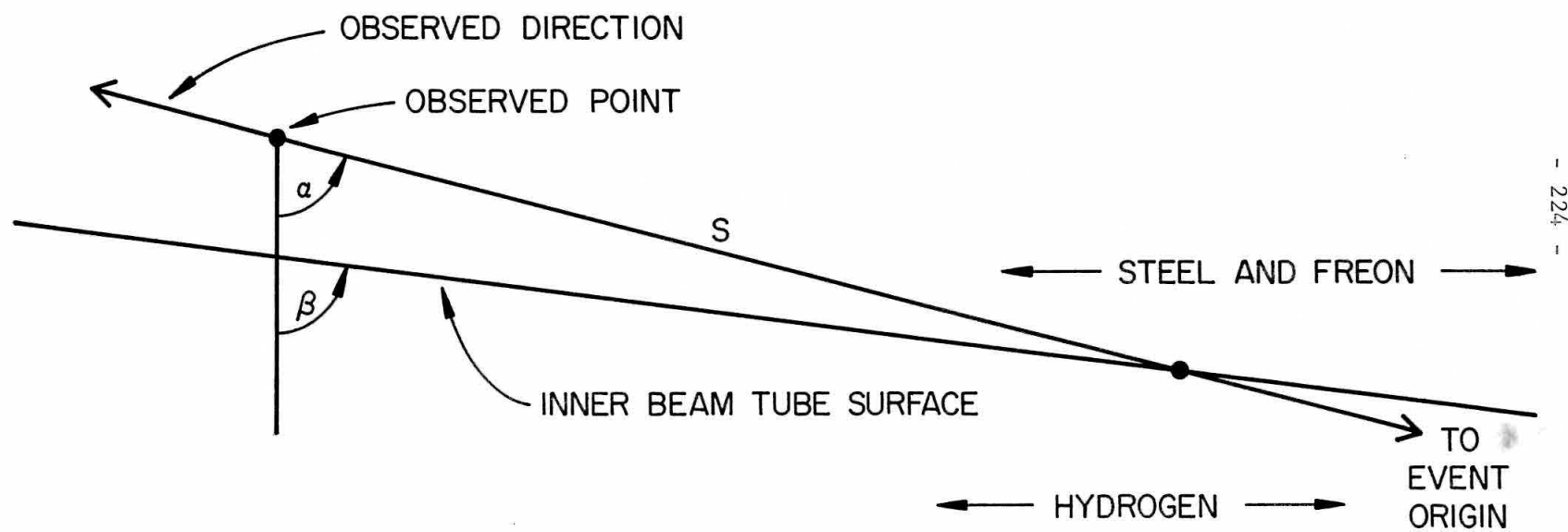


Figure A VII-2

Hidden Material Traversal Schematic

error of the last track point, ΔR_4 the direction uncertainty range error evaluated from Eq. (A VII-7), and the constant a reflection of the polynomial and theoretical uncertainties.

(5) Energy Loss Treatment for Steel and Hydrogen

The distance traversed by particles in steel was small, and the energy lost in the target hydrogen was small. Energy losses in both these media were taken into account by converting the distances in the media into "equivalent" distances in freon, and then treating the entire energy loss problem as if it had occurred in freon. An equivalent length is defined to be that distance which would produce the same amount of energy loss as that in the actual medium. Letting r_x denote the thickness in medium X and r_{freon} the equivalent distance in freon,

$$r_{\text{freon}} = r_x \frac{\left(\frac{dE}{dx}\right)_x}{\left(\frac{dE}{dx}\right)_{\text{freon}}} . \quad (\text{A VII-9})$$

This dE/dx ratio was calculated as a function of energy and approximated by polynomial forms good to better than 0.03 for steel and better than 0.001 for hydrogen. Since this ratio is a slowly varying function of energy for values of interest here, even a poor guess at particle energy will suffice as an argument for the ratio function. Errors introduced by these approximations in general would be quite small compared to the direction uncertainty range error, and were not included in the total range uncertainty.

B. Multiple Scattering Momentum Measurement

The mean square angle of scattering per unit length of a particle in the chamber is given by⁵²⁾

$$\theta_s^2 = \frac{K}{(P\beta)^2} \quad (\text{A VII-10})$$

with the constant K being evaluated in Appendix VIII for the chamber freon. P is particle momentum, β is velocity/C. Thus for particles of known mass, measurement of θ_s^2 provides a measurement of particle momentum.

Let $P(Z, \theta, X)$ denote the differential probability of a particle being deviant a distance Z (within dZ) and an angle θ (within d θ) from its original direction after going a distance along its initial direction equal to X. Let $P'(Z, X)$ represent $P(Z, \theta, X)$ integrated over all possible θ . Define $P^*(Z, Z^*)$ to be the differential probability that a measurement of the distance Z of a point on the track from the initial track direction yield Z^* . $P^*(\theta, \theta^*)$ denotes the corresponding expression for the initial direction measurement.

Now consider three points on a track characterized by Figure A VII-3, where the +X direction is taken to be the measured track direction at the first point and the origin the measured location of the first point. The likelihood function for obtaining measured values $\theta_0^* = 0$, $Y_0^* = 0$, Y_1^* , and Y_2^* is given by

$$\mathcal{L} = \int_{-\infty}^{\infty} \int_{-\infty}^{\infty} \int_{-\infty}^{\infty} \int_{-\infty}^{\infty} P(Y_1 - \theta_0 X_1, \theta_1 - \theta_0, X_1) P'(Y_2 - Y_1 - \theta_1 X_2, X_2) P^*(\theta_0, 0) P^*(Y_0, 0) \\ P^*(Y_1, Y_1^*) P^*(Y_2, Y_2^*) d\theta_0 d\theta_1 dy_0 dy_1 dy_2. \quad (\text{A VII-11})$$

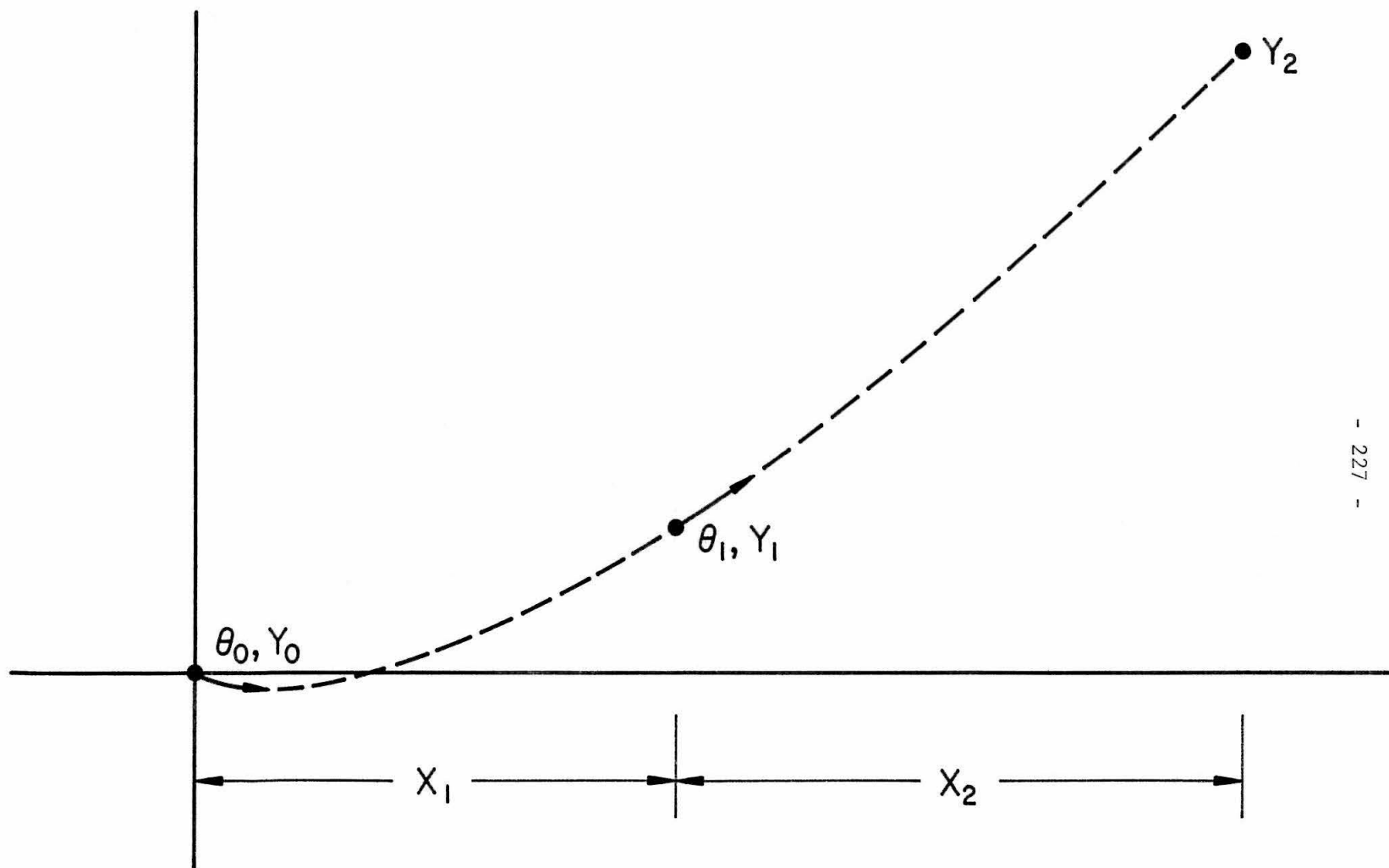


Figure A VII-3

Multiple Scattering Momentum Measurement Schematic

Using the multiple scattering probability distributions given in Rossi⁵²⁾ and normal distributions for the measurement error terms, and assuming large measurement error for the initial direction measurement and constant particle velocity in the region of measurement, one obtains

$$\mathcal{L} = \frac{\sqrt{3}}{2\pi X_0^{1/2} X_1 \sqrt{\frac{3}{X_2} + \frac{5}{X_1}} \sigma_2 \sqrt{\alpha_2}} e^{-\frac{X_2^2}{2\alpha_2 \sigma_2^2} \left(\frac{Y_1^*}{X_0} - \frac{Y_2^*}{X_2} \right)^2} \quad (\text{A VII-12})$$

where

$$\begin{aligned} X_0 &= \frac{X_1 X_2}{X_1 + X_2} \\ \alpha_0 &= 1 + \frac{\theta_s^2 (X_1 + X_2) X_1^2}{6\sigma_0^2} \\ \alpha_1 &= 1 + \frac{\alpha_0 \theta_s^2 (X_1 + X_2) X_0^2}{6(\alpha_0 - 1)\sigma_1^2} \\ \alpha_2 &= 1 + \frac{\alpha_1 \alpha_0 \theta_s^2 (X_1 + X_2) X_2^2}{6(\alpha_1 - 1)(\alpha_0 - 1)\sigma_2^2} \end{aligned}$$

and σ_0 , σ_1 , and σ_2 are the measurement errors associated with points y_0 , y_1 , and y_2 , respectively.

The maximum likelihood solution for θ_s^2 will be given by

$\frac{d\mathcal{L}}{d\theta_s^2} = 0$. This yields

$$\alpha_2 = \frac{X_2^2}{\sigma_2^2} \left(\frac{Y_1^*}{X_0} - \frac{Y_2^*}{X_2} \right)^2 \quad (\text{A VII-13})$$

Inherent in this derivation was the assumption that the error in the initial direction estimate was large. Thus one may choose the initial direction so that $Y_1^* = 0$ and obtain

$$\alpha_2 = \frac{Y_2^{*2}}{\sigma_2^2} \quad . \quad (\text{A VII-14})$$

The mean square scattering angle per unit length is given by

$$\theta_s^2 = \frac{6\sigma_0^2}{(X_1 + X_2)X_1^2} \left[\frac{X_1^2 \sigma_1^2}{X_0^2 \sigma_0^2} \left\{ \frac{X_2^2 \sigma_2^2}{X_2^2 \sigma_1^2} (\alpha_2 - 1) - 1 \right\} - 1 \right]. \quad (\text{A VII-15})$$

Note that Eq. (A VII-15) may give a negative value for θ_s^2 for sufficiently small Y_2^* ; such a case may be interpreted to mean that the measured "scattering" is attributable to the point measurement errors alone, with attendant loss of all statistical significance in the calculation of θ_s^2 .

For positive values of θ_s^2 , the error $\Delta\theta_s^2$ in θ_s^2 may be calculated by assuming the likelihood function to be Gaussian in the region of the solution, which yields)

$$\Delta\theta_s^2 = \left[- \frac{\partial^2 \ln \mathcal{L}(\theta_s^{2'})}{\partial \theta_s^{2'}} \right]^{-1/2} \theta_s^{2'} = \theta_s^2 = \frac{6\sqrt{2}\sigma_2^2}{X_2^2 (X_1 + X_2)} \alpha_2 \quad (\text{A VII-16})$$

When more than three points were measured on a track, the scattering was calculated for each consecutive group of three and averaged:

$$\theta_s^2 = \frac{\sum_i \theta_{si}^2 \frac{1}{(\Delta\theta_{si}^2)^2}}{\sum_i \frac{1}{(\Delta\theta_{si}^2)^2}}$$

(A VII-17)

$$\overline{\Delta\theta_s^2} = \left[\sum_i \frac{1}{(\Delta\theta_{si}^2)^2} \right]^{-1/2}.$$

Momentum may then be calculated by using Eq. (A VII-10). The measurement was assumed to yield the momentum corresponding to the mid-point of the observed region of the track, and the range-energy relationship was used to obtain the production momentum. Equation (A VII-10) was applied again to calculate the mean square angle of scattering per unit length, θ_s^{*2} , at the production point.

The error in θ_s^{*2} , $\Delta\theta_s^{*2}$, was taken to be $\overline{\Delta\theta_s^2}$. This larger error was chosen primarily because of the arbitrariness in the assignment of the momentum measurement to the mid-point of the observed region; it is just the case of a particle close to stopping where that assumption is worst that the error augmentation is largest.

To include this momentum measurement in the likelihood function by means of the normal term

$$\left[\frac{(\theta_s^2 - \theta_s^{*2})^2}{2(\Delta\theta_s^{*2})^2} \right]$$

is not correct since the parameter error is comparable to the parameter itself, and the term in the denominator should really be a function of θ_s^2 . For one measurement alone, the probability distribution for θ_s^{*2} approaches (at high energy):

$$P(\theta_s^{*2}) = \text{const.} \times \frac{1}{\theta_s \theta_s^*} e^{-\frac{\theta_s^{*2}}{2\theta_s^2}}. \quad (\text{A VII-18})$$

A good approximation to this form in the region of $\theta_s^2 = \theta_s^{*2}$ can be obtained by multiplying $(\Delta\theta_s^{*2})^2$ in the normal term by

$$\left(\frac{3}{4} \frac{\theta_s^2}{\theta_s^{*2}} + \frac{1}{4} \frac{\theta_s^4}{\theta_s^{*4}} \right);$$

this was then the form used in the likelihood function.

APPENDIX VIII

MULTIPLE SCATTERING

A. Single Medium Distribution

Rossi⁵²⁾ gives a position and direction probability distribution for multiple scattering in a single medium in terms of the mean square scattering angle per unit length, θ_s^2 . In order for that expression to be valid, it should be true that $X/X_0 \gg 46 A^{-2/3}$, where X_0 is the radiation length in the substance (11.5 cm in CF_3Br), A the atomic weight, and X the distance involved. Since the Br atom is responsible for the vast majority of the scattering, one may use its value of A (80) and the validity condition becomes $X/X_0 \gg 2$. This condition means that $\theta_s \sqrt{X}$ is much larger than the maximum angle of single scattering. For cases of interest here, X/X_0 is of the order of unity, implying that large single scatterings could occasionally affect the distribution. However, a large single scattering in the hidden regions would cause a particle to fail to line up with the event origin and the event would not have been found; and when a large single scattering occurs in the visible region of the chamber, the track is only analyzed up to the kink because of the possibility of an inelastic interaction at that point. Thus, tracks needing multiple scattering analysis should not contain large single scatterings and Rossi's distribution was used in the calculations.

For a homogeneous medium, θ_s^2 is given by⁵²⁾

$$\theta_s^2 = 16\pi N \frac{Z^2}{A} r_e^2 \rho \left(\frac{m_e c}{P\beta} \right)^2 \ln \left[196Z^{-1/3} \left(\frac{Z}{A} \right)^{1/6} \right] \quad (A \text{ VIII-1})$$

where N is Avogadro's number, Z and A the charge and mass numbers of the material, r_e the classical electron radius ($e^2/m_e C^2$), m_e the electron mass, β the particle velocity/ C , P the particle momentum, and ρ the material density. The validity criterion for Eq. (A VIII-1) is that⁵²⁾

$$280 A^{-1/3} \frac{m_e C}{P} < 1. \quad (\text{A VIII-2})$$

Again using $A = 80$, the case of a pion 0.1 cm from stopping in the freon gives 0.88 for the expression above. Any pion of interest is more energetic than that, and a proton is even further from the troublesome region, so Eq. (A VIII-1) can be used for all calculations here.

Extending Eq. (A VIII-1) to molecules composed of several atoms,

$$\theta_s^2 = \frac{1}{(P\beta)^2} \cdot 16\pi N R_e^2 (m_e C)^2 \frac{\rho}{\sum_i A_i} \sum_i Z_i^2 \ln \left[196 Z_i^{-1/3} \left(\frac{Z_i}{A_i} \right)^{1/6} \right] = \frac{k^2}{(P\beta)^2}, \quad (\text{A VIII-3})$$

where the sum is taken over all the atoms in the molecule.

Application of Eq. (A VIII-3) yields the following values for k^2 :

Freon (CF_3Br)	38.22
Steel (Stainless)	246.7
Hydrogen (50 atm. pressure)	0.01496

This formulation of multiple scattering theory cannot be expected to yield answers to better accuracy than about 5 percent. However,

it should suffice for a 30 percent momentum measurement or calculation of relative path likelihood in hidden regions.

B. Multiple Scattering in Two Media

The multiple scattering distributions discussed above are for scattering in a single medium. In order to treat particle multiple scattering in the steel and freon between the event origin and particle observation point, one needs the distribution for scattering in two media (scattering in the hydrogen is negligible and will be ignored). Angular and point measurement errors at the observation point are also included.

Let $P(Z, \theta, X)$ denote the differential probability of a particle being deviant a distance Z (within dZ) and an angle θ (within $d\theta$) from its original direction after going a distance along its initial direction equal to X in one medium. Define $P^*(\theta, \theta^*)$ to be the differential probability that a measurement of direction θ at the observation point yield θ^* , and $P'(Y_2, Y)$ the differential probability that a measurement of position Y_2 at the observation point yield Y . If $P(Z, \theta; X_1, X_2)$ is the two-medium differential probability distribution analogous to \mathbb{P} ,

$$\mathbb{P}(Y, \theta_0; X_1, X_2) = \iiint_{-\infty}^{\infty} P(Y_1, \theta_1, X_1) P(Y_2 - Y_1 - \theta_1 X_2, \theta_2 - \theta_1, X_2) P^*(\theta_2, \theta_0) P'(Y_2, Y) d\theta_2 d\theta_1 dy_1 dy_2 \quad (\text{A VIII-4})$$

where X_1 and X_2 are the thicknesses of the two media, y_1 and θ_1 the position and direction at the interface, y_2 and θ_2 the true position and direction at the exit from medium 2, and y and θ_0 the measured

position and direction there. The origin is taken to be the entrance point to medium 1 with the X axis aligned along the initial particle direction.

Using the single medium distribution function given in Rossi⁵²⁾, a normal distribution for the measurement errors, and assuming constant particle velocity in media 1 and 2, one obtains

$$P(y, \theta_0; X_1, X_2) \frac{\sqrt{3\alpha_2^2}}{\sqrt{2\pi} \sqrt{\rho\sigma}} e^{-\frac{1}{\rho} \left\{ 3y^2 \left[4\beta_2(\alpha_2^2 + \alpha_1^2) + \alpha_2^2 \right] - 12\beta_2\theta_0 y \right.}$$

$$\left. \left[(\alpha_2^2 + 2\alpha_1^2)X_2 + \alpha_1^2 X_1 \right] \right.}$$

$$\left. + 24\Delta^2\beta_2\theta_0^2 + 4\beta_2\theta_0^2 \left[(\alpha_2^2 + 3\alpha_1^2)X_2^2 + 3\alpha_1^2 X_1 X_2 + \alpha_1^2 X_1^2 \right] \right\}$$

(A VIII-5)

where

σ = Angular measurement error

Δ = Point measurement error

$\theta_{s1}^2, \theta_{s2}^2$ = Mean square scattering angle per unit length, media 1 and 2 respectively.

$$\alpha_1^2 = \theta_{s1}^2 X_1$$

$$\alpha_2^2 = \theta_{s2}^2 X_2$$

$$\beta_2 = \frac{\alpha_2^2}{8\sigma^2}$$

$$\rho = \beta_2 (\alpha_2^4 X_2^2 + 4\alpha_1^2 \alpha_2^2 X_2^2 + 6\alpha_1^2 \alpha_2^2 X_1 X_2 + 4\alpha_1^2 \alpha_2^2 X_1^2 + \alpha_1^4 X_1^2)$$

$$+ (\alpha_2^4 X_2^2 + 3\alpha_1^2 \alpha_2^2 X_2^2 + 3\alpha_1^2 \alpha_2^2 X_1 X_2 + \alpha_1^2 \alpha_2^2 X_1^2)$$

$$+ 6\Delta^2 \left[4\beta_2^2 (\alpha_2^2 + \alpha_1^2) + \alpha_2^2 \right].$$

Equation (A VIII-5) describes a two-dimensional projection of the scattering. The three-dimensional description may be obtained by also considering the XZ plane perpendicular to the XY plane. Then the distribution function becomes $P(y, \theta_y; X_1, X_2) P(Z, \theta_z; X_1, X_2)$. Its form is analogous to (A VIII-5) with $y^2 \rightarrow y^2 + Z^2$, $\theta_y \rightarrow y\theta_y + Z\theta_z$, $\theta_0^2 \rightarrow \theta_y^2 + \theta_z^2$.

Let \vec{a} denote the initial direction unit vector, \vec{U} the observed direction unit vector, and \vec{R} the vector from a point a distance X_0 along the particle direction before medium 1 to the particle observation point at the end of medium 2. In the notation of Eq. (A VIII-5) (invoking small angle approximations)

$\vec{a} = (1, 0, 0)$, $\vec{U} = (1, \theta_y, \theta_z)$, and $\vec{R} = (X_0 + X_1 + X_2, Y, Z)$. Since $(\vec{a} \times \vec{U}) = (0, -\theta_z, \theta_y)$ and $(\vec{a} \times \vec{R}) = (0, -Z, Y)$,

$$\theta_y^2 + \theta_z^2 = (\vec{a} \times \vec{U}) \cdot (\vec{a} \times \vec{U}) = 1 - (\vec{a} \cdot \vec{U})^2$$

$$Y\theta_y + Z\theta_z = (\vec{a} \times \vec{U}) \cdot (\vec{a} \times \vec{R}) = (\vec{U} \cdot \vec{R}) - (\vec{a} \cdot \vec{U})(\vec{a} \cdot \vec{R}) \quad (\text{A VIII-6})$$

$$Y^2 + Z^2 = (\vec{a} \times \vec{R}) \cdot (\vec{a} \times \vec{R}) = (\vec{R} \cdot \vec{R}) - (\vec{a} \cdot \vec{R})^2.$$

Defining β = particle velocity/C, P = particle momentum, σ = three-dimensional angular measurement error, $k_1^2 = \theta_{s1}^2 (P\beta)^2$, and $k_2^2 = \theta_{s2}^2 (P\beta)^2$, one obtains for the three dimensional scattering distribution function

$$\begin{aligned} \mathbb{P} = & \frac{6\sigma^2(\mathbb{P}\beta)^4}{\pi^2\rho'} e^{-\frac{4(\mathbb{P}\beta)^2}{\rho'}} \left\{ 3 \left[\vec{R} \cdot \vec{R} - (\vec{a} \cdot \vec{R})^2 \right] \left[k_1^2 X_1 + k_2^2 X_2 + \sigma^2 (\mathbb{P}\beta)^2 \right] \right. \\ & - 3 \left[\vec{U} \cdot \vec{R} - (\vec{a} \cdot \vec{U})(\vec{a} \cdot \vec{R}) \right] \left[k_1^2 (X_1 + X_2)^2 + X_2^2 (K_2^2 - k_1^2) \right] + \\ & \left. \left[1 - (\vec{a} \cdot \vec{U})^2 \right] \left[k_1^2 (X_1 + X_2)^3 + X_2^3 (K_2^2 - k_1^2) + 3\Delta^2 (\mathbb{P}\beta)^2 \right] \right\} \quad (\text{A VIII-7}) \end{aligned}$$

where

$$\begin{aligned} \rho' = & (k_2 X_2 + k_1 X_1)^4 + 4k_1 k_2 X_1 X_2 (k_1 - k_2) (k_2 X_2^2 - k_1 X_1^2) + 4\Delta^2 (\mathbb{P}\beta)^2 \\ & \left[3k_1^2 X_1 + 3k_2^2 X_2 \right] + 4\sigma^2 (\mathbb{P}\beta)^2 \left[k_1^2 (X_1 + X_2)^3 + X_2^3 (k_2^2 - k_1^2) \right] \\ & + 12 (\mathbb{P}\beta)^4 \Delta^2 \sigma^2. \end{aligned}$$

Equation (A VIII-7) is almost the term used in the likelihood function in the event reconstruction computer program; the small remaining change is discussed in Appendix V.

APPENDIX IX

EVENT GENERATION COMPUTER PROGRAM

A computer program was written for the IBM 7094 to generate events in a variety of configurations for two general purposes:

(A) testing the event reconstruction computer program, and (B) generation of events from specific models for comparison with the data. The purpose of this appendix is to summarize its capabilities and usage.

The parameters relevant to this experiment of a pion pair photoproduction event in the bubble chamber may be determined by specifying seven quantities. Two of these are independent of kinematics: the event origin location along the beam line (the finite width of the beam was ignored since it was so small), and the azimuthal orientation of the event about the beam line. The five model and kinematics dependent parameters may be chosen to be the incoming gamma ray energy, the invariant mass of one pair of particles (called the diparticle), the angle between the diparticle direction and the gamma direction in the over-all center-of-momentum (COM) system, and the two angles specifying the direction of one of the diparticle constituents in the diparticle COM system.

Figure A IX-1 shows a plot of the accepted event origin distribution along the beam line. In all event generation, origins were chosen to be uniformly randomly distributed between -13 and +7 cm in order to match the data. The azimuthal event orientation angle was also taken to be uniformly randomly distributed between 0 and 2π .

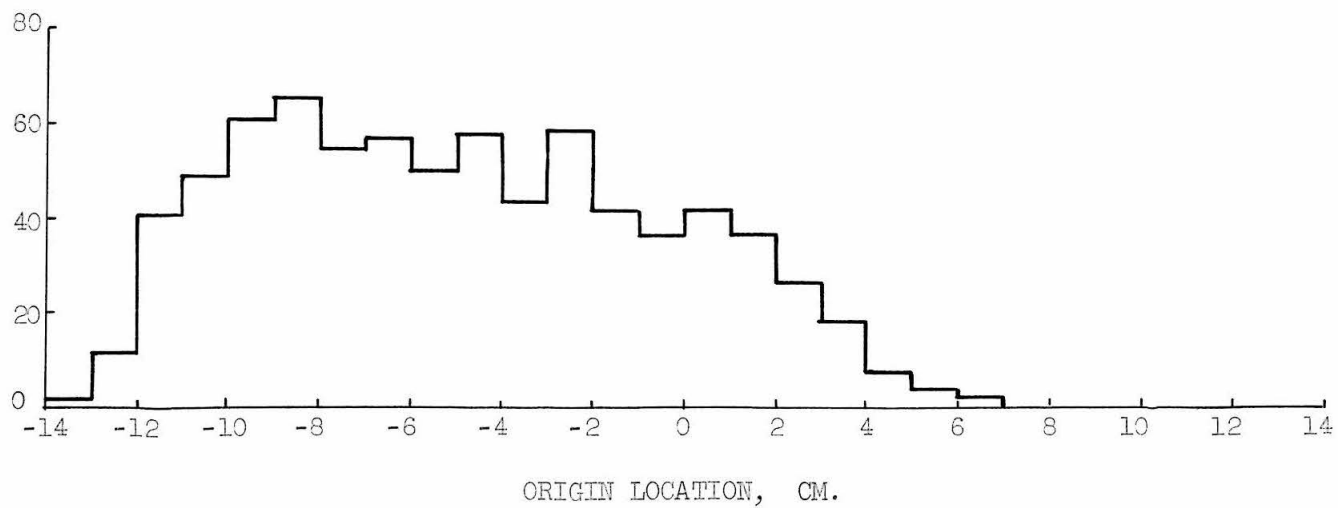
FIGURE A IX-1

Accepted Event Origin Distribution

Beam tube outline is shown above for reference.



EVENTS



Incoming gamma energies were chosen randomly in accordance with the bremsstrahlung gamma energy distribution. For program testing where the actual distribution was not so important the gamma energy spectrum function $B(K, E_0)$ ⁴⁵⁾ was taken to be constant, but for model comparison with data $B(K, E_0)$ was calculated by interpolating the spectrum downstream of the lithium hydride as computed by BPAK³⁷⁾ (see Appendix I for details of this computation).

The diparticle could either be chosen to contain the two pions, or the proton and a pion. Diparticle mass could then be randomly chosen according to the invariant phase space distribution⁵⁷⁾

$$P(M^2) dM^2 = \frac{R_2(P; M, m_3) R_2(M; m_1, m_2)}{R_3(P; m_1, m_2, m_3)} dM^2$$

or the Breit-Wigner resonance distribution with an energy-dependent width³⁸⁾

$$P^1(M^2) dM^2 = C P(M^2) \frac{M}{q} \frac{\Gamma(M)}{(M^2 - M_0^2)^2 + M_0^2 \Gamma^2(M)} dM^2.$$

In these expressions M is the diparticle mass, m_1 and m_2 the masses of the components of the diparticle, m_3 the other final state particle mass, P the total system invariant mass, C a normalization constant, q the 3-momentum of particle 1 or 2 in the diparticle COM system, M_0 the mass of the resonance, and $\Gamma(M)$ is the energy-dependent width of the resonance.

Both polar decay angles could be randomly chosen from probability distributions given by polynomials ranging up to sixth power in

the cosine of the angle. The azimuthal diparticle decay angle could be uniformly distributed or first power in the cosine of the angle from the normal to the diparticle production plane. In practice, these distributions were usually taken uniform.

After event selection, the three tracks were developed into the bubble chamber. Multiple Coulomb scattering could be applied to the tracks in the steel and freon, or it could be ignored. If it was used, steps were taken such that the root mean square lateral displacement would be 0.01 cm, and at the end of each step the direction was changed randomly consistent with the expected angular distribution⁵²⁾ for a step of that size. The range-energy relationship was applied continually throughout track development to keep track of the stopping point and the current energy for multiple scattering purposes. While in the visible region of the chamber, occasional points could be recorded to act as track measurements; these points were then translated back to their film image locations, and random "measurement errors" applied before they were punched onto cards to simulate data. These "visible" points were chosen such that the relative error in track length due to the track segmentation would be 0.02 percent, then a fraction of them based on the number chosen were taken as data (one out of six if there were many); this was done in an attempt to duplicate the decisions made by someone analyzing an event as to where to measure points (which was usually related to track curvature). On very straight tracks the computer, like the analyzer, was instructed to take the first visible point, the last visible point, and a mid-point. On

the average the computer seemed to pick the same number of points as the analyzers, but its choice of second point and next-to-last point on the track was a little more erratic than theirs, occasionally resulting in larger errors in initial track direction and multiple scattering measurement than an analyzer would have made. The major effect of these larger errors would be to increase background acceptance, so that the background rates quoted in Appendix VI might be slightly high.

Each track was tested for whether it would be visible, and event acceptance could be based on whether one, two, or all three tracks were visible (fewer than three tracks being visible was useful in background studies). The distribution of track lengths in the chamber projected onto the plane of sight was plotted for all accepted events, and the average minimal lengths are given in Table A IX-1. Track visibility then could be based on seeing the track at all, or its having the appropriate minimum length.

In addition to pion pair production, the program could also generate single pion events and triple pion events. For single pion production the gamma energy was chosen from a distribution that averaged π^+ and π^0 cross-sections^{58, 59}, taking into account the bremsstrahlung distribution and the first resonance. Triple pion generation had the gamma energy taken from the bremsstrahlung distribution, and two intermediate particle masses chosen from phase space distributions. All directional distributions were taken isotropic. All particles generated were considered charged so that each generated event might represent a sum of several processes, saving

computer time. The program could variously be run to generate a pion pair event with all three prongs visible, a triple pion event with all four prongs visible, a pion pair with two visible prongs plus a single pion event (at least one visible prong) with its origin within 2 cm of the pion pair origin, or a pion pair with one visible prong plus two single pion events, each having at least one visible prong and originating within 2 cm of the pion pair.

Most chamber parameters were determined by direct measurement. As discussed in Appendix IV, the beam depth was determined from the valid event origin distribution. One parameter yet was needed for event generation - the "rubber bag radius", i.e., the effective edge of the chamber where the lighting cut off. Lighting intensity measurements indicated that lighting at beam depth was full strength out to a radius of about 10 cm, gone at 12 cm, but gave little hint of where to establish a cutoff in between. A radial distribution of track end points corrected to beam depth agreed beautifully with the above conclusions and was equally ambiguous. Finally it was discovered that the shape of the generated event origin distribution was sensitive to this quantity. Best agreement with Figure A IX-1 yielded a value of 11.0 ± 0.4 cm for the effective chamber radius at beam depth.

A summary of qualities combined in the principal applications of this program is given below.

A. Event Reconstruction Program Testing

100 pion pair events, 20 triple pion events, 180 two-prong pion pair plus one single pion events, and 130 single-prong pion pair plus two single pion events were generated and run with the

reconstruction program. In the pion pair generations dipion masses were phase space selected and all directional distributions were taken to be isotropic. Multiple scattering was included in track generation. Minimum track length was set to zero so that no bias would be introduced against short tracks.

B. Model Comparison and Chamber Efficiency

Diparticle mass and directional distributions for pion pairs generated here depend on the particular model being studied. To save computer time, no track multiple scattering was included since these events were not being analyzed by the reconstruction program. The minimum track lengths given in Table A IX-1 were used to approximate scanning biases as closely as possible.

Table A IX-1

Average Minimum Projected Track Length*

for Valid Events

	Stopping	Non-Stopping
Protons	0.5	1.5
Pions	0.5	2.0

* Track length in cm projected onto plane of sight in bubble chamber.

REFERENCES

1. V.Z. Peterson and I.G. Henry, Phys. Rev. 96, 850 (1954).
2. M. Sands, M. Bloch, J.G. Teasdale and R.L. Walker, Phys. Rev. 99, 652 (1955).
3. V.Z. Peterson, Bull. Am. Phys. Soc. Series II, 1, 173 (1956).
4. R.M. Friedman and K.M. Crowe, Phys. Rev. 105, 1369 (1957).
5. M. Bloch and M. Sands, Phys. Rev. 108, 1101 (1957).
6. M. Bloch and M. Sands, Phys. Rev. 113, 305 (1959).
7. D.D. Elliott, Ph.D. Thesis, California Institute of Technology, 1959.
8. J.M. Sellen, G. Cocconi, V.T. Cocconi, and E.L. Hart, Phys. Rev. 113, 1323 (1959).
9. B.M. Chasan, G. Cocconi, V.T. Cocconi, R.M. Schectman, and D.H. White, Phys. Rev. 119, 811 (1960).
10. J.R. Kilner, R.E. Diebold, and R.L. Walker, Phys. Rev. Letters 5, 518 (1960).
11. S.D. Drell, Phys. Rev. Letters 5, 278 (1960).
12. K. Itabashi, Phys. Rev. 123, 2157 (1961).
13. A.R. Erwin, R. March, W.D. Walker, and E. West, Phys. Rev. Letters 6, 628 (1961).
14. D. McLeod, S. Richert, and A. Silverman, Phys. Rev. Letters 7, 383 (1961).
15. L.M. Brown and P. Singer, Phys. Rev. 133, B812 (1964).
16. K. Nishijima, Phys. Rev. Letters 12, 39 (1964).
17. N.P. Samios, A.H. Bachman, R.M. Lea, T.E. Kalogeropoulos, and W.D. Shephard, Phys. Rev. Letters 9, 139 (1962).
18. R. Del Fabbro, M. De Pretis, R. Jones, G. Marini, A. Odian, G. Stoppini, and L. Tau, Phys. Rev. Letters 12, 674 (1964).
19. R. Del Fabbro, M. de Pretis, R. Jones, G. Marini, A. Odian, G. Stoppini, and L. Tau, Phys. Rev. 139, B701 (1965).

20. H.R. Crouch, Jr., et al. Phys. Rev. Letters 13, 636 and 640 (November 1964).
21. H.R. Crouch, Jr., et al. Proceedings of the International Symposium on Electron and Photon Interaction at High Energies, Hamburg (1965), to be published.
22. U. Brall et al., "Photoproduction of Pion and Nucleon Resonances at Energies up to 5.5 GeV", DESY report 65/11, September 1965.
23. P. Stichel and M. Scholz, Nuovo Cimento 34, 1381 (1964).
24. S.M. Berman and S.D. Drell, Phys. Rev. 133, B791 (1964).
25. R.E. Cutkosky and F. Zachariasen, Phys. Rev. 103, 1108 (1956).
26. P. Carruthers and H. Wong, Phys. Rev. 128, 2382 (1962).
27. H. Joos and G. Kramer, Zeitschrift fur Physik 178, 542 (1964).
28. L. Guerriero, H. Mark, I.A. Pless, L. Rosenson, Y. Shapira, A. Tuchman, and R.K. Yamamoto, Review of Scientific Instruments 31, 1040 (1960).
29. J.H. Mullins, Ph.D. Thesis, California Institute of Technology, 1959.
30. E.D. Alyea, Jr., Ph.D. Thesis, California Institute of Technology, 1962.
31. J.H. Mullins, E.D. Alyea, Jr., and J.M. Teem, "A Pulsed-Resonant-System Bubble Chamber," Instrumentation Conference for High Energy Physics, Lawrence Radiation Laboratory, Berkeley, California, 1960 (Interscience Publishers, New York, London).
32. H. Cramer, Mathematical Methods of Statistics (Princeton University Press, Princeton, New Jersey (1958), p. 498.
33. J. Orear, UCRL-8417 (1958), unpublished.
34. W.C. Davidon, ANL-5990 Rev. (1959), unpublished.
35. U. Maor, private communication.
36. H.A. Thiessen, "A Re-Calibration of the Beam Energy Meter", CTSL Internal Report 21, Feb. 14, 1966 (unpublished).
37. F. Wolverton, private communication.

38. J.D. Jackson, Nuovo Cimento 34, 1644 (1964).
39. Aachen, Birmingham, Bonn, Hamburg, London, Munich Collaboration, Nuovo Cimento 31, 485 (1964).
40. N.N. Biswas, I. Derado, N. Schmitz, and W.D. Shephard, Phys. Rev. 134, 901 (1964).
41. A.R. Erwin, R. March, W.D. Walker, E. West, Phys. Rev. Letters 6, 628 (1961).
42. E. Pickup, D.K. Robinson, E.O. Salant, Phys. Rev. Letters 7, 192 (1961).
43. J. Kirz, J. Schwartz, and R.D. Tripp, Phys. Rev. 130, 2481 (1963).
44. E.L. Hart, and D.H. White, Rev. Sci. Instr. 31, 33 (1960).
45. R. Gomez, Beam Monitoring at the Caltech Synchrotron (1962), unpublished.
46. H.A. Thiessen, private communication.
47. H. Cramer, Mathematical Methods of Statistics (Princeton University Press, Princeton, New Jersey, 1958) p. 234.
48. A.D. MacInturff, private communication.
49. C.W. Peck, Ph.D. Thesis, California Institute of Technology, 1964.
50. R.L. Anderson, E. Gabathuler, D. Jones, B.D. McDaniel, and A.J. Sadoff, Phys. Rev. Letters 9, 131 (1962).
51. A.D. MacInturff, Ph.D. Thesis, Vanderbilt University, 1964.
52. B. Rossi, High Energy Particles (Prentice-Hall, Inc., New York, 1952), p. 63-77.
53. B. Rossi, High Energy Particles (Prentice-Hall, Inc., New York, 1952), p. 22-37.
54. R.M. Sternheimer, Phys. Rev. 115, 137 (1959); and Phys. Rev. 103, 511 (1956).
55. W.H. Barkas, "Range Measurements of Singly and Multiply Charged Particles in Emulsion", Proceedings Informal Conference, Gatlinburg, Tenn., Sept., 1958 (1960).
56. K.R. Symon, Ph.D. Thesis, Harvard University (1948).

57. R. Hagedorn, Relativistic Kinematics (W.A. Benjamin, Inc., New York, 1964), Chapter 7.
58. C.R. Clinesmith, private communication.
59. J.R. Kilner, Ph.D. Thesis, California Institute of Technology, 1963.